Single-pixel Imaging: development and applications of adaptive methods

Florian Rousset

PHD OF THE UNIVERSITÉ DE LYON

performed within

the Institut National des Sciences Appliquées de Lyon

in an international co-agreement with

the Politecnico di Milano

defended publicly on October 27th, 2017 by

Florian ROUSSET

SINGLE-PIXEL IMAGING: DEVELOPMENT AND APPLICATIONS OF ADAPTIVE METHODS

in front of the jury composed of:

Richard BARANIUK	University of Rice	Reviewer
Charles SOUSSEN	CentraleSupélec	Reviewer
Simon ARRIDGE	University College London	Examinator
Paola TARONI	Politecnico di Milano	Examinator
Cosimo D'ANDREA	Politecnico di Milano	PhD co-director
Nicolas DUCROS	INSA Lyon	PhD co-director
Françoise PEYRIN	INSERM	PhD director

Centre de Recherche en Acquisition et Traitement de l'Image pour la Santé (CREATIS) – Lyon
Dipartimento di Fisica, Politecnico di Milano – Milan

ACKNOWLEDGMENTS

I would first like to express my deepest appreciation to my three Supervisors, Françoise Peyrin, Nicolas Ducros, and Cosimo D'Andrea.

I thank Françoise for accepting to act as my PhD Director. This gave me the opportunity to benefit from her broad experience, and her reviews and advice during my research work. Although setting up the videoconferencing was quite tricky, our meetings were always very constructive and fruitful, which undoubtedly contributed to the success of my Project.

I express my special thanks to Nicolas, who was by my side at CREATIS and has always been here to answer my questions. His knowledge in optics, and image processing in general, has been a great help throughout these 3 years. His scientific rigor, enthusiasm, and passion were a source of motivation and will surely bring success to his accepted project in single-pixel imaging. I also thank him for giving me the opportunity to do some teaching hours at INSA.

I wish to thank Cosimo, without whom I could not have performed any of the experimental acquisition presented in this thesis. My somewhat basic knowledge in optics was definitely not enough to understand everything, but Cosimo always made things clear with simple, yet efficient, explanations. I am also grateful for the help Cosimo provided upon my arrival in Milan, regarding paperwork and housing.

I would like to express my gratitude to Isabelle Magnin, for welcoming me to the CREATIS laboratory, which she managed until 2015, to Olivier Beuf, who followed as CREATIS Director, and to Franco Ciccacci, Head of the Dipartimento di Fisica at the Politecnico di Milano. They all gave me the opportunity to conduct my work in friendly and peaceful environments.

Furthermore, I would also like to acknowledge with much appreciation the roles of Andrea Farina and David Rousseau. Andrea's help during my time in Milan regarding the setting up of the experimental acquisition was crucial. David provided some optical equipment and knowledge without which the single-pixel camera set-up at CREATIS would not have been implemented.

I would like to express my gratitude to the members of the Jury for accepting to be part of it. My special thanks go to Richard Baraniuk and Charles Soussen, for taking the role of Reviewers of my thesis. Their insightful comments and suggestions undoubtedly helped me to improve the quality of my thesis.

I finally give my warmest thanks to everyone I had the opportunity to meet or interact with at

CREATIS and at the Politecnico di Milano.

I am grateful to my office mates in Lyon : Anca, Miaomiao, Manu, Rémi, Paul, Tom, and Matthieu. They were always respectful and quiet, which created a very propitious environment for work. I thank Laure, Eric, and Simon for some good city sightseeing during the ISBI'16 Conference in Prague, Pierre for giving me tons of TV series/ movies to watch, Juan for offering the opportunity to help in the experiments at the European synchrotron (ESRF), and Pierrick for all of the paperwork he completed for me. I would also like to acknowledge the pleasure I had in teaching practicals alongside Sarah, Thomas, Olivier, Philippe, and Nicolas.

On the Italian side, I had the chance to share two offices during two different stays. I thank my first office buddies Sara M., Laura, and Sanathana, also known as the three minions, for a very fun 6-month stay; although not as quiet as my office in Lyon, it was still as enjoyable. My second batch of office mates also get my thanks for leaving me the responsibility of the AC remote during the crazy summer heat of Milan : Rebecca, Lina, and Marta (for AC) vs Alessia C. and Edo (against AC). I also thank the people often present on the terrace on the 5th floor for lunch : Maurizio, Alessia A., Sara B., and Andrea B.. Finally, I give my gratitude to Paola Taroni, who made possible the joint PhD agreement and always helped me with my paperwork and courses in Milan.

This is also the opportunity for me to thank and acknowledge the numerous sources of funding for this PhD Project, with the main grant provided by the VINCI program of the Université Franco-Italienne. It was also supported in part by Cariplo Foundation, under Grant 20130615, LASERLAB-EUROPE, under Grant 284464, and the EC Seventh Framework Programme.

I was fortunate enough to attend and participate in the ISBI 2016 and SPIE Photonics West 2017 International Conferences thanks to the EEA Doctoral School and Labex Primes (ANR-22-LABX-0063) of the Université de Lyon ("Investissements d'Avenir", ANR-11-IDEX-0007; operated by the French National Research Agency), which covered my expenses for attendance at these conferences (EEA for ISBI; Primes for SPIE). I further acknowledge the France Life Imaging (FLI) infrastructure, which covered my inscription for the RITS 2015 National Congress, GDR-Isis for my travels to JIONC (2015, 2016, 2017), and the CNRS throughout the Monopix+ Project, which allowed me to attend a Summer School on "Structured Regularization" in Paris, and to travel to GRETSI in 2017.

My two stays in Milan were also supported by the PALSE program (May to October, 2015), and by the Région Rhône-Alpes (June to November, 2016). This funding allowed me to go to Milan twice, to conduct the experimental part of my PhD Project.

ABSTRACT

SINGLE-PIXEL IMAGING is a recent paradigm that allows the acquisition of images at reasonably low cost by exploiting hardware compression of the data. The architecture of a single-pixel camera consists of only two elements : a spatial light modulator, and a single-point detector. The key idea is to measure the projection at the detector (i.e., the inner product) of the scene under view –the image– with some patterns. The post-processing of a sequence of measurements obtained with different patterns permits the restoring of the desired image.

Single-pixel imaging has several advantages, which are of interest for different applications, and especially in the biomedical field. In particular, a time-resolved single-pixel imaging system benefits fluorescence lifetime sensing. Such a set-up can be coupled to a spectrometer, to supplement the lifetime with spectral information. However, the main limitation of single-pixel imaging is the speed of acquisition and/or image restoration, which is, as of today, not compatible with real-time applications.

This thesis investigates fast acquisition/ restoration schemes for the targeting of biomedical applications using a single-pixel camera. First, a new acquisition strategy is reported, based on wavelet compression algorithms. This shows that these algorithms can significantly accelerate image recovery, compared to conventional schemes of the compressive sensing framework. Secondly, a novel technique is proposed to alleviate an experimental positivity constraint of the modulation patterns. With respect to the classical approaches, the proposed nonnegative matrix-factorization-based technique halves the number of patterns sent to the spatial light modulator, and hence halves the overall acquisition time. Finally, the applicability of these techniques is demonstrated for multispectral and/or time-resolved imaging, which are common modalities in biomedical imaging.

KEY-WORDS : Single-pixel imaging, wavelets, nonnegative matrix factorization, multispectral measurements, time-resolved measurements, fluorescence lifetime imaging

RÉSUMÉ

L'IMAGERIE MONO-PIXEL est un concept récent qui permet l'obtention d'images à un coût relativement faible par une compression des données durant l'acquisition. L'architecture d'une caméra mono-pixel comprend seulement deux éléments, un modulateur spatial de la lumière et un détecteur ponctuel. L'idée est de mesurer, au niveau du détecteur, la projection de la scène observée –l'image– avec un certain motif. Le post-traitement d'une séquence de mesures obtenues avec différents motifs permet de restaurer l'image de la scène.

L'imagerie mono-pixel possède plusieurs avantages qui sont d'un intérêt pour différentes applications, en particulier dans le domaine biomédical. Par exemple, une caméra mono-pixel résolue en temps bas coût est bénéfique pour l'imagerie de temps de vie de fluorescence. Un tel système peut également être couplé à un spectromètre afin de compléter le temps de vie avec une information spectrale. Cependant, la limite principale de l'imagerie mono-pixel est la vitesse d'acquisition et/ou de l'étape de restauration d'image qui est, à ce jour, non compatible avec des applications temps réel.

Le but de cette thèse est de développer des méthodes rapides d'acquisition et de restauration des images à visée d'applications biomédicales. Tout d'abord, une stratégie d'acquisition basée sur les algorithmes de compression dans le domaine ondelettes est proposée. Celle-ci accélère le temps de restauration de l'image par rapport aux schémas d'acquisition classiques basés sur l'acquisition comprimée. Dans un second temps, une nouvelle méthode pour lever une contrainte expérimentale de positivité sur les motifs est détaillée. Comparée aux approches classiques, cette méthode basée sur une factorisation en matrices non-négatives permet de diviser par deux le nombre de motifs envoyés au modulateur spatial de la lumière, entrainant ainsi une division par deux du temps d'acquisition total. Enfin, l'applicabilité de ces techniques est démontrée pour de l'imagerie multispectrale et/ou résolue en temps, modalités courantes dans le domaine biomédical.

MOTS-CLÉS : Imagerie mono-pixel, ondelettes, factorisation en matrices non-négatives, mesures multispectrales, mesures résolues en temps, imagerie du temps de vie de fluorescence.

N.B. : un résumé étendu en français est donné en Annexe C.

RIASSUNTO

L'ACQUISIZIONE di immagini tramite single-pixel camera è un concetto recente che permette di ottenere immagini ad un costo relativamente basso e di realizzare la compressione dei dati durante l'acquisizione. L'architettura di una single-pixel camera comprende due soli elementi : un modulatore spaziale di luce ed un sensore puntuale. L'idea consiste nel modulare la scena osservata (immagine) con un certo pattern luminoso e di focalizare la luce in uscita dal campione sul sensore. Infine, elaborando la sequenza di misure ottenute con diversi pattern è possibile ricostruire l'immagine desiderata.

L'acquisizione di immagini tramite single-pixel camera presenta diversi vantaggi per varie applicazioni ed in particolare nel campo biomedicale. Ad esempio, permette di realizzare un sistema di imaging risolto nel tempo a basso costo per la mappatura del tempo di vita di fluorescenza. Tale configurazione può anche essere accoppiata ad uno spettrometro aggiungendo, così, l'informazione spettrale. Tuttavia, la limitazione principale della single-pixel camera è la velocità di acquisizione e/o ricostruzione delle immagini che, ad oggi, non è compatibile con le applicazioni che richiedono di essere realizzate in tempo reale.

Lo scopo di questa tesi di dottorato è lo sviluppo di metodi rapidi di acquisizione e ricostruzione delle immagini per applicazioni in campo biomedico. In primo luogo, si propone una strategia di acquisizione delle immagini sulla base di algoritmi di compressione nel dominio wavelet. Questo approccio permette di ricostruire più velocemente l'immagine rispetto ai metodi di acquisizione tradizionali basati sul compressed sensing. In secondo luogo, un altro metodo permette di utilizzare solo patterns positivi. Rispetto agli approcci tradizionali, questo metodo basato sulla fattorizzazione matriciale non-negativa permette di dimezzare il numero di pattern inviati al modulatore spaziale di luce e, quindi, il tempo complessivo di acquisizione. Infine, l'applicabilità di queste tecniche è dimostrata nel campo dell'imaging biomedico tramite misure multispettrali e/o risolte nel tempo.

PAROLE CHIAVE : Single-pixel camera, wavelet, fattorizzazione matriciale non-negativa, misure multispettrali, misure risolte nel tempo, imaging del tempo di vita di fluorescenza.

TABLE OF CONTENTS

List of Figures

LIST OF TABLES

ACRONYMS & ABBREVIATIONS

Abbreviation or acronym	Signification
ABS	Adaptive Basis Scan
ABS-WP	Adaptive Basis Scan by Wavelet Prediction
BS	Basis Scan
ADC	Analog-to-Digital Converter
CCD	Charge Coupled Device
CMOS	Complementary Metal Oxide Semiconductor
CS	Compressive Sensing
DCT	Discrete Cosine Transform
DMD	Digital Micromirror Device
FFT	Fast Fourier Transform
LCD	Liquid Crystal Display
LCoS	Liquid Crystal on Silicon
LED	Light-Emitting Diode
MMA	Metamaterial Absorber
NMF	Nonnegative Matrix Factorization
PMT	Photomultiplier
PSNR	Peak Signal-to-Noise Ratio
PWM	Pulse Width Modulation
RIP	Restricted Isometry Property
SFDI	Spatial Frequency Domain Imaging
SLM	Spatial Light Modulator
SNMF	Semi Nonnegative Matrix Factorization
SNR	Signal-to-Noise Ratio
SPC	Single-Pixel Camera
SPD	Single Point Detector
SPI	Single-Pixel Imaging
TCSPC	Time-Correlated Single Photon Counting
TOF	Time-of-flight
TR	Time-resolved

NOTATIONS & SYMBOLS

General conventions

x and X	are two scalars
$\mathbf{x}$	is a column vector
$\mathbf{X}$	is a matrix

Mathematical sets

$\mathbb{N}$	set of natural elements
$\mathbb{Z}$	set of integers
$\mathbb{R}$	set of real elements
$\mathbb{R}_+$	set of non-negative real elements i.e. $\{x \in \mathbb{R} \quad \text{s.t.} \quad x \geq 0\}$
$\mathbb{R}^{K\times 1}$	set of vectors with K real elements
$\mathbb{R}_+^{K\times 1}$	set of vectors with K non-negative real elements
$\mathbb{R}^{K\times I}$	set of matrices with K rows and I columns of real elements
$\mathbb{R}_+^{K\times I}$	set of matrices with K rows and I columns of non-negative real elements

Vectors and matrices

x_n or $(\mathbf{x})_n$	n-th element of the vector $\mathbf{x}$
$\mathbf{x}_n$	n-th column of the matrix $\mathbf{X}$
$X_{i,j}$ or $(\mathbf{X})_{i,j}$	element at the i-th row and j-th column of $\mathbf{X}$
$\mathbf{X}_{\vert n}$	matrix $\mathbf{X}$ deprived of its n-th column
$\mathbf{X}_{-n}$	matrix $\mathbf{X}$ deprived of its n-th row
$\mathbf{x}^\top$	transpose of the vector $\mathbf{x}$ (row vector)
$\mathbf{X}^\top$	transpose of the matrix $\mathbf{X}$
$\text{tr}(\mathbf{X})$	trace of the matrix $\mathbf{X}$
$\mathbf{X}^{-1}$	inverse of the matrix $\mathbf{X}$

INTRODUCTION

SINGLE-PIXEL IMAGING (SPI) is a trendy paradigm that allows the acquisition of images at reasonably low cost, and with hardware compression of the data. The architecture of a *single-pixel camera* (SPC) indeed consists of only two elements : a spatial light modulator, and a single-point detector. The key idea is to modulate the image that is observed with a certain pattern, and to collect the corresponding measurements at the single detector. The desired image can then be restored by post-processing the sequence of measures performed with several patterns.

Probably, the first concept of modulation of a light field and collection of the output light on a single detector was reported in 1982, through the work of Ben-Yosef *et* Sirat. They proposed to use the piezoelectric-elasto-optic effect of crystals for modulation, such that the light output is proportional to the Fourier transform of the imaged object. However, at that time, building small and numerous crystals was not as accessible as it is today, and Ben-Yosef *et* Sirat only provided proof of concept with a few crystals, without restoring an image of the object. As a result, the credit for the SPC has been attributed to Rice University, where the first SPC images were obtained almost 25 years later. At that time, the pioneering idea of *compressive sensing* (CS) proposed by Donoho in 2006 opened the door for Takhar *et al.* to use the SPC with random patterns in the same year, to reconstruct an image using a ℓ_1-minimization algorithm. Since then, the algorithms have evolved, and new acquisition strategies have been proposed, and the SPC has found many different applications.

At first glance, having a single pixel can appear to be counterproductive, as the cameras of today embed several millions of pixels. However, several advantages stand out when compared to cameras based on an array of sensors (i.e., CCD or CMOS cameras architectures). First, single-point detectors usually have high efficiency, and can therefore detect weak light intensity changes (Hadfield, 2009). In medical applications, this can be very useful, as tissue absorption is usually quite high (Jacques, 2013). Secondly, there is intrinsic compression at the hardware level when using a SPC, which hence needs small storage memory. This is a key advantage in applications where the data rate for transmission would be low, such as remote-imaging applications (e.g., aerospace remote sensing) (Ma, 2009b,a). Finally, a single-point sensor imaging device is usually less expensive than a sensor-array-based camera. The SPC is therefore well suited to infrared imaging (Shin *et al.*, 2016), where the use of a conventional imaging system that operates at these wavelengths would be costly (Rogalski, 2012).

The latter advantages of SPI and the nonionizing nature of the optical imaging makes the SPC an excellent candidate for biomedical imaging applications. For instance, a low-cost, time-resolved imaging system can benefit fluorescence lifetime imaging (Becker, 2012), by coupling the point de-

tector with a photon-counting board (Pian *et al.*, 2016a; Rousset *et al.*, 2017b). Adding a spectrometer further allows a complete multispectral time-resolved system to be obtained (Pian *et al.*, 2016b), to supplement the lifetime information of tissues with its spectral content.

The SPC can also be used for imaging through scattering media (Tajahuerce *et al.*, 2014; Duran *et al.*, 2015), for diffuse optics (e.g., skin lesion detection or intraoperative (Gibson *et* Dehghani, 2009)), for ophthalmology (Lochocki *et al.*, 2016, 2017), and to characterize tissue properties using near infrared illumination (Torabzadeh *et al.*, 2017). The SPC has also been successfully transposed on a microscope (Studer *et al.*, 2012; Radwell *et al.*, 2014; Rodriguez *et al.*, 2016). Through exploiting several SPC images, this can provide fluorescence molecular tomography and diffuse optical tomography (D'Andrea *et al.*, 2010; Ducros *et al.*, 2013; Pian *et al.*, 2015; Ducros *et al.*, 2016), with applications for molecular imaging and oximetry.

The goal of this thesis is to investigate SPI for biomedical applications. One of the main limitations of the SPC in these last cited studies is the speed of acquisition and/or image restoration. In such cases, real-time applications cannot be considered, which rules out interventional imaging (e.g., fluorescence-guided surgery), for instance. Therefore, for biomedical imaging using a SPC, it is necessary to develop specific techniques for acquisition and/or restoration.

To meet the goals of this thesis, a new acquisition strategy for SPC was proposed to reduce the reconstruction times, along with an alternative innovative technique to reduce the acquisition times. The applicability of these techniques for medical imaging is demonstrated for multispectral and/or time-resolved measurements.

This Project was performed as a joint agreement between INSA Lyon and the Physics Department of the Politecnico di Milano (Polimi), to fund a PhD in each of these institutions (PhD in signal/image processing for INSA; PhD in Physics for Polimi). The experimental part was carried out at Polimi, where a SPC set-up is available. The algorithms and methodologies were conducted within the CREATIS laboratory, which has a long history of dealing with signal-processing techniques for medical imaging.

This thesis is divided into six Chapters. The first two Chapters define the general principles of SPI, with the related state-of-the-art in the field. The remaining four Chapters are aimed at answering the problematics of this thesis through different contributions. These Chapters contain some parts of personal publications, as listed in Appendix D.

In Chapter I, the SPC concept is detailed, with several possible implementations. Many different applications for the use of this device are presented, as well as new trends in SPI.

In Chapter II, the mathematical formulation of SPC acquisition is given, to present the possible acquisition/ restoration strategies proposed along the years. Two main categories of techniques stand out : the *nonadaptive* one, which belongs to the CS framework, and the *adaptive* ones, where some measurements are performed based on previous measures. This Chapter ends with a conclusion as to the state-of-the-art with respect to this thesis problem.

In Chapter III, the two experimental set-ups involved in the results of the next Chapters are presented. One is the optical set-up at the Politecnico di Milano, to which some improvements were made to control the different instruments. The second system is the one that was implemented in

the CREATIS laboratory.

In Chapter IV, our proposed acquisition strategy is reported, which is referred to as *adaptive basis scan by wavelet prediction* (ABS-WP). The wavelet transform for two-dimensional (2D) images is detailed before defining the proposed acquisition strategy based on fast interpolations and multiresolution approximations. Simulated and experimental data show the efficiency of ABS-WP, compared to some of the other SPC acquisition techniques highlighted in Chapter II. This Chapter mainly contains an article published in *IEEE Transactions on Computational Imaging* in 2017 (Rousset *et al.*, 2017a).

In Chapter V, a method to halve the number of measurements is proposed. This was designed because patterns with both positive and negative entries cannot be implemented on a spatial light modulator. To deal with this technique, it is common to separate the pattern into its positive and absolute negative parts, whereby the subtraction of these two measurements provides the desired measurement. This, however, doubles acquisition times, as twice the number of measurements need to be performed. In this Chapter, the problem is formalized, with the demonstration that a *semi nonnegative matrix factorization* (SNMF) algorithm can be used to overcome the experimental constraints, and therefore to reduce the necessary number of measurements. The data presented in this Chapter were filed as a patent (Rousset *et al.*, 2017c) and submitted to *IEEE Transactions on Computational Imaging* (Rousset *et al.*, 2017d).

In Chapter VI, the SPC with the techniques developed in the previous chapters is used for applications that can benefit biomedical imaging. A temporal dimension was added to the SPC to perform fluorescence lifetime sensing, with this lifetime being an important parameter for biologists to assess the tissue micro-environment (e.g., pH). These data were presented at the *SPIE Photonics West* Conference in February 2017 (Rousset *et al.*, 2017b). Then, a spectral dimension was further added, to obtain multispectral, time-resolved measurements. The obtained SPC system coupled to our acquisition strategy of Chapter IV allows complete differentiation between the different components of the imaged object using the spectral and temporal information. These data will soon be submitted for publication in *Optics Express*.

CHAPTER I

THE SINGLE-PIXEL CAMERA

Contents

CHAPTER I

THE term single-pixel camera (SPC) encompasses various hidden ideas and possible optical implementations. The goal of this Chapter is to provide the main concepts behind the SPC, along with its possible hardware implementations defined through the years. Some applications where the SPC is a key element are presented, as well as new trends in the optical field where the use of a SPC is relevant.

I.1 Concept

The theory and data from Donoho in 2006 on *compressive sensing* showed that a signal can be recovered from only a small number of projections, revisiting the standard Shannon-Nyquist sampling theorem. This enabled Takhar *et al.* to propose a new camera architecture in the same year that was based on a single-point detector, and to build a compressive imaging system (Duarte *et al.*, 2008; Baraniuk *et al.*, 2014; Miao *et* Amirparviz, 2015). Such a system measures one-dimensional (1D) data instead of the classical 2D data from a conventional sensor array (e.g., CCD or CMOS cameras). A *spatial light modulator* (SLM) is placed between the scene under view – the image – and the *single-point* (i.e., pixel) *detector* (SPD), so as to modulate the light coming out of the scene, and to collect the corresponding projection at the sensor. Sequential measurements are taken with different patterns loaded on the SLM, and the post-processing of the data allows image recovery of the scene under view [1].

The simplest implementation of the SPC can be schematized as in Fig. I.1, where the SLM is either a transmissive device or a reflective one, depending on the technology employed. The image of

1. The different acquisition/ restoration schemes for SPI are detailed in the next Chapter.

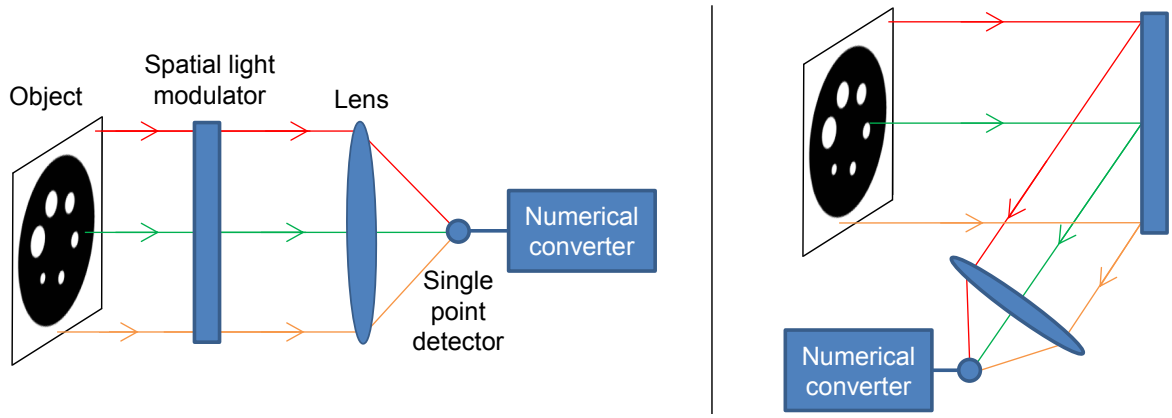

FIGURE I.1 – Optical set-up of the single-pixel camera using a transmissive spatial light modulator (left), or a reflective one (right).

the object/ scene under view is formed in the SLM plane, and a lens is added to focus the modulated light rays on the single-point detector. A numerical converter is used to obtain the numerical data from the single-point detector. Note that the positions of the SLM and the object are interchangeable. If the SLM is placed before [2] the object, it is said to modulate the light in illumination, if it is placed after, the detection side is modulated.

I.2 Hardware implementation

Many different hardware implementations of the SPC have been proposed through the years. Depending on the desired applications, specific technologies should be chosen to obtain the best from the SPC. This section provides some examples [3] of the most used SLM and SPD technologies, as well as the different means to obtain numerical measurements to process these data.

I.2.1 Spatial light modulators

DMD The original work of Takhar *et al.* and Duarte *et al.* used a *digital micromirror device* (DMD; Fig. I.2a), which was invented by Hornbeck at *Texas Instruments* in 1987. Such a device comprises thousands of tiny mirrors that are arranged in a matrix array of size $H \times W$. The value of H (resp. W) typically ranges from 768 (resp. 1024) to 1600 (resp. 2560), with a mirror pitch of 7 to 14 μm, which depends on the model. Each of the mirrors is independently controlled and can be tilted into two positions. At +12°, the so-called ON state reflects the light towards the detector, and is therefore collected by the detector. At −12°, the OFF state sends the light in the opposite direction. The DMD can thus load binary patterns where a 0 corresponds to the OFF state and a 1 to the ON state. The DMD also offers the possibility to load 8-bit gray-level patterns using the principle of *pulse width modulation* (PWM). For this, a single 8-bit pattern is separated into the corresponding 8 binary bit planes. Each of these is associated to a particular display time that is a multiple of a power of 2, to recreate an 8-bit pattern. More details about the PWM for DMD are given in Appendix A.

LCD In 2013, Huang *et al.* used a *liquid crystal display* (LCD; Fig. I.2b) panel as a transmissive [4] SLM. This kind of device uses polarizing filters, and the properties of the liquid crystal orientations were tuned using an electric field. Each of the $H \times W$ pixels (i.e., crystals) of this system are arranged in a matrix and can also take two states. The difference with the DMD is that the ON state corresponds to a transparent element, which lets the light pass to the detector, whereas the OFF state represents an opaque element. Values for H and W cover a vast range, with LCDs encountered in everyday life, from calculators to television screens.

MMA Watts *et al.* in 2014 proposed an in-house SLM defined as a liquid crystal *metamaterial* [5] *absorber* (MMA; Fig. I.2c) SLM. A maximum of 8×8 pixels are available in their design, where the properties of the metamaterials are each individually controlled by applying a bias voltage. As for

2. In the direction of the light
3. As a nonexhaustive list
4. Reflective LCD devices also exist, but are not presented here as they are outperformed by DMDs, due to their higher refresh rates
5. Defined for an engineered material where its properties are not found in Nature

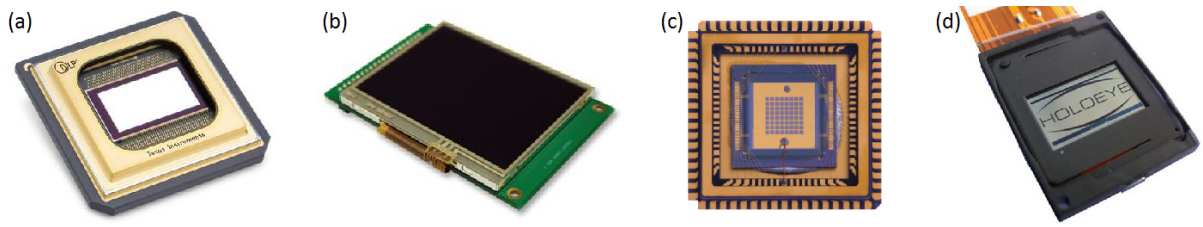

FIGURE I.2 – Examples of spatial light modulators. (a) Digital micromirror device. (b) Liquid crystal display. (c) Metamaterial absorber. (d) Liquid crystal on silicon. The images were extracted and adapted from Texas Instruments website (a), STMicroelectronics website (b), Watts *et al.* (2014) (c), and Holoeye website (d).

the DMD, each pixel is reflective and can take two states [0,1]. This set-up, however, allows the use of patterns with [-1,0,1] values through modulation of the pixels +1 in phase and the pixels −1 out of phase with a reference. Watts *et al.* (2014) showed that the MMA SLM is well adapted and efficient for terahertz imaging.

LCoS Unlike the previous intensity modulators, a *liquid crystal on silicon* (LCoS; Fig. I.2d) SLM can modulate the light phase. As for the LCD, an electric field tunes the crystals to create binary patterns. Such a device was, for instance, used in Clemente *et al.* (2013) to perform compressive holography. Note that a LCoS device can be used along with polarizers to recreate an intensity-based SLM.

Table I.1 summarizes the principal characteristics of the different SLM technologies. The use of a DMD for SPC is by far the most common, as it offers fast refresh rates and is easy to set up.

Technology	Geometry	Modulation	Refresh rate	Number of pixels	Pixel pitch	Active area
DMD	Reflective	Intensity	32 kHz	1600 × 2560	7 – 14 μm	~ mm^2
LCD	Transmissive	Intensity	50 – 600 Hz	4320 × 7680	~ 50 to 300 μm	mm^2 to m^2
MMA	Reflective	Intensity	~ kHz	8 × 8	~ 250 μm	4.8 mm^2
LCoS	Reflective	Phase	~ 60 Hz	768 × 1024	~ 20 μm	~ mm^2

TABLE I.1 – Summary of the main characteristics of the different SLM technologies.

I.2.2 Single-point detector

Photodiode A photodiode (Fig. I.3, left) is a semi-conductor element that can receive photons and convert them into an electrical current. Photodiodes are usually made of a PN junction [6] or a PIN junction [7]. The photons of the light rays arriving at the photodiode are absorbed, and if their energy is over a certain value, they can move to the conductive band, which induces an electric current. Different materials can be used to create a photodiode, each of which imparts certain properties to the detector, and these are summarized in table I.2.

Photomultiplier The *photomultiplier* (PMT; Fig. I.3, right) promotes the conversion of the detection photons into an electrical current. It comprises a photocathode [8], a focusing electrode, dy-

6. A junction where the doping changes sharply, going from a positive (P) doped side to a negative (N) one
7. PN junction with an undoped intrinsic semiconductor in between
8. Negatively charged electrode covered by a material to free electrons

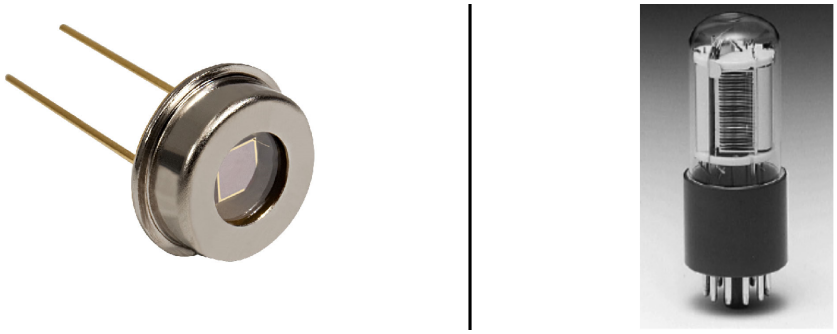

FIGURE I.3 – Examples of single-point detectors, as a photodiode (left) and a photomultiplier (right). The images were extracted and adapted from ThorLabs website (photodiode) and Horiba Scientific website (PMT).

nodes [9], and a final anode, all of which are embedded in a vacuum tube. When a photon reaches the photocathode, this releases an electron that passes to the focusing electrode. There, the electron is accelerated toward the dynodes, to which a certain electric tension is applied, to multiply the electron. The bigger the tension applied to the dynodes, the more the electrons are multiplied. Finally, the anode collects the electrons as an electric current.

Table I.2 summarizes the principal features of the different single-point detectors [10]. Photodiodes are mostly used as they are easy to use and cheap, due to their simple structure, and they cover a wide spectral range.

Technology	Material	Spectral range	Active area	Dark current
Photodiode	Silicon	200 nm - 1100 nm	~mm^2 - cm^2	~ 1 - 600 nA
	Indium Gallium Arsenide	800 nm - 1700 nm	~mm^2	~ 50 nA
	Germanium	800 nm - 1800 nm	~mm^2	~ 1 μA
Photomultiplier	Multialkali	160 nm - 900 nm	~cm^2	~ 3 nA
	Bialkali	185 nm - 650 nm	~cm^2	~ 0.1 nA
	Indium Gallium Arsenide	185 nm - 1010 nm	~mm^2	~ 1 nA

TABLE I.2 – Summary of the main features of the different SPD technologies. The data are mainly taken from ThorLabs and Horiba Scientific websites.

I.2.3 Numerical converter

Regardless of the kind of detector used, the measurement that is wanted by the user needs to be a numerical measurement in order to process the SPC data. Several technologies can be used to perform such a conversion.

ADC The electrical signal provided by the photodiode or PMT can be digitized using an *analog-to-digital converter* (ADC). This device samples the current intensity (or tension) at a given frequency, whereby the sampled value is proportional to the magnitude of the intensity (or tension). ADCs are widely available and their features should be chosen according to the needs of the single-point detector (i.e., sampling rate, input voltage/ intensity, number of bits).

9. Electrodes in a vacuum tube used to multiply electrons
10. As a nonexhaustive list

TCSPC Some single-point detectors [11] can be coupled to a *time-correlated single photon counting* (TCSPC) board, which should be used with a pulsed laser, to illuminate the scene under view. TCSPC provides the number of photons, although due to the reference laser pulse, this is done for different time channels according to the time-of-flight of the photons. In this case, the SPC measurement is not simple scalar data, but a vector of scalar measurements for each time channel.

I.3 Pros and cons

The hardware implementation of the SPC provides some insight and ideas about the possible pros and cons of a SPI system. These are detailed in the next paragraphs.

I.3.1 Advantages

As mentioned in the Introduction, several advantages stand out when using a SPC as an imaging system compared to traditional digital cameras with arrays of sensors.

One of the most important advantages is the optical compression at the hardware level. Cameras of today acquire tens of megapixels, which results in huge computer files. As a consequence, most images are compressed to reduce their size on the disk, and to be suitable for transfer (e.g., by email; for websites). This throws away roughly 80% of the information that was acquired with the conventional camera. With SPC, the idea is to directly perform the compression during the acquisition, so that only the remaining 20% of the useful information is acquired. As well as reducing the memory storage, this acquisition of only a few numbers of measurements reduces the energy consumed, by a factor of 5 according to the example above. Small memory storage and power consumption are key elements for devices where the storage unit and the battery life are limited (e.g., robots, cellphones).

As shown in table I.1 and table I.2, the active area of most SLMs and SPDs are in the mm^2 range, which therefore opens the door to very compact devices. In addition, restoration of SPC images without the lens of Fig. I.1 has been demonstrated at Bell Laboratories (Huang *et al.*, 2013), which is a big step toward SPC miniaturization.

Last but not least, the price of a SPC is relatively low compared to traditional cameras. First, while visible CCD or CMOS cameras are inexpensive due to well-controlled and cheap silicon technology, silicon sensors are not as efficient outside the visible range, and another component needs to be used. In this sense, the SPC has the huge advantage, in that for a system working in the ultraviolet or infrared, it uses a SPD that can have high efficiency (Hadfield, 2009) and is less costly than a sensor array (Rogalski, 2012). Secondly, a SPC can be easily turned into a hyperspectral/ multispectral camera by replacing the detector with a single-point spectrometer. Such spectrometers provide nanometer spectral resolution for some thousands of euros, where conventional imaging systems with similar resolution would be about ten-fold more expensive. Thirdly, the cost gain is also important if the single-point detector is coupled to TCSCP to obtain a *time-resolved* (TR) imaging system. Spectrometery and TCSPC can finally be used together to build a multispectral/ hyperspectral time-resolved device. Hence, SPI provides low-cost systems with high spatial, temporal, and/or spectral resolution that is difficult to achieve with conventional arrays of sensors.

11. Mostly PMTs or single-photon avalanche diodes

I.3.2 Disadvantages

While a conventional digital camera simultaneously acquires each pixel of the image, a SPC needs to perform sequential measurements, which inevitably makes it slower than traditional cameras. The speed of acquisition is limited by the SLM, the SPD, and/or the device for numerical measurements. For instance, table I.1 shows that at the present time [12], the maximum frame rate for the available SLMs is 32 kHz. If, for example, a 1024×1024 pixels image is acquired and 20% of the number of pixels are acquired in terms of the measurement, this leads to a minimum of $1024^2 \times 0.2/32000 \approx 6.6$ s for the acquisition time, whereas a conventional camera would take a few hundred milliseconds.

A second disadvantage that is also linked to the speed of SPI is the post-processing of the sequence of measurements to obtain the desired image. As will be shown in Chapter II, some image restoration techniques take less than a second, but others can take up to minutes, depending on the resolution of the image and the number of sampled measurements.

Overall, at the moment, SPI is not well suited for capturing high-resolution images, as both acquisition times and restoration times increase with the number of measurements.

I.4 Applications

Owing to its numerous advantages, the SPC has found several applications since the first recovered images of Takhar *et al.* in 2006. Some examples are given below, to which the medical applications mentioned in the Introduction can be added.

I.4.1 Static imaging

Color imaging Color images were proposed in the first studies on SPCs by Duarte *et al.* in 2008. For this, to get three measurements for one pattern, they used RGB filters placed in front of the photodiode. The restoration of the image in each RGB canal led to a color image. In Welsh *et al.* (2013), a full-color SPC was presented using a dichroic beamsplitter. This decomposed the white light into three outputs (i.e., red, green, blue) and three photodiodes collected the resulting light. One image per color channel can therefore be restored so as to get a color image (see Fig. I.4, left). Salvador-

12. Refresh rates of DMDs have kept on increasing since their creation

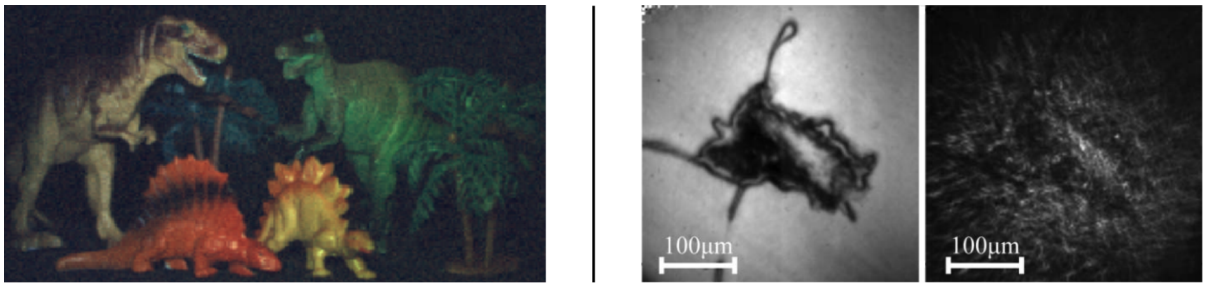

FIGURE I.4 – Examples of static imaging using a single-pixel camera. Left : color image of a dinosaur scene adapted from Welsh *et al.* (2013). Right : visible (left) and short-wave infrared (right) images obtained from the single-pixel–camera-based microscope of Radwell *et al.* (2014).

Balaguer *et al.* (2016) used the same approach as Duarte *et al.*, but with one photodetector. The difference lies in the use of a color wheel with RGB filters on the illumination side, and not on the detection side.

Infrared imaging Radwell *et al.* (2014) designed a SPC-based microscope to image both in the short-wave infrared and the visible spectrum (see Fig. I.4, right). For this, a short-wave infrared source was used, and the two DMD arms (i.e., the ON, OFF states) were coupled to two different detectors, a visible-light-sensitive sensor, and an infrared-sensitive sensor. A similar idea was used by Edgar *et al.* (2015), where visible and infrared images were recorded. The light emitted from the DMD was split into a short-wave-dependent beam and a visible beam, using a hot mirror [13]. Shin *et al.* (2016) illuminate the object with a near-infrared tunable continuous-wave laser that was coupled to a single-mode fiber, to illuminate the object with random speckled patterns [14](Shin *et al.*, 2017). A sensitive infrared photodiode was used as the detector, to obtain an image of the object in the infrared. Recently, in Gibson *et al.* (2017), methane gas leaks were observed using an infrared SPI system, which showed the potential of infrared imaging based on SPC.

Ghost imaging Ghost imaging systems usually combine a CCD camera that does not see the object (hence the term *ghost*) with a single-point detector on the object path, to get the image of the observed object. In 2008, with the advances in SPC, Shapiro showed that ghost imaging was possible using only the SPD. The idea of using simply the SPC arm was taken up by Aßmann *et* Bayer (2013) and then Yu *et al.* (2014a), who used different computational approaches. In Onose *et al.* (2016), a new hardware technology was used for ghost imaging, with an array of *light-emitting diode* (LED) lights that performed modulation of the illumination to recreate a SPI system.

Terahertz imaging Shortly after the first SPC images, Chan *et al.* in 2008 showed that the ideas of SPI could be applied to terahertz imaging. A terahertz transmitter was used to illuminate the object, the SPC patterns were printed on printed-circuit boards, and a single terahertz receiver served as the detector. Ma *et al.* (2012) considered the use of a Nipkow disk to create a SPC-based imaging system suited for terahertz imaging. A terahertz SLM was created by Shrekenhamer *et al.* (2013) through photoexcitation of semiconductors that were coupled to a classic DMD, and this was used to obtain a SPC terahertz imaging system. The same authors, as Watts *et al.* (2014), changed their design slightly to use the single MMA SLM presented in I.2.1 as proof for a terahertz SLM. In Fursich *et al.* (2016), a system based on a single terahertz detector and frequency modulated continuous wave radar was reported. This SPC-based imaging system radar can be used by airport security for weapon detection. A single-pixel terahertz system based on a metal mask structure was also presented in Duan *et al.* (2016), which allowed imaging at 1.75 THz.

Microscopy In Studer *et al.* (2012), a conventional microscope was transformed into a compressive microscope using the principle of compressive sensing; this was shown to successfully image fluorescent beads, cells, and tissues. In the study of Rodriguez *et al.* (2016), a microscope was created to

13. Mirror reflecting the infrared light and letting past the visible light
14. Note that in this particular design, no SLM was used

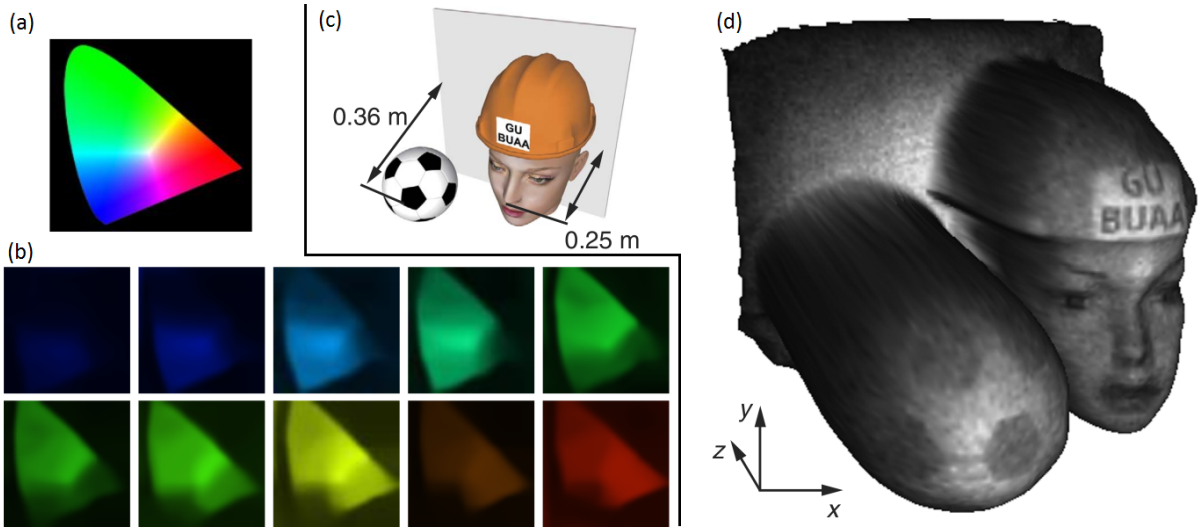

FIGURE I.5 – Examples of multidimensional imaging using a single-pixel camera. (a) Object used for multispectral imaging in Bian *et al.* (2016b). (b) The corresponding 10 single-pixel camera restored images in different spectral channels, from 450 nm to 650 nm. (c) Scene imaged in Sun *et al.* (2016a). (d) Recovered three-dimensional image from the single-pixel camera measurements.

image in both reflective and transmissive geometries based on SPC. A DMD was used for illumination, and two PMTs served to create two SPCs, one in reflection and one in transmission. The dual infrared/ visible SPC of Radwell *et al.* for infrared imaging was also mounted on a microscope, to image objects of a few hundreds of μm in size (see Fig. I.4, right).

Telescopic imaging A telescopic system was used in Yu *et al.* (2014b) to image an object from 2 km away. They showed that reduction of the measurements could be achieved using both arms of the DMD (i.e., the ON and OFF beams) with two PMTs. Their set-up had the advantage of having a large field of view over long distances, and could be used for applications in remote target imaging.

Digital holography Digital holography was reported by Martínez-León *et al.* (2017), who used phase-structured illumination and bucket detection, which allowed them to image complex amplitude objects. The advantages in this design were the use of only one phase SLM, and an improvement by a factor of two for the signal-to-noise ratio.

I.4.2 Multidimensional imaging

Multispectral/ hyperspectral imaging In Magalhaes *et al.* (2012), a hyperspectral imaging system based on SPC was proposed. The single-point detector of the SPC was replaced by a spectrum analyzer that could reach a spectral resolution of 10 pm. A hyperspectral spectrometer coupled to a SPC was also used in Hahn *et al.* (2014), but with a different acquisition strategy at the software level. A patent for a dual spectral SPC acquisition set-up has also been filed by Xerox Corporation (Bernal *et al.*, 2015), which also filed a patent for hyperspectral imaging using a Fabry-Perot filter and a single-point detector (Nystrom *et al.*, 2016). In the recent studies of Bian *et al.* (2016b), a multispectral imaging system that used a single bucket detector was reported to provide a high-sensitivity imaging system (see Fig. I.5a, b). They used classical SPC architecture with a DMD, but further modulated their data

with a rotating film that allowed for sinusoidal modulation in the spectral dimension. A spectrometer based on SPC was reported in Starling *et al.* (2016), where their design measured both the absorption and emission spectra with 90% reduction of the dataset used by a commercial spectrometer. In Li *et al.* (2017), a system that used only one photodiode for multispectral imaging was presented. In their set-up, the light emitted from the object went to a spectral splitter that created eight different beams that went to eight different areas of the SLM, and then everything was collected on the photodiode. As the areas of the SLM were encoded with their own particular patterns, post-processing of the measurements allowed the eight images in eight different spectral channels to be recreated.

Three-dimensional imaging In Sun *et al.* (2013), a projector illuminated a scene with random speckle patterns, and four photodetectors were placed at different angles to collect the outgoing light. Post-processing of the data from the four single-point detectors allowed reconstruction of a 3D image of the scene. The same group extended their data to 3D video imaging in Zhang *et al.* (2016) and Sun *et al.* (2016a) (see Fig. I.5c, d). In Yu *et al.* (2015), the depth information and 3D reflectivity of the scene were reconstructed using simple algebra. A Fourier-based technique to retrieve 3D information was presented in Zhang *et* Zhong (2016). The depth information was modulated by well-chosen patterns in illumination and collected by the SPD, which enabled 3D reconstruction of the object with Fourier analysis. Salvador-Balaguer *et al.* (2016) performed stereoscopic color imaging using a color projector [15] for illumination from two different angles, to create a stereoscopic pair.

Time-resolved imaging A time-resolved photodetector was used by Kirmani *et al.* (2011) to perform *time-of-flight* measurements using a SPC. The exploitation of this time-of-flight for each pixel of the image provided a depth map for the scene under view. The same idea was presented by Howland *et al.* (2013) using a SPC with a PMT as a detector coupled to a TCSPC board. In Dai *et al.* (2016), the same technology was used with a different acquisition strategy, to obtain both the reflectivity and the depth map.

I.4.3 Video acquisition

Judging by the number of publications in recent years, video imaging is a growing application for SPC. A recent review of state-of-the-art compressed video sensing techniques was given in Baraniuk *et al.* (2017). Although SPC acquisition and restoration schemes can be relatively slow, the idea was to exploit the temporal redundancy to reduce the number of measurements, and thus to speed up both the acquisition and restoration times. Such approaches therefore made video recovery computationally more demanding than static image restoration.

To compress further by exploiting temporal redundancy, different techniques have been proposed, such as the methods based on motion estimation in Sankaranarayanan *et al.* (2015, 2016) (see Fig. I.6) and Goldstein *et al.* (2015), and minimization of the image spatial-curvature in Edgar *et al.* (2015), with techniques that mimicked animal imaging in Phillips *et al.* (2016). A different approach for image acquisition/ restoration was used by Zhang *et al.* (2016) that allowed faster image recovery. In Gibson *et al.* (2017), the same group proposed a similar approach for video surveillance of

15. Most projectors produced nowadays use DMDs

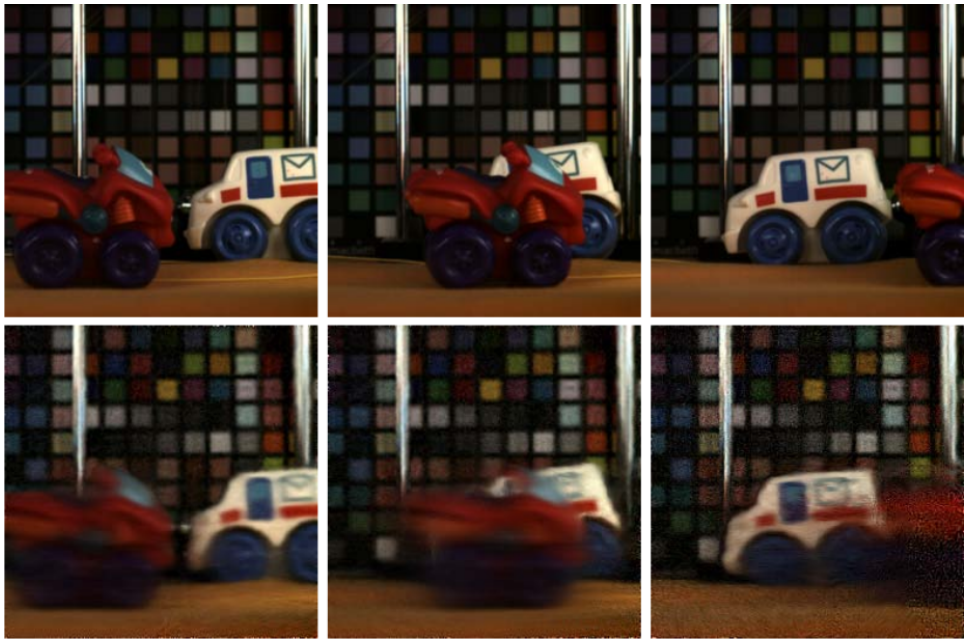

FIGURE I.6 – Examples of video imaging of a red toy car that was moving from left to right using a single-pixel camera adapted from Sankaranarayanan *et al.* (2015). Ground truth images (top row) and single-pixel camera recovered video images (bottom row) are shown.

methane gas leaks. A time-varying 2D ultrasonic field was encoded in Huynh *et al.* (2016) to enable video rate imaging of ultrasound fields.

I.5 New trends in SPC optical methods

In recent years, some new ideas and optical system designs have been reported in the optical field, to simplify imaging systems or make the best use of new materials. The use of a SPC for some of these new trends might be relevant, and is presented in the next paragraphs.

I.5.1 Lensless imaging

Lensless imaging has become an important topic in optics over the last decade, as it offers large fields of views with compact imaging systems (Allier *et al.*, 2010; Ozcan *et* McLeod, 2016; Boominathan *et al.*, 2016). New imaging systems without focusing lenses have been designed, such as the PicoCam (Stork *et* Gill, 2013) and the FlatCam (Asif *et al.*, 2015b,a; Boominathan *et al.*, 2016).

In 2013, Bell Laboratories proposed a SPC architecture without a lens in Huang *et al.* (see Fig. I.7, left). Their design comprised an LCD screen as SLM, and a photovoltaic sensor. Here, no physical image was formed before it was digitally captured. The use of a SPI in this design reduced the size, cost, and complexity of the final camera architecture.

I.5.2 Emerging photodetectors

In the last decade, new technologies and materials have allowed for the creation of new photodetectors with improved features. For instance, carbon nanotubes (Chen *et al.*, 2011, 2014), and more

FIGURE I.7 – Lensless single-pixel camera images adapted from Huang *et al.* (2013) (left), and the single-pixel camera image obtained with a carbon nanotube photodetector adapted from Chen *et al.* (2014) (right).

recently, graphene (Li *et al.*, 2016), have been used as photodetectors to enhance some or several SPC possibilities.

Owing to their opto-electronic properties, *carbon nanotubes* can be used as a photodetector that outperforms most infrared detectors. The high surface-to-volume ratio of carbon nanotubes can increase the signal-to-noise ratio, and photon scattering suppression and size shrinking can reduce the noise associated with these detectors (Kuo *et al.*, 2001). As the fabrication of large-scale carbon nanotube photodetectors is difficult, Chen *et al.* (2011, 2014) proposed to use the sensor in a SPI system, to extend the possible applications of the SPC with classic photodetectors (see Fig. I.7, right).

Since its first discovery in 2004, graphene has been investigated more and more by laboratories due to its remarkable properties. Among these, graphene is stronger than any steel, and it is as good an electricity conductor as copper. Graphene can be made luminescent, its transmittance is almost wavelength independent, and it can be used as a saturable absorber (Bonaccorso *et al.*, 2010). Combining its electronic and optical properties, graphene-based photodetectors can convert received light into voltage in an extremely short time (Xia *et al.*, 2009). Li *et al.* showed in 2016 that such a detector can be used for SPI. This showed the potential of graphene, which might allow high-speed imaging in the future, as it can convert light into voltage at high frequency.

I.6 Conclusion

This Chapter presents the main ideas behind the SPC and its possible hardware implementations, which can take on various forms, both in transmissive and reflective geometries. The many advantages of the simple set-up, and particularly the low-cost aspect of using a single-point detector, has made SPI an emerging imaging technique over the last decade. Based on the numerous applications presented in this Chapter, the SPC should still remain an attractive topic in future years.

While this Chapter presents the hardware side of the SPC, several essential questions related to its software side remain unanswered. How can an image be obtained from single-point measurements? What are the mathematical tools and concepts behind this? These questions are addressed in the following Chapter, along with the possible acquisition/ restoration scheme for SPCs that have been proposed since 2006.

CHAPTER II

ACQUISITION/ RESTORATION SCHEMES FOR SINGLE-PIXEL IMAGING

Contents

CHAPTER II

UNLIKE for CCD or CMOS cameras, hardware acquisition of an image with single-pixel imaging (SPI) is linked to its software restoration. With an array of sensors, a single measure acquires each pixel of the image in parallel, which is impossible to perform with a single-pixel camera (SPC). A sequence of SPC measurements with different spatial light modulator (SLM) patterns are thus performed, and the post-processing of these measurements provides the image. This Chapter aims to answer the following two questions : How are the SLM patterns chosen? Knowing the SLM patterns and the measurements, how is the image recovered?

The first part of this Chapter describes the mathematical formulation of SPC acquisition. Then the state-of-the art acquisition/ restoration schemes are reported. Two main categories of approaches stand out, the *nonadaptive* and *adaptive* techniques. The first considers a fixed set of patterns regardless of the image, while the second *adapts* the set of patterns based on previous SPC measurements. Finally, hybrid methods that combine different approaches are presented.

II.1 Mathematical formulation

II.1.1 Simple modeling

As mentioned in Section I.1, SPC acquisition consists of modulating the light field emitted by the object (i.e., the image) with a given SLM pattern. A single-point detector (SPD) then integrates the modulated light rays (see Fig. I.1) ; i.e., the inner product of the image with the SLM pattern is measured at the SPD. We denote $\mathbf{f} \in \mathbb{R}^{D\times 1}$ as the image of the object, with $D = H \times W$ as the size of the image. We denote further $\mathbf{p}_k \in \mathbb{R}^{D\times 1}$ as the pattern loaded on the SLM, and m_k as the measure collected by the single sensor, whereby

$$m_k = \sum_{i=1}^{D} \left(\mathbf{p}_k\right)_i (\mathbf{f})_i = \mathbf{p}_k^\top \mathbf{f}, \tag{II.1}$$

where $\left(\mathbf{p}_k\right)_i$ (resp. $(\mathbf{f})_i$) is the i-th element of the vector $\mathbf{p}_k$ (resp. $\mathbf{f}$), $i \in [1, D]$.

As mentioned before, recovery of the image of the object with a single measurement is not possible, and so sequential measurements with different SLM patterns $\mathbf{p}_k$ are carried out. The matrix containing the sequence of K SLM patterns is denoted $\mathbf{P} = (\mathbf{p}_1, \ldots, \mathbf{p}_K)^\top \in \mathbb{R}^{K\times D}$. The measurement vector $\mathbf{m} = (m_1, \ldots, m_K)^\top \in \mathbb{R}^{K\times 1}$ that contains the corresponding sequence of measures is mathematically modeled by

$$\mathbf{m} = \mathbf{P}\mathbf{f}. \tag{II.2}$$

II.1.2 Real measurement modeling

In practice, the measure obtained at the SPD is collected over a certain integration time Δt (in s). A light source that emits a certain number of photons per second N_0 (in ph/s) is also used to illuminate the object. If $\mathbf{f}$ and $\mathbf{p}$ (no units) are normalized, then the measurement is obtained as the number of photons and Equation (II.1) becomes

$$m_k = \Delta t N_0 \mathbf{p}_k^\top \mathbf{f}. \tag{II.3}$$

A final component should be added to Equation (II.3). If the light source is switched off, i.e., $N_0 = 0$ ph/s, the measurement m_k is not null. This is mainly because of the dark current of the SPD; i.e., an electric current is induced even when no photons reach the device. In addition to the SPD dark current, even when acquisitions are performed in the dark [1], there is always a small amount of light that remains, which creates a nonzero measure at the SPD. To account for all of this, we denote α (in ph/s) as a single component that regroups the data read by the SPD when $N_0 = 0$. This component will be referred to as the *dark current* of the SPC system. Hence, the final measure can be modeled (Takhar *et al.*, 2006; Duarte *et al.*, 2008) as

$$m_k = \left(N_0 \mathbf{p}_k^\top \mathbf{f} + \alpha\right) \Delta t. \tag{II.4}$$

Including the previous results, the matrix Equation (II.2) for sequential measurements becomes

$$\mathbf{m} = \left(N_0 \mathbf{P}\mathbf{f} + \alpha \mathbf{1}_K\right) \Delta t \tag{II.5}$$

where $\mathbf{1}_K = (1, \ldots, 1)^\top \in \mathbb{R}^{K \times 1}$.

Note that in all of the above Equations, the 'equals' sign is used, but it should be understood as proportional. The measurements are indeed collected by the SPD and are then converted into scalars by one of the devices of Section I.2.3. Conversions also appear in the SPD to convert photons to electrical current or tension. The measurements given by Equations (II.4) and (II.5) model the number of photons that reach the SPD, and not exactly the final numerical data given to the user.

II.1.3 Problem

As mentioned in the Introduction to this Chapter, the acquisition/ restoration schemes for SPI induce two problems. The last Equation (II.5) indeed suggests that SPC acquisition requires the answering of the following two questions :

1. **Acquisition :** how is the sequence of SLM patterns $\mathbf{P}$ designed and/or chosen?
2. **Restoration :** knowing the patterns $\mathbf{P}$ and the measurements $\mathbf{m}$, how is the image $\mathbf{f}$ restored?

For the sake of simplicity, in the rest of the Chapter, Equation (II.2) is followed. As a first approximation, the additive component $\Delta t \alpha \mathbf{1}_K$ of Equation (II.5) can simply be measured by setting $N_0 = 0$ ph/s, and then it can be deducted from each SPC measurement [2]. Regarding the term $\Delta t N_0$, as this is a constant for each measurement, Equation (II.2) remains valid up to a scaling factor.

1. Note that this is not required, as SPC acquisitions can be performed in ambient light
2. Different strategies to deal with this component are revealed throughout this thesis, mostly in Chapter V

II.2 Compressive sensing

The first category of algorithms that provided the first SPC images in 2006 were based on the compressive-sensing (CS) paradigm. The next sections give the mathematical tools behind this, as well as some examples of CS-based SPC acquisitions.

II.2.1 Acquisition/ restoration in the compressive-sensing framework

CS theory The first studies with a SPC in 2006 by Takhar *et al.* took advantage of the recent CS paradigm (Donoho, 2006; Candes *et al.*, 2006; Baraniuk, 2007; Baraniuk *et al.*, 2010). The idea is that most signals are compressible on a certain basis, and can hence be recovered from only a small (sub Nyquist) number of projections (i.e., measurements). We denote $\mathbf{\Lambda} \in \mathbb{R}^{D\times D}$ as a transform operator for which the image $\mathbf{f}$ has a sparse representation. Mathematically,

$$\mathbf{f} = \mathbf{\Lambda s} \tag{II.6}$$

where $\mathbf{s} \in \mathbb{R}^{D\times 1}$ is L-sparse, which means that $\mathbf{s}$ only has L nonzero entries. In other words, the image $\mathbf{f}$ can be restored from only L basis vectors, and an optimal basis would be the one for which $L \ll D$, with the smallest possible value. Wavelets, Fourier, and *discrete cosine transform* (DCT) basis are common choices for $\mathbf{\Lambda}$.

As the L basis vectors are not known, the idea of CS is to acquire $K < D$ projections of the image $\mathbf{f}$ with a collection of vectors $\mathbf{p}_k$ arranged in a matrix $\mathbf{P}$, and the corresponding SPC measurement vector is given by

$$\mathbf{m} = \mathbf{Pf} = \mathbf{P\Lambda s} = \mathbf{\Psi s} \qquad \text{with} \quad \mathbf{\Psi} = \mathbf{P\Lambda} \in \mathbb{R}^{K\times D} \tag{II.7}$$

Acquisition The problem now lies in the design of the matrix $\mathbf{P}$, such that it captures enough information to restore the image of size D from only K measurements. As we assumed that the signal has an L-sparse representation in some basis $\mathbf{\Lambda}$, K must be greater than or equal to L. It was shown that to obtain a good estimate of $\mathbf{f}$, the matrix $\mathbf{\Psi}$ must satisfy the so-called *restricted isometry property* (Donoho, 2006) :

$$(1-\epsilon)\|\mathbf{b}\|_2^2 \leq \|\mathbf{\Psi b}\|_2^2 \leq (1+\epsilon)\|\mathbf{b}\|_2^2 \tag{II.8}$$

where $\mathbf{b} \in \mathbb{R}^{D\times 1}$ is any vector that has the same L nonzero entries as $\mathbf{s}$ for some $\epsilon > 0$. It has been shown that the selection of $\mathbf{P}$ as a random matrix can ensure the restricted isometry property for $\mathbf{\Psi}$ (Donoho, 2006; Baraniuk *et al.*, 2007). For instance, an independent identically distributed Gaussian matrix has a restricted isometry property with high probability if

$$K \geq cL\log\left(\frac{D}{L}\right) \tag{II.9}$$

for some values of c typically in the range of $1-100$ (Donoho, 2006; Candes *et al.*, 2006; Baraniuk *et al.*, 2007). Hence, the elements of $\mathbf{P}$ for the SPC are generally chosen (Candes *et* Tao, 2006; Takhar *et al.*, 2006; Duarte *et al.*, 2008) as

$$(\mathbf{P})_{i,j} \sim \mathscr{B}(\mu = 0, p = 1/2) \tag{II.10}$$

where $\mathscr{B}(\mu, p)$ accounts for the Bernoulli distribution with probability p and mean μ. Such a distribution is often chosen because the resulting patterns with ± 1 entries are well suited to any SLM technology.

Restoration To find the image $\mathbf{f}$ from the measurement $\mathbf{m}$ of Equation (II.7), the following optimization problem must be solved :

$$\mathbf{s}^* = \arg\min \|\mathbf{s}\|_p \quad \text{such that} \quad \mathbf{\Psi s} = \mathbf{m}. \tag{II.11}$$

where $\|\mathbf{x}\|_p = \left(\sum_{i=1}^{D} |x_i|^p \right)^{\frac{1}{p}}$ is the ℓ_p norm of vector $\mathbf{x} \in \mathbb{R}^{D\times 1}$ and $0 \leq p \leq 1$. The image is finally restored in the original domain according to Equation (II.6), i.e.,

$$\mathbf{f}^* = \mathbf{\Lambda s}^* \tag{II.12}$$

However, many $\mathbf{s}^*$ that are L-sparse signals are solutions of $\mathbf{\Psi s} = \mathbf{m}$ in Equation (II.11) as we chose $K < D$. The norm should therefore be carefully chosen to obtain the best solution $\mathbf{s}^*$.

ℓ_0 "norm" Given that we search for an L-sparse vector, it is intuitive to use the ℓ_0 "norm" [3] in Equation (II.11), as $\|\mathbf{x}\|_0$ counts the number of nonzero elements in $\mathbf{x}$. This sparsity-measure-based minimization is, however, an NP-complete problem that is numerically unstable. This therefore requires many computations to find the possible locations of the nonzero entries in $\mathbf{s}$.

ℓ_2 norm As is commonly used in several optimization problems, the ℓ_2 norm can be set to solve Equation (II.11). The advantage is that it is possible to directly find a closed-form solution by simple algebra; i.e., $\mathbf{s}^* = \mathbf{\Psi}^\top \left(\mathbf{\Psi\Psi}^\top \right)^{-1} \mathbf{m}$. However, with this norm, the energy is minimized and the found solution will almost never be an L-sparse vector $\mathbf{s}$, which is therefore not the best solution.

ℓ_1 norm It was shown that under the conditions that $K \geq cL\log(D/L)$, the image can be exactly or closely recovered in the transform domain by solving the problem of Equation (II.11) with the ℓ_1 norm (Donoho, 2006). Different algorithms (Candes *et* Romberg, 2005; Candes *et al.*, 2006; Foucart *et* Rauhut, 2013) can efficiently solve this convex optimization problem.

TV minimization In the context of SPI, it is standard to obtain $\mathbf{f}$ directly in the image domain using total variation (TV)-minimization (Li, 2009), instead of the ℓ_1-minimization and Equation (II.12). Although CS theory is not applicable in this case, TV-minimization is a popular alternative, as it allows for much faster image restoration while being almost similar to performing ℓ_1-minimization in the wavelet domain (Candes *et al.*, 2006). The problem is hence formulated as below :

$$\mathbf{f}^* = \arg\min \|\mathbf{f}\|_{\text{TV}} \quad \text{such that} \quad \mathbf{Pf} = \mathbf{m}. \tag{II.13}$$

If $\mathbf{F} \in \mathbb{R}^{H\times W}$ represents the 2D version of $\mathbf{f} \in \mathbb{R}^{D\times 1}$, $D = H \times W$, then the TV norm of $\mathbf{f}$ can be defined in its isotropic or anisotropic versions as

$$\begin{cases} \|\mathbf{f}\|_{\text{TV}}^{\text{iso}} = \|\mathbf{F}\|_{\text{TV}}^{\text{iso}} = \sum_{h=1}^{H-1} \sum_{w=1}^{W-1} \sqrt{|F_{h+1,w} - F_{h,w}|^2 + |F_{h,w+1} - F_{h,w}|^2} \\ \|\mathbf{f}\|_{\text{TV}}^{\text{aniso}} = \|\mathbf{F}\|_{\text{TV}}^{\text{aniso}} = \sum_{h=1}^{H-1} \sum_{w=1}^{W-1} |F_{h+1,w} - F_{h,w}| + |F_{h,w+1} - F_{h,w}| \end{cases} \tag{II.14}$$

3. This is not exactly a norm in the mathematical sense of the term

Depending on the problem to solve, anisotropic TV can be easier to minimize, and is often preferred. This kind of minimization works well if the gradient of **f** is sparse; i.e., if **f** is a piecewise constant image.

In summary, the acquisition/ restoration scheme using CS is referred to as a *nonadaptive* acquisition strategy, in the sense that the matrix **P** for a given size D and number of measurements K can be used for different objects to image. Figure II.1 illustrates the main scheme of such an acquisition strategy.

FIGURE II.1 – Scheme of a nonadaptive acquisition framework for a single-pixel camera.

II.2.2 Examples of a compressive-sensing-based single-pixel camera

Figure II.2 gives an example of CS-based SPC acquisitions from the first studies of Takhar *et al.* (2006) and Duarte *et al.* (2008). They imaged the black-and-white letter R using random patterns and ℓ_1-minimization or TV-minimization for image restoration. It can be seen that the TV-minimization led to the creation of spots, and worked well for this image, which is piecewise constant.

Compressive-sensing-based SPC has been widely applied to various applications, as presented in Section I.4 (Chan *et al.*, 2008; Ma, 2009b,a; Magalhaes *et al.*, 2011; Studer *et al.*, 2012; Magalhaes *et al.*, 2012; Welsh *et al.*, 2013; Tajahuerce *et al.*, 2014; Duran *et al.*, 2015; Edgar *et al.*, 2015; Zhang *et al.*, 2016; Rodriguez *et al.*, 2016), as the patterns are very easy to create and open-source codes are available for ℓ_1-minimization and TV-minimization.

II.2.3 Pros and cons

Advantages The simple design of the matrix **P** with random ± 1 variables is an advantage, as for a given size D and number of measurements K, it is possible to create this matrix once and for all. The second advantage is that as most signals are L-sparse in a basis, the number of measurements K can be relatively small compared to the number of pixels D of the restored image. For instance, in Fig. II.2d, only 1300 measurements were acquired for a 256×256 image, thus giving a compression ratio of 98%.

Disadvantage The biggest drawback with CS is the restoration step based on ℓ_1-minimization. Such an optimization process indeed needs some heavy computation, and the reconstruction time suffers greatly when D and K increase, taking from seconds to minutes. It is thus relatively difficult to consider real-time applications that need high-resolution images with CS.

II.3 Basis scan

To have straightforward image recovery without ℓ_1-minimization or TV-minimization, a *basis scan* (BS) approach can be used; i.e., the SPC progressively acquires the scene under view on a user-

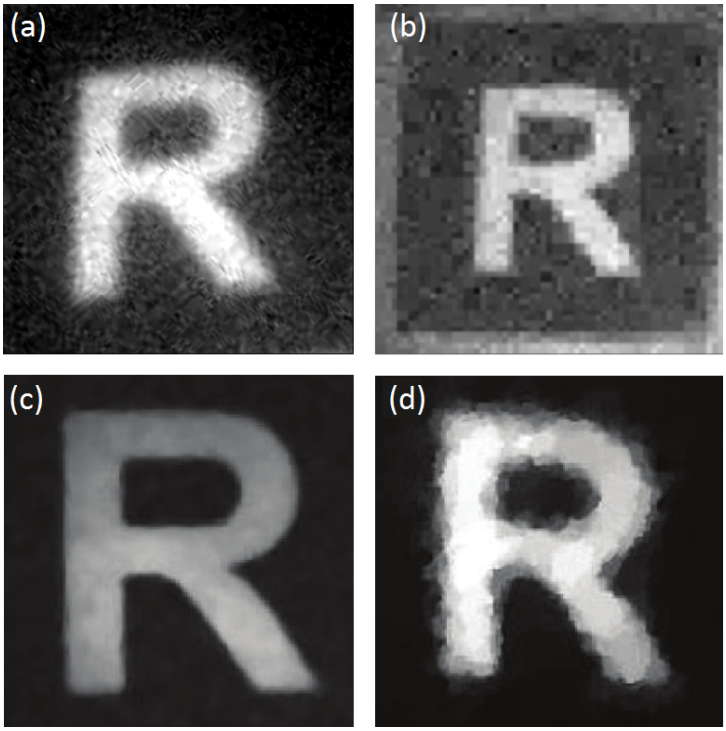

FIGURE II.2 – Example of single-pixel camera images obtained using the compressive-sensing paradigm. (a) Image of the object on the spatial light modulator . (b) A 64×64 single-pixel camera image recovered from 1600 measurements using ℓ_1-minimization. (c) Charge coupled device image of the object. (d) A 256×256 single-pixel camera image recovered from 1300 measurements using total-variation-minimization. Images extracted and adapted from Takhar *et al.* (2006) (a, b) and Duarte *et al.* (2008) (c, d).

chosen basis. The next sections provide the mathematical tools behind BS-based acquisition, as well as some examples and advantages/ disadvantages of this technique.

II.3.1 Acquisition/ restoration in the basis-scan framework

Acquisition As mentioned earlier, a BS acquires the image directly in the chosen orthonormal basis. We denote $\mathbf{B} \in \mathbb{R}^{D \times D}$ as the transform operator of a given basis, and $\widetilde{\mathbf{f}} \in \mathbb{R}^{D \times 1}$ as the image $\mathbf{f}$ in the basis $\mathbf{B}$. Each element of $\widetilde{\mathbf{f}}$ therefore represents a coefficient in that basis and corresponds to the inner product of a row of $\mathbf{B}$ with image $\mathbf{f}$. BS acquisition can thus be formalized as :

$$\mathbf{m} = \mathbf{P}\mathbf{f} \qquad \text{with} \quad \mathbf{P} = \mathbf{B} \quad \text{s.t.} \quad \mathbf{m} = \widetilde{\mathbf{f}} \tag{II.15}$$

The possible choices for $\mathbf{B}$ consist of a natural, Hadamard, wavelet, Fourier, or discrete cosine transform basis, among others.

Restoration Using Equation (II.15), and if $\mathbf{B}$ is invertible, the image recovery of $\mathbf{f}$ from its coefficients $\widetilde{\mathbf{f}}$ in basis $\mathbf{B}$ is straightforward :

$$\mathbf{f} = \mathbf{B}^{-1}\widetilde{\mathbf{f}} = \mathbf{B}^{-1}\mathbf{m} \qquad \text{or} \qquad \mathbf{f} = \sum_{k=1}^{K} m_k \mathbf{p}_k \tag{II.16}$$

$\mathbf{B}^{-1}$ accounts for the inverse basis transform of the chosen basis; e.g., inverse Fourier transform.

As we will show in the examples of BS-based SPC, it is in practice time-consuming to send the complete basis $\mathbf{B}$, as the number of patterns is equal to the number of pixels D of the desired image. A subset of $\mathbf{B}$ denoted $\mathbf{B}_K$ with $L < K \leq D$ patterns is considered, for which the choice of these K patterns is decided before the acquisition, no matter the object to image. The image restoration Equation (II.16) is still valid, provided that the elements of $\widetilde{\mathbf{f}}$ that were not acquired are set to 0.

As for the CS technique presented in Section II.2, the BS approach belongs to the category of nonadaptive approaches outlined in Fig. II.1, as the matrix $\mathbf{P} = \mathbf{B}$ or $\mathbf{P} = \mathbf{B}_K$ is the same regardless of the object to image.

II.3.2 Examples of basis-scan-based single-pixel cameras

Hadamard basis The Hadamard basis (Pratt *et al.*, 1969) is well suited for implementation on a SPC, as the corresponding patterns have [-1,0,1] values. Such a basis was considered in Welsh *et al.* (2015), with a fully sampled Hadamard space that allowed for near video-rate restoration of the image. Its application is demonstrated for color imaging, and Stokes parameters were obtained using photodetector signals from orthogonal linear polarization states. In Sun *et al.* (2016b), the same group recently reported a way to improve the signal-to-noise ratio of the measurements when a digital micromirror device (DMD) was considered as a SLM. Their solution consisted of slightly shifting each pattern spatially in the x, y, and x/y (diagonal) directions so as to obtain four different measurements for a similar pattern. The approach was shown using a Hadamard BS, where the four measurements were finally combined. Improved image quality can be obtained by repeating the approach for each pattern.

Fourier basis In Zhang *et al.* (2015), the Fourier basis was used to restore an image with *fast Fourier transform* algorithms. They illuminated the scene with phase-shifting sinusoids to assemble the Fourier coefficients. As a BS approach generally acquires the D coefficients of the image, Zhang *et al.* used a subset $K < D$ of the patterns that corresponded to the low frequencies of the Fourier domain, as shown in Fig. II.3, top. In Zhang *et* Zhong (2016), they then used their Fourier strategy (Zhang *et al.*, 2015) with a more complex experimental set-up, which allowed them to obtain depth information. They showed that by estimating a fringe phase map, the height information of the scene under view can be exploited to obtain a 3D image. Fourier patterns were also used in Bian *et al.* (2016a), with a different choice of the subset $K < D$. To create this subspace, they took the Fourier transform of a database of 44 natural images and computed the average magnitude map of these spectra. The thresholding of this map for different values of threshold yielded different subspaces of the Fourier space (see Fig. II.3, bottom). Then SPC acquisitions were performed with the corresponding patterns that belonged to the Fourier subspace, independent of the image in the scene.

DCT basis The DCT basis was considered in Liu *et al.* (2017). The full set of the D DCT patterns can be sent for acquisition, or subsets $K < D$ of the DCT domain can also be considered. The results of full-color imaging here are given in Fig. II.4.

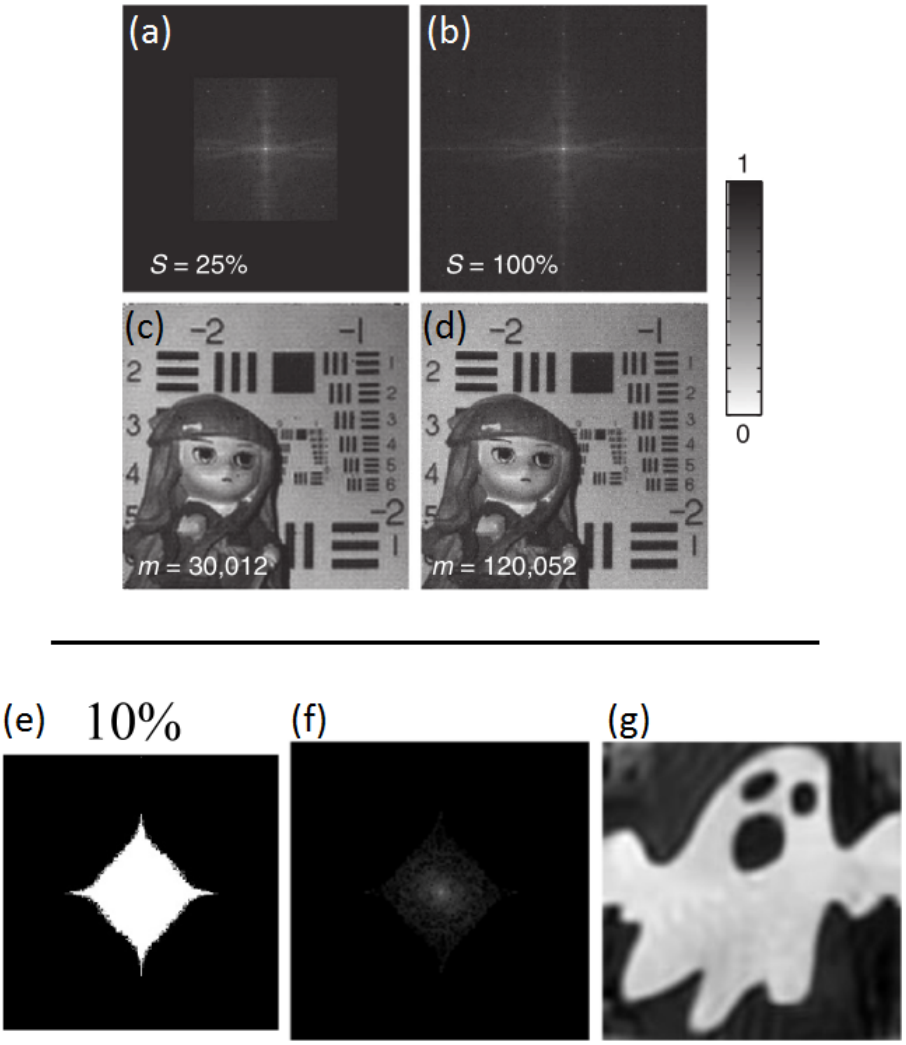

FIGURE II.3 – Examples of single-pixel camera acquisitions with a basis-scan approach in the Fourier domain. A sampled Fourier transform with a subset corresponding to 25% (a) of the full spectrum (b), and the corresponding single-pixel camera restored images with $K = 25\% \times D$ (c) and $K = D$ (d). Images extracted and adapted from Zhang *et al.* (2015). A Fourier subspace with 10% of the full spectrum (e), the sampled coefficients (f), and the image obtain from the sampled coefficients (g). Images extracted and adapted from Bian *et al.* (2016a).

II.3.3 Pros and cons

Advantage The best-known advantages of BS-based SPI is the inverse basis transform for image restoration. The matrix computation of Equation (II.16) is quite rapid, and for some well-chosen basis, there are fast algorithms, such as fast Fourier transform or filter banks [4] for wavelet basis. For such algorithms, the complexity ranges from $O(D\log(D))$ to $O(D)$, which is much better than a CS algorithm, for which the complexity can reach $O(D^3)$ (Foucart *et* Rauhut, 2013).

Disadvantage In a BS approach, the matrix $\mathbf{P}$ of Equation(II.15) becomes $\mathbf{B}$, which leads to $K = D$; i.e., D measurements are acquired for an image of D pixels. The acquisition time is thus dramatically increased compared to a CS-based approach for which $K \ll D$. No compression is performed, and

4. This will be detailed in Chapter IV

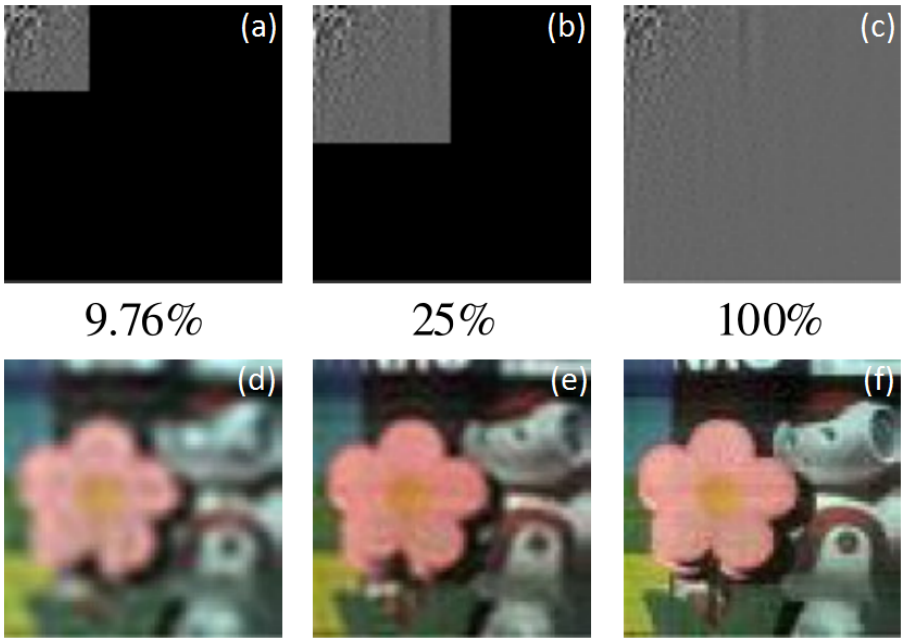

FIGURE II.4 – Examples of single-pixel camera acquisition with a basis-scan approach in the discrete cosine transform domain. The coefficients were acquired in the discrete cosine transform domain with a sampling rate of 9.76% (a), 25% (b), and 100% (c), with (d-f) showing the corresponding restored single-pixel camera images. Images extracted and adapted from Liu *et al.* (2017).

acquisition times increase linearly with the number of pixels, which makes it again not practicable for real-time applications or to obtain high-resolution images. When a subset of the full basis domain is considered, this allows the number of measurements to be reduced. However, such an approach relies on an *a-priori* from a database of images that is not necessarily representative of the scene under view. For instance, in the Fourier example of Fig. II.3, no coefficients that correspond to the high frequencies are acquired. This might be a problem if the scene under view has lots of high frequencies, which would therefore not be well restored using this approach.

II.4 Adaptive basis scan

As the number of measurements in a BS is a big limit to its use, the idea of an *adaptive basis scan* (ABS) approach is to sample only the K useful elements in the basis $\mathbf{B}$; i.e., the K significant coefficients in that basis. In Section II.2, it was said that most signals have sparse representation on a well-chosen basis, and therefore have L non-zeros entries. An ABS strategy therefore tries to search for these L entries using $K \geq L$. The following section presents the general framework of an ABS strategy, with some examples of ABS-based SPCs.

II.4.1 Acquisition/ restoration in an adaptive basis scan framework

Finding the sparse coefficients in basis $\mathbf{B}$ is easy when the whole image is known. $\widetilde{\mathbf{f}} = \mathbf{Bf}$ is simply computed, with a search for the locations of the K significant coefficients. For this, the D coefficients of $\widetilde{\mathbf{f}}$ can be sorted in order of decreasing magnitude [5], and the first K coefficients of the sorted vector

5. Value of the coefficient taken as the absolute value

are retained. In SPI, however, the whole image of the object is not known, and each value of the coefficients in $\widetilde{\mathbf{f}}$ cannot be computed.

Acquisition The principal idea of an ABS approach is to acquire first some of the coefficients of the basis, and based on these measurements, predict the next coefficients to sample. Once the new coefficients are added, the total set of measurements can be further analyzed to predict again the next elements to sample, and so on. Hence, the acquisition step of an ABS strategy consists of an iterative process with a prediction technique that decides which are the next coefficients of $\widetilde{\mathbf{f}}$ that should be sampled; i.e., which coefficients are *predicted* to be significant.

We denote J as the maximum number of iterations, and $j \in [1, J]$ as the iteration index. The set of predicted significant coefficients is denoted as $\mathcal{I}$:

$$\mathcal{I} = \left\{ i \in [1, D] \quad \text{s.t.} \quad \tilde{f}_i \text{ is significant} \right\} \tag{II.17}$$

The set $\mathcal{I}$ is therefore constructed with the J iterations with subsets denoted as $\mathcal{I}^{(j)}$, such that

$$\bigcup_{j=1}^{J} \mathcal{I}^{(j)} = \mathcal{I} \quad \text{and} \quad \bigcap_{j=1}^{J} \mathcal{I}^{(j)} = \varnothing \tag{II.18}$$

with

$$\text{card}\left(\mathcal{I}\right) = \sum_{j=1}^{J} \text{card}\left(\mathcal{I}^{(j)}\right) = \sum_{j=1}^{J} K^{(j)} = K. \tag{II.19}$$

Note that the cardinality of $\mathcal{I}$ depends on the metric used to judge whether $\tilde{f}_i$ is significant or not, which is detailed in the next section. The nonacquired coefficients are neglected and set to 0; i.e., $\tilde{f}_i = 0 \quad \forall i \notin \mathcal{I}$.

The formulation of an ABS acquisition scheme for SPC can be expressed by algorithm 1, where $\bigoplus_{l=1}^{L} \mathbf{v}_l$ denotes the concatenation of the L vectors $\mathbf{v}_l$.

Algorithm 1 Adaptive basis scan acquisition

Initialization : Set $\widetilde{\mathbf{f}} = \mathbf{0} \in \mathbb{R}^{D\times 1}$ so that $\forall i \in [1, D] \quad \tilde{f}_i = 0$
for $j = 1$ **to** J **do**
1. Compute $\mathcal{I}^{(j)}$ with the chosen prediction method and set $K^{(j)} = \text{card}\left(\mathcal{I}^{(j)}\right)$
2. Compute $\mathbf{P}^{(j)} = \bigoplus_{i\in\mathcal{I}^{(j)}} \mathbf{b}_i$ with $\mathbf{b}_i$ the i-th row of $\mathbf{B}$
3. Acquire $\mathbf{m}^{(j)} = \mathbf{P}^{(j)}\mathbf{f}$ with the SPC
4. Update $\widetilde{\mathbf{f}}$:
    for $k = 1$ **to** $K^{(j)}$ **do**
    4.1. Set $i = \mathcal{I}_k^{(j)}$ where $\mathcal{I}_k^{(j)}$ is the k-th value of $\mathcal{I}^{(j)}$
    4.2. Set $\tilde{f}_i = m_k^{(j)}$
    end for
end for

Restoration During the ABS acquisition presented in algorithm 1, $\widetilde{\mathbf{f}}$ is partially filled with some coefficients that were predicted to be significant; i.e., for coefficients at index $i \in \mathcal{I}$. The image $\mathbf{f}$ can therefore simply be restored as in the BS scheme, i.e.,

$$\mathbf{f} = \mathbf{B}^{-1}\widetilde{\mathbf{f}} \qquad \text{or} \qquad \mathbf{f} = \sum_{j=1}^{J} \sum_{k=1}^{K^{(j)}} m_k^{(j)} \mathbf{p}_k^{(j)}. \tag{II.20}$$

Fig. II.5 illustrates the general framework of the adaptive idea, which compared to the nonadaptive scheme of Fig. II.1, adds a prediction step that is performed J times.

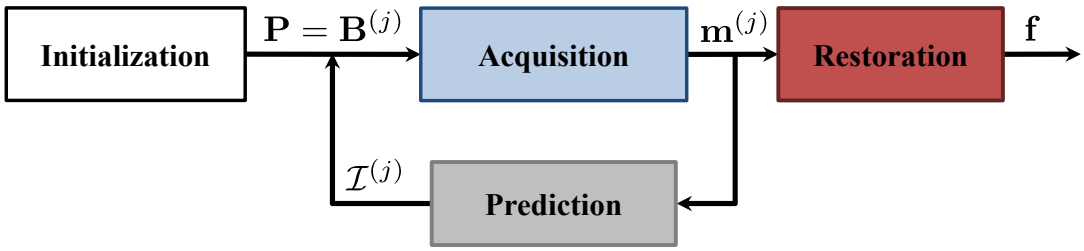

FIGURE II.5 – Framework of an adaptive single-pixel imaging acquisition strategy.

II.4.2 Examples of adaptive-basis-scan-based single-pixel cameras

ADS Deutsch *et al.* (2009) used a Haar[6] wavelet basis with an adaptive technique that is referred to as *adaptive direct sampling* (ADS). They considered a 'father-son' relationship between wavelet coefficients, based on the tree structure of the wavelet decomposition (Mallat, 1989; Shapiro, 1993; Mallat, 2008). The wavelet decomposition of an image is indeed structured in J levels, as can be seen in Fig. II.6 (arrows in colour, except blue), and this relationship means that a coefficient at j has four 'sons' at the next scale $j-1$[7]. In their technique, Deutsch *et al.* used a thresholding strategy based on the Lipschitz exponent (Mallat, 2008) to predict the relevant coefficients at finer and finer scales. If a 'father' coefficient was found to be significant, then its four 'sons' at the next scales were considered for acquisition. The use of the father-son relationship in their strategy is justified because the wavelet coefficients tend to persist through the scales; i.e., a significant coefficient at j might have four significant 'sons' at the scale $j-1$.

ADS using dictionaries Similar to what was done in 2009 with ADS, in Averbuch *et al.* (2012) the same authors proposed to change their prediction strategy using dictionaries. The technique was refered to as *adaptive direct sampling* using dictionaries, and it used statistical modeling of images found in compression algorithms. Discrete probability distributions were estimated, and the mutual information between a pair of two wavelet coefficients was evaluated. A predictor to estimate the absolute value of a wavelet coefficient was also proposed, so that this value could be compared to a threshold and the evaluated mutual information, to decide whether the coefficient was significant or not.

6. Such a wavelet is well adapted to the ON/OFF technology of SLM, as the patterns only have [-1,0,1] values
7. We take the convention of arranging the scales in a decreasing order from J to $j = 1$ with $J \geq 1$

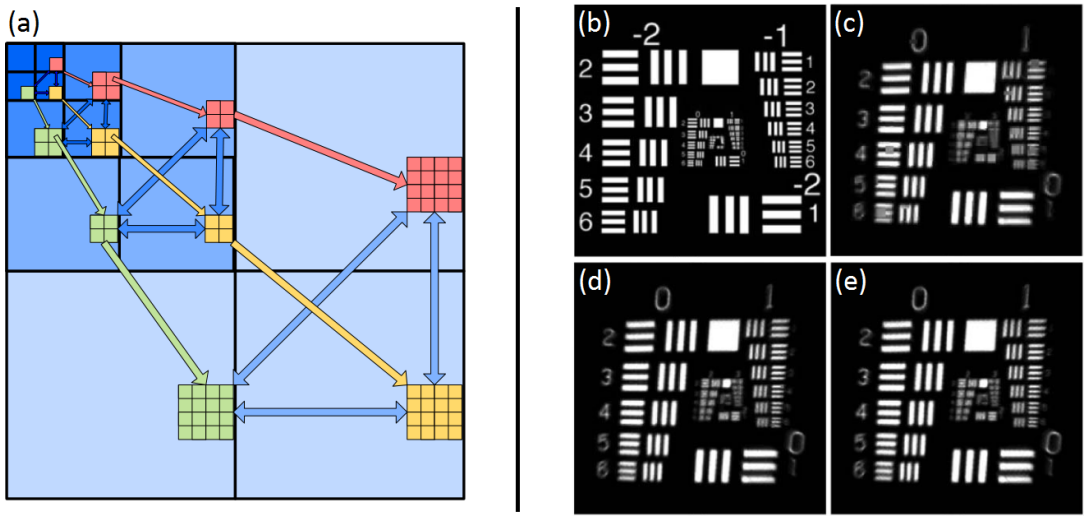

FIGURE II.6 – Wavelet tree and results of extended wavelet trees adaptive compressed sampling acquisitions. Structure of the wavelet tree (a), ground truth image (b) and single-pixel camera acquisitions with extended wavelet trees adaptive compressed sampling for a compression rate of 90% (c), 67% (d), and 58% (e). Images extracted and adapted from Dai *et al.* (2014).

ADS with red-black tree The ADS strategy with a Haar wavelet was derived in Hahn *et al.* (2014) with a threshold-free prediction strategy. Instead, Hahn *et al.* chose the coefficients where the 'parents' had the largest absolute value using an ordered queue implemented by a red-black tree. This particular kind of binary tree [8] allows for a somewhat self-adapting approach that does not sample coefficients up to a certain detail level. Overall, this overcomes the choice of thresholds that can impact on the quality of the restored image in ADS if they are badly chosen. A demonstration of hyperspectral imaging using a Haar wavelet is proposed.

EWT-ACS Dai *et al.* reported an ABS strategy in 2014 that was refered to as *extended wavelet trees adaptive compressed sampling* (EWT-ACS). This approach is close to ADS, as the technique is derived from the Haar wavelet and makes use of the father-son relationship. The difference lies in a more refined thresholding strategy that they showed to outperform ADS (Deutsch *et al.*, 2009). This strategy not only uses the father-son relationship, but also the sibling relationship. As depicted in Fig. II.6 (blue arrows), this information links the information between wavelet coefficients at the same scale, as it comes from the same area of the image. In addition, Dai *et al.* showed that there is some redundancy in the sampled SPC measurement when Haar is considered, and some acquisitions are not necessary to obtain certain wavelet coefficients. This allowed them to further compress the number of measurements for a same number of sampled wavelet coefficients.

Guided coefficients In the recent study of Huo *et al.* (2017), the strategy of EWT-ACS (Dai *et al.*, 2014) in the Haar domain was derived using what they called guided coefficients. These elements corresponded to some unsampled 'sibling' coefficients in EWT-ACS that were localized by a same-scale prediction method that was based on thresholding. They further showed that Dai *et al.* did not completely make use of the redundancy using the Haar wavelet to compute the wavelet coefficients.

8. Particular types of containers to store the data, and mostly used to implement dynamic sets

Overall, their technique needed fewer measurements for the same image quality compared to EWT-ACS, through more efficient sampling of the significant Haar elements.

II.4.3 Pros and cons

Advantages The most well-known advantage of an ABS approach is the image restoration that can still be performed as in the BS framework with an efficient inverse transform. This allows fast algorithms to be used, which makes it possible to consider high-resolution images for which the reconstruction times do not suffer much as the complexity of these algorithms can reach $O\big(D\log(D)\big)$. The second advantage is the small number of measurements that need to be performed. In theory, if the prediction step is perfect, it is possible to obtain $K = L$ and acquire only the L significant coefficients, which therefore drastically reduces the number of measurements compared to a BS approach. In practice, reaching $K = L$ is close to impossible, as perfect prediction without knowing the entire image is hardly achievable.

Disadvantages A disadvantage of an ABS approach is that it does not allow for a perfectly restored image. When the term L-sparse is used, this is up to a certain threshold. This means that the $D - L$ zero coefficients in a given basis are not exactly equal to zero, and they therefore contribute to the final quality of the restored image. Of course, most of the features of the restored image come from the L significant coefficients, so the prediction step should be good enough to at least sample these coefficients. The latter stage should also be relatively rapid, as it is applied between two SPC acquisitions, and thus increases the overall acquisition time. A fast and efficient prediction step is thus needed.

II.5 Hybrid methods

Some acquisition/ restoration schemes for SPI combine the use of CS, BS and/or ABS. In this section, we review some of these techniques, which we refer to as hybrid methods.

II.5.1 Examples of hybrid techniques

Wavelet combined with CS In Yu *et al.* (2014a), a partial wavelet transform of the scene under view was built from CS measurements. Random patterns (i.e., chosen as in Eq. (II.10)) were first sent for acquisition of a coarse image (recovered with TV-minimization) that was one-level wavelet transformed. Using a thresholding strategy and the idea of the ADS scheme presented in Section II.4.2, they decided on the next four coefficients to sample at a finer scale. To acquire these, random CS patterns were again considered with a different structure size to get finer information. These steps were then repeated, to build the wavelet transform of the image, an image that was quickly obtained by the corresponding inverse transform.

Wavelet combined with Hadamard In Soldevila *et al.* (2015) (see Fig. II.7), several BS were performed at different resolutions with Hadamard patterns to build the wavelet transform of the image. They started by acquiring a coarse image of the scene with a complete set of Hadamard patterns,

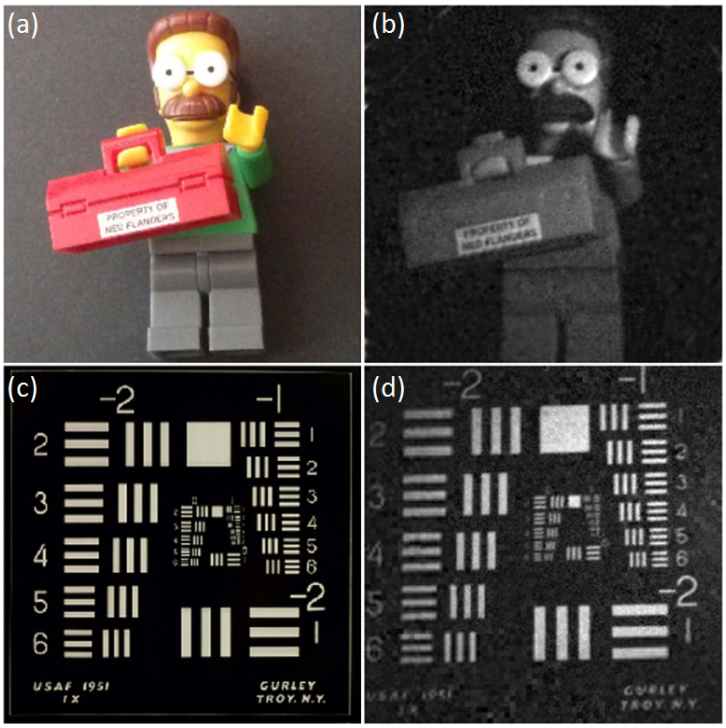

FIGURE II.7 – Examples of a hybrid acquisition technique using wavelets and the Hadamard basis. (a) (resp. (c)) Ground truth 256×256 (resp. 512×512) image. (b) (resp. (d)) Corresponding single-pixel camera image obtained with $K = 88\% \times D$ (resp. $K = 55\% \times D$) measurements using the hybrid method proposed in Soldevila *et al.* (2015). Images extracted and adapted from Soldevila *et al.* (2015).

and a one-level wavelet transform was applied to this coarse image. A search was performed for the quadrants with higher densities of the borders, and if a quadrant did not show borders then it was discarded at the next stage. For the remaining quadrants, another BS with Hadamard patterns was performed at a finer resolution and localized on the remaining quadrants, and so on. This adaptive technique therefore enabled them to build a wavelet transform that had fast image restoration.

Noiselets with CS In the study of Zhao *et al.* in 2015, a noiselet-sensing matrix (Coifman *et al.*, 2001) was considered. Noiselet functions are related to wavelet functions, in the sense that they can be used in CS as a sensing matrix to restore a signal that has sparse representation in the wavelet domain[9]. If 100% of the noiselet sensing basis was taken for acquisition, then the inverse noiselet transform could be applied, which resulted in fast image recovery. In their design, in order not to sample the $K = D$ coefficients, Zhao *et al.* randomly chose some of the noiselet patterns for acquisition. In this case, a basis pursuit denoising algorithm was applied, similar to what can be done in the CS framework.

Hadamard combined with CS In Radwell *et al.* (2014), a method referred to as *evolutionary CS* was briefly reported. In this technique, they used information from a previous frame to decide which Hadamard patterns should be sent to the SLM, by simply sorting the measurements of the previous frame in order of magnitude. The K Hadamard patterns that corresponded to the highest responses were then chosen for acquisition of the current frame. Among these K patterns, 70% were retained

9. Noiselet functions are, for instance, perfectly incoherent with the Haar functions

and 30% were randomized, which showed good balance between image quality and image restoration speed based on the subset of Hadamard patterns. Instead of sampling with the complete Hadamard basis, Herman *et al.* (2015) and Sankaranarayanan *et al.* (2016) used Hadamard patterns as patches on the image. For instance, if the scene under view was 768×1024 and 8×8 Hadamard patterns were considered, which resulted in 64 Hadamard patterns that could be sent to 96×128 positions in the image, this yielded to 64 images of size 96×128 that were images filtered with the Hadamard patterns. In order not to sample each coefficient, some of the 64 Hadamard patterns scanned the full scene, while others only scanned randomly chosen positions with scrambled Hadamard patterns; i.e., random patterns as in CS-based SPC. In the end, a TV-minimization algorithm was used to restore the image of the scene under view.

CS with sinusoidal mask Random patterns of illumination were considered by Torabzadeh *et al.* (2017), along with a *spatial frequency domain imaging* technique. To perform spatial frequency domain imaging, the light from three different LEDs was modulated by a linear stage with a sinusoidal mask before reaching the DMD. Several images that corresponded to different phase-shifted sinusoidal projections were classically recovered using a CS algorithm. A reflectance image was finally estimated using temporal frequency domain analysis.

Adaptivity in CS In the context of CS, it is worth noting that adaptivity has also been examined out of the scope of SPI. Some authors have argued that the benefit is relatively small (Donoho, 2006), while others have claimed an improvement in measurement accuracy (Davenport *et* Arias-Castro, 2012; Malloy *et* Nowak, 2014) and/or that the number of measurements can be reduced (Indyk *et al.*, 2011). Moreover, CS with nonuniform sampling was recently considered in Petrovici *et al.* (2016), where they selected samples in the contour vicinity.

II.5.2 Pros and cons

For a given hybrid technique, both the pros and cons of the techniques reported earlier in this Chapter can be combined. Some examples of advantages and disadvantages of some of these hybrid approaches for SPI are given below.

Advantages The study of Yu *et al.* (2014a) and Soldevila *et al.* (2015) allowed for fast image recovery as only an inverse wavelet transform was needed. These methods were partially *adaptive*, in the sense that the locations of the patterns to send to the SLM were decided based on previous measurements. However, the set of patterns (CS for Yu *et al.* (2014a) ; Hadamard for Soldevila *et al.* (2015)) was the same regardless of the object, as opposed to an ABS strategy. In Zhao *et al.* (2015), it was claimed that using deterministic noiselet matrices for acquisition instead of the random patterns involved in CS yields better results. The *evolutionary CS* of Radwell *et al.* (2014) made it possible to dispose of the reconstruction algorithm of CS by using a sort of partially random BS approach based on data collected from a previous frame. Image restoration was therefore faster, and video applications are within reach.

Disadvantages In the design of Soldevila *et al.* (2015), if an object falls into a quadrant without touching a border, this quadrant will be discarded for acquisition, and no information about this object will be collected. Furthermore, the BS with Hadamard acquired in some way insignificant wavelet coefficients, as whole quadrants were acquired. This produced a higher number of samples (see Fig. II.7) compared to what can be achieved using an ABS approach. The sampling of insignificant coefficients was also part of the strategy of Yu *et al.* (2014a), which used CS patterns instead of Hadamard patterns to sample coarse images. The approaches described in Yu *et al.* (2014a); Herman *et al.* (2015); Sankaranarayanan *et al.* (2016) and Torabzadeh *et al.* (2017) were computationally demanding for the image restoration step, as they were based on CS recovery algorithms.

II.6 Conclusion

This Chapter reports the acquisition and restoration schemes found in the literature for acquisitions of images using a SPI device. These are mainly divided into four approaches, the main features of which are summarized in table II.1.

Approach	**Adaptivity**	**Patterns**	**# of patterns K**	**Image restoration**
Compressed Sensing	No	Random	$L < K \ll D$	ℓ_1/TV minimization
Basis Scan	No	Basis	$L < K \leq D$	Inverse transform
Adaptive Basis Scan	Yes	Basis	$L \leq K \ll D$	Inverse transform
Hybrid	Yes/no	Random/Basis	$L < K < D$	ℓ_1/TV or inverse transform

TABLE II.1 – Comparison of the main characteristics of the four major categories of acquisition/ restoration schemes for single-pixel imaging.

The CS approach is efficient, as it requires few measurements K (about L, for a L-sparse signal in a given basis). However, the heavy computational cost of the restoration process pushed investigations toward faster image recovery schemes. BS strategies are a solution, as these benefit from fast inverse transform, which allows for almost instant image recovery. However, this approach is not practical yet, due to the large number of measures that is required (i.e., the number D of pixels of the desired image). To fill this gap, ABS techniques have been proposed. The number of measurements can be as low as in the CS paradigm, while having straightforward image recovery. Finally, hybrid methods combine features of these three strategies.

Overall, the ABS strategy is very attractive as it allows the reduction of both the number of measurements, i.e., the acquisition time, and the restoration time. This is the reason why such an approach is considered in this thesis, as is reported in Chapter IV.

The end of this Chapter marks a break between the bibliography in SPI presented at the hardware (Chapter I) and software (Chapter II) levels and the contributions of this thesis reported in the following Chapters. Before detailing the adopted adaptive technique, the experimental set-ups that were used for testing the techniques developed are presented in the next Chapter.

CHAPTER III

EXPERIMENTAL SYSTEMS

Contents

CHAPTER III

THE acquisition of experimental data is essential to the design of new algorithms, as it allows the developments to be validated and/or adjusted. Most algorithms rely on assumptions based on a system that should work in theory. However, when moving to experimental acquisition, these underlying assumptions might be proven wrong. This is especially true in the case of single-pixel imaging (SPI), where some experimental constraints limit the applicability of certain techniques [1].

This Chapter describes the two experimental systems used that allowed the proposed techniques of this thesis to be tested experimentally. One is the optical set-up at the Politecnico di Milano, to which some improvements were made to control the different devices. The second system is a new set-up that was implemented in the CREATIS laboratory. The hardware design of these systems is presented, along with the software to control them and to perform single-pixel camera (SPC) measurements with an *adaptive* approach.

The system for time-resolved measurements at the Politecnico di Milano was described in Rousset *et al.* (2017a) and Rousset *et al.* (2017b).

III.1 Politecnico di Milano set-up

Most of the experiments presented in the following Chapters were carried out at the Politecnico di Milano, where a SPC set-up is available. This set-up was initially designed to perform fluorescence tomographic imaging (D'Andrea *et al.*, 2010; Ducros *et al.*, 2013, 2016), using a digital micromirror device (DMD) for structured illumination, and a CCD camera instead of the single-point detector (SPD). A second DMD was then added along with a SPD to obtain the SPC set-up schematized in Fig. III.1.

The contributions of this thesis to this particular system were two-fold. First, a spectrometer was added to the already existing time-resolved SPC, to obtain multispectral time-resolved measurements. Secondly, a method to control the different devices with an *adaptive* strategy was implemented within the existing programs.

III.1.1 Set-up overview

Light source The experimental set-up at the Politecnico di Milano includes a supercontinuum pulsed white laser source. Two options are possible for the source. The first option is an SC-450 from Fianium, and the second is a SuperK Extreme EXW-12 from NKT Photonics. Both have adjustable repetition rates up to 80 MHz, and visible power up to 1200 mW. As the object is usually illuminated

1. These constraints are addressed in Chapter V

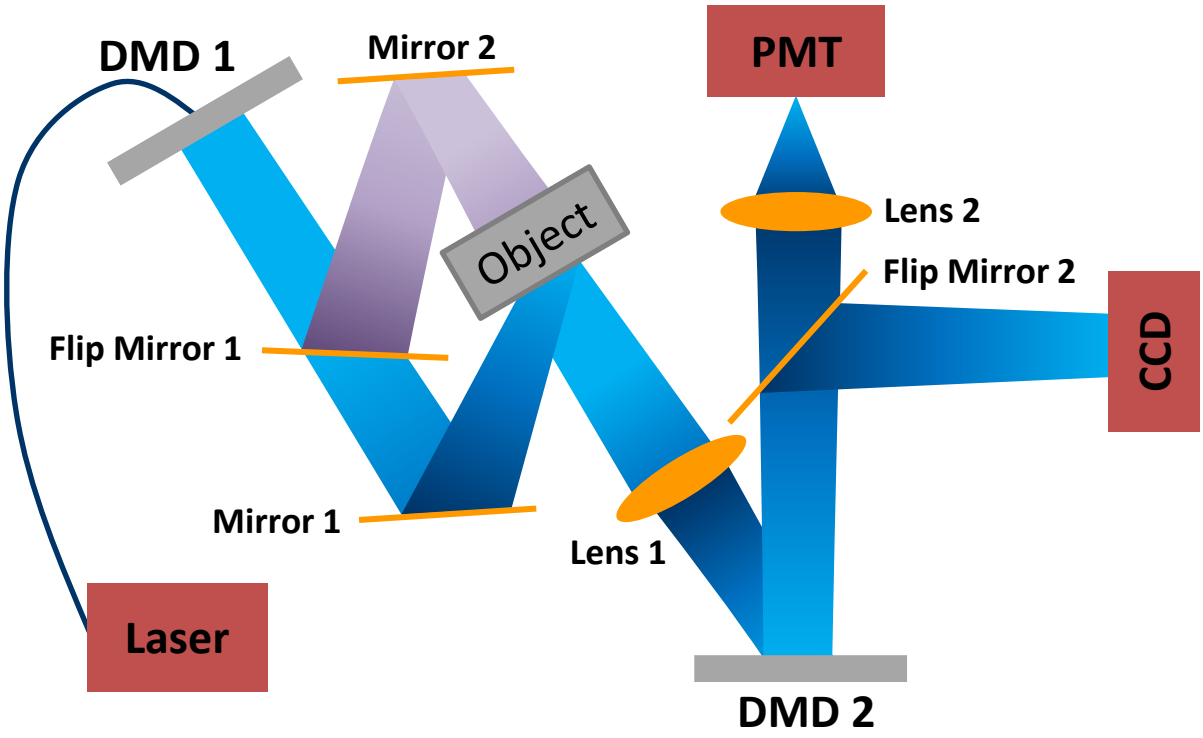

FIGURE III.1 – Experimental set-up at the Politecnico di Milano.

in a certain spectral band, a bandpass filter (ThorLabs) was added to the laser path when the SC-450 was used. When the EXW-12 was used, a tunable wavelength filter (SuperK Select, NKT Photonics) was coupled to the laser, to choose one or several spectral bands [2] .

Light modulation Initially, a 768 × 1024 DMD (DLP7000-V7001, Vialux GmbH) was used for illumination of the imaged object. The light was used to brighten the object either in transmittance or reflectance through a set of mirrors (Fig. III.1, mirrors 1, 2, flip mirror 1). The image of the object was then formed on a second 768 × 1024 DMD (DLP7000-V7001, Vialux GmbH) via the first lens (Fig. III.1, lens 1 ; $f = 60$ cm). This particular geometry with two DMDs allowed the modulation of the light in either illumination or detection (Fig. III.1, DMD1, DMD 2, respectively). If the first (resp. second) DMD was used for modulation, then the pattern on the second (resp. first) DMD was a completely white pattern [3]. For each of these DMDs, it was possible to load 8-bit patterns. This was performed by the DMD software (ALP Controller Suite, Vialux GmbH), which split each 8-bit pattern and assigned to them a particular display time on the DMD that was a multiple of a power of 2, so as to recreate the 8-bit pattern. Further details on this are given in Appendix A. Although two DMDs were included in this set-up, note that in the experiments described in the next Chapters, DMD 1 always displayed a white image, so as to obtain uniform illumination of the object. The modulation was thus performed with DMD 2 only.

Detection For the detection, the light reflected from the second DMD was imaged either on a 16-bit cooled CCD (Versarray 512, Princeton Instruments) or a SPD, through the actions of a second flip

2. Up to eight
3. The DMDs were therefore equivalent to a mirror

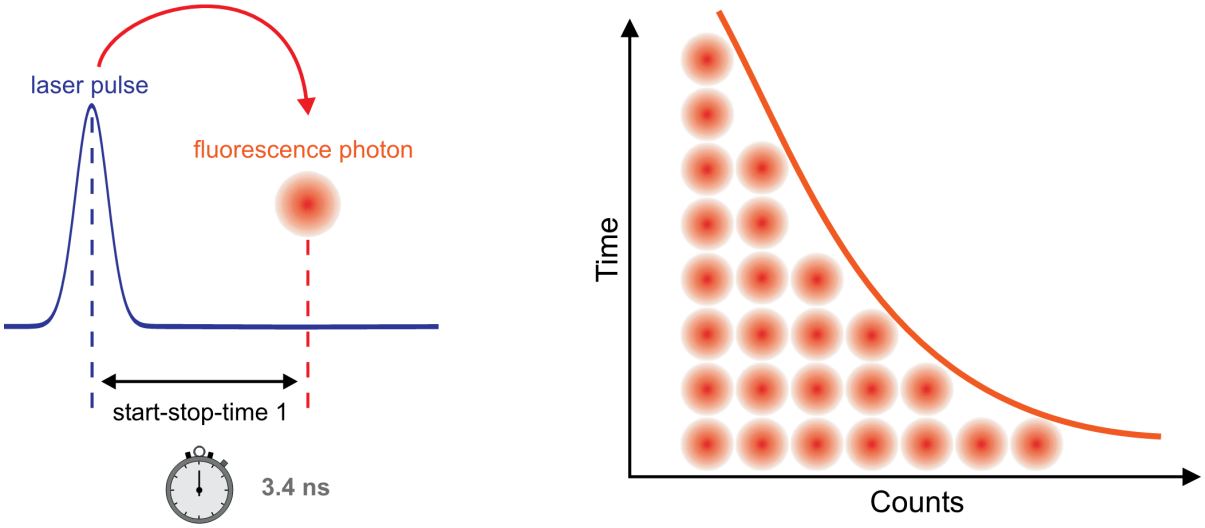

FIGURE III.2 – Principal of the time-correlated single photon counting board. The board measured the time-of-flight of each photon through its synchronization with the pulse of the laser. A histogram of the number of photons for the different time channels was built. Images extracted and adapted from Wahl (2014).

mirror (Fig. III.1, flip mirror 2). The SPD consisted of a 10 × /0.25 long-working-distance objective (Fig. III.1, lens 2), which focused the light onto an optical fiber. The light exiting the fiber was finally collected by a photomultiplier tube (PMT) (HPM-100-50, Becker & Hickl GmbH).

III.1.2 Time-resolved measurements

To obtain a time-resolved system, a *time-correlated single photon counting* (TCSPC) board (SPC-130 or SPC-630, Becker & Hickl GmbH) was connected to the PMT. This device was synchronized with a pulsed laser so that the TCSPC board assessed the time-of-flight of each of the detected photons (Fig. III.2, left). Depending on the assessed time-of-flight, the board updated the number of counts in the corresponding time bin. This process was repeated for each photon that reached the board, and it allowed a histogram of the photon time of flight to be constructed; i.e., it provided the number of photons detected in T time channels (Fig. III.2, right).

The time step that can be achieved with a TCSPC mostly depends on the detector used. In this set-up, a time step of about 3 ps per time channel was reached for $T = 4096$ channels. Instead of the single scalar measurement by a classical SPC, a vector of size T was then directly obtained when one pattern was sent to the spatial light modulator (SLM). This resulted in the possibility of restoring one image per time channel[4].

III.1.3 Multispectral measurements

Multispectral measurements can be easily performed by a SPC by replacing the SPD with a spectrometer. The principle is schematized in Fig. III.3. The spectrometer is usually composed of a slit coupled to the fiber where the light comes from. This light is then collimated on a mirror, before being dispersed at different angles through a grating. Finally, a second focusing mirror sends the different light rays to an array of Λ SPDs.

4. The mathematical formulation of these acquisitions is formalized in Chapter VI

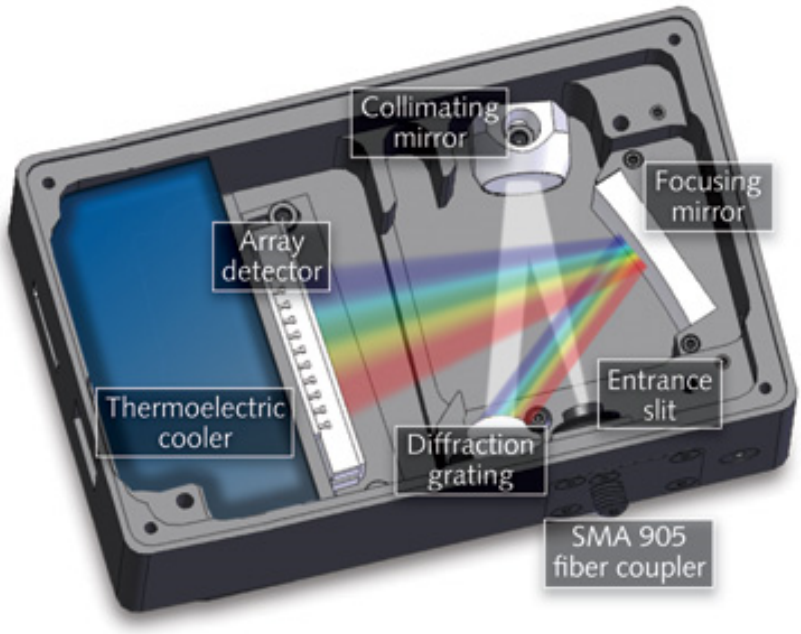

FIGURE III.3 – Example of a spectrometer and its components. Image extracted from http://www.laserfocusworld.com.

In this system, the array of detectors was a $\Lambda = 16$-channel PMT (PML-16-1, Becker & Hickl GmbH). Then with the detector still coupled to the TCSPC board (SPC-630, Becker & Hickl GmbH), a time-of-flight histogram for the Λ spectral channels was obtained. For this, the TCSPC was used in its routing mode, which revealed on which of the Λ detectors a photon was detected. Overall, the simple scalar measurement of a classical SPC system becomes a vector measurement of size $(\Lambda \times T)$ for one pattern sent to the SLM [5].

III.2 CREATIS set-up

A simpler experimental set-up was constructed at the CREATIS laboratory during the studies for this thesis, to validate the tools developed in Chapter V. To the best of our knowledge, besides that used in the studies of Studer *et al.* that date back to 2012, no SPC platform is available in France. This recently built set-up is illustrated in Fig. III.4.

Light source The experimental set-up in the CREATIS laboratory was composed of a white LED array (LIUCWHA, ThorLabs) for illumination of the object. A wheel with absorptive filters of different optical densities (NEXXB, ThorLabs) was positioned in front of the LED array, to control the illumination intensity (Eq. (II.5), parameter N_0).

Light modulation The image of the object was formed by lens 1 ($f = 75$ mm) on the SLM plane (Fig. III.4). The SLM was a 768×1024 DMD (DLP700-V7001, Vialux) that was able to load 8-bit patterns.

5. This mathematical formulation is also formalized in Chapter VI

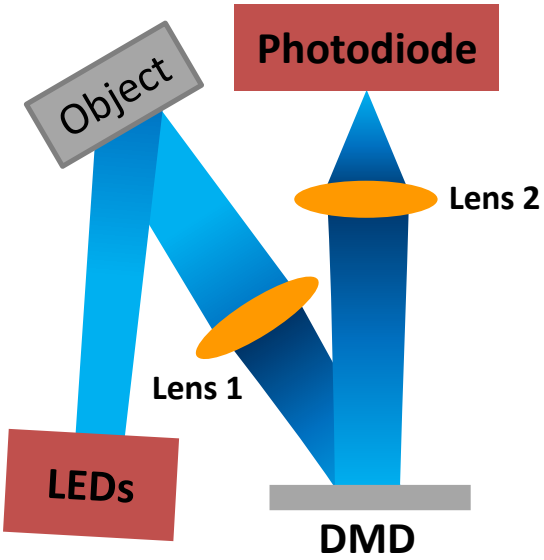

FIGURE III.4 – Experimental set-up at CREATIS.

Detection The light that exited the DMD converged onto the sensitive area of a photodetector (PDA36A-EC, ThorLabs) through lens 2 (f = 25 mm) (Fig. III.4). The detector was finally coupled to an analog-to-digital converter (ADC; USB-6210, National Instruments).

III.3 Software control

As mentioned in the Conclusion of Chapter II, an *adaptive* approach is implemented in this thesis, which means that the patterns sent to the SLM are chosen based on previous measurements. Communication between the control of the instruments using Labiew and the adaptive algorithm in Matlab was thus needed. This section details the Labview software for the control of the SPC, and the main features of the Matlab algorithm, before providing the operation mode to implement automatic feedback between these two programs.

III.3.1 Labview control of the instrumentation

As is often the case for optical and electronic devices, they can be controlled through Labview. During this study, an easy-to-use and intuitive application was therefore implemented to command the DMD, the CCD, and the SPD (PMT+TCSPC at Polimi; photodiode+ADC at CREATIS). The graphical user interface allowed manual acquisitions to be performed by tuning the main parameters :

- Path of the folder containing the patterns;
- Number of DMD patterns to send;
- DMD refresh rate;
- Integration time Δt of the detector;
- Frame rate of the CCD, if the CCD is used;
- ADC sampling frequency;
- Path of the folder where the measurements are saved;

- Name of the measured dataset.

Note that the power N_0 of the light source was controlled directly from the laser itself (Polimi set-up) or by using a special absorptive filter in front of the LED array (CREATIS set-up).

Once the parameters are set, a sequence of measurements can be manually started : the software reads the first pattern from the given folder, loads it onto the DMD, which launches the measure during Δt, with the data finally stored in the given saving folder. The second pattern is then automatically read, and so on, until the number of patterns that was set on the user interface is reached. In addition, the software shown in Fig. III.5 displays the pattern that is currently loaded on the DMD, as well as the current measurement.

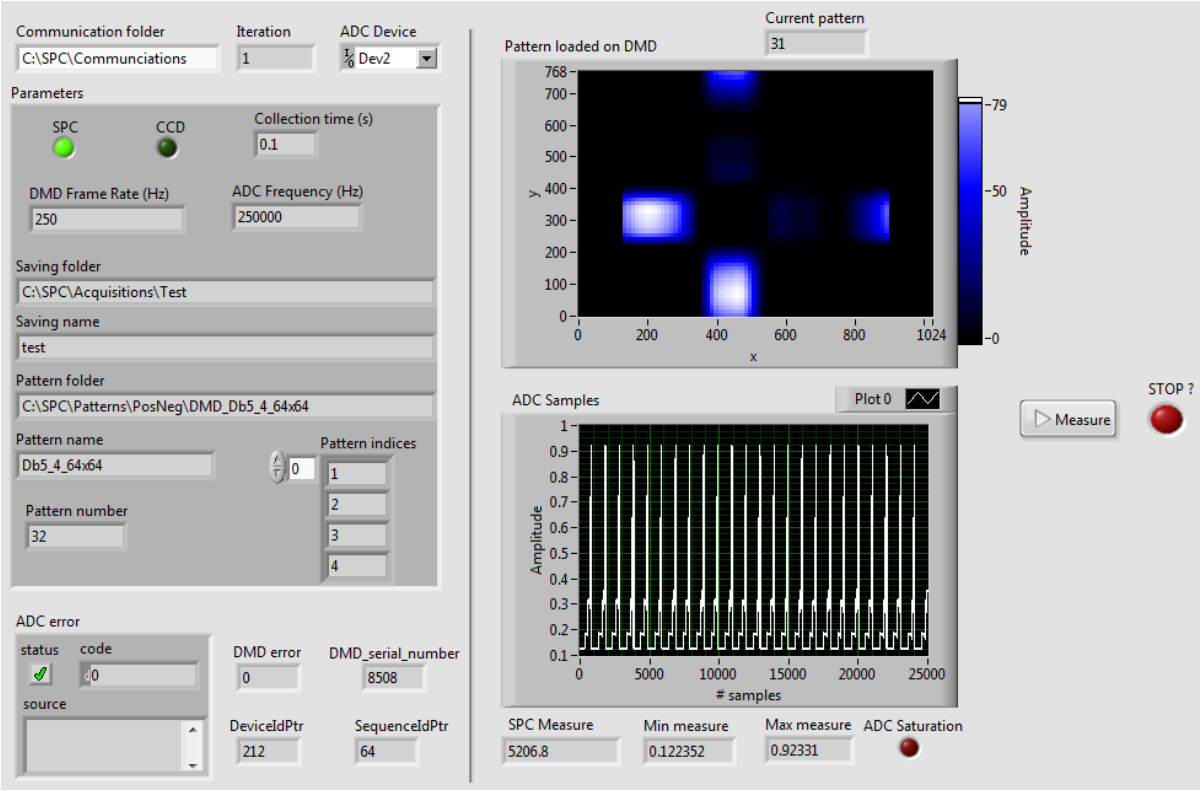

FIGURE III.5 – Graphical user interface of the Labview software to control the different instruments.

III.3.2 Matlab for the data processing

Matlab was used to create the patterns, and to implement the acquisition and restoration techniques, by processing the data saved by the Labview software. Some parameters are also tunable in the Matlab script :

- Number of iterations J if an *adaptive* scheme is considered;
- Path of the folder where the measurements are stored;
- Name of the acquired dataset;
- Pattern type/ basis;
- Total number of patterns; i.e., compression rate;

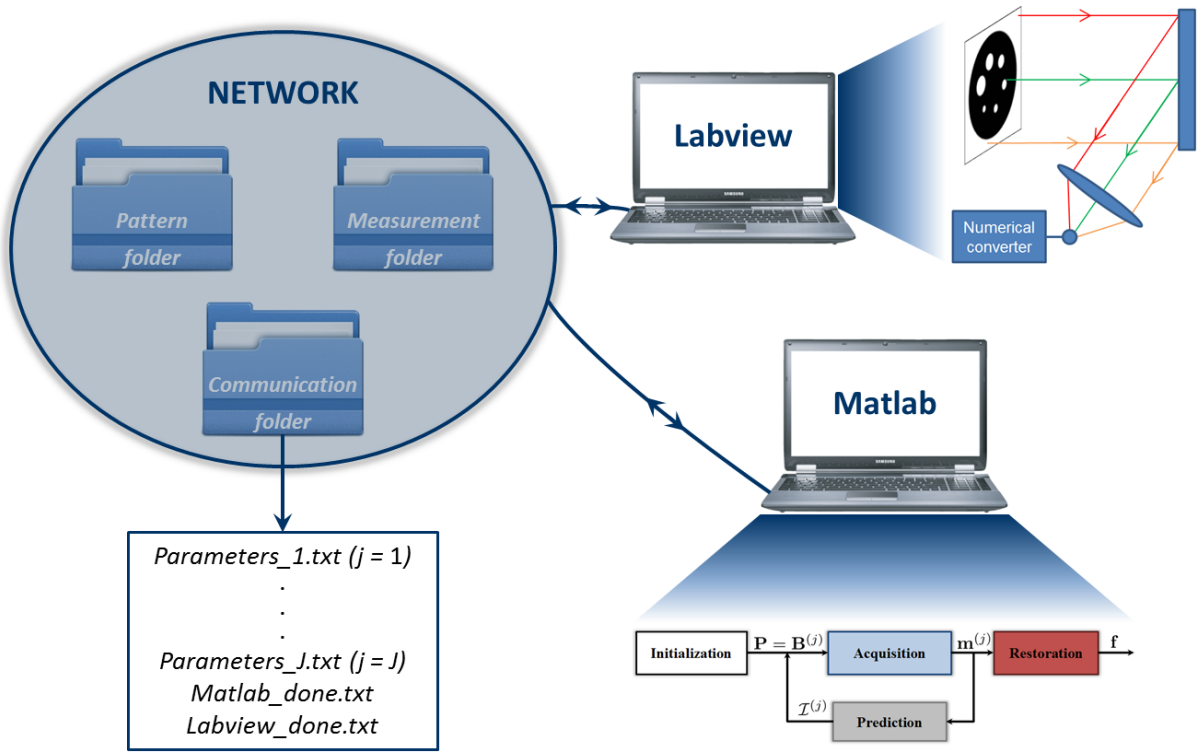

FIGURE III.6 – Scheme of the communication implemented between Matlab and Labview.

- Path of the folder where the patterns are stored;
- Parameters of the acquisition/ reconstruction algorithm.

Once some measurements have been performed by the Labview software, Matlab starts processing them, to either restore an image or to decide on the next measurements to be performed.

III.3.3 Matlab/ Labview communication

The two programs presented in the previous two sections worked independently, and to perform a complete set of measurements and restore an image, they were started manually one after the other. To further implement an *adaptive* scheme for acquisition/ restoration, Matlab/ Labview communication was put into place so as to have automatic feedback between the two softwares. According to the lists of parameters that were given above for both programs, it can be seen that some are redundant. A choice was therefore made to only tune all of the necessary parameters through Matlab. In other words, in the final implementation, Matlab was the master and Labview was the slave, as it followed the Matlab instructions.

The general framework of this implementation is outlined in Fig. III.6, where two different computers are used, one to control the instruments with Labview, and another one with Matlab for the processing. The operation works as follows :

1. The user sets all of the parameters needed through Matlab. In particular, three folders are created on a common network, the pattern and measurement folders, and a communication folder. The value j (iteration index) is set to 1.
2. The path to the *communication folder* is set in the Labview interface.

3. The Matlab and Labview programs are manually launched in any order. If Labview is started first, it goes into an infinite loop (i.e., wait mode), waiting for instructions from Matlab.
4. Matlab creates the necessary patterns for the *pattern folder*, and a parameter file called *Parameters_j.txt* is written in the *communication folder*. Once this is done, a file *Matlab_done.txt* is created, and Matlab enters its wait mode.
5. In its infinite loop, Labview tries to open *Matlab_done.txt*. If this opening fails, Labview stays in its loop. Once the file is created by Matlab, Labview detects that Matlab has finished its processing, and it therefore goes out of its wait mode. The file *Matlab_done.txt* is deleted by Labview.
6. Labview reads the j-th acquisition parameter file and starts the acquisition, and picks up the patterns in the *pattern folder*.
7. Once the measurements are performed, Labview saves them in the *measurement folder* and a file *Labview_done.txt* is created for the *communication folder*.
8. In its wait mode, Matlab tries to open *Labview_done.txt*. If this opening fails, Matlab stays in its loop. Once the file is created by Labview, Matlab detects that Labview has finished the measurements, and it therefore goes out of its wait mode. The file *Labview_done.txt* is deleted by Matlab.
9. Matlab performs the data analysis from the measurements in the *measurement folder* according to the chosen acquisition/ restoration scheme. It then defines the next patterns to send for acquisition, with the corresponding parameters for the iteration $j = j + 1$.
10. Steps 4 to 9 are repeated until $j = J$.

The advantage of such a communication process is that it can be done from two different computers as long as they can access a common network. This allows the instrumentation to be remotely controlled from another room than the laboratory where the optical set-up is. Note that this implementation can also be done using only one computer that runs both programs, without the use of folders on a network, but with local folders instead.

III.4 Conclusion

This Chapter has presented the experimental set-ups that were used for the acquisition of the experimental data presented in the next Chapters. The set-up at the Politecnico di Milano is very complete as it implements a multispectral time-resolved SPC. The object can also be illuminated in reflection or transmission, which means that different applications can be considered. At CREATIS, the newborn set-up consists of basic SPC implementation, although at this time it remains the only one of its kind in France [6]. For both set-ups, a Labview program provides the control of the optical instruments, while Matlab is used for the data processing. Communication between the two softwares is possible using a common network and through the writing of different files. A possible improvement would be to write everything in *C/C++*, to gain time on both sides. For instance, for the

6. To the best of our knowledge

acquisition side in Labview, if the collection time at the detector is set to $\Delta t = 1$ s, a single acquisition is actually around 1.2 s due to the reading of the pattern, initialization of the DMD, etc. Cleaner implementation that would prepare the next acquisition during the previous one would allow this to be closer to 1 s, saving 20% of the time.

As mentioned at the end of Chapter II, *ABS* strategies are very effective acquisition/ restoration schemes in terms of both the number of patterns and the image restoration time. The set-ups and software described in this Chapter allow the implementation of the proposed ABS approach, as is reported in the following Chapter.

CHAPTER IV

ADAPTIVE BASIS SCAN BY WAVELET PREDICTION

Contents

CHAPTER IV

ADAPTIVE acquisitions for single-pixel imaging (SPI) exploit sets of previously obtained measurements to decide the next spatial light modulator (SLM) patterns for a new set of measurements. In particular, as highlighted in Chapter II, *adaptive basis scan* (ABS) schemes are powerful, as their number of measurements can be relatively small, and quick image recovery techniques are available.

In this Chapter, we report our novel ABS strategy that we refer to as *adaptive basis scan by wavelet prediction* (ABS-WP). Some of the material in this Chapter comes from two conferences proceedings : *IEEE EMBC 2015* (Rousset *et al.*, 2015), where a slightly different prediction strategy was reported; and *IEEE ISBI 2016* (Rousset *et al.*, 2016), where a comparison with compressive sensing (CS) was given. This Chapter also mostly contains an article published in *IEEE Transactions on Computational Imaging* in 2017a (Rousset *et al.*, 2017a).

IV.1 Introduction

In most ABS schemes, wavelet basis are often used, as most images are known to have sparse representation in the wavelet domain, while fast inverse transform algorithms are available to recover the image (Mallat, 2008). These are the main reasons why wavelets have been, and always are, important in compression algorithms, such as JPEG2000 (Taubman *et* Marcellin, 2001). The ABS schemes proposed in the literature and detailed in Chapter II with the wavelet basis show two main drawbacks. The first is that these techniques usually use thresholding, which is image dependent, and the algorithms are therefore not so easy to tune. The second limitation regards the wavelet used; experimental acquisitions have only been demonstrated for the Haar wavelet [1], which is not necessarily the best wavelet to draw the best compression ratio out of it, depending on the image.

In this Chapter, we propose an entire framework for SPI that uses our new ABS technique, ABS-WP. Our approach comprises two main characteristics. First, we report a threshold-free prediction strategy based on the nonlinear wavelet approximation. The second characteristic is the possibility to use any desired wavelet for acquisition. We show that wavelets other than Haar can provide improved image quality. To begin with, the wavelet transform is detailed, followed by our acquisition and prediction strategies. The conditions in which the experiments were performed are then reported, as well as the data on the simulated and experimental acquisitions. ABS-WP is compared to the conventional CS framework and another ABS strategy, and then the results are discussed.

1. The Haar wavelet is well suited for the digital micromirror device ON/OFF states

IV.2 Wavelet transform

The wavelet transform is a very powerful and popular tool (Taubman *et* Marcellin, 2001; Mallat, 2008). This transform allows the signal to be interpreted as a superposition of oscillating functions, called wavelets, that are localized both in time and frequency. As we are interested in the wavelet transform of 2D images with dyadic wavelets, our image $\mathbf{f}$ is now considered as a $D = N \times N$ vector, with N as a power of 2. In this section, the wavelet decomposition is described, with the corresponding equations leading to the obtaining of the different wavelet coefficients via filter banks. A simplification of the notation is giving next, and then the nonlinear approximation of the wavelet transform is shown to lead to very good image quality with few coefficients.

IV.2.1 Wavelet decomposition

The so-called scaling function $\phi : \mathbb{R} \to \mathbb{R}$ and mother wavelet function $\psi : \mathbb{R} \to \mathbb{R}$ are defined as follows :

$$\phi(x) = \sqrt{2} \sum_{i \in \mathbb{Z}} h_i \phi(2x - i) \qquad \psi(x) = \sqrt{2} \sum_{i \in \mathbb{Z}} g_i \phi(2x - i) \tag{IV.1}$$

where $\mathbf{h}$ is a low-pass filter, and $\mathbf{g}$ is a high-pass filter, with coefficients chosen such that $g_i = (-1)^i h_{1-i}$, $i \in \mathbb{Z}$. This multiresolution analysis (Mallat, 1989) with dyadic wavelets is made possible through the functions $\phi_{j,i}$ and $\psi_{j,i}$, which correspond to dilated and translated versions of ϕ and ψ :

$$\phi_{j,i}(x) = 2^{-j/2} \phi\left(2^{-j}x - i\right) \qquad \psi_{j,i}(x) = 2^{-j/2} \psi\left(2^{-j}x - i\right) \tag{IV.2}$$

The function $\phi_{j,i}(x)$ is the function $\phi(x)$ defined by a scale factor 2^j with a translation of $2^j i$. The set of functions $\phi(2x - i)$ generates a subspace V_{-1} that includes functions of another resolution than that from the set V_0 generated by $\phi(x - i)$: $V_0 \subset V_{-1}$. This inclusion of subspaces can be generalized, and it is the key to the multiresolution analysis.

When image processing is considered, Equations (IV.1) and (IV.2) can easily be generalized to the 2D case considering separable functions. Such a function is defined as $\mathbf{\Phi} : \mathbb{R}^2 \to \mathbb{R}$, such that $\Phi(\mathbf{x}) = \Phi(x_1, x_2) = \phi(x_1)\phi(x_2)$ with $\mathbf{x} = (x_1, x_2)^\top$. The tensor product between the two 1D subspaces generates four functions : the scaling function $\mathbf{\Phi}_{j,\mathbf{i}}$, and three wavelet functions $\mathbf{\Psi}^1_{j,\mathbf{i}}$, $\mathbf{\Psi}^2_{j,\mathbf{i}}$ and $\mathbf{\Psi}^3_{j,\mathbf{i}}$, which are defined as :

$$\begin{cases} \Phi_{j,\mathbf{i}}(\mathbf{x}) = \phi_{j,i_1}(x_1)\phi_{j,i_2}(x_2) \\ \Psi^1_{j,\mathbf{i}}(\mathbf{x}) = \phi_{j,i_1}(x_1)\psi_{j,i_2}(x_2) \\ \Psi^2_{j,\mathbf{i}}(\mathbf{x}) = \psi_{j,i_1}(x_1)\phi_{j,i_2}(x_2) \\ \Psi^3_{j,\mathbf{i}}(\mathbf{x}) = \psi_{j,i_1}(x_1)\psi_{j,i_2}(x_2) \end{cases} \quad \text{with} \quad \mathbf{i} = (i_1, i_2)^\top. \tag{IV.3}$$

Using these functions, any image $\mathbf{f}$ can be decomposed into approximated and detailed coefficients. These coefficients are obtained as projections of the image on one of the four functions. Some are called approximation coefficients, $\boldsymbol{\beta}_j$, as they result from low-pass filtering. The others,

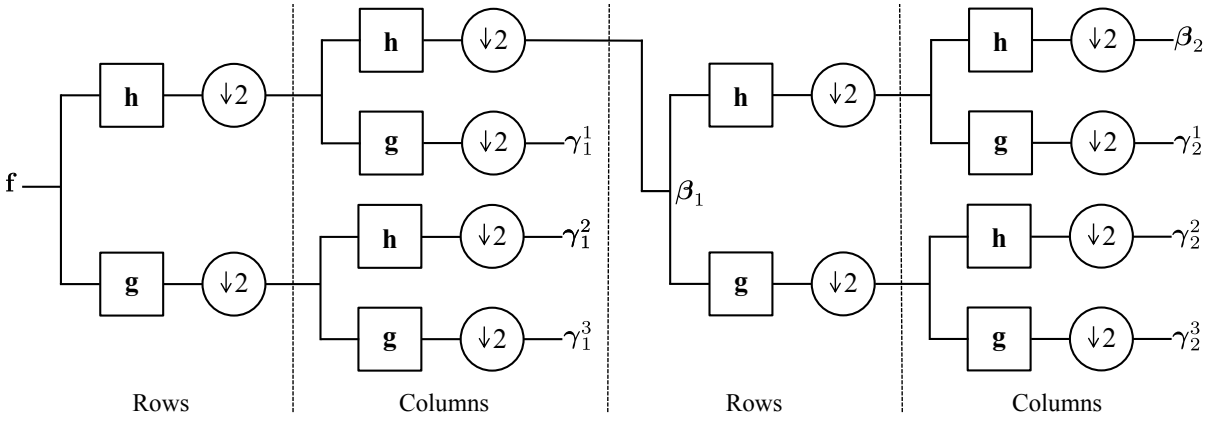

FIGURE IV.1 – Filter-bank representation of two-level wavelet decomposition.

$\boldsymbol{\gamma}_j^o$, represent the vertical ($o = 1$), horizontal ($o = 2$) and diagonal ($o = 3$) coefficients after high-pass filtering. It can be shown that the coefficients can be calculated as follow :

$$\begin{cases} \beta_{j,\mathbf{i}} = \langle \mathbf{f}, \boldsymbol{\Phi}_{j,\mathbf{i}} \rangle = \sum_{m_1 \in \mathbb{Z}} \sum_{m_2 \in \mathbb{Z}} h_{m_1-2i_1} h_{m_2-2i_2} \beta_{j-1,\mathbf{m}} \\ \gamma^1_{j,\mathbf{i}} = \langle \mathbf{f}, \boldsymbol{\Psi}^1_{j,\mathbf{i}} \rangle = \sum_{m_1 \in \mathbb{Z}} \sum_{m_2 \in \mathbb{Z}} h_{m_1-2i_1} g_{m_2-2i_2} \beta_{j-1,\mathbf{m}} \\ \gamma^2_{j,\mathbf{i}} = \langle \mathbf{f}, \boldsymbol{\Psi}^2_{j,\mathbf{i}} \rangle = \sum_{m_1 \in \mathbb{Z}} \sum_{m_2 \in \mathbb{Z}} g_{m_1-2i_1} h_{m_2-2i_2} \beta_{j-1,\mathbf{m}} \\ \gamma^3_{j,\mathbf{i}} = \langle \mathbf{f}, \boldsymbol{\Psi}^3_{j,\mathbf{i}} \rangle = \sum_{m_1 \in \mathbb{Z}} \sum_{m_2 \in \mathbb{Z}} g_{m_1-2i_1} g_{m_2-2i_2} \beta_{j-1,\mathbf{m}} \end{cases} \tag{IV.4}$$

where $\mathbf{m} = (m_1, m_2)^\top$. The multiresolution analysis allows the image to be studied at different scales : a small value of j will give fine details, whereas a larger value gives coarser details. The coefficient computation in Equation (IV.4) shows two convolutions and two decimations, one of each applied on the rows of the image and then on the columns. This can be illustrated as in Fig. IV.1, using filter banks.

Given the decimation by two on the rows and columns, the discrete wavelet of an image $N \times N$ can be arranged in an $N \times N$ image, as can be seen in Fig. IV.2a. With orthogonal wavelets (Daubechies, 1992), perfect recovery of the image is possible from its coefficients, using the inverse wavelet transform :

$$\mathbf{f} = \sum_{\mathbf{i} \in \mathbb{Z}^2} \beta_{J,\mathbf{i}} \boldsymbol{\Phi}_{J,\mathbf{i}} + \sum_{o=1}^{3} \sum_{j=1}^{J} \sum_{\mathbf{i} \in \mathbb{Z}^2} \gamma^o_{j,\mathbf{i}} \boldsymbol{\Psi}^o_{j,\mathbf{i}} \tag{IV.5}$$

where J is the chosen decomposition level with $1 \leq J \leq \log_2(N) = R$. When $J = R$, the approximation is reduced to only one coefficient.

IV.2.2 Notation simplification

For the sake of simplicity, in the rest of this thesis, we denote $\widetilde{\mathbf{f}} \in \mathbb{R}^{D \times 1}$ as the wavelet coefficients of $\mathbf{f}$ for a given wavelet. The vector $\widetilde{\mathbf{f}}$ hence regroups the different coefficients of Equation (IV.4) and represents $\mathbf{f}$ in the wavelet domain (see Fig. IV.2, c). The value $j = 1 \ldots J$ represents the scale at which

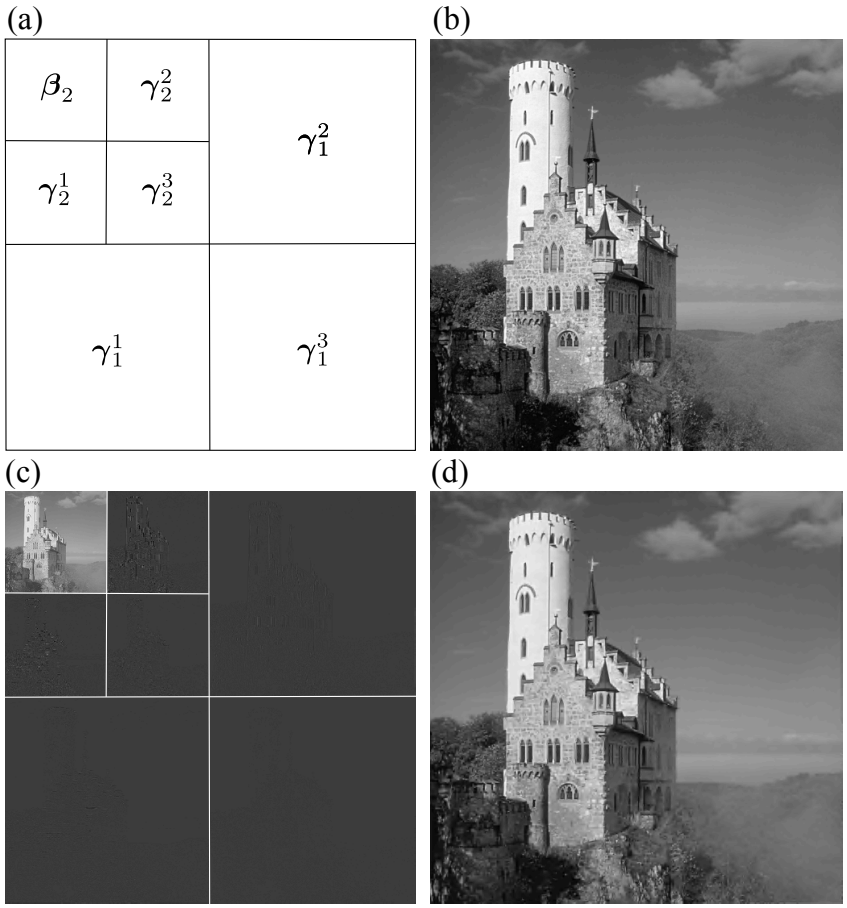

FIGURE IV.2 – Example of a two-level wavelet transform on a 512×512 pixels image. (a) Disposition of the wavelet coefficients. (b) Ground truth image of Lichtenstein castle. (c) Two-level wavelet transform of (b). (d) Recovered image with only 10% of the largest coefficients in (c).

the image $\mathbf{f}$ is observed with J as the decomposition level. A location is specified by the vector $\mathbf{i}$, such that

$$\mathbf{i} = (i_1, i_2)^\top \in \left\{1, \ldots, 2^\ell\right\}^2 \quad \text{with} \quad \ell = R - j \tag{IV.6}$$

The wavelet transform of $\mathbf{f}$ depicted by $\widetilde{\mathbf{f}}$ is given by :

$$\widetilde{\mathbf{f}} = \mathbf{B}\mathbf{f} \tag{IV.7}$$

where $\mathbf{B} \in \mathbb{R}^{D \times D}$ is an orthonormal operator (Daubechies, 1992). Each element of $\widetilde{\mathbf{f}}$ can be fully identified and located by its unique triplet k :

$$k = \{o, j, \mathbf{i}\} \tag{IV.8}$$

where $o = 0, 1, 2$ or 3 corresponds to the approximation, and the vertical, horizontal and diagonal coefficients, respectively. In addition, each row of $\mathbf{B}$ corresponds to a unique triplet k. The image $\mathbf{f}$ can be perfectly recovered from $\widetilde{\mathbf{f}}$, similar to Equation (IV.5), using the inverse wavelet transform :

$$\mathbf{f} = \mathbf{B}^{-1}\widetilde{\mathbf{f}} \tag{IV.9}$$

IV.2.3 Nonlinear approximation

The wavelet transform was shown to give sparse signals, which allows many coefficients to be discarded at the recovery step. The best possible approximation of the wavelet transform is the nonlinear approximation, where a number $K \ll D$ of the largest coefficients are retained across all of the scales. The other elements are set to 0, and the image restoration using Equation (IV.5) shows excellent image quality (Mallat, 2008). There is therefore simply the need to hard-threshold the elements of $\widetilde{\mathbf{f}}$ for a given threshold γ to obtain the nonlinear approximation image $\mathbf{f}_\gamma$ of $\mathbf{f}$:

$$\mathbf{f}_\gamma = \mathbf{B}^{-1}\widetilde{\mathbf{f}}_\gamma \quad \text{with} \quad \left(\widetilde{\mathbf{f}}_\gamma\right)_n = \begin{cases} \left(\widetilde{\mathbf{f}}\right)_n & \text{if} \quad \left|\left(\widetilde{\mathbf{f}}\right)_n\right| \geq \gamma \\ 0 \quad \text{otherwise.} \end{cases} \tag{IV.10}$$

This approximation is nonlinear[2] as the set $\Gamma = \left\{n \,:\, \left|\left(\widetilde{\mathbf{f}}\right)_n\right| \geq \gamma\right\}$, with $\text{card}(\Gamma) = K$, changes with the image $\mathbf{f}$. Figure IV.2 shows an example of a nonlinear approximation with only 10% of the largest coefficients. This approximation is nonlinear in the sense that the set of retained coefficients is different for each image.

IV.3 The adaptive basis scan by wavelet prediction method : prediction strategy

IV.3.1 Concept

The ABS-WP method aims to record a nonlinear approximation of the wavelet transform. Our goal is to acquire the significant wavelet coefficients, and it is therefore necessary to predict the triplets k for each of these elements. The endgame consists of filling the matrix $\mathbf{P} = \left(\mathbf{p}_1, \ldots, \mathbf{p}_k, \ldots, \mathbf{p}_K\right)^\top$ of Equation (II.5) with the rows of $\mathbf{B}$ that correspond to the predicted triplet k, denoted $\bar{k}$. When SPC acquisition is considered, the whole wavelet transform of the image is not known. Hence, the concept is to perform several nonlinear approximations iteratively on the different scales of the wavelet decomposition.

IV.3.2 Strategy

For the sake of simplicity, and to better understand the sizes of the images involved in this ABS-WP scheme, the vector notation of the image $\mathbf{f} \in \mathbb{R}^{D\times 1}$, $D = N \times N$, is temporarily replaced by the matrix notation $\mathbf{F} \in \mathbb{R}^{N\times N}$. Similarly, $\widetilde{\mathbf{F}} \in \mathbb{R}^{N\times N}$ represents the wavelet transform of $\mathbf{F}$.

Our strategy can be decomposed into five steps. Step 1 is the initialization, where a predefined set of patterns is sent for acquisition. Steps 2 to 4 predict the next coefficients to sample ; i.e., the next wavelet patterns to send to the SLM. Step 5 consists of the experimental acquisition of the predicted significant wavelet elements :

2. The linear approximation of the image is the one that retains the first K coefficients of $\widetilde{\mathbf{f}}$; i.e., which includes all elements of the wavelet decomposition, starting from the largest scale J to $J-1$, and so on

1. The approximation image $\mathbf{A}_j$ at the coarse scale $j = J$ is completely acquired. This is a $2^\ell \times 2^\ell$ image with $\ell = R - j$. To be precise, this approximation image is obtained with the corresponding set of patterns at the coarse wavelet scale J. This can therefore be seen as a BS sampling the $2^{2\ell}$ coefficients.
2. $\mathbf{A}_j \in \mathbb{R}^{2^\ell \times 2^\ell}$ is oversampled by a factor of two, using an interpolation operator[3], $\mathcal{S}$. This leads to the high resolution image $\mathbf{H}_j = \mathcal{S}(\mathbf{A}_j) \in \mathbb{R}^{2^{\ell+1} \times 2^{\ell+1}}$.
3. This image $\mathbf{H}_j$ is one-level wavelet transformed to give $\widetilde{\mathbf{H}}_j \in \mathbb{R}^{2^{\ell+1} \times 2^{\ell+1}}$. This provides the *predicted* wavelet detail coefficients at scale j.
4. To obtain the triplets $\bar{k}$ of the largest predicted elements, a nonlinear approximation is performed by retaining a percentage p_j of the largest detail coefficients of $\widetilde{\mathbf{H}}_j$. This leads to the obtaining of the predicted significant elements and their corresponding predicted triplets, $\bar{k}$.
5. The coefficients are finally experimentally acquired using the patterns that match the rows of $\mathbf{B}$ that correspond to the triplets $\bar{k}$.

This description works for one scale of the wavelet transform, but it can be easily extended to the other scales. For step 1, instead of the whole sampling of the coarse image at scale $j = J$, the approximation image $\mathbf{A}_j$ is retrieved by the inverse wavelet transform of the coefficients acquired so far. Steps 2 to 5 are unchanged, except that a different value of p_j is used for each scale giving the overall set of percentages

$$\mathcal{P} = \{p_J, p_{J-1}, ..., p_1\}. \tag{IV.11}$$

This strategy thus alternates between acquisition of the wavelet coefficients on the real image (i.e., experimentally) and prediction using an interpolation technique. An illustration of the algorithm of ABS-WP is given in Fig. IV.3, where the number for each step corresponds to the steps given above. The image $\mathbf{F}$ (or $\mathbf{f}$) is obtained through Equation (IV.5) by inverse wavelet transform of the elements acquired up to scale $j = 1$.

IV.3.3 Compression rate

The whole acquisition at scale $j = J$ of the approximation image $\mathbf{A}_j$ leads to the sampling of $n_0 = 2^{2L} = 4^L$ wavelet coefficients with $L = R - J$. Then, a percentage p_j of the strongest predicted detail coefficients is acquired. Hence, the number of measurements at each scale j is given by

$$n_j = 3 \times 4^{R-j} \times p_j \tag{IV.12}$$

The total number of elements n acquired for each decomposition level is therefore controlled by modulation of the set of percentages $\mathcal{P}$ in Equation (IV.11). Using Equation (IV.12), it can be shown that

$$n = 4^L \left[1 + 3 \sum_{j=1}^{J} 4^{J-j} p_j \right] \tag{IV.13}$$

The compression rate (CR) is defined as

$$\mathrm{CR} = 1 - \frac{n}{D} \tag{IV.14}$$

which corresponds to a normalized quantity that ranges from 0 to 1.

3. The influence of the choice of the interpolation operator is reported in the results

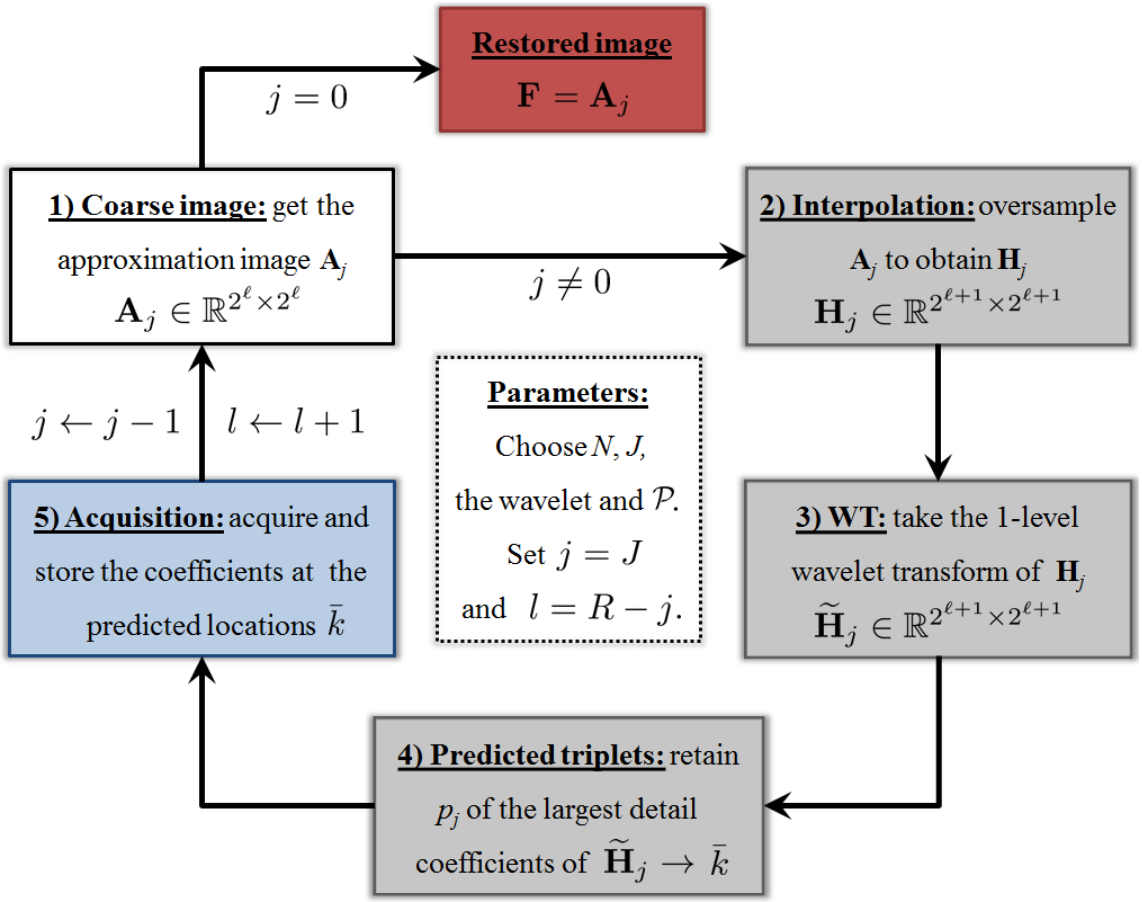

FIGURE IV.3 – Summary of the acquisition and prediction strategies of the *adaptive basis scan by wavelet prediction* technique. The blue box corresponds to the acquisition step, the gray boxes to the prediction, and the red box to the image recovery. The white boxes indicate initialization or general processes.

IV.4 Experiment overview

IV.4.1 Pattern creation

Generation To perform the acquisition, the set of patterns $\mathbf{P} = (\mathbf{p}_1, \ldots, \mathbf{p}_k, \ldots, \mathbf{p}_K)^\top$ that will be sent to the digital micromirror device (DMD) have to be generated. One pattern can be obtained as :

$$\mathbf{p}_k = \mathbf{B}^{-1}\mathbf{v}_k \tag{IV.15}$$

where $\mathbf{v}_k$ is a unit vector that is chosen from the canonical basis $\{\mathbf{e}_k\}$. In practice, a null image can be created, and the only pixel located at the triplet k can be set to 1. Taking the inverse wavelet transform of this image leads to the corresponding pattern for the acquisition of the wavelet coefficient located at the triplet k.

However, two practical problems arise in the sending of such images to any SLM : the patterns created have floating values, and have both negative and positive elements that cannot be physically implemented on any SLM.

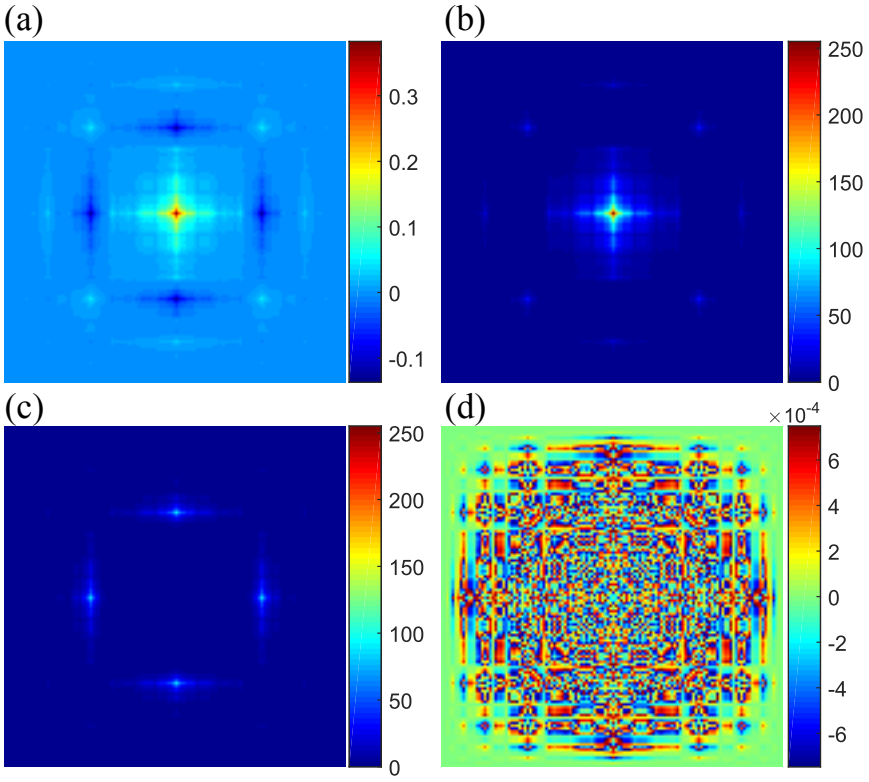

FIGURE IV.4 – Before and after quantization of one of the Le Gall wavelet patterns for $b = 8$ bits. (a) The real wavelet pattern $\mathbf{p}_k$. (b) The positive quantized part $\widehat{\mathbf{p}}_k^+$ of the pattern. (c) The negative quantized part $\widehat{\mathbf{p}}_k^-$ of the pattern. (d) The quantification error pattern $\widehat{\mathbf{e}}_k$.

Positive/negative separation To deal with the positivity problem [4], $\mathbf{p}_k$ is separated into its positive and absolute negative parts, so that $\mathbf{p}_k = \mathbf{p}_k^+ - \mathbf{p}_k^-$. As Equation (II.4) is linear, the final measurement m_k can be obtained numerically as

$$m_k = m_k^+ - m_k^- \tag{IV.16}$$

where

$$m_k^+ = \left(N_0 \mathbf{f}^\top \mathbf{p}_k^+ + \alpha\right)\Delta t \qquad \text{and} \qquad m_k^- = \left(N_0 \mathbf{f}^\top \mathbf{p}_k^- + \alpha\right)\Delta t \tag{IV.17}$$

are two experimental measurements acqired by the SPC. Note that in Equation (IV.16), the additive component $\alpha\Delta t$ is canceled out by the subtraction, which is convenient as it flaws the measurement [5].

Quantization To use any kind of wavelet, and to deal with the floating values of the patterns, a uniform quantization is performed that converts the patterns to b-bit patterns, where 2^b is the dynamic range that is used for the SLM [6]. The following transform is applied to each pattern to achieve this uniform quantization :

$$\widehat{\mathbf{p}}_k = \left\lfloor \frac{1}{q_k}\mathbf{p}_k \right\rfloor \qquad q_k = \frac{\max\left(|\mathbf{p}_k|\right)}{2^b - 1} \tag{IV.18}$$

where $\lfloor . \rfloor$ is a rounding operation. As the patterns $\mathbf{p}_k$ depend on the triplet k of Equation (IV.8), the quantization factor denoted as q_k also depends on the same triplet. Figure IV.4 shows an example

4. This problem is detailed in the next Chapter, with a proposed technique to deal with this constraint
5. Again, the next Chapter gives more detail concerning this problem
6. For a DMD, b ranges from 4 to 12, depending on the model

of pattern quantization using the Le Gall (CDF 5/3) biorthogonal wavelet (Gall *et* Tabatabai, 1988; Cohen *et al.*, 1992). This quantization step inevitably leads to an irreversible loss of information, which can be defined by the quantization error pattern $\widehat{\mathbf{e}}_k = q_k\widehat{\mathbf{p}}_k - \mathbf{p}_k$.

If this quantization error can be neglected, the measurement m_k in Equation (IV.16) is obtained numerically by applying the quantization factor to the measures :

$$m_k = q_k\left(\hat{m}_k^+ - \hat{m}_k^-\right) \tag{IV.19}$$

where

$$\hat{m}_k^+ = \left(N_0\mathbf{f}^\top\widehat{\mathbf{p}}_k^+ + \alpha\right)\Delta t \qquad \text{and} \qquad \hat{m}_k^- = \left(N_0\mathbf{f}^\top\widehat{\mathbf{p}}_k^- + \alpha\right)\Delta t \tag{IV.20}$$

are two experimental measurements acquired by the SPC. The value of $q_k\Delta t = \Delta t_k$ can also be directly used as an integration time, to obtain correctly scaled measurements (i.e., without post-processing) :

$$m_k^+ = q_k\left(N_0\mathbf{f}^\top\widehat{\mathbf{p}}_k^+ + \alpha\right)\Delta t = \left(N_0\mathbf{f}^\top\widehat{\mathbf{p}}_k^+ + \alpha\right)\Delta t_k \quad \text{and} \quad m_k^- = \left(N_0\mathbf{f}^\top\widehat{\mathbf{p}}_k^- + \alpha\right)\Delta t_k \tag{IV.21}$$

which are directly experimentally acquired by the SPC with Δt_k as the integration time, and the final measurement is numerically computed as in Equation (IV.16).

IV.4.2 Numerical experiments

To perform simulations, images that show different features are used. The well-known images of Lena and the peppers have been commonly used in image processing, and these were used here for a test with natural images. An image of vertebral bone tissue of a fetus was obtained by optical microscopy and is shown in Fig. IV.5, which serves as an indicator for textured images. As fluorescence imaging is a target application, a bioluminescence image of a mouse (Keramidas *et al.*, 2010) superimposed on its ambient light image is also considered, as shown in Fig. IV.6.

This ABS-WP method is compared to the use of the CS presented in Section II.2, which is the reference *nonadaptive* approach. For CS simulations, we directly reconstructed the image $\mathbf{f}$ from the measurements $\mathbf{m}$ using total variation (TV)-minimization (Eq. (II.13)) via TVAL3 (Li, 2009), as was done by Takhar *et al.* (2006) and Duarte *et al.* (2008). For the parameters of such an approach, these were chosen to give the best results in most cases. Among these, anisotropic TV with positivity was used.

Our data here are also compared to the *adaptive* method of extended wavelet trees adaptive compressed sampling (EWT-ACS), as proposed by Dai *et al.* and described in Section II.4.2. As a reminder, this *adaptive* technique is derived from the Haar wavelet, and a threshold has to be chosen to predict the relevant coefficients to sample. For each of the proposed images and compression rates, this threshold was tackled experimentally to provide the best possible peak signal-to-noise ratio (PSNR) of the restored image [7].

Noisy simulations are also reported, in which the measurements are corrupted by Poisson noise, which is noise that is generally present when an optical measurement with photons is considered [8].

7. The PNSR between the reference image $\mathbf{f}$ and image $\mathbf{g}$, defined as $\mathrm{PSNR}(\mathbf{f},\mathbf{g}) = 10\log_{10}\left(\frac{\max(\mathbf{f})^2}{\mathrm{MSE}(\mathbf{f},\mathbf{g})}\right)$ (in dB), with $\mathrm{MSE}(\mathbf{f},\mathbf{g}) = \frac{1}{D}\sum_{i=1}^{D}(f_i - g_i)^2$

8. There are other sources of noise, but the predominant one is the Poisson noise

Experimentally, this noise affects the number of photons read by the SPD, and thus it is applied numerically onto the two measurements of Equation (IV.21) ; i.e., Equation (IV.21) becomes

$$m_k^+ = \mathscr{P}\left(q_k\left(N_0\mathbf{f}^\top\widehat{\mathbf{p}}_k^+ + \alpha\right)\Delta t\right) \quad \text{and} \quad m_k^- = \mathscr{P}\left(q_k\left(N_0\mathbf{f}^\top\widehat{\mathbf{p}}_k^- + \alpha\right)\Delta t\right) \tag{IV.22}$$

where $\mathscr{P}$ is the Poisson distribution. Changing N_0 and/or Δt in Equation (IV.22) allows the simulation of several levels of noise for a given image $\mathbf{f}$. When the values of N_0 are small, the Poisson noise has indeed a greater effect, as less photons are received by the detector.

IV.4.3 Experimental acquisitions

The set-up at the Politecnico di Milano described in Section III.1 was used. This comprised the supercontinuum pulsed white laser source (SC-450, Fianium), followed by a filter with a center wavelength of 650 nm, for uniform illumination of the object. The one-channel photomultiplier tube (HPM-100-50, Becker & Hickl GmbH) coupled to the time-correlated single photon counting (TCSPC) board (SPC-130, Becker & Hickl GmbH) is used as a detector. Therefore, only time-resolved measurements are considered in this Chapter, with the use of the TCSPC board. For the given acquisitions, however, this information is not exploited, and the different measurements in the time channels are integrated (i.e., summed) to give only scalar measurements, which is equivalent to a system with an analog-to-digital converter instead of the TCSPC board [9].

Two Jaszczak phantoms commonly used in computerized tomography were chosen as objects. These targets were printed on white paper with a diameter of about 22 mm. Figure IV.7a and Fig. IV.8a show the corresponding experimental charge coupled device (CCD) images of these targets.

For the two proposed experimental acquisitions, 128×128 pixels patterns were used, thus giving 128×128 restored SPC images. To use most of the height of the DMD in our set-up, the patterns were further resized as 640×640 patterns. A box-shaped kernel was used to perform the resizing operation, which means that no pixel values other than those in the patterns were added. In other words, an area of 5×5 ($640/128 = 5$) DMD mirrors was used to represent one pixel of the 128×128 pattern. After the acquisition, the SPC images are compared to their reference CCD image. For visual comparisons, the dynamics of the SPC images were rescaled to the dynamic range of the CCD image.

IV.4.4 Integration time

The integration time Δt at the detector is only limited by the DMD frequency, as in most SPC architectures. However, as mentioned earlier, a TCSPC board is used in our set-up. The statistics constraints of the photon counting of the board restrict the use of the DMD at its highest speed. To work properly while having a good SNR [10], the TCSPC board indeed requires integration times of a few hundred milliseconds under standard illumination conditions. The integration time Δt at the SPD in this particular case is therefore always greater that the integration time without the TCSPC board. As a result, Δt is kept constant for each case of the following simulations and experimental data. The different techniques (CS, EWT-ACS, ABS-WP) are therefore relatively comparable for

9. The time information is exploited for applications such as fluorescence lifetime imaging in Chapter VI

10. The SNR is defined as $\text{SNR} = 10\log_{10}\left(\frac{P_{\text{signal}}}{P_{\text{noise}}}\right)$ (in dB), where P_{signal} (resp. P_{noise}) is the power of the observed signal (resp. noise)

Image	Technique	PSNR (dB)								Time (s)
		$j = J = 4$		$j = 3$		$j = 2$		$j = 1$ / Global		
		Before	*After*	*Before*	*After*	*Before*	*After*	*Before*	*After*	
Lena	Bicubic	16.92	**34.09**	19.62	**34.10**	22.72	**31.73**	26.25	**29.59**	**0.43**
	FZP	18.00	31.11	20.77	30.07	23.85	28.64	27.00	27.59	**0.43**
(256 × 256)	NEDI	**18.23**	30.32	**21.63**	29.22	**24.26**	28.20	26.97	27.30	6.46
	CS-WZP	18.13	31.45	21.22	31.11	24.25	29.84	**27.80**	28.30	1.02
Peppers	Bicubic	20.16	**37.95**	22.97	**38.60**	26.26	**37.50**	30.44	**34.83**	**0.43**
	FZP	21.19	36.40	24.34	35.46	28.06	33.69	31.93	32.66	**0.43**
(256 × 256)	NEDI	**21.43**	36.19	**25.05**	36.29	**28.44**	33.96	32.09	32.70	6.36
	CS-WZP	21.15	34.91	24.62	34.66	28.28	34.02	**32.10**	32.72	1.00
Bones	Bicubic	18.21	30.86	21.32	**30.72**	24.87	**30.13**	28.52	**30.29**	**0.43**
	FZP	18.33	**31.18**	22.44	30.46	26.30	29.81	**29.77**	29.96	**0.43**
(256 × 256)	NEDI	**19.14**	29.74	**22.72**	28.53	25.87	28.02	28.16	28.34	6.46
	CS-WZP	18.61	30.40	22.59	29.90	**26.40**	29.43	29.55	29.60	1.00
Mouse	Bicubic	20.53	65.77	25.27	66.86	31.38	61.76	37.57	**49.13**	**0.22**
	FZP	**22.95**	53.57	**28.57**	42.21	36.67	45.71	43.40	45.03	**0.22**
(128 × 128)	NEDI	21.41	**76.55**	27.92	**71.97**	35.80	**63.03**	44.90	47.72	1.94
	CS-WZP	22.38	53.30	28.47	54.48	**37.16**	55.14	**46.52**	49.04	0.48

TABLE IV.1 – Effects of the interpolation technique in our adaptive basis scan using the wavelet prediction method for different test images. The peak signal-to-noise ratios obtained *before* and *after* the acquisition of the significant predicted coefficients during adaptive basis scan by wavelet prediction for different interpolation methods are given. Le Gall 128 × 128 patterns were used with a compression rate of 85%. The computation time given in the last column includes the prediction and restoration of the image. FZP, Fourier zero padding; NEDI, new-edge directed interpolation; CS-WZP, cycle-spinning wavelet zero padding.

a given number of measurements. Once the set of measurements $\{\hat{m}_k\}$ of (IV.20) was acquired, they were post-processed with their quantization factor $\{q_k\}$ to obtain the correctly scaled measurements according to Equation (IV.19).

IV.5 Results

IV.5.1 Numerical experiments

Influence of the interpolation technique As was mentioned in the acquisition strategy, an interpolation operator $\mathcal{S}$ is used to predict the locations of the significant coefficients of the wavelet transform. Among the many existing interpolation techniques, we compared bicubic interpolation (Keys, 1981), the *Fourier zero padding* (FZP) technique, *new-edge directed interpolation* (NEDI) (Li *et* Orchard, 2001), and the *cycle-spinning wavelet zero padding* method (CS-WZP) (Temizel *et* Vlachos, 2005), for their ease of implementation and the speed of their computation time. The prediction indeed needs to be very fast, so that it is achieved as quick as possible. To judge which technique allows prediction of the coefficient locations with the best accuracy, a series of simulations were performed. The images produced can be compared at several points in our acquisition strategy. If we refer to Fig. IV.3, the interpolated image $\mathbf{H}_j$ in point 2 *before* acquisition of the predicted coefficients can

be compared to the ground truth high-resolution image. This ground truth high-resolution image is the one that is obtained without prediction but with knowledge of the complete wavelet transform up to level j. Then, *after* acquisition of the details in point 5, we can compare the restored approximation image $\mathbf{A}_j$ of point 1 with the same ground truth high-resolution image. The two comparisons of the *before* and *after* acquisitions can be carried out for any scale $1 \leq j \leq J$. These data are summarized in table IV.1, considering the four different test images for a CR of 85% obtained with $\mathcal{P} = \{0.90, 0.80, 0.45, 0.019\}$ and the Le Gall wavelet.

In the rest of this thesis, ABS-WP is always used with the bicubic interpolation, as the data in table IV.1 show that this interpolation technique provides the best accuracy in the prediction of the significant wavelet coefficients, and its computation times are also very fast.

Influence of the quantization The simulation results showing the quantization effects are given in table IV.2 for two images for our ABS-WP method using the Le Gall wavelet. One pattern of this particular wavelet can be seen in Fig. IV.4. In these simulations, the wavelet coefficients are computed exactly as they would be by the SPC : using the dot product between the image and the corresponding quantized patterns. The set of percentages used for these experiments is $\mathcal{P} = \{0.90, 0.80, 0.71, 0.02\}$, for a CR of 80%.

Influence of the prediction strategy The accuracy of the prediction strategy for our ABS-WP technique and the EWT-ACS method (Dai *et al.*, 2014) for the identification of the significant wavelet coefficients is reported in table IV.3. For each case, as the EWT-ACS is derived from the Haar wavelet, it was also used for our technique. Moreover, the set of percentages for each image in our technique was obtained from the EWT-ACS number of sampled wavelet elements at each scale, to compare fairly the influence of the prediction. Then, the locations of the true significant wavelet coefficients (obtained from the ground truth images) were compared to the locations of the coefficients found for the ABS-WP and EWT-ACS. This leads to the prediction accuracy in percentages in table IV.3.

Influence of the acquisition/restoration technique The visual simulated data for CS, EWT-ACS, and ABS-WP are given in Fig. IV.5 for the bone image. For our technique of ABS-WP, the Le Gall wavelet was used, as in several cases it was the most efficient wavelet. The PSNRs obtained for these SPC frameworks at two compression rates are given in table IV.4, while table IV.5 gives the associated

Image	**PSNR** (dB)					
	$b = 4$	$b = 6$	$b = 8$	$b = 10$	$b = 12$	$b \to \infty$
Bones (256×256)	24.73	29.98	30.87	31.18	31.18	31.18
Mouse (128×128)	33.20	43.80	47.82	49.18	49.23	49.23

TABLE IV.2 – Quantization effects in our adaptive basis scan by wavelet prediction for the Le Gall wavelet for a compression rate of 80% and different numbers of bits b. The last column is equivalent to simulation of the strategy without quantization.

Image	CR	**Correctly matched wavelet coefficients** (%)	
		Dai	*ABS-WP*
Bones	80	62	**69**
(256 × 256)	85	59	**65**
Mouse	80	82	**85**
(128 × 128)	85	79	**84**

TABLE IV.3 – Accuracy of the prediction strategy for the extended wavelet trees adaptive compressed sampling (Dai *et al.*, 2014) technique and our adaptive basis scan by wavelet prediction framework. The percentages are shown for the wavelet coefficients that were correctly predicted as significant, compared to the true significant wavelet coefficients.

average computation times.

Influence of the image As mentioned earlier, four different test images were considered : Lena and peppers as natural images, a textured image with the bone picture of Fig. IV.5, and a smooth image with the mouse picture depicted in Fig. IV.6. Note that the mouse image is particularly smooth compared to the high-frequency bone image.

Influence of noise Up to now, these data were obtained in a noise-free setting. Table IV.6 compares the performances of the CS, EWT-ACS, and ABS-WP strategies considering noisy measurements, as given by Equation (IV.22). Figure IV.6a serves as a test image for the different levels of noise, as simulated by several values of N_0 for $\Delta t = 1$ s. A low value of N_0 leads to a low average of photons received by the SPD, and makes the noise effect greater.

IV.5.2 Experimental acquisitions

Real SPC acquisitions of a Jaszczak target with CS and ABS-WP are presented in Fig. IV.7. In the case of our technique, both the Haar and Le Gall wavelets were used to show how the DMD handles

Image	CR	**PSNR** (dB)			**Dai's thresholds**
		CS	*EWT-ACS*	*ABS-WP*	
Lena (256 × 256)	80	29.55	29.90	**30.33**	11.52
	85	27.89	28.49	**29.59**	16.63
Peppers (256 × 256)	80	34.70	35.06	**35.35**	7.71
	85	32.96	33.42	**34.83**	11.77
Bones (256 × 256)	80	29.38	30.24	**31.18**	12.89
	85	28.14	28.59	**30.29**	17.61
Mouse (128 × 128)	80	45.36	47.65	**49.23**	385.65
	85	42.18	45.83	**49.13**	851.10

TABLE IV.4 – Peak signal-to-noise ratios obtained for the different single-pixel camera acquisition techniques at the two compression rates on several test images in a noise-free setting. The thresholds used for the Dai method are given in the last column. For adaptive basis scan by wavelet prediction, the Le Gall patterns were used with $\mathcal{P} = \{0.90, 0.80, 0.71, 0.02\}$ and $\mathcal{P} = \{0.90, 0.80, 0.45, 0.019\}$, to give compression rates of 80% and 85%.

Image size	**CR**	**Time** (s)		
		CS	*EWT-ACS*	*ABS-WP*
256 × 256	80	267.37	**0.12**	0.43
	85	213.62	**0.09**	0.42
128 × 128	80	15.50	**0.02**	0.19
	85	13.18	**0.02**	0.18

TABLE IV.5 – Average computation times for the different single-pixel camera acquisition techniques for the data from table IV.4. The time includes the image restoration for compressive sensing, and prediction plus restoration for the Dai method and our technique. The acquisition times are not included as they are the same for each technique (fixed compression rate).

$N_0(ph/s)$	**PSNR** (dB)			
	CS	*EWT-ACS*	*ABS-WP (Haar)*	*ABS-WP (Le Gall)*
58072	38.99	45.72	46.05	**47.20**
43554	39.29	45.61	45.98	**46.88**
29036	39.04	45.48	45.91	**46.54**
14518	38.47	45.31	45.71	**45.90**
5807	37.06	44.72	**45.01**	43.99

TABLE IV.6 – Noisy simulations for the different acquisition strategies at a compression rate of 85% for different values of N_0 on the mouse image of Fig. IV.6a. For adaptive basis scan by wavelet prediction, the set of percentages used for the Haar wavelet was $\mathcal{P} = \{0.77, 0.42, 0.24, 0.1\}$, and $\mathcal{P} = \{0.90, 0.80, 0.45, 0.019\}$ for Le Gall.

the 8-bit patterns [11].

Figure IV.8 shows the acquisitions of another target with our technique, to further judge the SPC set-up for discerning small dots, depending on the compression rates. The smallest dots have a diameter of about 1 mm, whereas the largest one is about 3 mm. In our set-up, a pixel size of 210 µm was measured, which can easily be changed by adjusting the optics and/or modifying the pattern size.

IV.6 Discussion

Our ABS-WP acquisition/ restoration scheme presented in this Chapter was mainly designed to overcome the limits of ℓ_1-minimization-based image restoration in the CS framework. Instead, the image is acquired directly in a wavelet basis, for which there is a fast inverse transform. In addition, our technique has the advantage of being threshold-free by using nonlinear approximations [12] as defined in Equation (IV.10). Uniform quantization of the patterns is performed in order to use any possible wavelet, to obtain the best possible compression ratio.

11. The library controlling our DMD model (DLP7000-V7001, Vialux GmbH) can load patterns coded on up to 8-bits
12. Threshold-free in comparison to other ABS techniques, for which a threshold has to be chosen before acquisition. In our ABS-WP framework, using the set of percentages $\mathcal{P}$, a threshold at each scale is automatically chosen

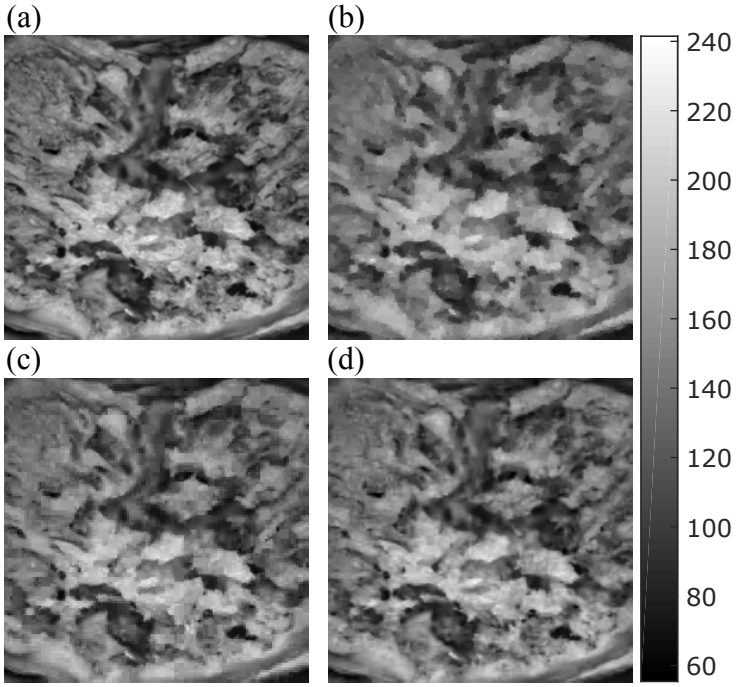

FIGURE IV.5 – Noise-free simulation of different single-pixel camera acquisition techniques on a 256×256 image of bone with a compression rate of 80%. (a) Ground truth image. (b-d) Images restored with the compressive sensing (b) and extended wavelet trees adaptive compressed sampling (c) methods, and with our adaptive basis scan by wavelet prediction (d) technique. The peak signal-to-noise ratios and parameters associated with these data are given in table IV.4.

Looking at the data given in table IV.1, it can be seen that the bicubic interpolation appears to perform the best for the prediction of the significant wavelet coefficients. The second to last column gives the final PSNRs obtained for the restored image, and these are always higher for the bicubic interpolation technique. However, it can be noted that *before* the acquisition of the coefficients, the other three techniques perform better in general. This performance is not unusual, as the NEDI or WZP-CS methods are designed to best interpolate the edges in images, while the bicubic interpolation tends to smooth edges. With NEDI or WZP-CS, we can assume that the locations of the significant coefficients should be better predicted, as in general the highest wavelet coefficients are near the edges (Mallat, 2008). In spite of the smoothness of the bicubic interpolation, it still performs better for locating these elements, which is why this technique is now considered in the rest of the proposed experiments here. Given the high number of interpolation or super-resolution techniques defined (Park *et al.*, 2003), we cannot be certain that bicubic interpolation is the best possible method. However, it has the advantage of being extremely fast and parameter free, while providing efficient results.

As was shown in Section II.4.2, when an ABS approach is considered, the Haar wavelet is often used (Deutsch *et al.*, 2009; Dai *et al.*, 2014; Averbuch *et al.*, 2012; Yu *et al.*, 2014a; Huo *et al.*, 2017). This is because up to a scale factor, the patterns have only 0 or 1, and hence the image quality is not impacted upon by the quantization process. Nevertheless, in the case of our proposed technique of ABS-WP with another wavelet, the quantization impacts upon the quality of the restored SPC images, as shown by the data given in table IV.2. For values of $b \leq 10$, the recovered images have indeed a

smaller PSNR than the ones restored with the real patterns (table IV.2, last column, with $b \to \infty$). The irreversible rounding operation in Equation (IV.18) explains this difference. When $b \geq 10$, the grayscale is extended and the quantization error can be considered to be negligible. As mentioned earlier, the quantization factor q_k has an impact on the effective integration time $\Delta t_k = q_k \Delta t$ at the SPD. In the experiments carried out in this Chapter, Δt was always kept constant and the measurements were post-processed by applying q_k, as defined by Equations (IV.19) and (IV.20). To obtain the best possible SNR, this is not the best possible solution. The optimum solution would be to increase or decrease the integration time, according to the pattern and its quantization factor. In other words, $\Delta t_k = q_k \Delta t$ would act as the new integration time, as in Equation (IV.21).

Looking at the data given in table IV.3 for the prediction accuracies of EWT-ACS (Dai *et al.*, 2014) and ABS-WP, our prediction strategy based on a simple bicubic interpolation performs better for the identification of the true significant wavelet coefficients. These data are provided for the Haar wavelet, as EWT-ACS is derived from this. However, the possibility to use another wavelet for our technique might greatly improve the image quality, provided that the wavelet is correctly chosen.

In light of the data given in table IV.4 where ABS-WP is compared to CS and EWT-ACS, numerically close or better results can be achieved by our ABS-WP technique. Visually, as can be seen in Fig. IV.5, the TV-minimization creates some spots/ patches for a high-frequency image, such as the textured image of bone. For EWT-ACS, because of the use of the Haar wavelet, some pixelation is

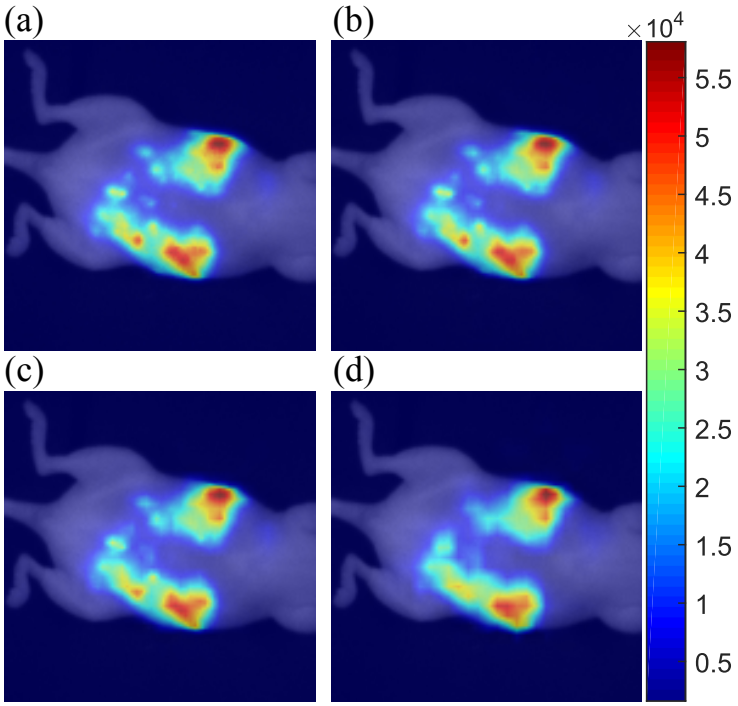

FIGURE IV.6 – Noise-free simulation of our adaptive basis scan by wavelet prediction acquisition strategy on a 128×128 bioluminescence image of a mouse. The bioluminescence images were overlaid on the ambient light image of the mouse. (a) Ground truth image. (b-d) Adaptive basis scan by wavelet prediction images restored using the Le Gall wavelet for a compression rate of 90% (b), 95% (c), and 98% (d). The peak signal-to-noise ratios compared to the ground truth image are 48.25 dB, 41.48 dB and 35.37 dB, respectively.

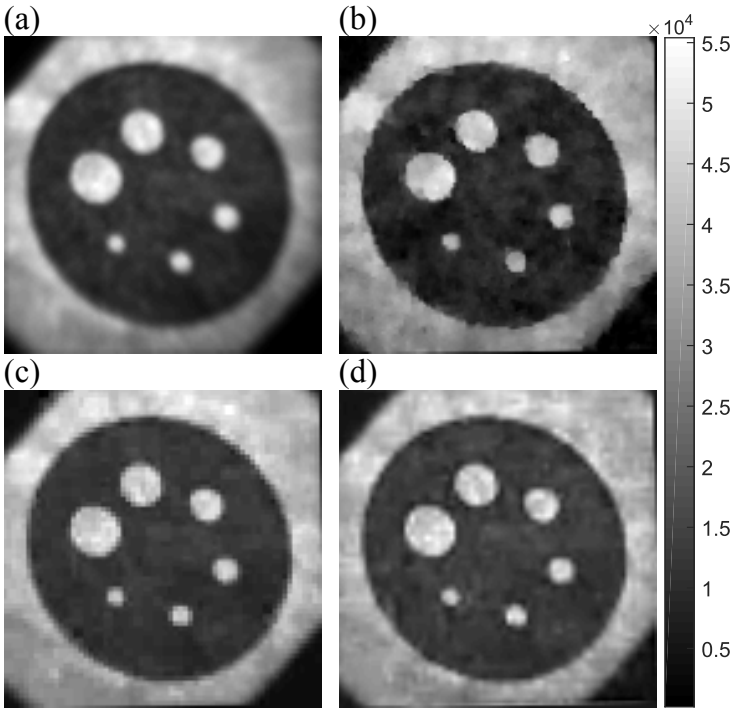

FIGURE IV.7 – Experimental acquisitions with the single-pixel camera on the Jaszczak target. (a) Experimental charge coupled device image of the target. (b-d) The recovered 128×128 pixels images with a compression rate of 85% using compressive sensing (b), and using adaptive basis scan by wavelet prediction with Haar (c) and Le Gall (d) wavelets. The peak signal-to-noise ratios obtained compared to the charge coupled device image after registration are 21.20 dB, 21.99 dB and 21.65 dB, respectively.

present in the SPC restored image that cannot be seen in our method with the Le Gall wavelet. The computation times given in table IV.5 also show the improvement obtained considering an ABS approach. When larger images are acquired, this improvement is again greater. However, ABS-WP takes a little longer than EWT-ACS, for which only the thresholding operations are extremely fast.

For EWT-ACS, the thresholds given in table IV.4 reveal their image dependency and should be adjusted for each image. In comparison, for ABS-WP and a fixed CR, a common set of percentages $\mathcal{P}$ is used for each image. Our ABS-WP strategy still recovers good quality images despite the clear difference in the images included in table IV.4. ABS-WP therefore adapts to the image, and no threshold needs to be adjusted. To obtain a relatively good set of percentages, these have been learned from several test images. In practice, in simulation, the nonlinear approximation of the wavelet transform can be applied to several images for a given CR. Then the number of coefficients retained at each level j can be obtained. Averaging these collected values between the images leads to a good candidate for $\mathcal{P}$. In the case of CS, many parameters have to be tackled for the TV-minimization. Depending on the choice of parameters, the quality of the SPC restored image can change dramatically.

Even with a CR as high as 98%, Fig. IV.6 demonstrates that an excellent image can be restored using ABS-WP for smooth images. For this kind of image, only a few wavelet coefficients are indeed needed to recover the principal features of the image. The decomposition level value J can thus be set closed to the limit of $R = \log_2(N)$. In addition, for small values of j, the percentages p_j can be set

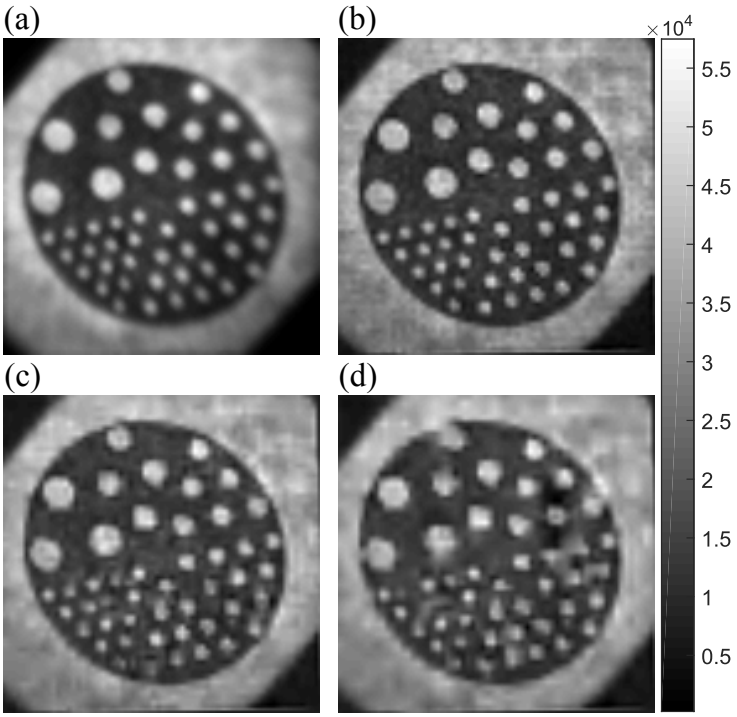

FIGURE IV.8 – Ability of the system to distinguish dots with diameters that range from 1 mm to 3 mm. (a) Experimental charge coupled device image of the target. (b-d) The recovered 128×128 pixels images with adaptive basis scan by wavelet prediction with Le Gall wavelets for a compression rate of 75% (b), 85% (c), and 90% (d). The peak signal-to-noise ratios obtained compared to the charge coupled device image after registration are 22.35 dB, 21.51 dB and 20.85 dB, respectively. A pixel size of 210 µm was measured.

to 0; i.e., no high-frequency details are needed. This is because smooth images have only very few details, and the coarser coefficients can be sufficient enough to restore a good quality image. On the contrary, it is necessary to choose high values for p_1 to obtain the finest details in the case of images with high frequency components. Both choices of J and $\mathcal{P}$ are thus linked to the chosen application and the type of object to image.

In a real-world setting, the noisy simulations given in table IV.6 show that ABS-WP still performs closer to or better than CS and EWT-ACS. It is worth noting, however, that the measurements for ABS-WP with the Le Gall wavelet are more rapidly corrupted by noise. This can be explained because compared to the patterns obtained with Haar, the Le Gall patterns have less elements where the value is 1, and so such patterns send less light to the SPD. The value of the measurements of Equation (IV.22) are therefore larger for Haar than for Le Gall, which leads to lower impact of the Poisson noise in the Haar case (table IV.6, last column). If extremely low light scenarios are considered, it would therefore be better to use the simple Haar wavelet. In the next Chapter, a strategy to modify any wavelet pattern is proposed that reduces the effects of the noise in such cases.

Moving on to the experimental results, a more sophisticated wavelet such as the Le Gall can be used for real acquisition using ABS-WP, as shown in Fig. IV.7. This even gives visually better results compared to Haar, with a smoother image. As for the textured image of Fig. IV.5, the TV-minimization of CS creates spots on the restored image. The Haar case for ABS-WP shows some pixelation, as p_1

was set to a small value, and only a few high frequency coefficients were sampled. In our ABS-WP strategy, an important feature therefore regards the choice of the wavelet. Depending on the object to image, some wavelets are better at sensing the scene than others; i.e., they capture the information in fewer coefficients, by giving sparser wavelet transform in one wavelet basis compared to another. For instance, if a very smooth object is considered, a Battle wavelet would be much more appropriate than the Haar wavelet, and fewer Battle coefficients would be needed compared to using Haar. With ABS-WP, it is possible to choose the wavelet that is best adapted to the desired application and the object to be acquired.

Finally, some insights about the possibilities of the system with ABS-WP are provided with the data of Fig. IV.8. In the actual configuration of the set-up at the Politecnico di Milano, objects of at least 1 mm can be discerned provided that the CR is well chosen. For instance, the small dots are all visible for a CR of 80% and 85%, but not for 90%, as not enough elements were sampled to restore the dots. A great feature of an adaptive basis scan approach and ABS-WP is that several passes of the algorithm can be performed to add more wavelet coefficients, and therefore more detail. In other words, a first pass with a certain CR can be done, and if the image quality is not judged sufficient, acquisitions of new wavelet coefficients can be added by lowering the CR and carrying out a second pass. A new restored image can easily be obtained with the quick inverse wavelet transform.

For the limitations of our technique, the use of 8-bit patterns in ABS-WP is one, as it reduces the maximum possible acquisition frame rate. The DMD in the set-up at the Politecnico di Milano can work at a maximum frequency of 290 Hz in 8-bit mode, but it can reach 22 kHz in 1-bit mode. Using 8-bit patterns is therefore slower than limiting the use to the ON/OFF states, which can be a problem depending on the application. The possibility to reach the maximum DMD frame rate is however practically limited by different issues, such as the weak SNR in low-light scenarios. In the field of biomedical optics, this can be particularly true; e.g., specific dyes emit weak fluorescence signals. Based on Fig. IV.7 and the data given in table IV.6, if fast measurements are required in any case, the Haar wavelet can still be used with ABS-WP to obtain better results compared to CS or EWT-ACS, due to its better prediction (table IV.3).

Overall, the proposed acquisition/ restoration scheme of ABS-WP is fast, threshold-free, and easy to adjust, with few parameters that need to be tuned. The perfect recovery of the signal is, however, not guaranteed, unlike for the CS approach [13]. The recovered image can nevertheless be refined in ABS-WP, using a second pass of the algorithm to complete the set of sampled wavelet coefficients. Such a process is more complex in the CS case, as the ℓ_1-minimization or TV-minimization that are time consuming have to be started from scratch.

IV.7 Conclusion

In this Chapter, we have reported a new framework for SPI. Nonlinear approximation of the wavelet transform inspired the philosophy of our approach. Significant wavelet coefficients that should

13. Under certain assumptions, see Chapter II

be experimentally acquired are predicted via an interpolation operator, while the other coefficients are discarded in the restoration process. The main advantage of ABS-WP is fast image recovery based on inverse wavelet transform with filter banks. It thus disposes of the computational overhead of the ℓ_1-minimisation and TV-minimization that are required by the CS theory.

To the best of our knowledge, experimental data in an *adaptive* strategy have never been acquired with a wavelet other than Haar. This is made possible by quantization of the patterns, so that more sophisticated wavelets can be used and chosen according to the desired application and object to image. Both good visual and quantitative results of ABS-WP are proposed in simulations and for experimental acquisitions. The technique has moreover been shown to adapt to different kinds of images with the same set of parameters.

As mentioned earlier in this Chapter, a common problem is the negative values in a pattern that cannot physically be implemented on any SLM. No matter the chosen acquisition and restoration scheme used, most patterns have both positive and negative values. In this Chapter, the acquisitions were performed using separation of the patterns into their positive and absolute negative parts, which doubles the acquisition times. In the next Chapter, another method is presented as well as a proposed general way to transform any pattern into a combination of positive patterns to deal with this problem.

CHAPTER V

PATTERN GENERALIZATION

Contents

CHAPTER V

NO MATTER the kind of acquisition and restoration techniques used for single-pixel imaging (SPI), the patterns that should be sent to the spatial light modulator (SLM) usually require both positive and negative values, which is physically impossible to achieve, as photon numbers cannot be negative. A second constraint is the dark current α described in Section II.1 that flaws the measurements.

This Chapter reports on a general way to deal with these experimental constraints. The materials of this Chapter were filed as a patent (Rousset *et al.*, 2017c) and submitted to *IEEE Transactions on Computational Imaging* (Rousset *et al.*, 2017d).

V.1 Introduction

Two constraints arise for the experimental implementation of single-pixel camera (SPC) image acquisition and restoration : pattern positivity, and dark current rejection. The positivity limitation and dark current rejection are often overcome by splitting (i.e., separating) patterns into their positive and negative parts (Dai *et al.*, 2014; Rousset *et al.*, 2017a). Subtraction between these two measurements leads to the desired measurement; i.e., the measurement that would have been acquired with the desired SLM pattern with both positive and negative values. While this approach is straightforward, it requires a doubling of the number of measurements, which also doubles the total acquisition time. A second approach is pattern shifting. This consists of adding the same background value to all of the patterns, such that they become positive (Duarte *et al.*, 2008). The desired measurements are then obtained by subtracting a measurement acquired for the background value from all of the measurements. Only one additional measurement is required, but pattern shifting is very sensitive to noise. Efficient strategies to get rid of the dark current are essential to restoration algorithms. Although these two constraints are of particular importance for experimental data acquisition and image restoration, they have not been addressed from a general perspective.

In this Chapter, we propose to tackle the experimental limitations by seeking positive patterns that are related to the desired SLM patterns through linear combinations. As image acquisition using an SPC is linear, the measurements obtained using the positive patterns can be linearly combined to provide the desired measurements. The *ad-hoc* solutions based on pattern splitting or shifting can be seen as two particular cases of this approach, which we refer to as pattern generalization.

By formalizing the problem, we show that pattern generalization can be related to nonnegative matrix factorization (NMF), which is the process of factorizing a matrix as a product of two matrices with only positive entries (Paatero *et* Tapper, 1994; Lee *et* Seung, 1999, 2001). NMF algorithms have various applications, including image analysis (Lee *et* Seung, 1999), text mining (Wang *et al.*, 2008),

blind source separation (Cichocki *et al.*, 2006), video tracking (Bucak *et* Gunsel, 2007), and financial data analysis (de Fréin *et al.*, 2008). Several algorithms can be used to address this problem; e.g., alternating least-squares algorithms (Paatero *et* Tapper, 1994), multiplicative update algorithms (Lee *et* Seung, 1999) and gradient descent algorithms (Lee *et* Seung, 2001; Lin, 2007). We refer the reader to the reviews of Berry *et al.* (2006); Wang *et* Zhang (2013); Gillis (2014) for extensive explanations of NMF and the different algorithms. More recently, NMF has been extended to semi-NMF (SNMF), which decomposes a matrix into a product of two matrices, with one having nonnegative entries (Ding *et al.*, 2010).

It is demonstrated in this Chapter that the single-pixel experimental constraints can be efficiently addressed through pattern generalization using a SNMF algorithm. We also show that for a given number of patterns, only one additional measurement has to be performed. Compared to the classical positive/ negative pattern-splitting method, this leads to a halving of the number of measurements. To the best of our knowledge, this is the first time that this pattern generalization problem has been addressed in SPI.

In this Chapter, we first present the conventional SPC technique used to deal with the experimental constraints. Then, our proposed pattern generalization problem is detailed and a way to solve it using a SNMF algorithm is given. A particular constraint linked to the dark current rejection is added in this algorithm. The conditions under which the experiments were carried out are then reported, with the associated results with simulations and experimental data. Finally, we discuss our findings and give our conclusions.

V.2 *Ad-hoc* methods for experimental constraints

Different approaches have been proposed to design a set of patterns $\mathbf{P}$ and recover the image $\mathbf{f}$ from the measurements $\mathbf{m}$, as mentioned in Chapter II. It is important to note that most of these have considered patterns with negative values. Patterns can indeed be chosen in bases such as Fourier (Zhang *et al.*, 2015; Zhang *et* Zhong, 2016), discrete cosine transform (Liu *et al.*, 2017), wavelets (Deutsch *et al.*, 2009; Averbuch *et al.*, 2012; Dai *et al.*, 2014; Hahn *et al.*, 2014; Huo *et al.*, 2017; Rousset *et al.*, 2017a), and Hadamard (Radwell *et al.*, 2014). In addition, it is common to assume that there is no dark current, so that the image formation model classically considered for image restoration is

$$\check{m} = N_0 \check{\mathbf{p}}^\top \mathbf{f}\, \Delta t \tag{V.1}$$

where $\check{\mathbf{p}} \in \mathbb{R}^{D\times 1}$ is a SLM pattern with positive and negative values. From now on, we will refer to $\check{\mathbf{p}}$ (resp. $\check{m}$) as the desired SLM pattern (resp. measurement). As a reminder, the real physical measurement is obtained as in Equation (II.4) :

$$m = \left(N_0 \mathbf{p}^\top \mathbf{f} + \alpha\right) \Delta t. \tag{V.2}$$

where $\mathbf{p} \in \mathbb{R}_+^{D\times 1}$. Unfortunately, patterns $\check{\mathbf{p}}$ cannot be physically implemented on a SLM, and the absence of the dark current α is unrealistic. However, two *ad-hoc* methods are (implicitly) used to correct for the two problems.

V.2.1 Pattern splitting

This natural method consists of separating each desired pattern $\check{\mathbf{p}} \in \mathbb{R}^{D\times 1}$ into its positive $\mathbf{p}_+ \in \mathbb{R}_+^{D\times 1}$ and absolute negative $\mathbf{p}_- \in \mathbb{R}_+^{D\times 1}$ (Dai *et al.*, 2014; Rousset *et al.*, 2017a) parts; i.e. :

$$\check{\mathbf{p}} = \mathbf{p}_+ - \mathbf{p}_- \quad \text{with} \begin{cases} \mathbf{p}_+ = \max(\mathbf{0}_D, \check{\mathbf{p}}) \\ \mathbf{p}_- = |\min(\mathbf{0}_D, \check{\mathbf{p}})| \end{cases} \tag{V.3}$$

where the $\max(.)$ and $\min(.)$ functions are applied to each entry of both vectors, with $\mathbf{0}_D$ as the null vector of size D. Then, the measurements m_+ and m_- acquired using the patterns $\mathbf{p}_+$ and $\mathbf{p}_-$, respectively, are subtracted, to give $\check{m}$. Indeed, we have

$$\begin{aligned} m_+ - m_- &= \left(N_0 \mathbf{p}_+^\top \mathbf{f} + \alpha\right)\Delta t - \left(N_0 \mathbf{p}_-^\top \mathbf{f} + \alpha\right)\Delta t && \text{(V.4)} \\ &= N_0 \left(\mathbf{p}_+ - \mathbf{p}_-\right)^\top \mathbf{f}\, \Delta t && \text{(V.5)} \\ &= \check{m}. && \text{(V.6)} \end{aligned}$$

It is important to note that the dark current α cancels out. The drawback of this natural solution is that if I is the number of desired measurements, $2I$ SPC measurements are needed to obtain them, which leads to increased acquisition time.

V.2.2 Pattern shifting

A second approach consists of shifting the pattern $\check{\mathbf{p}} \in \mathbb{R}^{D\times 1}$ toward the positive values (Duarte *et al.*, 2008). Mathematically,

$$\check{\mathbf{p}} = \mathbf{p}_\mathrm{s} - \mathbf{p}_\mathrm{b} \quad \text{with} \begin{cases} \mathbf{p}_\mathrm{s} = \check{\mathbf{p}} + \mathbf{p}_\mathrm{b} \in \mathbb{R}_+^{D\times 1} \\ \mathbf{p}_\mathrm{b} = (b, \ldots, b)^\top \in \mathbb{R}_+^{D\times 1} \end{cases} \tag{V.7}$$

where b is a background value chosen so that $b \geq |\min(\check{\mathbf{p}})| \in \mathbb{R}_+$. As for the positive/ negative separation, the subtraction of the two corresponding SPC measurements gives the desired measurement, while canceling out the dark current :

$$\check{m} = m_\mathrm{s} - m_\mathrm{b}. \tag{V.8}$$

Contrary to pattern splitting, it is *not* mandatory to double the number of measurements here. Indeed, choosing b large enough, the background value b can be the same for all of the desired measurements. Therefore, if I measurements are desired, only $K = I+1$ measurements need to be acquired. However, as will be shown later, this method suffers dramatically from noise.

V.3 Pattern generalization

V.3.1 Patterns as linear combinations

We denote $\check{\mathbf{P}} = (\check{\mathbf{p}}_1, \ldots, \check{\mathbf{p}}_I)^\top \in \mathbb{R}^{I\times D}$ as the set of I desired patterns, and $\check{\mathbf{m}} = (\check{m}_1, \ldots, \check{m}_I)^\top$ as the vector that contains the corresponding desired measurements. Applying Equation (V.1) to the collection of patterns $\check{\mathbf{P}}$ leads to

$$\check{\mathbf{m}} = N_0 \check{\mathbf{P}} \mathbf{f}\, \Delta t. \tag{V.9}$$

To acquire $\check{\mathbf{m}}$, which is not feasible in practice, our idea was to generalize the approaches described in Section V.2, looking for a collection of positive patterns $\mathbf{P} \in \mathbb{R}_+^{K \times D}$ such that

$$\check{\mathbf{P}} = \mathbf{T}\mathbf{P} \tag{V.10}$$

where $\mathbf{T} \in \mathbb{R}^{I \times K}$ is a transformation matrix. Applying $\mathbf{T}$ to the measurements $\mathbf{m}$ of Equation (II.5) acquired with the patterns $\mathbf{P}$ leads to

$$\mathbf{T}\mathbf{m} = \mathbf{T}(N_0\mathbf{P}\mathbf{f} + \alpha\mathbf{1}_K)\,\Delta t \tag{V.11}$$

$$= (N_0\check{\mathbf{P}}\mathbf{f} + \alpha\mathbf{T}\mathbf{1}_K)\,\Delta t \tag{V.12}$$

We note that the desired measurements $\check{\mathbf{m}}$ of Equation (V.9) can be obtained by transforming the acquired measurements $\mathbf{m}$ as in Equation (V.12), provided that

$$\mathbf{T}\mathbf{1}_K = \mathbf{0}_I \tag{V.13}$$

where $\mathbf{0}_I = (0,\ldots,0)^\top \in \mathbb{R}^{I \times 1}$. If Equation (V.13) is satisfied, then the desired measurements $\check{\mathbf{m}}$ of Equation (V.9) are directly obtained as

$$\check{\mathbf{m}} = \mathbf{T}\mathbf{m} \tag{V.14}$$

In summary, for a given $\check{\mathbf{P}} \in \mathbb{R}^{I \times D}$, the pattern generalization problem we address is the following :

$$\text{Find } \mathbf{T} \in \mathbb{R}^{I \times K} \text{ and } \mathbf{P} \in \mathbb{R}^{K \times D} \text{ s.t. } \begin{cases} \check{\mathbf{P}} = \mathbf{T}\mathbf{P} \\ \mathbf{P} \geq 0 \\ \mathbf{T}\mathbf{1}_K = \mathbf{0}_I \end{cases} \tag{V.15}$$

where $\mathbf{P} \geq 0$ is shorthand for $(\mathbf{P})_{k,n} \geq 0$, $\forall (k,n)$. The framework of the proposed pattern generalization method is presented in Fig. V.1.

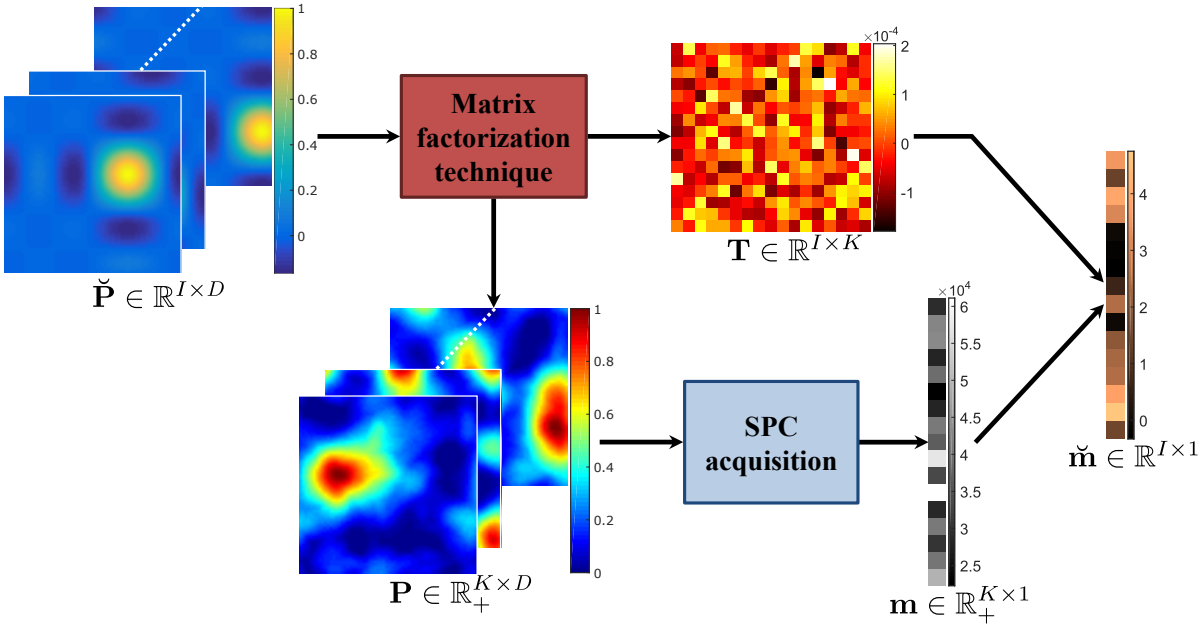

FIGURE V.1 – Framework of the proposed pattern generalization method.

V.3.2 Link with *ad-hoc* methods

The pattern splitting method described in Equation (V.3) is equivalent to choosing $\mathbf{T}$ and $\mathbf{P}$ in Equation (V.15), as

$$\mathbf{T} = \begin{pmatrix} 1 & -1 & 0 & \dots & 0 \\ 0 & 0 & 1 & -1 & \dots & 0 \\ \vdots & \vdots & \vdots & \vdots & \ddots & \vdots \\ 0 & \dots & & 0 & 1 & -1 \end{pmatrix} \in \mathbb{R}^{I\times 2I} \qquad \mathbf{P} = \begin{pmatrix} \mathbf{p}_1^\top \\ \mathbf{p}_2^\top \\ \vdots \\ \mathbf{p}_{2I-1}^\top \\ \mathbf{p}_{2I}^\top \end{pmatrix} = \begin{pmatrix} \max(\mathbf{0}_D, \check{\mathbf{p}}_1)^\top \\ |\min(\mathbf{0}_D, \check{\mathbf{p}}_1)|^\top \\ \vdots \\ \max(\mathbf{0}_D, \check{\mathbf{p}}_I)^\top \\ |\min(\mathbf{0}_D, \check{\mathbf{p}}_I)|^\top \end{pmatrix} \in \mathbb{R}_+^{2I\times D}. \tag{V.16}$$

The number of SLM patterns is $K = 2I$, where I is the number of desired patterns.

For the pattern shifting method described in Equation (V.7), $\mathbf{T}$ and $\mathbf{P}$ are given by the following formulae :

$$\mathbf{T} = \begin{pmatrix} 1 & \dots & 0 & -\frac{1}{M} & \dots & -\frac{1}{M} \\ \vdots & \ddots & \vdots & \vdots & \ddots & \vdots \\ 0 & \dots & 1 & -\frac{1}{M} & \dots & -\frac{1}{M} \end{pmatrix} \in \mathbb{R}^{I\times(I+M)} \qquad \mathbf{P} = \begin{pmatrix} \mathbf{p}_1^\top \\ \vdots \\ \mathbf{p}_I^\top \\ \mathbf{p}_{I+1}^\top \\ \vdots \\ \mathbf{p}_{I+M}^\top \end{pmatrix} = \begin{pmatrix} (\check{\mathbf{p}}_1 + \mathbf{p}_\mathrm{b})^\top \\ \vdots \\ (\check{\mathbf{p}}_I + \mathbf{p}_\mathrm{b})^\top \\ \mathbf{p}_\mathrm{b}^\top \\ \vdots \\ \mathbf{p}_\mathrm{b}^\top \end{pmatrix} \in \mathbb{R}_+^{(I+M)\times D}. \tag{V.17}$$

The number of SLM patterns is given by $K = I + M$ in this case. Setting M to 1 reduces the number of measurements. However, when there are noisy experimental measurements, it is better to average several measurements acquired with the same pattern $\mathbf{p}_\mathrm{b}$.

V.3.3 Optimization problem

To find two matrices $\mathbf{T}$ and $\mathbf{P}$ that satisfy Equation (V.15), a possibility is to seek two matrices that minimize the squared Frobenius norm of $\check{\mathbf{P}}$ minus $\mathbf{TP}$. With addition of the positivity constraint on $\mathbf{P}$, the condition of Equation (V.13) leads to the following optimization problem :

$$\min_{\mathbf{T},\,\mathbf{P}} \left\| \check{\mathbf{P}} - \mathbf{TP} \right\|_\mathrm{F}^2 \quad \text{such that} \quad \mathbf{P} \geq 0 \text{ and } \mathbf{T}\mathbf{1}_K = \mathbf{0}_I \tag{V.18}$$

V.4 Proposed semi-nonnegative matrix factorization algorithm

V.4.1 Algorithm overview

The minimization problem of Equation (V.18) can be solved by adapting algorithms that are designed for SNMF, which usually solve Equation (V.18) with the constraint $\mathbf{P} \geq 0$, but without the constraint on $\mathbf{T}$. Most SNMF methods are iterative and alternate between the minimization of $\left\| \check{\mathbf{P}} - \mathbf{TP} \right\|_\mathrm{F}^2$ for $\mathbf{P}$ and $\mathbf{T}$ (Berry *et al.*, 2006; Wang *et* Zhang, 2013; Gillis, 2014). Herein, we propose a similar approach, where each of the two minimization steps is solved with its respective constraint. An overview of our two-step iterative algorithm is given in algorithm 2.

Algorithm 2 Solve the pattern generalization problem of Equation (V.15) as Equation (V.18)

Initialization : $\mathbf{P} = \text{rand}(K, D)$
while $\left\|\check{\mathbf{P}} - \mathbf{TP}\right\|_{\text{F}}^2 > \epsilon$ **do**
  Step 1 : Minimize $\left\|\check{\mathbf{P}} - \mathbf{TP}\right\|_{\text{F}}^2$ w.r.t. $\mathbf{T}$ such that $\mathbf{T}\mathbf{1}_K = \mathbf{0}_I$
  Step 2 : Minimize $\left\|\check{\mathbf{P}} - \mathbf{TP}\right\|_{\text{F}}^2$ w.r.t. $\mathbf{P}$ such that $\mathbf{P} \geq 0$
end while

For each of the two steps in algorithm 2, different resolution methods are available, which include alternating least-squares algorithms (Paatero *et* Tapper, 1994), multiplicative update algorithms (Lee *et* Seung, 1999), and gradient descent algorithms (Lee *et* Seung, 2001; Lin, 2007). For fast computation and guaranteed convergence, we investigate the methods based on resolution with alternating least-squares to solve Equation (V.18).

V.4.2 Solution for T

Assuming $\mathbf{P}$ is fixed, the following subproblem must be solved :

$$\min_{\mathbf{T}} \left\|\check{\mathbf{P}} - \mathbf{TP}\right\|_{\text{F}}^2 \quad \text{such that} \quad \mathbf{T}\mathbf{1}_K = \mathbf{0}_I \tag{V.19}$$

In standard SNMF problems where no constraints act on $\mathbf{T}$, the subproblem of Equation (V.19) has a straightforward solution $\mathbf{T} = \check{\mathbf{P}}\mathbf{P}^\top \left(\mathbf{P}\mathbf{P}^\top\right)^{-1}$ when $\mathbf{P}\mathbf{P}^\top$ is invertible. In our case, the constraint of Equation (V.13) makes it an equality constrained optimization problem. Nevertheless, we show in Appendix B that this can still be solved analytically using the duality property. We have :

$$\mathbf{T} = \check{\mathbf{P}}\mathbf{P}^\top \left(\mathbf{P}\mathbf{P}^\top\right)^{-1} \left(\mathbf{I} - \frac{1}{\mathbf{1}_K{}^\top \left(\mathbf{P}\mathbf{P}^\top\right)^{-1} \mathbf{1}_K} \mathbf{1}_{K\times K} \left(\mathbf{P}\mathbf{P}^\top\right)^{-1}\right) \tag{V.20}$$

where $\mathbf{I}$ is the identity matrix of size $K \times K$, and $\mathbf{1}_{K\times K} = \mathbf{1}_K \mathbf{1}_K{}^\top$ is the matrix of size $K \times K$ with all entries equal to 1. If $\mathbf{P}\mathbf{P}^\top$ is not invertible, then Equation (V.19) does not have a unique solution, and a particular one can instead be obtained with Moore-Penrose pseudoinverse.

V.4.3 Solution for P

Assuming $\mathbf{T}$ is fixed, the following subproblem must be solved :

$$\min_{\mathbf{P}} \left\|\check{\mathbf{P}} - \mathbf{TP}\right\|_{\text{F}}^2 \quad \text{such that} \quad \mathbf{P} \geq 0 \tag{V.21}$$

This problem is a nonnegative least-square problem that does not have an explicit solution as it is. Gillis proposed a block coordinate descent method that leads to a closed-form solution for each block and to fast computation (Gillis *et* Kumar, 2015). Moreover, this method was shown to give very low factorization error using only $K = I + 1$ (Gillis *et* Kumar, 2015). For this block coordinate method, the cost function $\mathcal{F}(\mathbf{P}) = \left\|\check{\mathbf{P}} - \mathbf{TP}\right\|_{\text{F}}^2$ is rewritten as

$$\mathcal{F}(\mathbf{P}) = \mathcal{F}(\mathbf{P}_{-k}, \mathbf{p}_k) = \left\|\check{\mathbf{P}} - \mathbf{T}_{|k}\mathbf{P}_{-k} - \mathbf{t}_k \mathbf{p}_k^\top\right\|_{\text{F}}^2 \tag{V.22}$$

where $\mathbf{T}_{|k}$ (resp. $\mathbf{P}_{-k}$) is the matrix $\mathbf{T}$ (resp. $\mathbf{P}$) deprived of its column (resp. row) k, and $\mathbf{t}_k \in \mathbb{R}^{I\times 1}$ (resp. $\mathbf{p}_k^\top \in \mathbb{R}^{1\times D}$) is the k-th column (resp. row) of $\mathbf{T}$ (resp. $\mathbf{P}$). A partial solution to the problem of Equation

(V.21) is obtained by minimizing $\mathcal{F}(\mathbf{P})$ with respect to $\mathbf{p}_k$, and iterating over the K rows of $\mathbf{P}$ (Gillis *et* Kumar, 2015). Hence, at each iteration, the following problem has to be solved :

$$\min_{\mathbf{p}_k} \mathcal{F}(\mathbf{P}_{-k}, \mathbf{p}_k) \quad \text{such that} \quad \mathbf{p}_k \geq 0, \tag{V.23}$$

Interestingly, this allows an analytical solution :

$$\mathbf{p}_k = \max\left(\mathbf{0}_D, \frac{\left(\check{\mathbf{P}} - \mathbf{T}_{|k}\mathbf{P}_{-k}\right)^\top \mathbf{t}_k}{\|\mathbf{t}_k\|_2^2}\right) \tag{V.24}$$

where the max(.) function is applied entrywise and $\mathbf{0}_D$ is the null vector of size D. For consistency, a demonstration of Equation (V.22) is provided in Appendix B.

V.4.4 Proposed algorithm

Using the closed-formula Equations (V.20) and (V.24) allows to completely write algorithm 2 as in algorithm 3, to solve for $\check{\mathbf{P}} \approx \mathbf{TP}$ with only $K = I + 1$.

Algorithm 3 Solve $\check{\mathbf{P}} \approx \mathbf{TP}$ as in Equation (V.18)

Initialization : Set $K = I + 1$ and $\mathbf{P} = \text{rand}(K, D)$
while $\left\|\check{\mathbf{P}} - \mathbf{TP}\right\|_{\text{F}}^2 > \epsilon$ **do**
  1 : Update $\mathbf{T}$ using (V.20)
  2 : Update $\mathbf{P}$
    for $k = 1 : K$ **do**
      2.1 : $\mathbf{p}_k \leftarrow \max\left(\mathbf{0}_D, \frac{\left(\check{\mathbf{P}} - \mathbf{T}_{|k}\mathbf{P}_{-k}\right)^\top \mathbf{t}_k}{\|\mathbf{t}_k\|_2^2}\right)$
      2.2 : Update the k-th row of $\mathbf{P}$ with $\mathbf{p}_k^\top$
    end for
end while

As mentioned earlier, Equation (V.24) provides a partial solution to Equation (V.21) if the update of the rows of $\mathbf{P}$ is only performed once. To solve Equation (V.21), the state 2 of algorithm 3 should be within another 'while' loop. However, for faster computation, the update of $\mathbf{P}$ is only performed once, as seen in algorithm 3. When the algorithm starts to converge, $\mathbf{T}$ does not change much, and a minimizer of Equation (V.21) is thus obtained by several consecutive iterations of the update of $\mathbf{P}$.

V.5 Experimental overview

V.5.1 Pattern quantization

To be implemented on the digital micromirror device (DMD), or on any other SLM, the patterns should be quantized, as real-valued patterns cannot be sent directly to a SLM. Uniform quantization of the patterns on b bits is therefore performed, with 2^b as the maximum available dynamic range of the DMD. To realize this quantization, we apply the following transform to the set of patterns $\mathbf{P}$:

$$\widehat{\mathbf{P}} = \left\lfloor \frac{1}{q}\mathbf{P} \right\rfloor \qquad q = \frac{\max(\mathbf{P})}{2^b - 1} \tag{V.25}$$

where $\lfloor . \rfloor$ is a rounding operation. Assuming that the quantization errors can be neglected (Rousset *et al.*, 2017a), the desired measurement vector $\breve{\mathbf{m}}$ of Equation (V.14) can be obtained as

$$\breve{\mathbf{m}} = q\left(N_0 \mathbf{T}\widehat{\mathbf{P}}\mathbf{f} + \alpha \mathbf{T}\mathbf{1}_K\right)\Delta t = \widehat{\mathbf{T}}\widehat{\mathbf{m}} \tag{V.26}$$

where

$$\widehat{\mathbf{m}} = \left(N_0 \widehat{\mathbf{P}}\mathbf{f} + \alpha \mathbf{1}_K\right)\Delta t \qquad \text{and} \qquad \widehat{\mathbf{T}} = q\mathbf{T} \tag{V.27}$$

V.5.2 Numerical experiments

Our numerical simulations are based on the computation of the forward model Equation (II.4). The Jasczak target is chosen as the imaged object $\mathbf{f}$, which is classically considered to determine the resolution of an imaging device.

The measurements $\mathbf{m}$ are the numbers of photons collected at the single detector, and these are necessarily corrupted by Poisson noise [1]. Mathematically, the following noise model is used :

$$\mathbf{m} = \mathscr{P}\left(\left(N_0 \mathbf{P}\mathbf{f} + \alpha \mathbf{1}_K\right)\Delta t\right) \tag{V.28}$$

where $\mathscr{P}(.)$ is the Poisson distribution applied to each entry of the vector. Changing N_0 and/or Δt in Equation (V.28) allows several levels of noise to be simulated. The larger N_0 and Δt, the larger the number of collected photons, and hence the better the signal-to-noise ratio of the measurements.

The proposed SNMF method is compared to the pattern-splitting and pattern-shifting methods presented in Section V.2. The same matrix $\breve{\mathbf{P}}$ was considered both for the factorizations of Section V.3.2 and the SNMF algorithm 3. The stopping criterion for the SNMF method is set to $\epsilon = 10^{-6}$. For pattern shifting, we choose $M = 10$ in Equation (V.17), to reduce the influence of noise and to better estimate the background value.

Different acquisition scenarios are considered for the numerical experiments, which correspond to different values for the parameters of Equation (II.4). In particular, varying light power N_0 is considered. A low N_0 indicates a low-light scenario, while a large N_0 simulates a very bright object. Varying dark current α is also considered, as each specific optical set-up has its own value that depends on the single-point detector and the illumination conditions used, and also on other factors. The integration time Δt that scales the measurements linearly is set to 1. The charge coupled device (CCD) image of the Jaczczak target shown in Fig. V.2 serves as the reference image. Image acquisition is simulated for N_0 ranging from 100 ph/s to 3600 ph/s, and for α ranging from 500 ph/s to 80,000 ph/s. Different values for N_0 account for laser power variabilities that can go from milliwatts to a few watts. The dark current α, which regroups all of the components read by the SPD when $N_0 = 0$, can be quite low if acquisitions are performed in the dark, but high if they are taken in a luminous environment with undesirable photons reaching the detector.

V.5.3 Experimental acquisitions

To complete the numerical results of the previous section, the experimental data were acquired using the set-up at CREATIS presented in Section III.2. The lamp used was directly imaged so as to see its LED structure. Figure V.3 shows this object and the SPC reference image obtained from a

1. There are other sources of noise, but the predominant one is Poisson noise

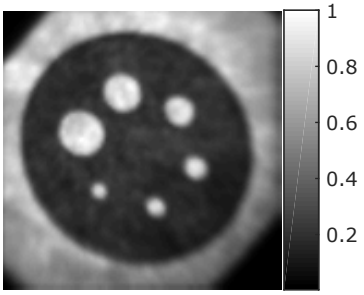

FIGURE V.2 – Charge coupled device image of the Jaszczak target used for the numerical experiments.

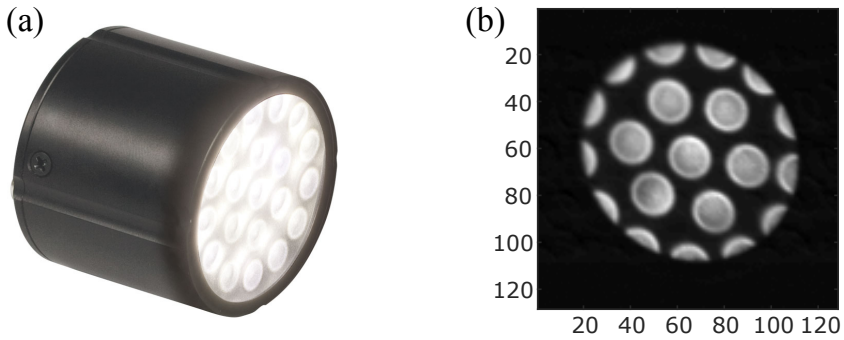

FIGURE V.3 – (a) The lamp that was used as an object in the set-up at CREATIS. (b) The single-pixel camera reference image of the lamp obtained with a basis scan of a 128 × 128 Hadamard basis.

basis scan of Hadamard 128 × 128 patterns. To recreate three values of N_0, different optical density (OD) filters (ThorLabs) were placed in front of the lamp (none, $OD = 0$; NE01B, $OD = 0.1$; NE02B, $OD = 0.2$). The collection time Δt at the photodetector was kept constant at $\Delta t = 100$ ms.

V.6 Results

V.6.1 Numerical experiments

Convergence of the proposed algorithm Figure V.4 illustrates the typical positive patterns obtained using the proposed SNMF method and using the *ad-hoc* methods. The Le Gall wavelet (CDF 5/3 biorthogonal) patterns of size $D = N \times N = 64 \times 64 = 4096$ are considered. The top row of Fig. V.4 shows the pattern generalization $\check{\mathbf{P}} = \mathbf{TP}$ obtained using our SNMF approach. In this example, the matrix $\check{\mathbf{P}}$ contains a sequence of $I = 4$ desired patterns, while the matrix $\mathbf{P}$ contains $K = I + 1 = 5$ (positive) patterns, which are also shown in the middle row of Fig. V.4. The positive patterns obtained using the pattern-splitting and pattern-shifting methods, for one of the desired patterns of $\check{\mathbf{P}}$, are given in the bottom row of Fig. V.4. As can be seen, the proposed SNMF method generates SLM patterns where their main structures and shapes are those of the desired patterns. The desired pattern Fig. V.4i indeed has a star shape in its center that is also visible in the SLM patterns created in Fig. V.4d-h.

The decrease in the pattern generalization error $\left\|\check{\mathbf{P}} - \mathbf{PT}\right\|_{\mathrm{F}}^2$ during the SNMF iterations is presented in Fig. V.5. The SNMF method is evaluated for several matrices $\check{\mathbf{P}}$ containing different numbers of patterns I and pattern sizes D. The resulting computation times and number of iterations are reported in table V.1.

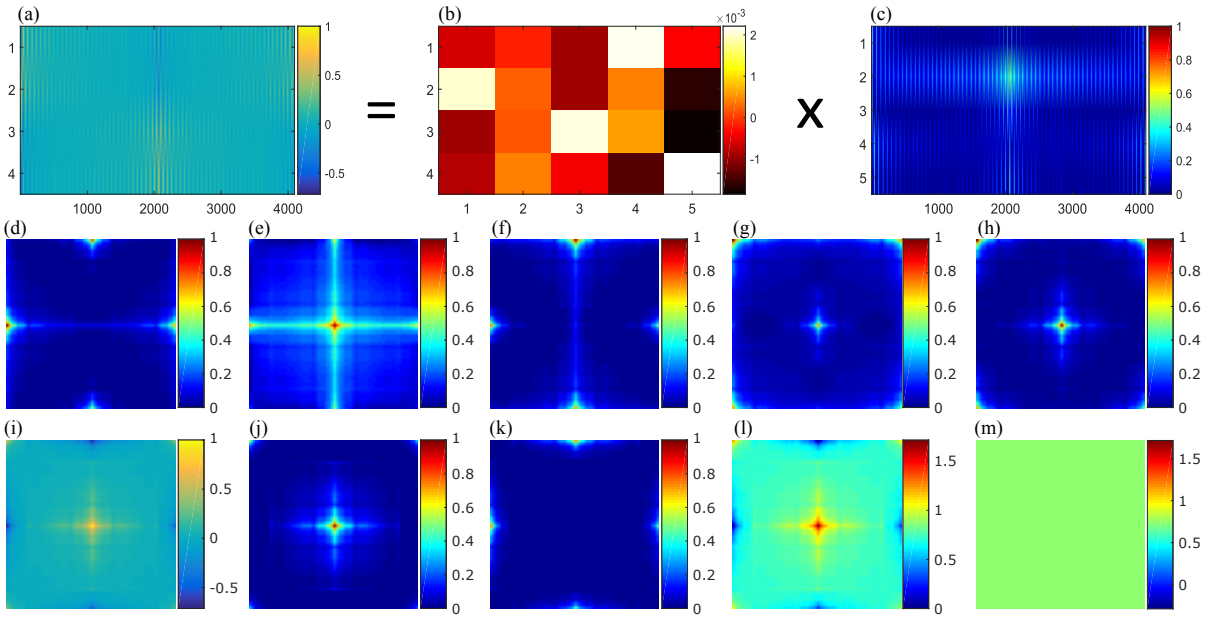

FIGURE V.4 – Examples of the patterns created with the proposed matrix factorization algorithm using Le Gall wavelet patterns. (a) Sequence matrix $\check{\mathbf{P}}$ of $I = 4$ desired spatial light modulator patterns of size $D = 64 \times 64 = 4096$. (b) Transformation matrix $\mathbf{T}$. (c) Sequence matrix $\mathbf{P}$ of $K = I + 1 = 5$ positive spatial light modulator patterns. (d-h) Five semi-nonnegative matrix factorization patterns of $\mathbf{P}$ (rows of image (c)). (i) Example of a desired pattern $\check{\mathbf{p}}$ (4th row of image (a)). (j) Positive part $\mathbf{p}_+ = \max(\mathbf{0}_D, \check{\mathbf{p}})$. (k) Negative part $\mathbf{p}_- = |\min(\mathbf{0}_D, \check{\mathbf{p}})|$. (l) Shifted pattern $\mathbf{p}_s = \check{\mathbf{p}} + \mathbf{p}_b$. (m) Background pattern $\mathbf{p}_b$.

Value of (I, D)	**Number of iterations**	**Computation time** (s)
$(4, 1024)$	18	0.01
$(16, 1024)$	72	0.10
$(64, 1024)$	100	0.68
$(4, 4096)$	13	0.02
$(16, 4096)$	54	0.25
$(64, 4096)$	173	3.58

TABLE V.1 – Number of iterations and computation time for the proposed semi-nonnegative matrix factorization algorithm 3 to converge for several values of (I, D). The convergence criterion ϵ was set to 10^{-6}.

Influence of the conditions for acquisition Single-pixel-camera recovered images of size 64×64 for four different paired (N_0, α) are shown in Fig. V.6. The Le Gall wavelet was used, and each wavelet coefficient from scale $J = 4$ to $j = 2$ was acquired ($CR = 75\%$), to only compare the influence of the splitting, shifting, and SNMF methods [2]. The PSNR of the restored images is shown as a function of N_0 for two values of α (20,000 ph/s, 80,000 ph/s) in Fig. V.7a, and as a function of α for two values of N_0 (600 ph/s, 1,600 ph/s) in Fig. V.7b. The larger the PSNR, the better the image quality. The PSNR of the restored images for all (N_0, α) pairs and pattern generalization methods are given in table V.2.

All of these three pattern-generalization methods perform better for increasing N_0 (see Fig. V.7a) and decreasing α (see Fig. V.7b). In all cases, pattern shifting provides the lowest PSNR. For low values of α, pattern splitting gives the best image quality. However, the pattern-splitting image quality

2. The prediction step of adaptive basis scan by wavelet prediction would indeed have a different outcome, as the values of the wavelet coefficients acquired by each technique can be different

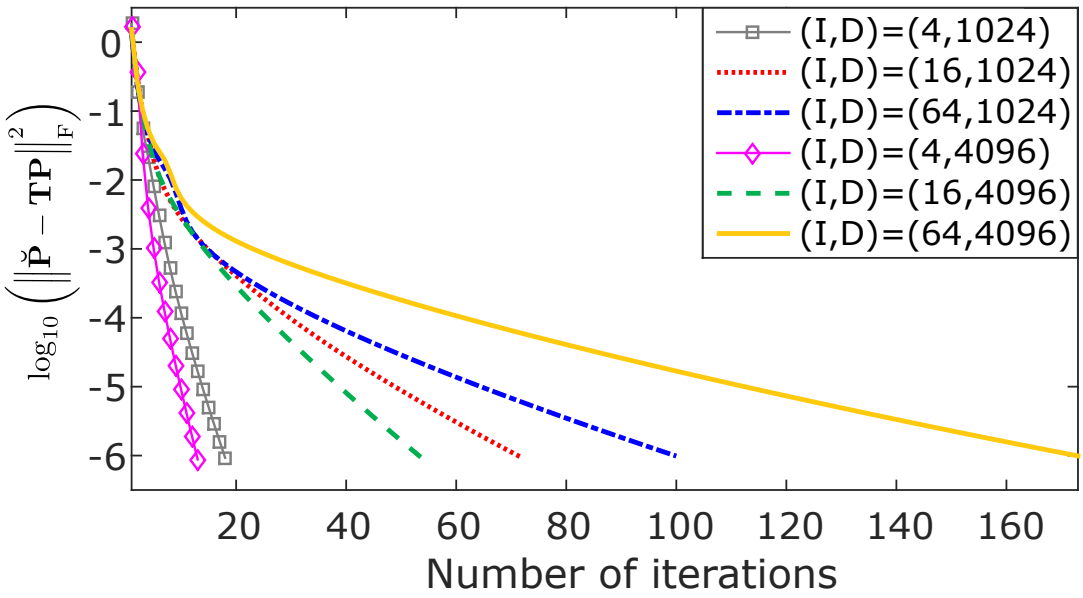

FIGURE V.5 – Logarithm (base 10) of the error $\left\|\check{\mathbf{P}}-\mathbf{TP}\right\|_F^2$ during the iterations of algorithm 3 for different values of desired patterns I and pattern sizes D. The convergence criterion ϵ was set to 10^{-6}.

degrades dramatically in low-light scenarios for increasing α (see Fig. V.7b). Overall, the proposed SNMF algorithm performs better in most of the scenarios assessed.

Influence of the constraint on T To motivate the transformation matrix constraint of Equation (V.13), the SNMF pattern generalization is performed for all of the previously described scenarios without the constraint $\mathbf{T1}_K = \mathbf{0}_I$. Table V.2 gives the PSNR of the images restored with no constraint on $\mathbf{T}$. If α is big enough, the image quality is dramatically improved when the equality constraint is added. For the case of table V.2 when α is small (i.e., 500, 5,000 ph/s), the data are close or even better without the constraint. As a reminder, this constraint is equivalent to saying that the sum on each row of $\mathbf{T}$ is equal to 0. If $\mathbf{T}$ is obtained as $\mathbf{T} = \check{\mathbf{P}}\mathbf{P}^\top\left(\mathbf{P}\mathbf{P}^\top\right)^{-1}$ (no constraint), the sum of the rows of $\mathbf{T}$ is around 10^{-4}. This is therefore sufficient enough to cancel small dark current values in this case. With the constraint, this sum is lowered to about 10^{-18}, which cancels any value of dark current.

V.6.2 Experimental data

Experimental data were acquired using 128×128 patterns from the Daubechies wavelet with 5 vanishing moments (Db5), using the CREATIS set-up. Wavelet coefficients from scale $J = 4$ to $j = 3$ ($CR = 93.75\%$) were acquired, to only judge the influence of the splitting, shifting, and SNMF methods. For the pattern-shifting technique, M of Equation (V.17) was set to 10, as for the simulations, to reduce the influence of the noise on the background measurement. The data are shown in Fig. V.8, and the PSNRs are given in table V.3, with respect to the reference image of Fig. V.3b.

As can be seen from these experimental results, the previous simulations are confirmed, with good SPC restored images using the pattern-splitting method or the proposed SNMF algorithm. The pattern-shifting method, however, fails to restore the object, even with the highest N_0 [3].

3. The highest N_0 corresponds to the lowest OD, as N_0 decreases if the optical density of the filter increases

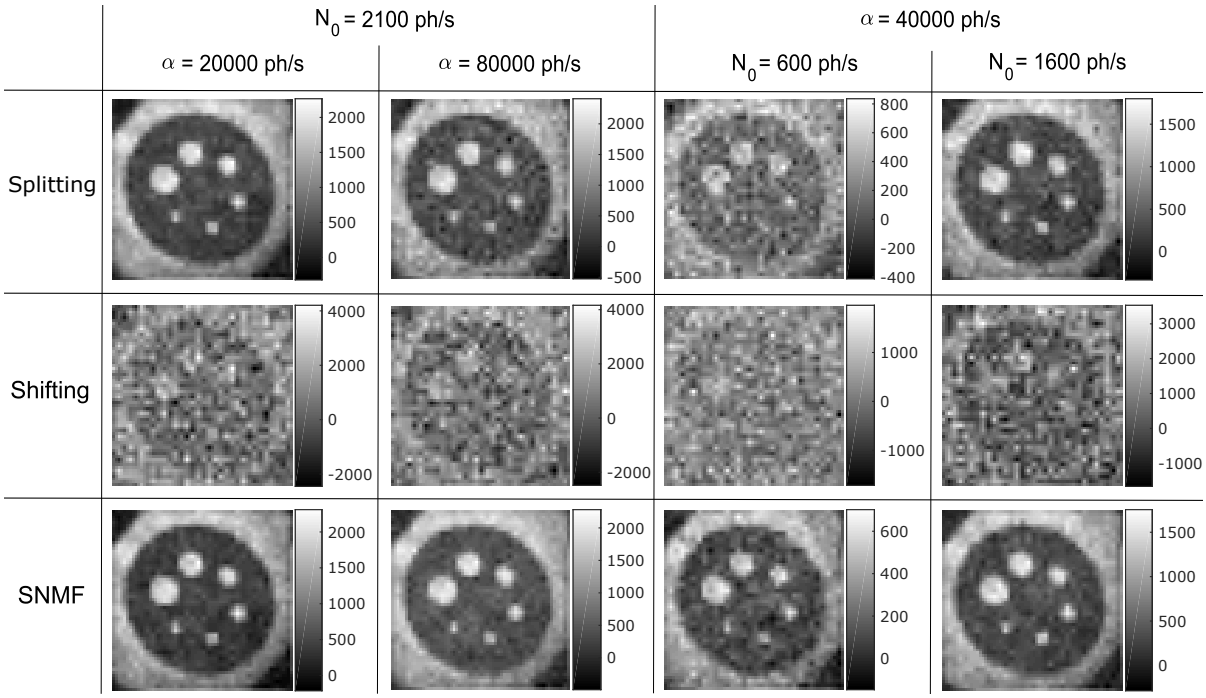

FIGURE V.6 – Single-pixel camera restored images using adaptive basis scan by wavelet prediction for the three matrix factorization techniques for different values of N_0 and α on the test image of Fig. V.7. The corresponding peak signal-to-noise ratio compared to the ground truth image (shown in Fig. V.7) can be read from Fig. V.7 and table V.2.

Value of α	**Technique**	**PSNR** (dB)							
		$N_0 = 100$	$N_0 = 600$	$N_0 = 1100$	$N_0 = 1600$	$N_0 = 2100$	$N_0 = 2600$	$N_0 = 3100$	$N_0 = 3600$
500	Pattern splitting	**17.56**	**25.74**	**26.95**	**27.33**	**27.63**	**27.77**	**27.83**	**27.94**
	Pattern shifting	-2.41	5.06	7.85	9.36	10.49	11.17	12.94	13.22
	SNMF with $\mathbf{T1}_K \neq \mathbf{0}_I$	16.00	22.63	24.70	25.32	25.90	26.29	26.42	26.81
	SNMF with $\mathbf{T1}_K = \mathbf{0}_I$	15.22	22.50	24.16	25.07	25.68	26.10	26.63	26.68
5000	Pattern splitting	9.34	**22.43**	**25.34**	**26.45**	**26.98**	**27.40**	**27.55**	**27.73**
	Pattern shifting	-2.63	5.49	7.92	10.03	10.18	11.33	12.34	13.36
	SNMF with $\mathbf{T1}_K \neq \mathbf{0}_I$	6.91	19.73	22.93	24.53	25.17	25.87	26.32	26.76
	SNMF with $\mathbf{T1}_K = \mathbf{0}_I$	**14.93**	22.10	24.29	25.32	25.52	26.14	26.40	26.73
20000	Pattern splitting	3.47	18.37	22.31	22.41	**25.70**	**26.30**	**26.75**	**27.04**
	Pattern shifting	-3.01	4.63	7.68	9.35	10.28	11.45	12.10	12.69
	SNMF with $\mathbf{T1}_K \neq \mathbf{0}_I$	-4.58	10.72	15.75	18.74	20.39	21.98	22.83	23.68
	SNMF with $\mathbf{T1}_K = \mathbf{0}_I$	**12.90**	**21.99**	**24.15**	**24.86**	25.59	25.89	26.47	26.47
40000	Pattern splitting	0.91	15.73	19.97	22.92	24.58	25.15	26.03	26.44
	Pattern shifting	-4.91	5.20	7.72	9.36	10.42	11.50	12.30	13.01
	SNMF with $\mathbf{T1}_K \neq \mathbf{0}_I$	-10.51	4.88	10.17	13.26	15.46	17.27	18.68	19.68
	SNMF with $\mathbf{T1}_K = \mathbf{0}_I$	**10.61**	**21.32**	**23.68**	**24.68**	**25.82**	**25.81**	**26.43**	**26.48**
80000	Pattern splitting	-2.57	12.84	17.53	20.69	22.32	23.74	24.23	25.38
	Pattern shifting	-6.08	4.62	7.69	9.23	10.59	11.17	12.61	12.47
	SNMF with $\mathbf{T1}_K \neq \mathbf{0}_I$	-16.62	-1.07	4.18	7.42	9.79	11.54	13.17	14.36
	SNMF with $\mathbf{T1}_K = \mathbf{0}_I$	**8.78**	**20.86**	**23.48**	**24.74**	**25.07**	**26.00**	**26.36**	**26.57**

TABLE V.2 – Peak signal-to-noise ratio values of the single-pixel-camera restored images for different values of N_0 and α for $\Delta t = 1$. Some cases correspond to the images shown in Fig. V.6 and the curves of Fig. V.7.

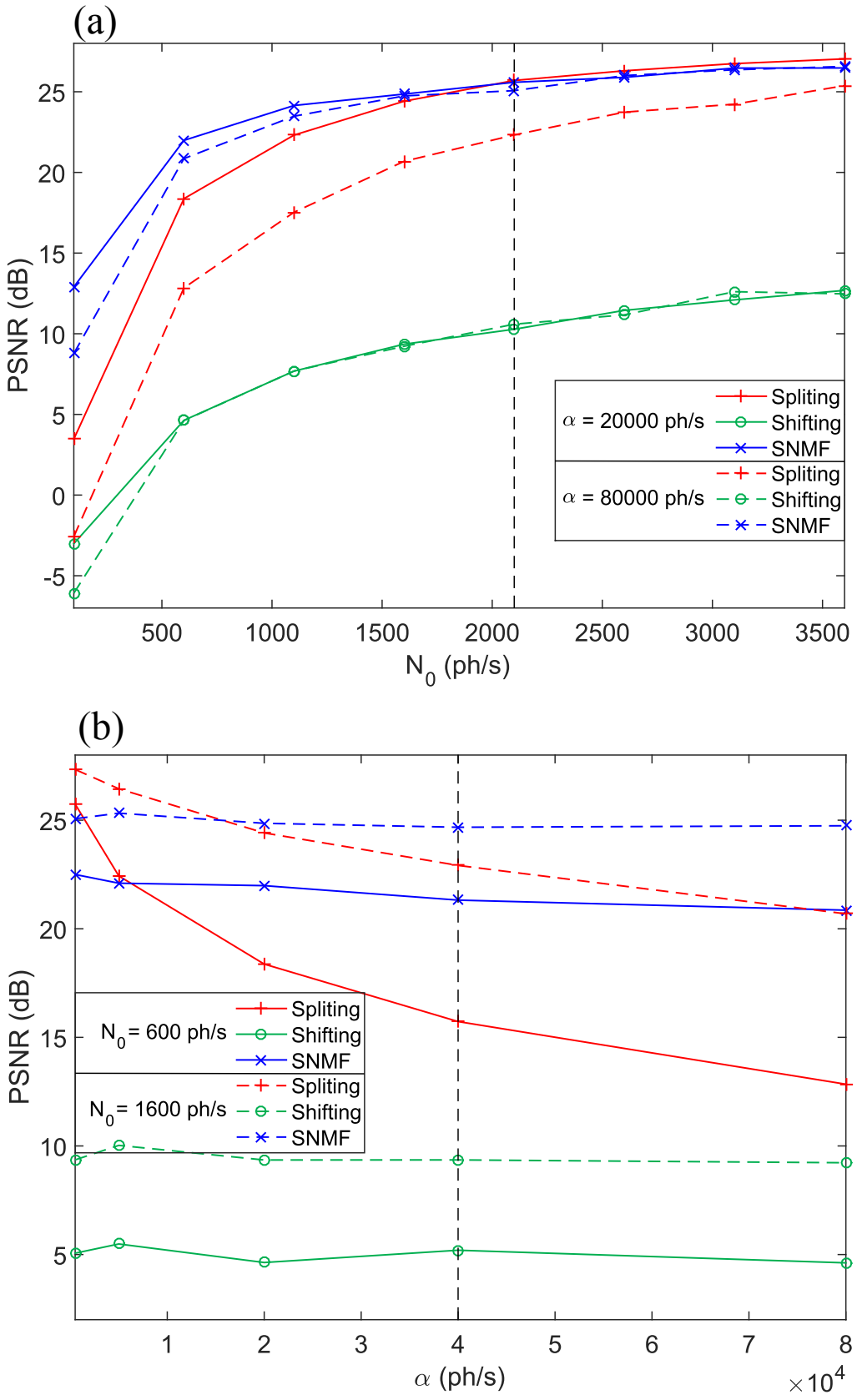

FIGURE V.7 – Jaszczak target and peak signal-to-noise ratio curves of single-pixel camera restored images for (a) (resp. (b)) two fixed values of N_0 (resp. α) and increasing values of N_0 (resp. α) for $\Delta t = 1$ s. The dotted black bars correspond to the results shown in Fig. V.6.

V.7 Discussion

The main advantage of our SNMF approach is that it guarantees a low factorization error for a low number of positive patterns; i.e., $K = I+1$ SLM patterns for I desired patterns. A low factorization error is crucial to obtain the desired measurements through measurement transformation without introducing model deviation. A low number of patterns K is necessary to limit the number of measurements, and hence the acquisition time. Most SNMF methods propose the choice of $K << I$, but the factorization error is often important. Here, using the block coordinate descent method (Gillis *et* Kumar, 2015), only $I+1$ measurements with positive patterns are required to obtain the I desired measurements, which gives a ratio of almost 1. This is much better than pattern splitting, which requires two positive patterns to acquire one datum. Overall, the proposed SNMF method allows the total acquisition time to be halved with respect to the conventional pattern-splitting approach. As for the SNMF method, the pattern-shifting method can reach $K = I+1$. However, it is shown to fail to restore good quality images in most cases.

The number of iterations and the computation time of the SNMF algorithm depends on the size of the problem. As the SNMF algorithm updates the rows of $\mathbf{P}$, increasing I (by extension, extending K, the number of rows of $\mathbf{P}$) has a bigger impact than increasing D (the number of columns of $\mathbf{P}$). This can be seen by comparing the computation times of table V.1 for $(I,D) = (16,4096)$ and $(I,D) = (64,1024)$, for which the matrix $\check{\mathbf{P}}$ has the same number of entries ($I \times D = 65536$). The SNMF algorithm converges more rapidly for the smaller values of I.

For high resolution images (i.e., large D and I), the SNMF computation can take up to several minutes. For nonadaptive SPC acquisition (e.g., based on compressed sensing), SNMF can be performed prior to the acquisition. However, long computation times can be a limitation for adaptive acquisition strategies where the set of patterns $\check{\mathbf{P}}$ is determined during the acquisition, from the knowledge of the previous measurements. Therefore, it is necessary to wait for the SNMF algorithm outputs $\mathbf{P}$ and $\mathbf{T}$ before proceeding with the acquisition. In this thesis, a computation time of about 4 minutes is required for $I = 1024$ and $D = 4096$ when running Matlab code on a single-core 2.10 GHz CPU. A *C++* implementation running on a GPU would significantly lower these computation times, and make them compatible with adaptive acquisition strategies.

The better results of the SNMF method compared to pattern splitting for most cases might be understood by looking at the patterns in Fig. V.4. The patterns (j) and (k), obtained from pattern splitting have many zeros. When α is large with respect to N_0, the useful part of the pattern (i.e., nonzeros) has only a small contribution to the SPC measurement. The SNMF patterns have fewer zeros and therefore this effect is reduced (see Fig. V.4, patterns (d)–(h)). The pattern-shifting method leads to the lowest image quality; only the shape of the target can be recovered (see Fig. V.6). An explanation here is that this method is very sensitive to noise, as the useful information of the shifted pattern is overwhelmed by the useless information from the background for Fig. V.4m. Looking at the shifted pattern in Fig. V.4l, it can be seen that all of the pixels contribute to the measurement, which leads to the collection of many undesired photons in the presence of noise. Overall, the SNMF technique works well when $N_0 \ll \alpha$, i.e., when the dark current cannot be neglected, which is always the case in real experiments.

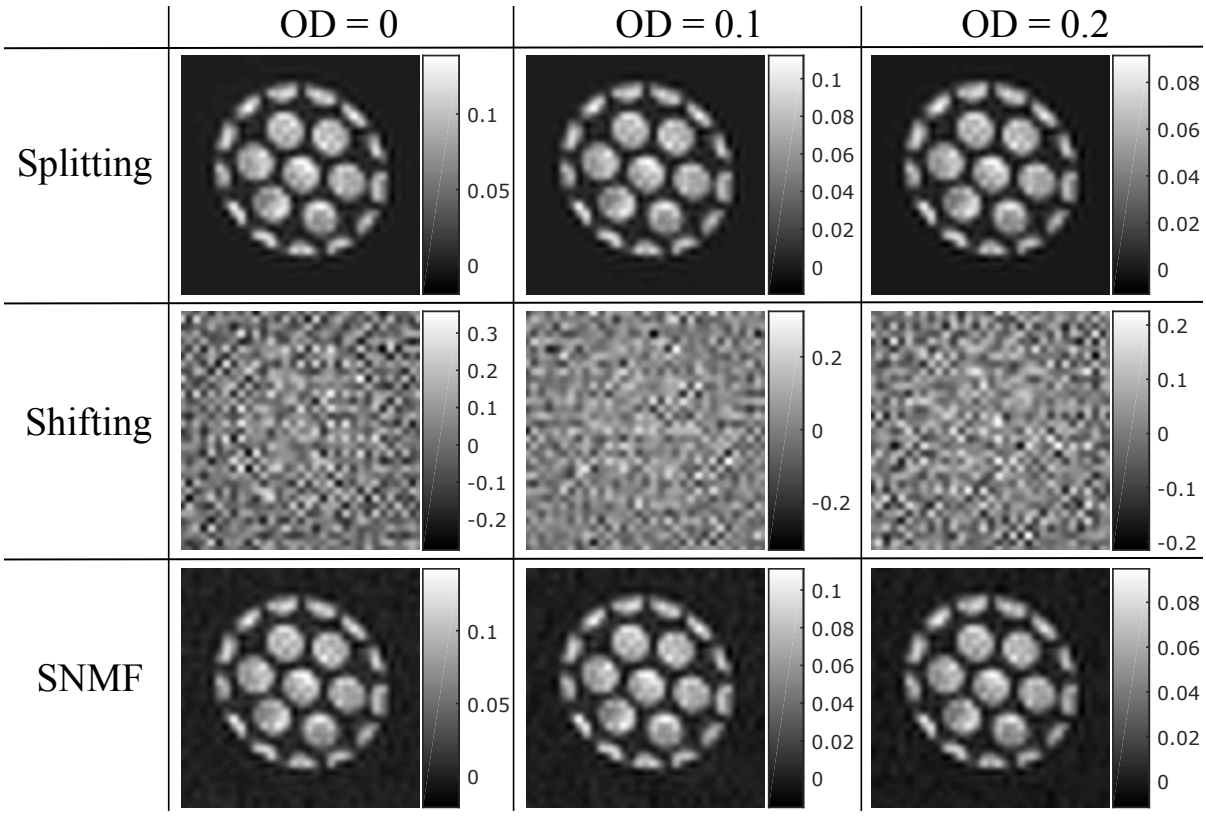

FIGURE V.8 – Experimental acquisitions using the pattern-splitting, pattern-shifting and proposed semi-nonnegative matrix factorization algorithm for three different optical densities (OD). The peak signal-to-noise ratios with respect to the reference image of Fig. V.3b are given in table V.3.

Technique	**PSNR** (dB)		
	$OD = 0$	$OD = 0.1$	$OD = 0.2$
Pattern splitting	**23.27**	**22.07**	**19.29**
Pattern shifting	4.73	6.25	7.65
SNMF	23.25	21.87	19.22

TABLE V.3 – Peak signal-to-noise ratio values for the images of Fig. V.8 for different optical densities (OD) (i.e., different N_0).

The pattern-splitting and SNMF methods give similar results, with a slight edge for pattern splitting for small values of α. A possible explanation regards the construction of the measurement vector. For the proposed SNMF technique, the measurements $\breve{\mathbf{m}}$ that are used for image restoration are obtained from the measurement transformation $\mathbf{Tm}$ (see Eq. (V.14)). In the presence of noise, the variance of $\breve{\mathbf{m}}$ depends on the sum of the variances of $\mathbf{m}$. While many measurements are combined when the SNMF method is used, only two measurements are combined when pattern splitting is used. Hence pattern splitting is less affected by noise than SNMF. However, compared to pattern splitting, the proposed SNMF method is an excellent compromise that gives an image quality similar to that obtained using pattern splitting, while halving the number of measurements.

The experimental acquisitions confirm what has been said up to this point. The visual results of Fig. V.8 are very close using the pattern-splitting technique or the proposed SNMF algorithm,

although the PSNRs of table V.3 are slightly lower for the SNMF method. The pattern-shifting technique is, however, not usable in practice, as the measurements are too corrupted by the noise, and no useful image can be obtained from them.

V.8 Conclusion

In this Chapter, we introduced a new problem in SPI that we refer to as pattern generalization. This consists of determining a set of positive patterns that can be actually loaded onto a SLM. We also show that a second issue that has to be addressed in pattern generalization is dark current removal. Our basis idea is to see the set of desired patterns (with negative entries) as a linear transform of positive patterns.

We report a SNMF that is shown to solve the problem. To our knowledge, this is the first time that a SNMF algorithm is used in the context of SPI. This provides an elegant way to dispose of both the positivity constraint induced by the use of a SLM, and the dark current. At the same time, it allows the number of measurements to be reduced compared to the conventional pattern-splitting method.

In the future, we will investigate algorithms for which the number of measurements is lower than the number of desired measurements; i.e., $K < I$ in Equation (V.15). This would further compress the data, to speed up the acquisition. The main challenge to perform this is the factorization error that would be much more important than what can be achieved using the Gillis method with $K = I + 1$. If this error is too large, the desired measurements obtained by Equation (V.14) are partially wrong, which would lead to poor image recovery.

While the adaptive basis scan by wavelet prediction (ABS-WP) method of Chapter IV improved the speed of the image restoration side of the SPC acquisition/ restoration, this SNMF-based method allows for faster acquisition with fewer measurements [4]. Acquisitions for real applications can now be considered, in particular for medical applications. The next Chapter deals with potential applications in this field, with multispectral time-resolved acquisitions.

4. The image restoration is slightly increased as Equation (V.14) has to be performed to get the desired measurements

CHAPTER VI

APPLICATION TO MULTISPECTRAL TIME-RESOLVED IMAGING

Contents

CHAPTER VI

BIOMEDICAL APPLICATIONS can take advantage of single-pixel imaging (SPI) systems. In particular, multispectral time-resolved imaging is of interest, as SPI allows good spectral, temporal, and spatial resolution to be obtained.

In this Chapter, we apply the previously developed tools for acquisition of multispectral and/or time-resolved single-pixel camera (SPC) measurements. Some of these data were presented at the *SPIE Photonics West* Conference (Rousset *et al.*, 2017b) in February 2017, and the other data are soon expected to be submitted to *Optics Express*.

VI.1 Introduction

As mentioned in the main Introduction, the SPC has been demonstrated to image through scattering media (Tajahuerce *et al.*, 2014; Duran *et al.*, 2015), such as biological tissues in ophthalmology (Lochocki *et al.*, 2016, 2017), for skin lesion detection (Gibson *et* Dehghani, 2009), and to characterize tissues with near-infrared acquisition (Torabzadeh *et al.*, 2017). In addition, diffuse optical tomography or fluorescence molecular tomography (D'Andrea *et al.*, 2010; Ducros *et al.*, 2013; Pian *et al.*, 2015; Ducros *et al.*, 2016) with applications to oximetry and molecular imaging can be performed by exploiting several SPC images. Another significant advantage of a SPC for biomedical applications relates to *time-resolved* and/or multispectral acquisitions. Coupling the point detector of a SPC with a photon-counting board (Pian *et al.*, 2016b,a; Rousset *et al.*, 2017b) provides a low-cost time-resolved system that can benefit fluorescence lifetime imaging (Becker, 2012). Such a set-up was first proposed with applications to fluorescence lifetime imaging by Pian *et al.* (2016b,a). This has improved performance compared to time-gated cameras (D'Andrea *et al.*, 2003), as it can combine good temporal and spatial resolution. Lifetime information can be further supplemented by spectral information by the addition of a spectrometer to the previous time-resolved system (Pian *et al.*, 2016b). The spectral and time information can be exploited to characterize biological tissues that contain several fluorophores with different fluorescence lifetimes. This enables assessment of the biological micro-environment of tissues (e.g., pH, temperature, ion concentration) (Marcu, 2012; Ma *et al.*, 2015), which is an essential parameter for biologists.

In the study of Pian *et al.*, a partial basis scan (BS) approach with Hadamard patterns was used; i.e., a subset of the complete basis coefficients are acquired regardless of the object to image (see Section II.3.1). Hence, high compression ratios cannot be reached without dramatic degradation of the image quality. In this Chapter, the simultaneous handling of time-resolved and multispectral image acquisition using the adaptive basis scan (ABS) by wavelet prediction (ABS-WP) technique (Chapter IV) to reduce the number of measurements is demonstrated [1]. The use of an ABS approach over

1. The semi-nonnegative matrix factorization technique presented in Chapter V is not used for the experimental ac-

a compressive sensing technique is motivated by the restoration step, which is particularly crucial when time-resolved measurements are considered. This step should indeed be as fast as possible, as a stack of images has to be recovered instead of a single image.

In this Chapter, the mathematical modeling of the SPC of Section II.1 is first extended to deal with time-resolved and/or multispectral measurements, and then the phantom and experiments considered are detailed. Results are then provided for fluorescence lifetime sensing and for multispectral time-resolved acquisition. These demonstrate that using both the spectral and temporal information, it is possible to completely differentiate the different components of the imaged object.

VI.2 Methods

VI.2.1 Extension to multispectral time-resolved measurements

Mathematical modeling To initially obtain a time-resolved system, a pulsed laser is used as the light source, and the detector is coupled to a time-correlated single-photon counting (TCSPC) board. Through its synchronization with the pulse of the laser, the TCSPC makes it possible to obtain a histogram that provides the number of photons for different times of flight (i.e., time channels). Then, to obtain a multispectral time-resolved system, the output light of the single-pixel arm is directed toward a spectrometer with Λ parallel single detectors that are coupled to the TCSPC board with T time channels. This results in a 2D+λ + t image $\mathbf{F} \in \mathbb{R}^{D\times\Lambda T}$ with $\mathbf{F} = \left(\mathbf{f}_{1,1},\ldots,\mathbf{f}_{\lambda,t},\ldots,\mathbf{f}_{\Lambda,T}\right)$. The image $\mathbf{f}_{\lambda,t} \in \mathbb{R}^{D\times 1}$ represents the image in the wavelength channel λ and time channel t with $(\lambda,t) \in \{1,\ldots,\Lambda\}\times\{1,\ldots,T\}$. As the spectral and temporal information are acquired simultaneously, Equations (II.4) and (II.5) of Chapter II are slightly changed, to

$$\mathbf{m}_k = \left(m_{k,1,1},\ldots,m_{k,\lambda,t},\ldots,m_{k,\Lambda,T}\right)^\top \in \mathbb{R}^{\Lambda T\times 1} \quad \text{with} \quad \mathbf{m}_k^\top = \left(N_0\mathbf{p}_k^\top\mathbf{F} + \alpha\mathbf{1}_{\Lambda T}^\top\right)\Delta t \tag{VI.1}$$

$$\mathbf{M} = \left(\mathbf{m}_1,\ldots,\mathbf{m}_k,\ldots,\mathbf{m}_K\right)^\top \in \mathbb{R}^{K\times\Lambda T} \quad \text{with} \quad \mathbf{M} = \left(N_0\mathbf{P}\mathbf{F} + \alpha\mathbf{1}_{K\times\Lambda T}\right)\Delta t \tag{VI.2}$$

where $\mathbf{1}_{\Lambda T} = (1,\ldots,1)^\top \in \mathbb{R}^{\Lambda T\times 1}$ and $\mathbf{1}_{K\times\Lambda T} \in \mathbb{R}^{K\times\Lambda T}$, the matrix with all entries is equal to 1. A measurement vector $\mathbf{m}_k \in \mathbb{R}^{\Lambda T\times 1}$ is directly obtained by the multispectral time-resolved SPC for each pattern $\mathbf{p}_k$, while a scalar measurement is acquired for each pattern of a classical SPC. A matrix of measurements $\mathbf{M} \in \mathbb{R}^{K\times\Lambda T}$ is thus obtained when a sequence of patterns $\mathbf{P} \in \mathbb{R}^{K\times D}$ is considered.

Time or spectral dependent images From the $\Lambda \times T$ restored images, it is possible to extract the T (resp. Λ) images $\mathbf{f}_t$ (resp. $\mathbf{f}_\lambda$) in each time (resp. wavelength) channel by summing $\mathbf{f}_{\lambda,t}$ over λ (resp. t) :

$$\mathbf{f}_\lambda = \sum_{t=1}^{T} \mathbf{f}_{\lambda,t} \qquad \mathbf{f}_t = \sum_{\lambda=1}^{\Lambda} \mathbf{f}_{\lambda,t} \tag{VI.3}$$

The images $\mathbf{f}_t$ (resp. $\mathbf{f}_\lambda$) are equivalent to those that would be obtained without the spectrometer (resp. TCSPC board) of the multispectral time-resolved system.

quisition in this Chapter, as chronologically this method had not yet been implemented

Prediction on CW measurements In the design of our acquisition/restoration scheme of Chapter IV, ABS-WP, the prediction step of the significant wavelet coefficients is based on scalar measurement; i.e., on a single image. To perform this prediction, we therefore consider the *continuous-wave* image $\mathbf{f}$ that is obtained by summing the images $\mathbf{f}_{\lambda,t}$ over λ and t :

$$\mathbf{f} = \sum_{\lambda=1}^{\Lambda} \sum_{t=1}^{T} \mathbf{f}_{\lambda,t} \tag{VI.4}$$

This continuous-wave image corresponds to that which would be acquired without the spectrometer and TCSPC board; i.e., using Equations (II.4) and (II.5) for the image-formation model. Note that when an acquisition/ restoration scheme is considered with a linear transform (e.g., typically with a BS or ABS approach), summing the images after the restoration step is equivalent to summing the corresponding measurements before image restoration, due to the linearity of Equations (VI.1) and (VI.4).

VI.2.2 Exponential fitting of fluorescence decay

A fluorophore is a chemical component that upon excitation at a certain wavelength, it will emit fluorescent light at a different wavelength. The emission of fluorescence is typically modeled by the sum of exponential decays. Here, we assume a mono-exponential decay; i.e., the fluorescence intensity $I(t)$ at t is given by

$$I(t) = Ae^{\frac{-t}{\tau}} \tag{VI.5}$$

where A is the amplitude and τ is the lifetime.

After restoration of the images $\mathbf{f}_t$, each pixel $n \in [1, D]$ is assumed to satisfy the model of Equation (VI.5) for each time point of the vector $(t_1, \ldots, t_T)^\top \in \mathbb{R}^{T\times 1}$. This latter vector represents the real-time delays in seconds associated to the different time channels of the TCSPC board. Using this vector, the model of Equation (VI.5) can first be discretized as

$$\mathbf{I}_n = (I_n(t_1), \ldots, I_n(t_T))^\top = \left(A_n e^{\frac{-t_1}{\tau_n}}, \ldots, A_n e^{\frac{-t_T}{\tau_n}}\right)^\top \in \mathbb{R}^{T\times 1} \tag{VI.6}$$

where $n \in [1, D]$ still accounts for the pixel considered.

An experimental time curve $\widehat{\mathbf{I}}_n \in \mathbb{R}^{T\times 1}$ that depicts $\mathbf{I}_n$ of Equation (VI.6) can be obtained for each pixel from $\mathbf{f}_t$, mathematically as

$$\widehat{\mathbf{I}}_n = ((\mathbf{f}_1)_n, \ldots, (\mathbf{f}_t)_n, \ldots, (\mathbf{f}_T)_n)^\top \tag{VI.7}$$

The experimental curves $\widehat{\mathbf{I}}_n$ of Equation (VI.7) for each pixel of the image can therefore be fitted to the model $\mathbf{I}_n$ of Equation (VI.6), which provides the parameters A_n and τ_n. The optimal parameters (A_n^*, τ_n^*) are obtained by minimizing the ℓ_2-norm of the difference between the model function curve $\mathbf{I}_n$ and the experimental curve $\widehat{\mathbf{I}}_n$:

$$\left(A_n^*, \tau_n^*\right) = \arg\min \left\| \widehat{\mathbf{I}}_n - \mathbf{I}_n \right\|_2^2 \tag{VI.8}$$

Here, the Matlab function `lsqcurvefit` is used to perform this optimization. Repeating the fitting of Equation (VI.8) for each of the $D = N \times N$ pixels of the image finally obtains the amplitude map $\mathbf{A} \in \mathbb{R}^{D\times 1}$ and the lifetime map $\boldsymbol{\tau} \in \mathbb{R}^{D\times 1}$. This process is summarized in Fig. VI.1.

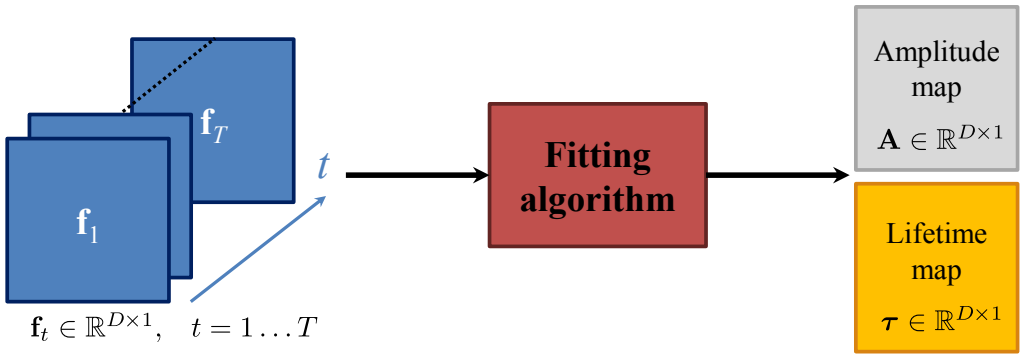

FIGURE VI.1 – Amplitude and lifetime maps obtained by a fitting algorithm using time-dependent images. Note that the vectors are displayed as images in this scheme.

VI.3 Experiments

VI.3.1 Phantom

Figure VI.3a shows the phantom that is considered, where different shapes have been created with a paper mask. Approximately, the wave has a 0.7-cm thickness and a 2.3-cm height. The circle diameter and square side are about 1 cm. The square (resp. wave) shape is a red (resp. green) fluorescence plastic slide (CHROMA). A solution of DCM dye in ethanol is used to make the circle shape that is painted on white paper. The spectral characterization of the fluorophores involved in the phantom is given in table VI.1.

VI.3.2 Experimental set-up and conditions

Setup The Polimi set-up described in Section III.1 was used for the experimental data acquisition. The supercontinuum pulsed white light laser source (SuperK Extreme EXW-12, NKT Photonics) serves for uniform illumination of the object. In the fluorescence lifetime imaging results of Section VI.4.1, a one-channel (spectral channel) photomultiplier tube (PMT; HPM-100-50, Becker & Hickl GmbH) is used, while in the multispectral experiments of Section VI.4.2, a sixteen-channel PMT (PML-16-1, Becker & Hickl GmbH) is used. In both configurations, the detector is coupled to the TCSPC board (SPC-630, Becker & Hickl GmbH). The TCSPC board has a maximum of 4,096 available time channels, and the pulse of the laser was repeated at a frequency of 40 MHz. To ensure a good signal-to-noise ratio while satisfying the statistical constraints of the TCSPC board photon

Area	Material	Absorption peak	Emission peak
Wave	Green fluorescence plastic slide	464 nm	525 nm
Square	Red fluorescence plastic slide	520 nm	625 nm
Circle	DCM dye painted on a white paper	468 nm	624 nm

TABLE VI.1 – Absorption and emission peaks of the different fluorophores embedded in the phantom.

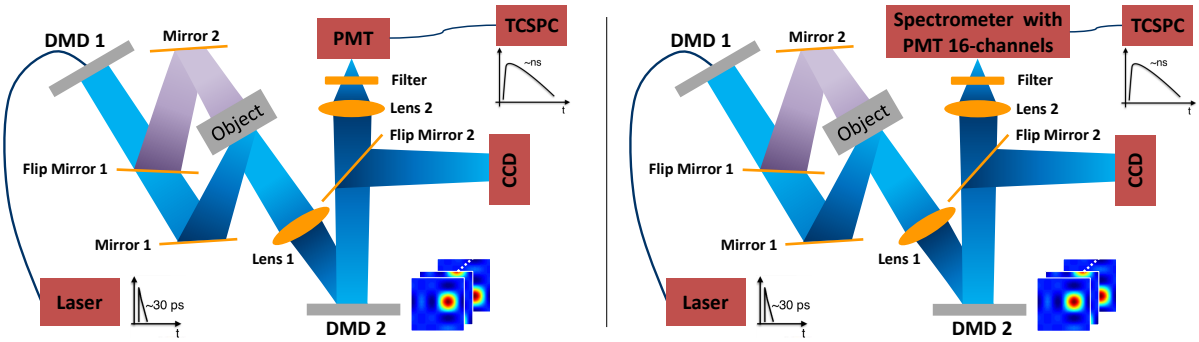

FIGURE VI.2 – Experimental set-up at the Polimi for the time and spectral information. Left : Time-resolved single-pixel camera. Right : Multispectral time-resolved single-pixel camera.

counting, an acquisition time $\Delta t = 1$ s was chosen for the detector. A long-pass filter (FEL0500, ThorLabs) with a cut-off wavelength at 500 nm was positioned before the detection, which selects the emitted fluorescence light based on the characteristics of the phantom (see table VI.1). The set-up in both configurations is shown in Fig. VI.2.

Experimental conditions For acquisition/ restoration using the SPC, our ABS-WP scheme described in Chapter IV was used. To deal with the positivity constraint on the patterns and the additive dark current, the classical positive/ negative separation presented in Section V.2 was used, because at the time of these measurements, the proposed semi-nonnegative matrix factorization algorithm reported in Chapter V was not available.

Adaptive basis scan by wavelet prediction was used with the Daubechies wavelet with 5 vanishing moments (Db5) (Mallat, 2008; Daubechies, 1992). A compression rate of 93% was obtained for the set of percentages $\mathcal{P} = \{1; 0.85; 0.075; 0\}$. As mentioned earlier, the prediction step of ABS-WP is based on continuous-wave measures (see Equation (VI.4)) gathered by integrating (i.e., summing) the measurements.

VI.4 Results

VI.4.1 Fluorescence lifetime sensing

For these results, the illumination of the object was performed in the 450 – 490 nm spectral band. To limit noise, the 4,096 time-channels of the SPC were partially binned. This led to $T = 72$ time points and a time vector $\mathbf{t}$ ranging from 0 ns to 21.66 ns, with a uniform time step of 0.305 ns.

A photograph of the phantom along with different SPC restored images is shown in Fig. VI.3. From the different images $\mathbf{f}_t$, temporal curves that give the intensity changes within each area of the phantom can be computed. For this, the pixels within each area are summed for each time point, and then normalized to give the curves of Fig. VI.4. In addition, for each pixel of the image, the fitting of Equation (VI.8) is performed, to obtain the amplitude and lifetime maps of Fig. VI.5.

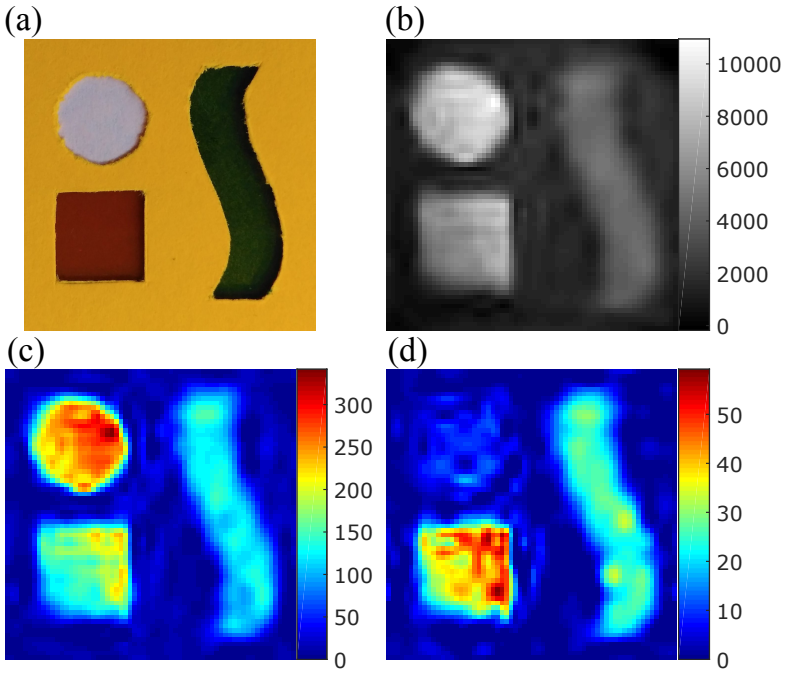

FIGURE VI.3 – Photograph of the phantom considered, and the 64×64 images restored from continuous-wave measurements or different time channels, with the Daubechies wavelet (Db5) and $\mathcal{P} = \{1; 0.85; 0.075; 0\}$ giving a compression rate of 93%. (a) Photograph of the phantom. (b) Continuous-wave image. (c, d) $\mathbf{f}_t$ restored for $t = 10$ (2.75 ns) (c) and $t = 50$ (14.95 ns) (d).

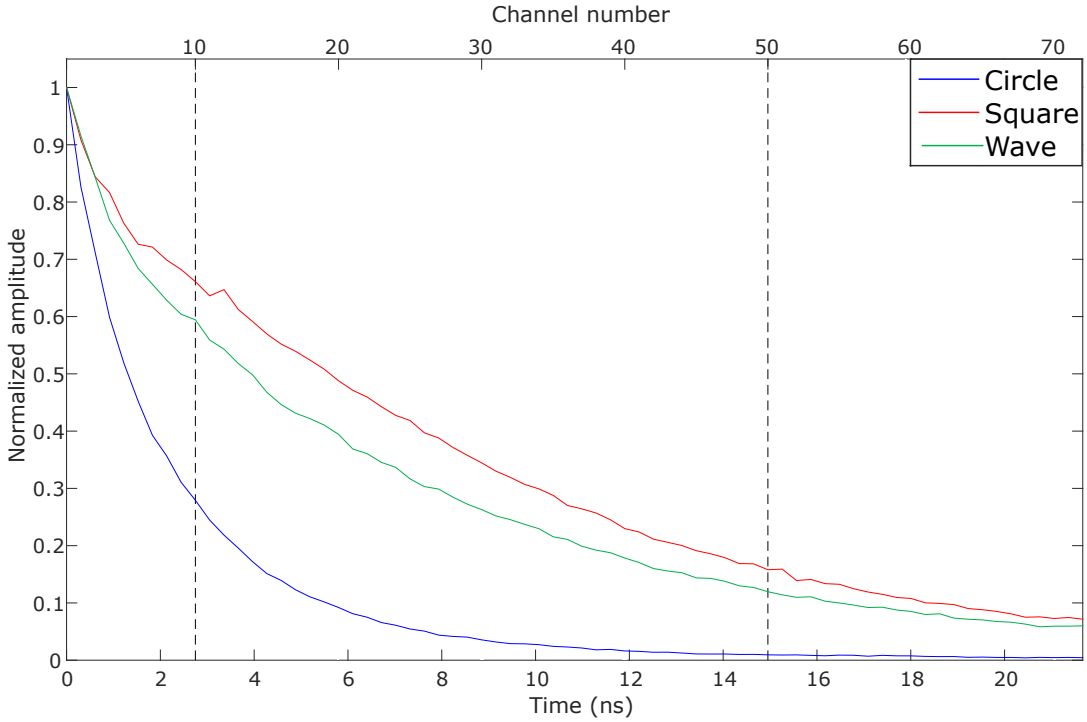

FIGURE VI.4 – Time curves obtained from the restored images $\mathbf{f}_t$ by summing the pixels in each area of the sample for each time channel. The dotted black vertical bars correspond to the time channels of the images shown in Fig. VI.3c, d.

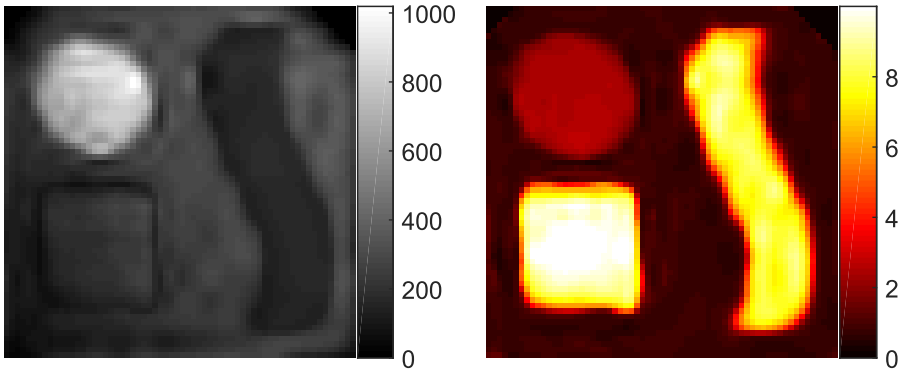

FIGURE VI.5 – Amplitude (arbitrary units, left) and lifetime (ns, right) maps obtained by fitting the experimental time curves for each pixel to an exponential decay function.

VI.4.2 Multispectral time-resolved acquisitions

For these measurements, after binning of the TCSPC time channels, a total of $T = 60$ time channels was obtained that covered the times from 0 ns to 18.00 ns. The object was illuminated in the spectral band of 470 – 490 nm. For the spectrometer settings, its central wavelength was chosen at $\lambda_c = 575$ nm. The $\Lambda = 16$ spectral channels covered wavelengths from approximately 505 ± 5 nm to 655 ± 5 nm, with a 10-nm step.

Figure VI.6 shows a photo of the phantom, as well as the restored 64×64 CW image $\mathbf{f}$ obtained through Equation (VI.4). It further shows several images $\mathbf{f}_t$ (resp. $\mathbf{f}_\lambda$) in different time (resp. spectral) channels obtained from Equation (VI.3).

Within each area of the phantom, the time (resp. spectral) curves are given in Fig. VI.7. These were computed by summing the pixels of $\mathbf{f}_t$ (resp. $\mathbf{f}_\lambda$) of Equation (VI.3) within the different areas of the sample for each time (resp. spectral) channel. The vertical dotted black bars correspond to the restored images shown in Fig. VI.6.

As was performed for the time-resolved measurements, if the spectral information is integrated to get $\mathbf{f}_t$ as in Equation (VI.3), the amplitude and lifetime maps can be estimated. Figure VI.8 shows these two maps, which were obtained with the exponential fitting described by Equation (VI.8) using the data from $\mathbf{f}_t$.

VI.5 Discussion

VI.5.1 Fluorescence lifetime sensing

Even with a compression rate as high as 93%, the data in Fig. VI.3 show that using our ABS-WP framework, it is possible to acquire a good quality image that shows the different shapes of the object. As this is a summed version of the time channels, and as expected, the continuous-wave image presents the three main structures of the phantom. However, Fig. VI.3c, d shows SPC restored images in two time gates that do not have exactly the same structure, as the lifetimes of the three fluorophores involved are not the same. In a late gate, the circle shape is almost not present anymore, compared to an early gate. The time curves of Fig. VI.4 confirm the differences in the lifetimes, with a much faster exponential decay for the circle compared to the other two structures. Once the fit of Equation (VI.8) is complete, the precise lifetimes for the three components can be measured with the data

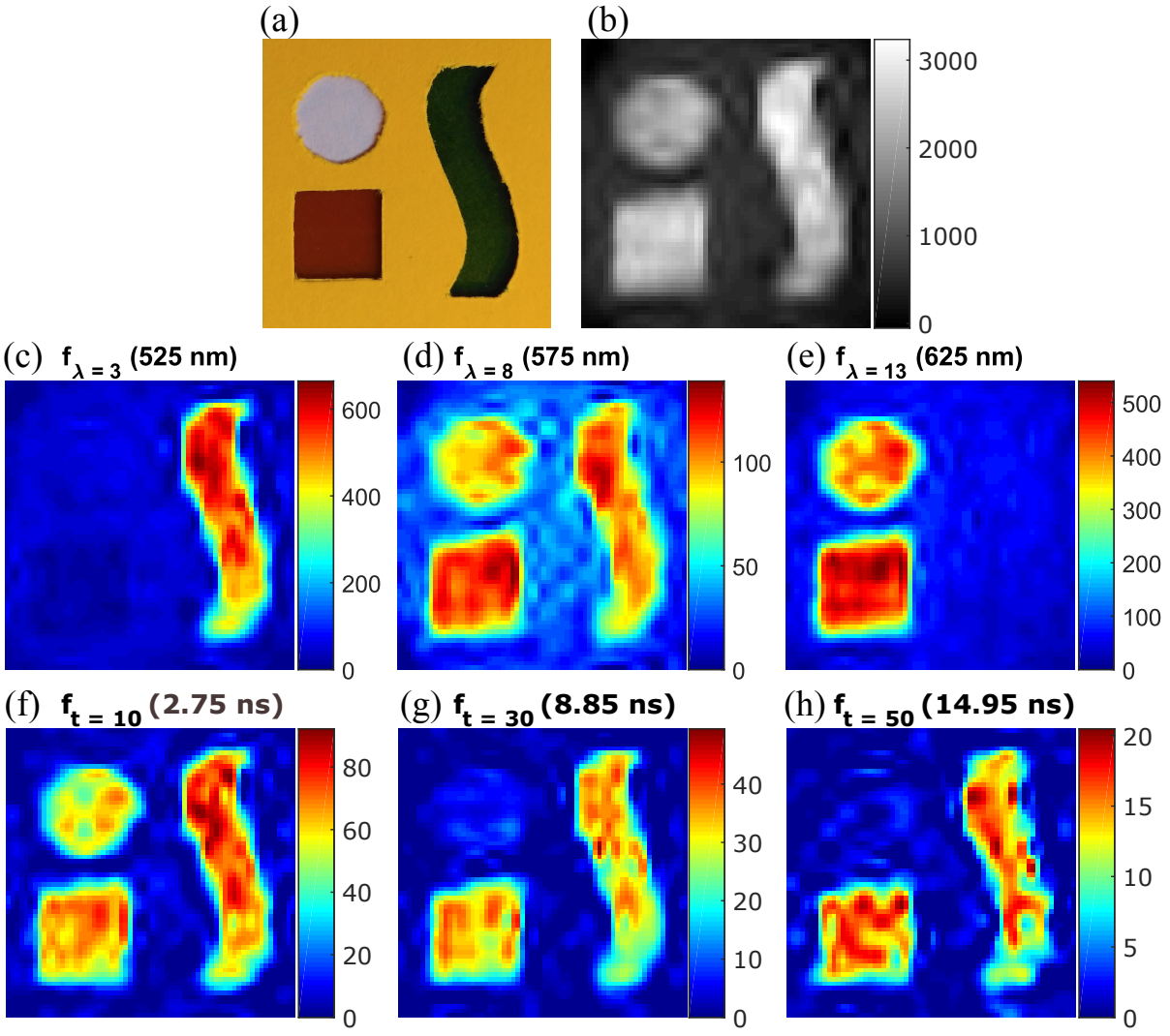

FIGURE VI.6 – Phantom, continuous-wave image and single-pixel camera restored images in different time and spectral channels using the Daubechies wavelet (Db5). (a) Photograph of the phantom. (b) Continuous-wave image. (c-h) Single-pixel camera restored images in three spectral channels (c-e) and three time channels (f-h).

from Fig. VI.5. The DCM dye can therefore be discriminated from the other two components using the time information alone.

Moving on to the capabilities of this system, the temporal resolution of the imaging set-up is mainly affected by the TCSPC board and detector, which is always better than what can be achieved with an array of detectors. As only one board is needed in a SPC design, this provides the choice of high-end boards, depending on the desired application. In our system, if the total time-window width is strongly reduced, a temporal resolution of tens of picoseconds can be reached, which is relatively good. The spatial resolution is provided by the SLM pattern size and the optics used, which allow for a wide range of possibilities, with the newest DMDs reaching pattern sizes of up to 1600×2560 pixels. A pixel pitch of about 500 μm was measured in this set-up. Consequently, the use of a SPC with a TCSPC board opens the possibility for a system with both high temporal and spatial resolution. The use of an *adaptive* technique such as ABS-WP provides for fast acquisition with few measurements,

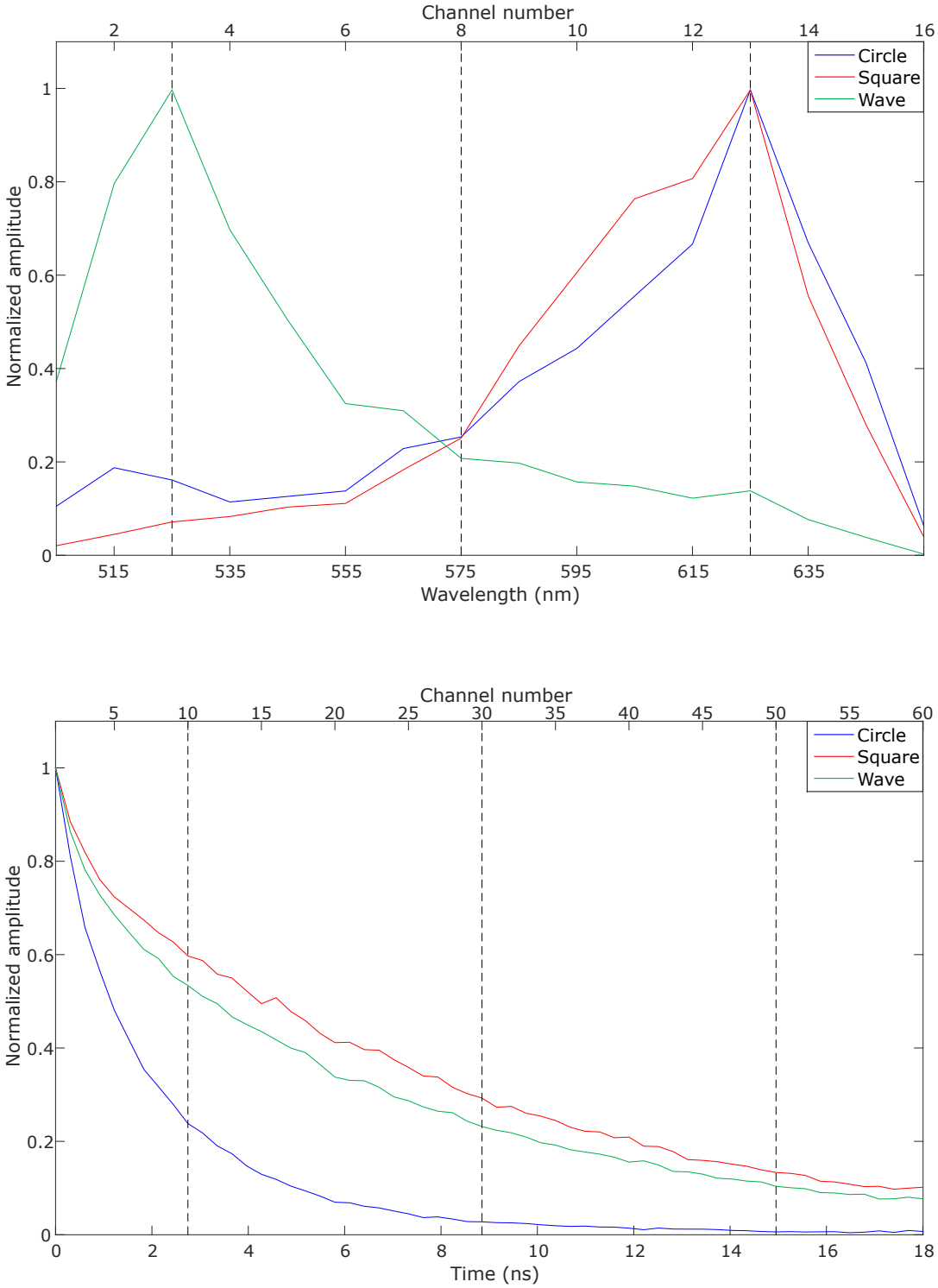

FIGURE VI.7 – Spectrum and time curves obtained from the restored images $\mathbf{f}_\lambda$ and $\mathbf{f}_t$ by summing the pixels in each area of the sample for each wavelength/ time channel. The dotted black vertical bars correspond to the time/ wavelength channels for the images shown in Fig. VI.6.

and straightforward image restoration. The use of the conventional *nonadaptive* compressive sensing approach would in the time-resolved case where T images have to be restored, suffer from long image restoration times, especially for high-resolution images.

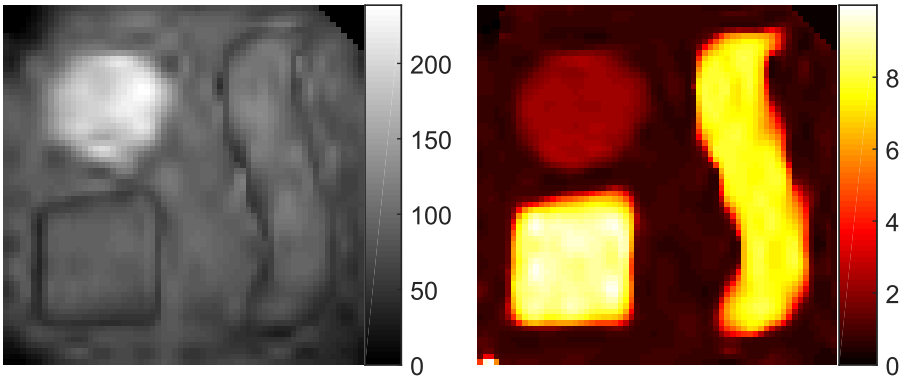

FIGURE VI.8 – Amplitude (arbitrary units, left) and lifetime (ns, right) maps obtained from $\mathbf{f}_t$ by fitting the experimental time curves for each pixel to an exponential decay function.

Overall, our ABS-WP framework coupled to the low-cost aspect of the time-resolved SPC makes it an efficient candidate for fluorescence lifetime imaging microscopy. The implementation of a SPC on a microscope using random compressive sensing (Rodriguez *et al.*, 2016) or Hadamard patterns (Radwell *et al.*, 2014) has indeed already been shown.

In conclusion, our adaptive wavelet-based acquisition strategy applied to a time-resolved single-pixel imaging system is demonstrated. The proposed system allows for efficient acquisition of time-resolved images with high compression rates and little degradation of the image quality. A possible application in the biomedical field is fluorescence lifetime imaging microscopy.

A limitation of the time-resolved set-up relates to the discrimination of objects with the same lifetime. As shown by the data in Fig. VI.3 and Fig. VI.5, the square and wave shapes have almost the same lifetime, and hence cannot be differentiated from each other. In addition to their lifetime, fluorophores emit light at different wavelengths. In the next section, a spectrometer is therefore added to the system to use both spectral and temporal information to discern the three chemical components.

VI.5.2 Multispectral time-resolved acquisitions

The data in Fig. VI.6 show that our ABS-WP framework allows the recovery of the stack of $\Lambda \times T$ images in the Λ spectral channels and T time channels with a compression rate as high as 93%. The use of the continuous-wave image of Fig. VI.6b is justified for the prediction step of ABS-WP, as it presents the different structures of the phantom. As a result, our strategy finds significant wavelet coefficients for each shape, and they are therefore accurately recovered.

If we look at the spectral dependent image $\mathbf{f}_\lambda$ of Fig. VI.6, only the wave stands out for the 525-nm wavelength channel, but disappears after the 625-nm wavelength channel. This is the other way around for the square and circle shapes. This was expected from the characterization given in table VI.1, for which the emission peak of the wave fluorophore is at 525 nm, and at around 625 nm for the other two fluorophores. The detailed spectral curves of Fig. VI.7 confirm these results and are in agreement with the characterization of the phantom in table VI.1.

For the time information using the temporal dependent images $\mathbf{f}_t$, similar measurements to those acquired in Section VI.4.1 are obtained without any surprises. The circle has a shorter lifetime compared to the square and the wave, as shown by Fig. VI.7 and the lifetime map of Fig. VI.8. While the latter is essentially the same as that obtained in Fig. VI.5 with the time-resolved system, the amplitude is slightly different, as it shows different numbers of counts. This is simply because the laser power on the days of these experiments and the experiments carried out previously (with the time-resolved system only) was set to a different value. The lifetimes, however, do not depend on the intensity of the laser, and do not change from one experiment to the other.

The addition of the spectral information compared to the results of Section VI.4.1 has a great impact. With the temporal information only, it is not possible to discriminate between the square shape and the wave. With the spectral information, the three fluorophores involved in the phantom can be completely differentiated using both spectral and temporal information. Overall, time-resolved spectral information can provide a way to better discriminate different fluorophores when spectral (or temporal) discrimination is not possible. This can be an important feature in biology to discriminate between different structures in tissues.

Moving on to the capability of this system, a discussion on the spectral side is given, as the temporal and spatial resolution have been discussed in Section VI.5.1. The spectral resolution of the system is given by the spectrometer used (slit and grating mostly). The SPC can therefore be used to produce images with high spectral resolution at much lower cost than standard imaging devices with arrays of sensors. A single-point spectrometer can indeed provide nanometer resolution for some thousands of euros, where conventional imaging systems with similar resolution would be about 10 times more expensive. The same can be obtained for a single detector with a scan (i.e., rotation) of the grating. However, SPC has the advantages of directly recovering spatial information (without scanning), and there is the possibility to cover a wider spectral range (e.g., infrared).

Overall, SPC acquisition represents a good trade-off between spatial, temporal, and spectral resolution that currently has no equivalent at the same price. The use of an *adaptive* strategy such as ABS-WP in this context is motivated by the speed of acquisition (i.e., high compression rates) and fast image recovery, which is crucial when a stack of $\Lambda \times T$ images needs to be recovered. ABS-WP is shown to perform multispectral time-resolved imaging with high compression rates on a phantom with the use of several fluorophores.

VI.6 Conclusion

In this Chapter, the applicability of ABS-WP proposed in Chapter IV is demonstrated on a (multispectral) time-resolved imaging system. Unfortunately, at the time of these experiments, the pattern generalization technique proposed in Chapter V was not yet implemented for testing. Experiments were performed on a phantom with fluorophores that emit light at different wavelengths and have different lifetimes. With high compression rates, our ABS-WP framework allows both spectral and temporal information to be recovered, such that complete discrimination of the fluorophores

can be obtained.

This is a first step toward medical applications, as a multispectral time-resolved imaging system can be exploited to characterize biological tissues. For instance, the biological micro-environment (e.g., pH, temperature, ion concentration) of a tissue (Marcu, 2012; Ma *et al.*, 2015) can be studied, which is an essential parameter for biologists.

Overall, a SPC is an excellent candidate to create multispectral (or hyperspectral) time-resolved systems at low cost. The single-point detector indeed provides the choice for high-quality photon counting boards (resp. spectrometers) with high temporal (resp. spectral) resolution. A SPC represents a fine trade-off between spatial, temporal, and spectral resolution that has currently no equivalent for the same price.

CONCLUSIONS, LIMITATIONS AND PERSPECTIVES

SINGLE-PIXEL IMAGING (SPI) captures the projection of the scene under view onto patterns with an optical set-up equipped with a single-point detector. This relatively low-cost simple implementation and the nonionizing aspect of optical imaging make SPI a good candidate for medical applications. Hence, the goal of this thesis was to investigate acquisition/ restoration schemes in SPI, and their application to biomedical imaging. One of the main limitations of a single-pixel camera is its relatively low speed of acquisition and/or image restoration. Real-time applications therefore cannot be considered, which rules out interventional imaging, for instance.

Our contributions here to improved speeds for acquisition and/or image restoration are three-fold :

— a complete framework to control the instruments, and data processing in an *adaptive* approach (Chapter III) ;

— the *adaptive basis scan by wavelet prediction* (ABS-WP) technique, which paves the way for the use of other wavelets than that of Haar, and reduces image restoration times compared to compressive-sensing-based techniques (Chapter IV) ;

— the pattern generalization method, which halves the number of measurements compared to conventional acquisition (Chapter V).

Overall, with ABS-WP implemented with the first contribution, this reduces image restoration times to less than a second (vs seconds to minutes for compressive sensing), while the pattern generalization algorithm allows the reduction of the acquisition times (i.e., halved).

As proof of concept for medical applications, Chapter VI finally presents multispectral time-resolved measurements on a phantom with the previous contributions. With compression rates as high as 93%, ABS-WP recovers both spectral and time information, to completely discriminate the fluorophores involved.

Limitations A first limitation of the contributions of this thesis regards the prediction of the significant wavelet coefficients in our ABS-WP framework. As depicted by the results given in table IV.3, our technique finds the correct significant wavelet coefficients with a maximum accuracy of 85%. If this accuracy can reach 100%, the best possible SPC image would be acquired, as the nonlinear approximation of the wavelet transform is one of the strongest possible approximations [2].

2. Strongest possible approximation in comparison to a nonlinear approximation in Fourier, discrete cosine transform, or any other basis.

ABS-WP allows the use of any kind of wavelet for which patterns have real floating values. The digital micromirror device (DMD) is thus used in its 8-bit mode to load such patterns, which is a second limitation, as the DMD refresh rate is affected. The DMD can indeed reach its highest frame rate when used in binary mode, but this frame rate is reduced when 8 bits are necessary, which results in increased acquisition times. In our experiments, this was not a problem as the acquisitions of the TCSPC board need a few hundreds of milliseconds, and the DMD frequency is 290 Hz in 8-bit mode. If fast acquisitions are required, this strategy can still be used with the Haar wavelet, as this creates binary patterns.

For pattern generalization, a limitation is the combination of several measurements, compared to the classical splitting or shifting methods that combine only two measures. In the presence of noise, the variance of the final desired measurement vector for the semi-nonnegative matrix factorization (SNMF) algorithm depends on the sum of the variances of the SPC-acquired measurements. If the measures are particularly noisy, this can increase the effects of noise, and hence reduce the quality of the recovered image. Such an effect is less visible for the classical splitting and shifting techniques with only two combinations.

While the proposed SNMF algorithm reduces the number of effective measurements, and thus the acquisition times, a final limitation arises because the positive patterns are computed on the fly for adaptive measurements. The data in Table V.1 show that as the dimensions of the problem increase, the computation times also increase. No acquisitions can be performed during this factorization, and this therefore increases the total acquisition time (acquisition + computation time) in an adaptive strategy. If a nonadaptive scheme is considered, this is not a limitation, as the set of positive patterns can be computed once and for all.

Perspectives A first perspective of this thesis is an improvement in the prediction strategy in ABS-WP. As mentioned earlier, some significant wavelet coefficients are not acquired, which impacts on the quality of the restored image. More robust methods for this prediction compared to those using bicubic interpolation can be considered. This prediction, however, should be fast enough not to slow down the total acquisition time, and so only fast techniques should be considered. One idea would be to use deep-learning techniques to predict either the value of the coefficients or their relevance. Such an approach would be fast, because the training part of a neural network can be done *a-priori* on a database of hundreds of images. Then the application of the network on the new data is relatively fast.

Another perspective relates to the proposed pattern generalization problem. This allows the creation of K positive patterns from a set of I patterns with positive and negative values. Using the proposed SNMF algorithm, this currently obtains $K = I + 1$. Most matrix factorization algorithms, however, search for factorization for which $K < I$. Such techniques can therefore be investigated to lower the number of effective measurements. A possible problem would be that the factorization error would be more important, which might lead to flawed measurements. Having $K < I$ would also allow the combination of fewer measurements, to lower the noise of the desired measurements. Another possibility to deal with the noise effect in the SNMF algorithm would be to add sparsity constraints to the matrix $\mathbf{T}$. If this matrix has zeros, the desired measurement vector would indeed be created from less combinations of measurements. A problem is that the rows of $\mathbf{T}$ should still add

up to 0, and adding the sparsity constraints might require the value of K to be increased.

For the multispectral time-resolved acquisitions of Chapter VI, the prediction step of our ABS-WP framework was based on continuous-wave measurements, which integrates all of the spectral and time channels. However, some of these channels do not receive much information, and hence do not bring much information in the continuous-wave measurements. To maximize the accuracy of the prediction in ABS-WP, another step can be added just before the prediction. This can search for the spectral and time channels that contain the least information, to discard them in the integration step of the channels, to create the continuous-wave measure [3].

On the application side, the next step is to apply the developed tools to interventional imaging; e.g, image-guided surgery. This is a completely new study in itself, as the tools developed in this thesis would have to be adapted to video imaging. Exploiting time information with some of the previous perspectives might allow for the achievement of much higher compression rates (i.e., fewer measurements acquired), so as to reach video rates.

3. By definition, if some channels are discarded, these would not exactly be continuous-wave measurements.

APPENDIX A

DMD IN b-BIT MODE

We note $\mathbf{p} \in \mathbb{R}^{D\times 1}$ the vector representing a DMD pattern and assume it is coded on b bits, i.e., each entry of $\mathbf{p}$ is an integer in $\{0,1,\ldots,2^b-1\}$. Such a pattern can be decomposed as a weighted sum of b different binary patterns noted $\mathbf{b}_i \in \mathbb{R}^{D\times 1}$, with $i = 1\ldots b$, which are referred to as the bit planes of $\mathbf{p}$. Mathematically we have

$$\mathbf{p} = \sum_{i=1}^{b} 2^{i-1}\mathbf{b}_i. \tag{A.1}$$

Note that each bit plane is associated to a weight that is a power of 2, e.g., the first bit plane $\mathbf{b}_1$ correspond to $2^0 = 1$.

Let us take an example for $b = 4$ and the pattern given in Fig. A.1 where each pixel codes a unique integer value in $\{0,1,\ldots,15\}$, hence the obtained pattern size is 4×4. The corresponding 4 bit planes are given in Fig. A.2.

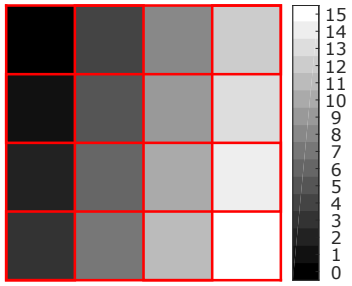

FIGURE A.1 – Considered pattern coded on $b = 4$ bits with each pixel having a unique integer value in the range $[0,15]$. The top left corner pixel has the value 0 while the bottom right one has the value 15. In between, the other pixels pave the remaining pixel values.

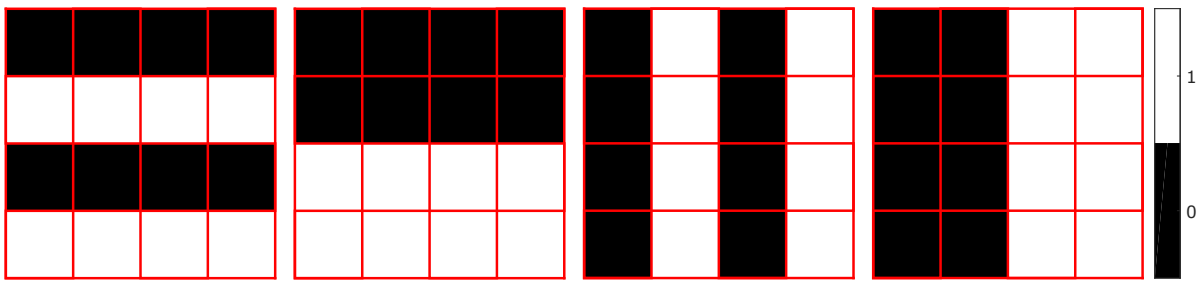

FIGURE A.2 – The four bit planes of the pattern displayed in Fig. A.1. From left to right, bit planes $\mathbf{b}_0$ to $\mathbf{b}_3$.

For example, the pixel at top right corner of $\mathbf{p}$ in Fig. A.1 corner has a value of 12. This value is coded on 4 bits as $0\times 2^0+0\times 2^1+1\times 2^2+1\times 2^3$ hence the same pixel has the value 0 (resp. 1) in $\mathbf{b}_0$ and $\mathbf{b}_1$ (resp. $\mathbf{b}_2$ and $\mathbf{b}_3$) in Fig. A.2.

At this stage, the DMD can work with the binary patterns $\mathbf{b}_i$ with the 0 (resp. 1) corresponding to the OFF (resp. ON) sate of the DMD. To recreate a pattern on b-bits, the power of 2 of (A.1) are divided by 2^b-1 so as to give the weights

$$w_i=\frac{2^{i-1}}{2^b-1} \quad \text{with} \quad \sum_{i=1}^{b} w_i = 1. \tag{A.2}$$

These weights can be encoded as the display time of each bit plane $\mathbf{b}_i$ in order to recreate the pattern of (A.1) [1]. For instance, if the DMD's frame rate is set to f in Hz, then the total display time of a b-bit plane is $t_d=1/f$ and each bit plane is allocated a display time of $t_i=w_i\,t_d$ to form the b-bit pattern. For instance, in our previous example, we have the display times t_i given in Fig. A.3.

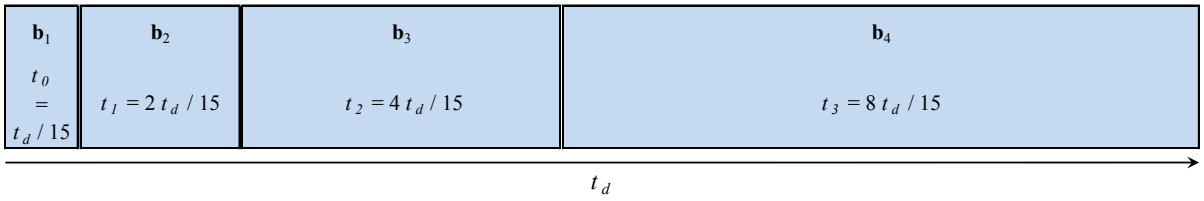

FIGURE A.3 – Display time of the four bit planes to recreate a four bit pattern.

Note that in the DMD employed in the experimental acquisitions of this thesis, the ALP library provided with the DMD manages itself the splitting of the b-bits patterns on its bit planes and associates automatically the display time. Only the DMD's frame rate is chosen which corresponds to the frequency at which a new pattern can be loaded.

1. Up to the scalar factor $\frac{1}{2^b-1}$.

APPENDIX B

COMPLEMENTS TO CHAPTER V

Below are some complements of Chapter V leading to the final matrix $\mathbf{T}$ and $\mathbf{P}$ employed in the SNMF algorithm. For the matrix and vector derivatives used below, we refer the reader to the Matrix Cookbook Petersen *et al.* (2008).

B.1 Dual problem to solve for T

As a reminder of what was exposed in Chapter V, the problem to solve to find the solution for $\mathbf{T}$ is the following :

$$\min_{\mathbf{T}} \left\| \check{\mathbf{P}} - \mathbf{TP} \right\|_{\mathrm{F}}^2 \quad \text{such that} \quad \mathbf{T}\mathbf{1}_K = \mathbf{0}_I. \tag{B.1}$$

To solve the dual problem, we first write the Lagrange function $\mathcal{L}$:

$$\mathcal{L}(\mathbf{T}, \boldsymbol{\lambda}) = \left\| \check{\mathbf{P}} - \mathbf{TP} \right\|_{\mathrm{F}}^2 + \boldsymbol{\lambda}^\top \mathbf{T}\mathbf{1}_K$$

$$\mathcal{L}(\mathbf{T}, \boldsymbol{\lambda}) = \mathrm{tr}\left(\left(\check{\mathbf{P}} - \mathbf{TP} \right) \left(\check{\mathbf{P}} - \mathbf{TP} \right)^\top \right) + \boldsymbol{\lambda}^\top \mathbf{T}\mathbf{1}_K$$

$$= \mathrm{tr}\left(\mathbf{TPP}^\top \mathbf{T}^\top - \mathbf{TP}\check{\mathbf{P}}^\top - \check{\mathbf{P}}\mathbf{P}^\top \mathbf{T}^\top + \check{\mathbf{P}}\check{\mathbf{P}}^\top \right) + \boldsymbol{\lambda}^\top \mathbf{T}\mathbf{1}_K \tag{B.2}$$

where $\boldsymbol{\lambda} = (\lambda_1, ..., \lambda_I)^\top \in \mathbb{R}^{I \times 1}$ are the Lagrange multipliers. We now write the dual function $\mathcal{D}$:

$$\mathcal{D}(\boldsymbol{\lambda}) = \min_{\mathbf{T}} \mathcal{L}(\mathbf{T}, \boldsymbol{\lambda}) = \mathcal{L}(\mathbf{T}(\boldsymbol{\lambda}), \boldsymbol{\lambda})$$

with $\mathbf{T}(\boldsymbol{\lambda}) = \arg\min_{\mathbf{T}} \mathcal{L}(\mathbf{T}, \boldsymbol{\lambda})$ for $\boldsymbol{\lambda}$ fixed. If the dual function $\mathcal{D}$ is differentiable, then $\mathbf{T}(\boldsymbol{\lambda}^*) = \mathbf{T}$, if $\boldsymbol{\lambda}^* = \arg\max_{\boldsymbol{\lambda}} \mathcal{D}(\boldsymbol{\lambda})$ is the solution of the primal problem (V.19).

First, we search $\mathbf{T}(\boldsymbol{\lambda}) = \arg\min_{\mathbf{T}} \mathcal{L}(\mathbf{T}, \boldsymbol{\lambda})$ by expressing the derivative of $\mathcal{L}$, using (B.2) :

$$\frac{\partial \mathcal{L}(\mathbf{T}, \boldsymbol{\lambda})}{\partial \mathbf{T}} = 2\mathbf{TPP}^\top - 2\check{\mathbf{P}}\mathbf{P}^\top + \boldsymbol{\lambda}\mathbf{1}_K{}^\top \tag{B.3}$$

$\mathbf{T}(\boldsymbol{\lambda})$ is found when (B.3) is null. This gives

$$\mathbf{T}(\boldsymbol{\lambda}) = \left(\check{\mathbf{P}}\mathbf{P}^\top - \frac{1}{2}\boldsymbol{\lambda}\mathbf{1}_K{}^\top \right) \left(\mathbf{PP}^\top \right)^{-1} \tag{B.4}$$

We now use (B.4) in the equality constraint (V.13) to get the optimal Lagrange multipliers $\boldsymbol{\lambda}^*$:

$$\mathbf{T}(\boldsymbol{\lambda}^*)\mathbf{1}_K = \mathbf{0} \Rightarrow \left(\check{\mathbf{P}}\mathbf{P}^\top - \frac{1}{2}\boldsymbol{\lambda}^*\mathbf{1}_K{}^\top \right) \left(\mathbf{PP}^\top \right)^{-1} \mathbf{1}_K = \mathbf{0}$$

leading to

$$\boldsymbol{\lambda}^* = \frac{2}{\mathbf{1}_K{}^\top \left(\mathbf{P}\mathbf{P}^\top\right)^{-1} \mathbf{1}_K} \check{\mathbf{P}}\mathbf{P}^\top \left(\mathbf{P}\mathbf{P}^\top\right)^{-1} \mathbf{1}_K \tag{B.5}$$

Finally, one can get the final expression of $\mathbf{T}$ solving the problem (V.19) by replacing (B.5) in (B.4) :

$$\mathbf{T} = \check{\mathbf{P}}\mathbf{P}^\top \left(\mathbf{P}\mathbf{P}^\top\right)^{-1} \left(\mathbf{I} - \frac{1}{\mathbf{1}_K{}^\top \left(\mathbf{P}\mathbf{P}^\top\right)^{-1} \mathbf{1}_K} \mathbf{1}_{K\times K} \left(\mathbf{P}\mathbf{P}^\top\right)^{-1} \right) \tag{B.6}$$

where $\mathbf{I}$ is the identity matrix of size $K \times K$ and $\mathbf{1}_{K\times K} = \mathbf{1}_K \mathbf{1}_K{}^\top$ is the matrix of size $K \times K$ with all entries equal to one.

B.2 Block coordinate descent for P

This time, $\mathbf{T}$ is considered fixed and the problem to solve is

$$\min_{\mathbf{p}_k} \mathcal{F}(\mathbf{P}_{-k}, \mathbf{p}_k) \quad \text{such that} \quad \mathbf{p}_k \geq 0 \tag{B.7}$$

with

$$\mathcal{F}(\mathbf{P}_{-k}, \mathbf{p}_k) = \left\| \check{\mathbf{P}} - \mathbf{T}_{|k}\mathbf{P}_{-k} - \mathbf{t}_k \mathbf{p}_k^\top \right\|_{\mathrm{F}}^2 = \left\| \boldsymbol{\Sigma} - \mathbf{t}_k \mathbf{p}_k^\top \right\|_{\mathrm{F}}^2 \tag{B.8}$$

where $\boldsymbol{\Sigma} = \check{\mathbf{P}} - \mathbf{T}_{|k}\mathbf{P}_{-k}$, $\mathbf{T}_{|k}$ (resp. $\mathbf{P}_{-k}$) is the matrix $\mathbf{T}$ (resp. $\mathbf{P}$) deprived of its column (resp. row) k and $\mathbf{t}_k \in \mathbb{R}^{I\times 1}$ (resp. $\mathbf{p}_k \in \mathbb{R}^{D\times 1}$) is the k-th column (resp. row) of $\mathbf{T}$ (resp. $\mathbf{P}$).
Let us rewrite $\mathcal{F}(\mathbf{P}_{-k}, \mathbf{p}_k)$ as

$$\left\| \boldsymbol{\Sigma} - \mathbf{t}_k \mathbf{p}_k^\top \right\|_{\mathrm{F}}^2 = \mathrm{tr}\left(\left(\boldsymbol{\Sigma} - \mathbf{t}_k \mathbf{p}_k^\top\right) \left(\boldsymbol{\Sigma} - \mathbf{t}_k \mathbf{p}_k^\top\right)^\top \right)$$

for which we now take its derivative with respect to $\mathbf{p}_k$:

$$\frac{\partial \mathcal{F}(\mathbf{P}_{-k}, \mathbf{p}_k)}{\partial \mathbf{p}_k} = 2\mathbf{p}_k \mathbf{t}_k{}^\top \mathbf{t}_k - 2\boldsymbol{\Sigma}^\top \mathbf{t}_k = 2\left(\mathbf{p}_k \|\mathbf{t}_k\|_2^2 - \boldsymbol{\Sigma}^\top \mathbf{t}_k\right). \tag{B.9}$$

The minimum of (B.7) is found when (B.9) is null and adding the projection operation onto the feasible set $\mathbb{R}_+^{D\times 1}$ leads to the solution

$$\mathbf{p}_k = \max\left(\mathbf{0}_D, \frac{\boldsymbol{\Sigma}^\top \mathbf{t}_k}{\|\mathbf{t}_k\|_2^2} \right) \tag{B.10}$$

with the max function applied to each entry of both vectors.

APPENDIX C

RÉSUMÉ ÉTENDU EN FRANÇAIS

Table des matières

Introduction

La caméra mono-pixel (*single-pixel camera*, SPC) est un dispositif émergent permettant l'acquisition d'images à bas coût. En effet, l'architecture de cette caméra comporte seulement deux éléments, un modulateur spatial de la lumière (*spatial light modulator*, SLM) et un détecteur ponctuel (*single point detecteur*, SPD). L'idée est de moduler la scène à imager avec des motifs chargés au niveau du SLM et la mesure correspondante est obtenue par le détecteur ponctuel. Le post-traitement d'une séquence de mesures obtenue pour différent motifs permet de restaurer l'image de la scène observée.

Les premières images par une SPC ont été obtenues à l'Université de Rice en 2006. A l'époque, les idées pionnières de l'acquisition comprimée (*compressive sensing*, CS) proposées par Donoho ont rendu possible l'utilisation de motifs aléatoires et la restauration d'images par minimisation ℓ_1 pour la SPC par Takhar *et al.*. Depuis, de nouvelles stratégies d'acquisitions ont été proposées et la SPC a trouvé de nombreuses applications.

A première vue, avoir un seul pixel peut sembler contre-productif puisque la plupart des caméras actuelles contiennent des millions de pixels acquis simultanément. Cependant, plusieurs avantages ressortent quand la SPC est comparée avec les architectures de caméras CCD ou CMOS. Tout d'abord, les détecteurs ponctuels ont souvent un haut rendement si bien qu'ils sont capables de détecter de très faibles changement d'intensité lumineuse (Hadfield, 2009). Pour des applications médicales, ceci peut être très utile puisque l'absorption des tissus est bien souvent élevée (Jacques, 2013). Le second avantage est la compression réalisée au niveau matériel (i.e. un détecteur donc une donnée), peu de mémoire de stockage est ainsi nécessaire. Ceci est un point clé pour des applications comme l'imagerie à distance (e.g. télédétection aérospatiale) où le taux de transmission des données est relativement faible (Ma, 2009b,a). Enfin, un détecteur ponctuel est généralement moins couteux qu'une matrice de capteurs. La SPC devient alors un candidat parfait pour l'imagerie infrarouge (Shin *et al.*, 2016) pour laquelle un imageur conventionnel fonctionnant à ces longueurs d'ondes serait onéreux (Rogalski, 2012).

Tous ces avantages et la nature non-ionisante de l'imagerie optique rendent la SPC très attrayante pour des applications en imagerie médicale. Par exemple, un système résolu en temps à bas coût est bénéfique pour l'imagerie du temps de vie de fluorescence (Becker, 2012) en couplant le détecteur à une carte de comptage des photons (Pian *et al.*, 2016a; Rousset *et al.*, 2017b). L'ajout d'un spectromètre (Pian *et al.*, 2016b) permet d'obtenir une information spectrale supplémentaire pour étudier le micro-environnement (pH par exmple) des tissus biologiques. D'autres applications dans le domaine médical sont possibles parmi lesquelles l'imagerie à travers des milieux diffusants (Tajahuerce *et al.*, 2014; Duran *et al.*, 2015), l'imagerie optique diffuse (e.g. intra-opératoire ou la détection des lésions de la peau (Gibson *et* Dehghani, 2009)), l'ophtalmologie (Lochocki *et al.*, 2016, 2017), la tomographie optique diffuse (D'Andrea *et al.*, 2010; Ducros *et al.*, 2013; Pian *et al.*, 2015; Ducros *et al.*, 2016) (e.g. oximétrie et imagerie moléculaire), ou encore la caractérisation des propriétés des tissus par illumination infrarouge (Torabzadeh *et al.*, 2017).

Le but de cette thèse est l'étude de techniques pour l'acquisitions d'images SPC à visée médicale. Une des principales limitations de ce système optique dans les travaux cités précédemment est la durée de l'acquisition et/ou de la restauration d'images. Dans ces cas, des applications en temps réel ne peuvent être considérées, excluant ainsi l'imagerie interventionnelle par exemple. Il est alors souhaitable d'avoir des techniques plus rapides pour l'acquisition et/ou la restauration par SPC pour l'imagerie médicale.

Pour parvenir à ces objectifs, nous avons proposé une nouvelle stratégie d'acquisition SPC pour réduire le temps de restauration ainsi qu'une technique innovante pour réduire les temps d'acquisitions d'un autre côté. L'applicabilité de ces méthodes pour l'imagerie biomédicale a été démontrée par des mesures multispectrales résolues en temps.

Ce travail a été réalisé dans le cadre d'une cotutelle entre l'INSA de Lyon et le Politecnico di Milano. Les parties expérimentales de cette thèse ont été réalisées à Milan où une SPC est disponible. Les méthodes et algorithmes ont quant à eux été développés au sein du laboratoire CREATIS.

Ce manuscrit de thèse est divisé en six chapitres. Les deux premiers donnent l'état de l'art de la SPC alors que les quatre suivants répondent à la problématique de cette thèse avec ses différentes contributions.

Au Chaptitre I, le concept de la SPC et son implémentation matérielle sont présentés.

Au Chaptitre II, l'état de l'art concernant l'implémentation logicielle de la SPC est cette fois ci détaillée. Deux grandes catégories de techniques existent séparant les approches *non-adaptatives* des approches *adaptatives*.

Au Chaptitre III, les deux systèmes expérimentaux ayant servis à la validation expérimentale des algorithmes développés sont présentés. Le premier système est celui existant au Politecnico de Milan et le second est celui récemment monté au laboratoire CREATIS.

Au Chaptitre IV, notre stratégie d'acquisition *Adaptive Basis Scan by Wavelet Prediction* (ABS-WP) est expliquée. Cette méthode permet d'acquérir une image directement dans le domaine d'ondelettes et compare favorablement par rapport à d'autres méthodes d'acquisitions d'images par SPC. Ce chapitre contient principalement un article de revue publié dans *IEEE Transactions on Computational Imaging* en 2017 (Rousset *et al.*, 2017a).

Au Chaptitre V, une méthode pour diviser par deux le nombre de mesures est proposé. Cette méthode a été inventée pour contourner le fait que des motifs ayant à la fois des valeurs positives et négatives ne peuvent être mis en œuvre sur un SLM. Nous proposons dans ce chapitre une solution générale au problème qui peut être solutionnée par un algorithme de factorisation en matrices semi non-négatives. Les résultats de ce chapitre ont été déposés sous forme de brevet (Rousset *et al.*, 2017c) et soumis à *IEEE Transactions on Image Processing* (Rousset *et al.*, 2017d).

Au Chaptitre VI, la SPC avec les techniques des chapitres précédents est employée pour des applications susceptibles d'être bénéfiques pour l'imagerie médicale. Une dimension temporelle et spectrale est ajoutée à la SPC afin d'obtenir des mesures multispectrales résolues en temps. Ceci permet d'imager un fantôme avec différents fluorophores afin d'en déduire leurs caractéristiques. Une partie de ces résultats ont été présentés à la conférence *SPIE Photonics West* (Rousset *et al.*, 2017b) en Février 2017.

C.1 CHAPITRE I - IMAGERIE MONO-PIXEL

Sous le nom imagerie mono-pixel se cachent différentes mises en œuvre optiques possibles pour lesquelles existent plusieurs stratégies d'acquisitions/restaurations. Ce chapitre donne le concept de la SPC puis regroupe la plupart de ses configurations matérielles existantes.

C.1.1 Concept

La théorie et les résultats de Donoho en 2006 sur l'acquisition comprimée (*compressive sensing*, CS) ont montré qu'un signal peut être restauré à partir d'un faible nombre de projections. Ceci a permis à Takhar *et al.* de proposer la même année une nouvelle architecture de caméra basée sur un simple détecteur ponctuel afin de produire un système d'imagerie compressive (Duarte *et al.*, 2008; Baraniuk *et al.*, 2014; Miao *et* Amirparviz, 2015).

Un tel système mesure une donnée 1D au lieu d'une information classique 2D obtenue par une matrice de capteurs conventionnelle (e.g. cameras CCD ou CMOS). Un modulateur spatial de la lumière (*spatial light modulator*, SLM) est placé entre la scène à imager et le détecteur ponctuel (i.e. pixel unique) de façon à moduler la lumière émanant de la scène et d'obtenir la projection correspondante au niveau du détecteur. Une séquence de mesures est prise avec différents motifs chargés sur le SLM qui, après post-traitement, permet de restaurer l'image de la scène. La mise en œuvre la

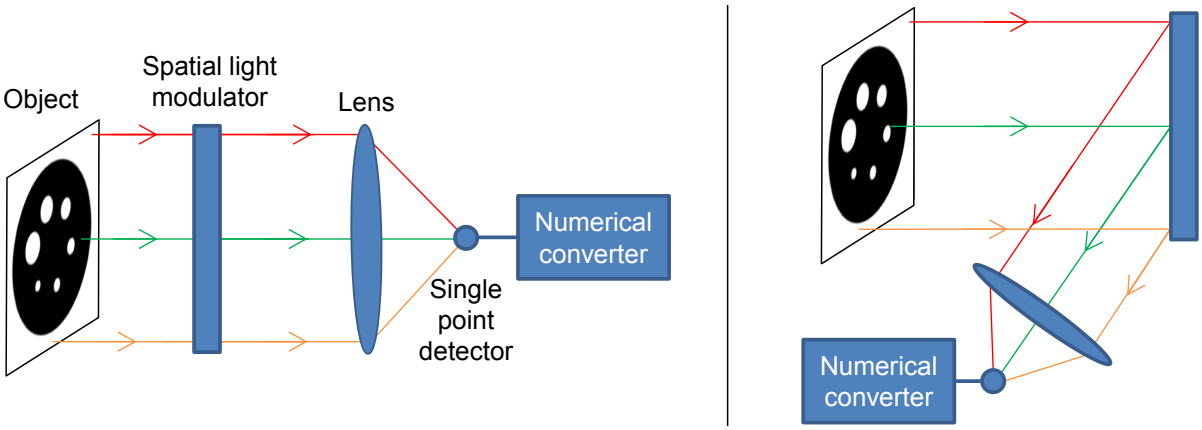

FIGURE C.1 – Montage optique d'une caméra mono-pixel en géométrie de transmission (gauche) ou de réflexion (droit).

plus simple d'une SPC peut être schématisée selon la Fig. C.1 où le SLM est soit un appareil réfléchissant, soit un système transmissif selon la technologie utilisée. L'image de l'objet est formée dans le plan du SLM et une lentille est ajoutée afin de concentrer les rayons lumineux modulés au niveau du détecteur ponctuel. Un convertisseur numérique est enfin utilisé afin d'obtenir des données scalaires à partir du détecteur. Il est à noter que l'objet et le SLM sont complètement interchangeables. Si le SLM est placé avant [1] l'objet, on dit que la lumière est modulée en illumination, si placé après, le côté détection est modulé.

1. Dans la direction de la lumière.

C.1.2 Configurations matérielles

A travers les années, plusieurs configurations matérielles de la SPC ont été proposées. Suivant l'application visée, une technologie spécifique devrait être choisie afin d'en tirer le meilleur. Cette section donne des exemples [2] de SLM et détecteurs ponctuels les plus employés ainsi que les différentes technologies pour obtenir des mesures numériques.

Modulateur spatial de la lumière Les travaux originels de Takhar *et al.* et Duarte *et al.* utilisent une matrice de micro-miroirs (*digital micromirror device*, DMD) inventée par Hornbeck à *Texas Instruments* en 1987. Ce dispositif comporte des milliers de petits miroirs arrangés sous forme de matrice de taille $H \times W$. Chacun de ces miroirs peut être indépendamment basculé dans deux positions. L'état ON à +12° réfléchit la lumière vers le détecteur qui est donc collectée. A −12°, l'état OFF envoie la lumière dans la direction opposée. Le DMD peut donc charger des motifs binaires pour lesquelles une valeur 0 (resp. 1) correspond à l'état OFF (resp. ON). Des motifs sur b-bits [3] peuvent également être chargés en utilisant le principe de modulation de largeur d'impulsion. Pour cela, un motif sur b-bits est décomposé en ses b motifs binaires (*bit planes*). A chacun d'eux est associé un certain temps de chargement sur le DMD, temps multiple d'une puissance de 2, ce qui permet de recréer un motif sur b-bits (voir Annexe A pour plus de détails).

En 2013, Huang *et al.* utilisent un écran à cristaux liquides (*liquid crystal display*, LCD) en tant que modulateur en géométrie de transmission [4]. Ce dispositif emploie des filtres polarisant et les propriétés d'orientation des cristaux liquides contrôlées par un courant électrique. Un état ON (resp. OFF) correspond ici à un élément transparent (resp. opaque) laissant passer (resp. bloquant) la lumière.

Contrairement aux précédents modulateurs d'intensité, un écran à cristaux liquides sur silicium (*liquid crystal on silicon*, LCoS) peut moduler la phase des rayons lumineux. Comme pour le LCD, un courant électrique contrôle les cristaux pour créer des motifs binaires. Ce dispositif est utilisé dans Clemente *et al.* (2013) pour faire de l'holographie compressée.

Détecteur ponctuel Une photodiode est classiquement employée dans la mise en œuvre de la SPC du fait de son prix généralement très bon marché. Elle est en effet simplement constituée d'un semiconducteur capable de recevoir des photons et de les convertir en courant électrique.

Un autre détecteur ponctuel souvent utilisé est le photomultiplicateur qui permet également la détection des photons et leur conversion en courant électrique. La différence est que les photons captés lâchent des électrons dont le nombre peut être multiplié par application d'un courant électrique.

Convertisseur numérique Le signal électrique donné par la photodiode ou photomultiplicateur peut être digitalisé par un convertisseur analogique numérique (CAN). La valeur échantillonnée est proportionnelle à l'amplitude de l'intensité ou tension appliquée au CAN.

2. Liste non-exhaustive.
3. Suivant les modèles, b peut varier de 4 à 12 bits.
4. Des LCD en réflexion existent aussi mais ne sont pas présentés ici car les performances des DMDs sont bien meilleures.

Certains détecteurs peuvent être couplés à une carte de comptage des photons (*time-correlated single photon counting*, TCSPC) employée en lien avec un laser pulsé illuminant l'objet. Un tel dispositif compte le nombre de photons et ceci pour différents canaux temporels suivant le temps de vol des photons grâce à la référence donnée par le laser pulsé. Dans ce cas, la mesure SPC n'est pas une simple donnée scalaire mais un vecteur de données scalaires pour chaque canal temporel.

C.1.3 Conclusion du chapitre

Ce chapitre a présenté les idées principales derrière la SPC et ses configurations matérielles possibles. Ces dernières peuvent prendre plusieurs formes, que ce soit en géométrie de transmission ou de réflexion. L'avantage principal de ce système est l'aspect bas coût du montage optique qui réalise une compression directement pendant l'acquisition.

Le côté matériel ayant été présenté dans ce chapitre, de nombreuses questions essentielles n'ont pas encore trouvé réponse : comment obtenir une image à partir de mesures sur un détecteur ponctuel? Quels sont les concepts et outils mathématiques derrière la SPC? Ces questions sont étudiées dans le prochain chapitre qui présente les différentes techniques d'acquisition et de restauration d'images par une SPC.

C.2 CHAPITRE II - TECHNIQUES D'ACQUISITION/RESTAURATION DES IMAGES

Contrairement à une matrice de capteurs type CCD ou CMOS où chaque pixel de l'image est acquis en parallèle, une acquisition SPC nécessite le traitement de plusieurs mesures afin de remonter à l'information spatiale de l'image. Différentes stratégies d'acquisition et de restauration des images par une SPC existent que l'on peut principalement séparer en deux catégories, les méthodes *non-adaptatives* et les méthodes *adaptatives*. Avant de détailler ces deux techniques, la modélisation mathématique d'une acquisition par une SPC est donnée.

C.2.1 Modélisation mathématique

On note N_0 (en photons par seconde, ph/s) la puissance émise par la source lumineuse et α (en ph/s) le courant d'obscurité mesuré au niveau du capteur quand $N_0 = 0$ ph/s. Soit $\mathbf{f} \in \mathbb{R}^{D\times 1}$ l'image $H \times W$ de la scène observée avec $D = H \times W$. La mesure m_k (ph) obtenue au niveau du détecteur durant le temps d'intégration Δt (en s) peut-être modélisée par

$$m_k = \Delta t \left(N_0 \mathbf{p}_k^\top \mathbf{f} + \alpha \right) \tag{C.1}$$

où $\mathbf{p}_k \in \mathbb{R}_+^{D\times 1}$ est un motif chargé sur le SLM. On note $\mathbf{P} = \left(\mathbf{p}_1, \ldots, \mathbf{p}_K\right)^\top \in \mathbb{R}_+^{K\times D}$ la matrice regroupant la séquence de K motifs à charger sur le SLM. Le vecteur de mesure $\mathbf{m} = (m_1, \ldots, m_K)^\top \in \mathbb{R}_+^{K\times 1}$ (ph) contient la séquence des K mesures correspondantes obtenues. Mathématiquement,

$$\mathbf{m} = \Delta t \left(N_0 \mathbf{P}\mathbf{f} + \alpha \mathbf{1}_K \right) \tag{C.2}$$

avec $\mathbf{1}_K = (1, \ldots, 1)^\top \in \mathbb{R}^{K\times 1}$.

Deux problèmes interviennent suite à l'écriture de ce modèle. Le premier concerne le choix de la séquence de motifs **P** alors que le second cherche à restaurer l'image **f** connaissant le vecteur de mesure **m** et les motifs **P**.

C.2.2 Implémentation logicielle

Méthodes non-adaptatives Les premières méthodes de type *non-adaptatives* reposent sur la théorie de l'acquisition comprimée (*compressive sensing*, CS) (Donoho, 2006). L'idée est que la plupart des signaux sont compressibles dans une certaine base et ils peuvent ainsi être obtenus à partir d'un faible nombre de projections, i.e. $K << D$ mesures SPC. Les premières mesures CS par une SPC ont été proposées par Takhar *et al.* in 2006. La séquence de motifs **P** est alors choisie en tant que motifs aléatoires dont les valeurs sont ± 1 ce qui est bien adapté à la technologie ON/OFF des DMD par exemple. L'étape de restauration des images fait ensuite intervenir un algorithme de minimisation de la norme ℓ_1 afin de remonter, à partir des mesures **m**, à l'image **f**. Sous certaines conditions, il est possible de montrer que l'image **f** peut être parfaitement restaurée. L'avantage de cette méthode est le faible nombre de mesures $K << D$. En revanche, l'étape de restauration est lourde en calculs et peut prendre plusieurs minutes pour des images hautes résolutions.

Une autre possibilité *non-adaptative* est l'acquisition complète d'une image dans une certaine base (Hadamard, Fourier, ondelettes, transformée en cosinus, etc.), on parle alors de *basis scan*. La séquence de motifs est alors choisie comme $\mathbf{P} = \mathbf{B} \in \mathbb{R}^{D\times D}$ où **B** représente l'opérateur de transformation dans la base choisie. L'image est alors restaurée de façon directe avec l'opérateur de transformée inverse $\mathbf{B}^{-1}$. Par exemple, si la base choisie est celle de Fourier, les coefficients de Fourier sont acquis par la SPC dans le vecteur **m** auquel est appliqué la transformée de Fourier inverse pour obtenir l'image **f** de l'objet. L'avantage de cette méthode est donc l'étape de restauration qui est extrêmement rapide puisqu'elle ne nécessite aucune optimisation par rapport à l'approche CS. En revanche $K = D$ mesures doivent être acquises ce qui est trop long en pratique.

En résumé, les méthodes *non-adaptatives* peuvent être schématisées selon la Fig. C.2. Le choix de la séquence de motif est la même quelle que soit l'image observée d'où le nom de ces approches.

FIGURE C.2 – Schématisation d'une méthode d'acquisition non-adaptative.

Méthodes adaptatives Les méthodes *adaptatives* réalisent l'acquisition de l'image en plusieurs itérations j avec $1 \leq j \leq J$. Les mesures à l'itération j sont basées sur l'étude des mesures effectuées à l'étape $j-1$ d'où le nom *adaptatif*. L'idée principale est que, dans la plupart des bases, une image est compressible, c'est-à-dire que seuls $K << D$ coefficients sont nécessaires afin de remonter à l'image. La difficulté est qu'avec une SPC, l'image n'est a priori pas connue et les K coefficients à acquérir ne sont donc pas connus. Un schéma itératif permet ainsi de procéder à une première série de mesure $\mathbf{m}^{(j)}$ avec un sous ensemble $\mathbf{B}^{(j)} \in \mathbb{R}^{K^{(j)}\times D}$ de la base $\mathbf{B} \in \mathbb{R}^{D\times D}$ avec $K^{(j)} << D$. Cette série de mesures $\mathbf{m}^{(j)}$ est traitée afin de *prédire* l'ensemble $\mathcal{I}^{(j+1)}$ des prochains $K^{(j+1)}$ coefficients à acquérir à l'itération $j+1$. Au final, J itérations sont effectuées afin d'obtenir $K = \sum_{j=1}^{J} K^{(j)}$ coefficients avec

$K << D$. L'image est alors restaurée en utilisant la transformée inverse $\mathbf{B}^{-1}$ de la base choisie comme dans le cas du *basis scan*. On parle ici d'*adaptive basis scan* qui tire avantage de la restauration rapide de l'image tout en effectuant que très peu de mesures. L'inconvénient est l'étape de prédiction qui doit être fiable pour prédire les bons coefficients significatifs dans la base $\mathbf{B}$ [5]. Cette étape doit également être rapide afin de ne pas perdre de temps lors de l'acquisition. La Fig. C.3 résume ce type d'approche.

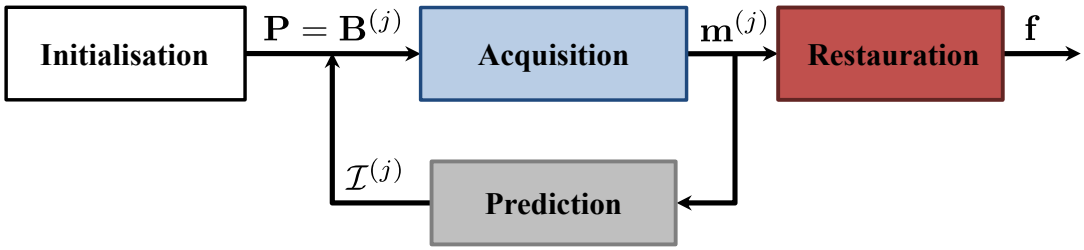

FIGURE C.3 – Schématisation d'une méthode d'acquisition adaptative.

C.2.3 Conclusion du chapitre

Nous avons vu dans ce chapitre les principales méthodes d'acquisition et de restauration des images par une caméra mono-pixel. Trois techniques principales existent qui sont résumées dans le tableau C.1.

Approche	Adaptatif?	Motifs	# de motifs K	Restauration de l'image
Acquisition comprimée (CS)	Non	Aléatoires	$K << D$	Minimisation ℓ_1
Basis Scan (BS)	Non	Ceux de la base	$K = D$	Transformée inverse
Adaptive Basis Scan (ABS)	Oui	Ceux de la base	$K << D$	Transformée inverse

TABLEAU C.1 – Comparaison des caractéristiques principales des techniques d'acquisition et restauration des images par une SPC.

En résumé, ABS est la méthode la plus favorable puisqu'elle nécessite peu de mesures K et la restauration des images par transformée inverse est extrêmement rapide. Ce sont pour ces raisons qu'une méthode *adaptative* est considérée dans le Chaptitre IV.

La fin de ce chapitre marque une rupture entre la bibliographie des caméras mono-pixel présentée jusqu'à ce chapitre et les chapitres suivants qui rapportent les contributions de ce travail de thèse. Avant de détailler la technique *adaptative* choisie, les systèmes expérimentaux sur lesquels sont réalisés des tests en conditions réelles sont présentés.

C.3 CHAPITRE III - SYSTÈMES EXPÉRIMENTAUX

Les acquisitions expérimentales sont essentielles à la conception de nouveaux algorithmes puisqu'elles permettent de valider et/ou d'ajuster les développements. Ce chapitre décrit deux systèmes expérimentaux sur lesquels ont été testées les méthodes développées dans les chapitres suivants.

5. Les K coefficients ayant la plus forte magnitude.

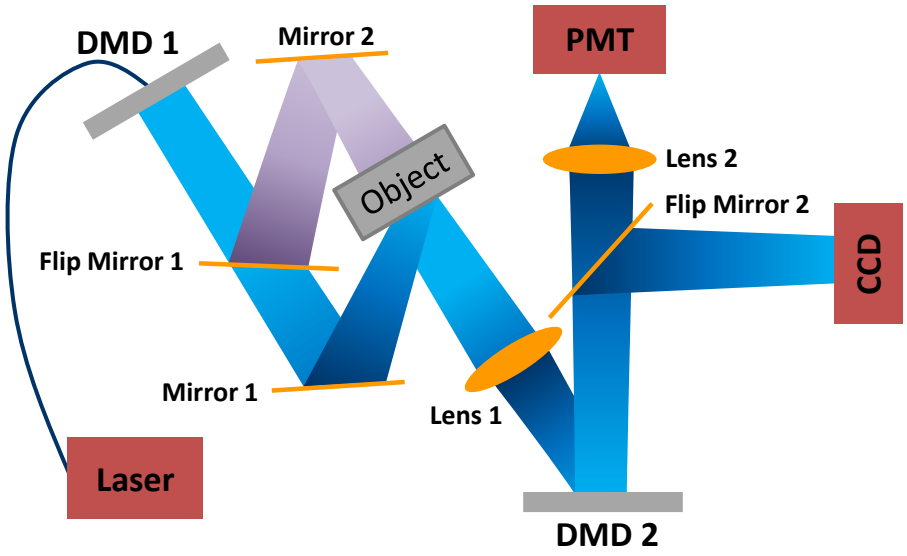

FIGURE C.4 – Système expérimental du Politecnico di Milano.

Le premier est le montage SPC déjà existant du Politecnico di Milano auquel quelques améliorations ont été apportées. Le second a été monté récemment au laboratoire CREATIS. Un logiciel pour contrôler ces dispositifs optiques de manière *adaptative* est également proposé.

C.3.1 Montage au Politecnico di Milano

Le système présent au Politecnico di Milano a initialement été conçu pour faire de la tomographie optique diffuse (D'Andrea *et al.*, 2010; Ducros *et al.*, 2013, 2016) en utilisant un DMD pour de l'illumination structurée et une caméra CCD en place du détecteur ponctuel. Plus tard, un second DMD a été ajouté ainsi qu'un détecteur ponctuel pour obtenir le système complet de la Fig. C.4.

Les contributions de cette thèse sur ce système couvrent deux parties. En premier lieu, un spectromètre a été ajouté pour obtenir des mesures multispectrales. Dans un second temps, un logiciel permettant de contrôler les différents éléments de manière *adaptative* a été implémenté puisque une technique d'acquisition/restauration des images *adaptative* est considérée dans les prochains chapitres.

Système Le système est composé d'une source laser à impulsions supercontinues (SC-450, Fianium ou SuperK Extreme EXW-12, NKT Photonics). L'objet étant généralement illuminé dans une bande spectrale particulière, un filtre (ThorLabs) est ajouté sur le chemin du laser si le SC-450 est employé. Quand le SuperK Extreme est utilisé, un filtre à longueur d'onde ajustable (SuperK Select, NKT Photonics) est couplé au laser afin de choisir une ou plusieurs (jusqu'à 8) bandes spectrales pour l'illumination de l'objet.

Un premier DMD (DLP7000-V7001, Vialux GmbH) de taille 768×1024 est employé pour l'illumination de l'objet. La lumière issue de ce DMD peut éclairer l'objet en transmission ou réflexion grâce au jeu de miroirs (mirror 1, 2 et flip mirror 1). L'image de l'objet est ensuite formée par la première lentille sur le second DMD (DLP7000-V7001, Vialux GmbH) également de taille 768×1024. Pour nos expériences, le DMD 1 sera toujours chargé avec un motif blanc afin d'avoir une illumination uniforme de l'objet et le DMD 2 sert à la modulation.

Enfin, par action sur le second miroir à bascule (flip mirror 2), la lumière réfléchie du DMD 2 peut être imagée sur une caméra CCD (Versarray 512, Princeton Instruments) ou est concentrée sur un PMT (HPM-100-50, Becker & Hickl GmbH) grâce à la seconde lentille.

Mesures résolues en temps Afin d'obtenir un système résolu en temps, une carte de comptage des photons (SPC-130 or SPC-630, Becker & Hickl GmbH), *time-correlated single photon counting* board (TCSPC), est couplée au PMT. Un tel dispositif est synchronisé avec l'impulsion du laser de sorte que la TCSPC puisse estimer le temps de vol de chacun des photons détectés. Après un certain temps d'intégration, la carte donne un histogramme des temps de vols des photons i.e. elle donne le nombre de photons détectés dans T canaux temporels. En place d'une simple mesure scalaire par une SPC classique, un vecteur de taille T est à présent directement obtenu quand un motif est envoyé au SLM. Cela donne la possibilité de restaurer une image par canal temporel [6].

Mesures multispectrales Des mesures multispectrales peuvent également être réalisées en remplaçant le détecteur ponctuel par un spectromètre. En quelques mots, la lumière issue de la seconde lentille est renvoyée dans le spectromètre où un prisme disperse cette dernière. La dispersion entraîne une séparation de la lumière en différents rayons lumineux correspondants à différentes bandes spectrales (i.e. plages de longueur d'onde). Une barrette de Λ détecteurs ponctuels en parallèle collecte alors ces différents rayons lumineux. Chaque détecteur mesure ainsi une information spectrale différente. Dans notre montage, un PMT de $\Lambda = 16$ canaux spectraux (PML-16-1, Becker & Hickl GmbH) est utilisé. Ces détecteurs sont toujours couplés à la TCSPC (SPC-630, Becker & Hickl GmbH) qui permet d'obtenir un histogramme de temps de vol des photons pour chacun des Λ canaux spectraux. La mesure scalaire d'une SPC classique devient cette fois-ci un vecteur de taille $(\Lambda \times T)$ pour un motif envoyé au SLM [7].

C.3.2 Montage au laboratoire CREATIS

Un montage expérimental plus simple a été monté au laboratoire CREATIS pendant la thèse afin de valider les expériences du Chaptitre V. A notre connaissance, outre les travaux de Studer *et al.* datant de 2012, aucune autre plateforme SPC n'est disponible en France. Le montage est schématisé en Fig. C.5.

Ce dernier est composé d'un lampe à LED blanche (LIUCWHA, ThorLabs) pour l'illumination de l'objet. Une roue contenant différents filtres de densité (NEXXB, ThorLabs) est placée devant la LED afin de contrôler l'intensité de l'illumination (paramètre N_0 introduit en (C.2)).

L'image de l'objet est formé par la première lentille dans le plan du SLM. Ce dernier est un DMD de taille 768×1024 (DLP700-V7001,Vialux) exploité pour moduler spatialement l'image avec la possibilité de charger des motifs sur 8-bits.

La lumière réfléchie du DMD est enfin concentrée, grâce à la seconde lentille, sur la partie sensible d'un photo-détecteur (PDA36A-EC, ThorLabs) couplé à un convertisseur analogique numérique (USB-6210, National Instruments).

6. La modélisation mathématique de ces acquisitions est donnée au Chaptitre VI.
7. La modélisation mathématique de ces acquisitions est donnée au Chaptitre VI.

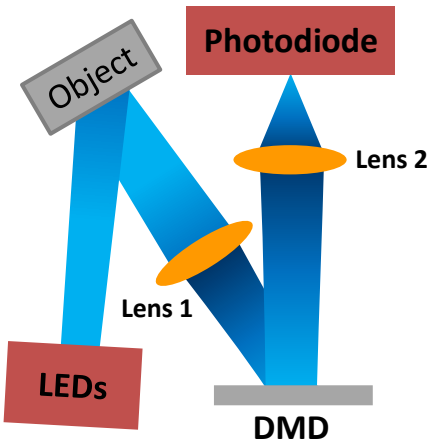

FIGURE C.5 – Montage expérimental à CREATIS.

C.3.3 Contrôle logiciel

Comme mentionné dans la conclusion du Chaptitre II, une approche *adaptative* est considérée dans cette thèse. Ceci signifie que les motifs envoyés au SLM sont choisis en se basant sur les mesures précédentes. Une communication entre le contrôle de l'instrumentation avec Labview et l'algorithme adaptatif codé en Matlab est donc nécessaire.

Labview pour l'instrumentation Comme c'est souvent le cas pour le contrôle de dispositifs optiques et électroniques, Labview peut être utilisé. Un logiciel a donc été implémenté dans ce langage pour commander le DMD, la caméra, le détecteur ponctuel et le convertisseur numérique. L'interface graphique permet de réaliser plusieurs acquisitions en réglant manuellement les différents paramètres de ces instruments.

Matlab pour traiter les données Matlab est de son côté employé pour créer les motifs à envoyer au SLM et implémenter la technique d'acquisition/restoration des images en traitant les données sauvegardées par le logiciel précédent codé sur Labview. Une fois les mesures réalisées par Labview, Matlab peut donc commencer le traitement des données afin de restaurer une image ou décider des prochaines mesures à effectuer.

Communication Matlab/Labview Les deux programmes précédents travaillent indépendamment et doivent être lancés manuellement l'un après l'autre pour effectuer un jeu complet de mesures et restaurer une image. Afin de mettre en œuvre une méthode *adaptative*, une étape de communication entre les deux programmes a été ajoutée. Le choix a été fait de choisir Matlab comme "maître", c'est-à-dire que tous les paramètres sont choisis dans le script Matlab. Le principe de cette implémentation est imagée en Fig. C.6. Un ordinateur avec le programme Labview contrôle les instruments et un autre contrôle l'algorithme adaptatif en Matlab. Des dossiers partagés sur un réseau commun permettent à Matlab de donner à Labview les paramètres (fichiers *Parameters_j.txt*). Le fichier *Matlab_done.txt* (resp. *Labview_done.txt*) permet au programme Labview (resp. Matlab) de connaitre quand Matlab (resp. Labview) a terminé sa tâche et celui-ci peut alors prendre le relais.

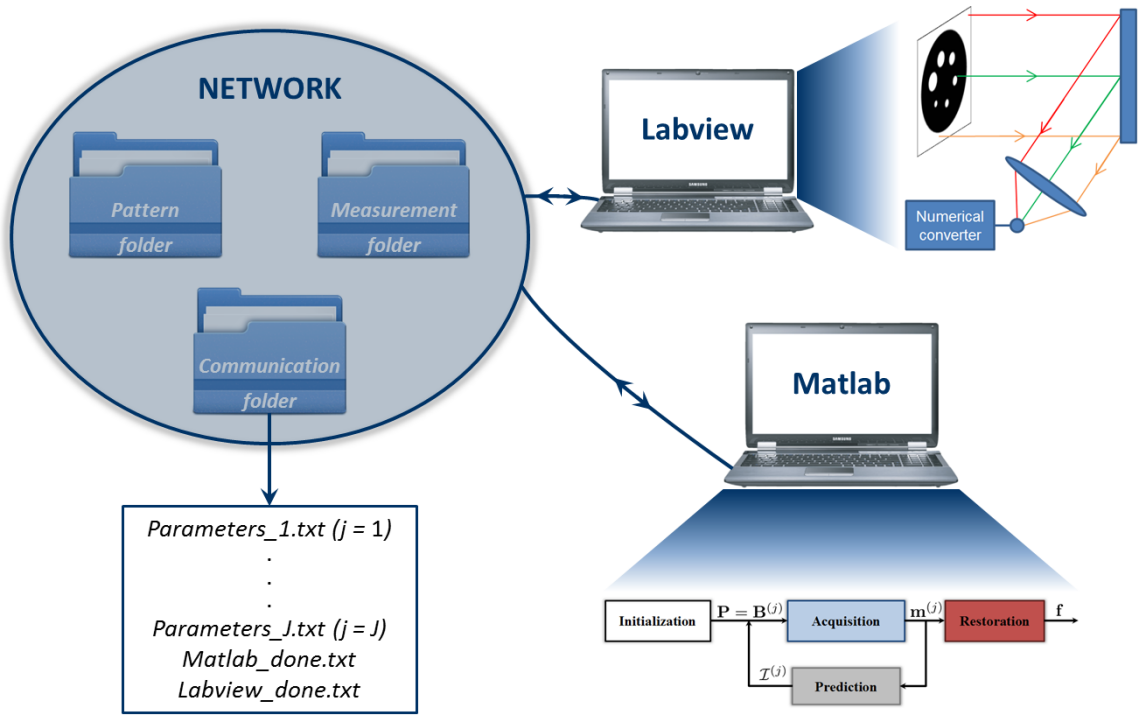

FIGURE C.6 – Fonctionnement de la communication entre Matlab et Labview.

C.3.4 Conclusion du chapitre

Ce chapitre a présenté les systèmes expérimentaux qui sont employés pour des acquisitions réelles dans les prochains chapitres. Le système de Milan est très complet puisqu'il permet d'avoir des mesures multispectrales résolues en temps avec une SPC. Au laboratoire CREATIS, le système est plus basique mais constitue une plateforme SPC unique en France.

Comme mentionné en fin de Chaptitre II, les méthodes *adaptive basis scans* sont les plus efficaces pour l'acquisition et la restauration d'images SPC. Les systèmes décrits dans ce chapitre permettent de mettre en œuvre la technique adaptative proposée dans le chapitre suivant.

C.4 CHAPITRE IV - TECHNIQUE ABS-WP

Les acquisitions adaptatives pour l'imagerie mono-pixel exploitent l'ensemble de mesures acquises à une itération précédente pour décider des prochains motifs SLM à envoyer, i.e. décider les nouvelles mesures à réaliser. En particulier, les méthodes *adaptive basis scan* (ABS) sont performantes avec un faible nombre de mesures et une restauration d'image très rapide. Une base d'ondelettes est souvent choisie car la plupart des images ont une représentation parcimonieuse dans cette base.

Dans ce chapitre, nous proposons une méthode complète pour l'imagerie mono-pixel en utilisant une nouvelle technique appelée *adaptive basis scan by wavelet prediction* (ABS-WP). Notre approche bénéficie de deux caractéristiques. Dans un premier temps, une étape de prédiction sans seuillage est proposée, étape inspirée par l'approximation non-linéaire de la transformée en ondelettes. La seconde caractéristique est la possibilité d'utiliser n'importe quelle ondelette ce qui permet

de mieux compresser les données. On présente dans un premier temps la technique ABS-WP avant de donner des résultats simulés et expérimentaux. Une comparaison avec l'acquisition comprimée (CS) et une autre stratégie ABS est également donnée avant d'ouvrir une discussion sur les résultats.

Certains résultats de ce chapitre viennent de deux papiers de conférences, *IEEE EMBC 2015* (Rousset *et al.*, 2015) où une stratégie de prédiction légèrement différente a été présentée et *IEEE ISBI 2016* (Rousset *et al.*, 2016) où une comparaison avec le CS a été donnée. Il contient également en grande partie un article publié dans *IEEE Transactions on Computational Imaging* en 2017a (Rousset *et al.*, 2017a).

C.4.1 Méthodes

Transformée en ondelettes La transformée en ondelettes fonctionnant sur des images carrés dont la taille est une puissance de 2, on considère à présent une image $\mathbf{f} \in \mathbb{R}^{D\times 1}$ de taille $N \times N = D$. On note $\widetilde{\mathbf{f}} \in \mathbb{R}^{D\times 1}$ les coefficients d'ondelettes de $\mathbf{f}$ pour une ondelette donnée :

$$\widetilde{\mathbf{f}} = \mathbf{B}\mathbf{f} \tag{C.3}$$

avec $\mathbf{B} \in \mathbb{R}^{D\times D}$ un opérateur orthonormal (Daubechies, 1992) traduisant la transformée en ondelettes. La valeur $j = 1 \dots J$ représente l'échelle à laquelle l'image $\mathbf{f}$ est observée avec J le niveau de décomposition. Une position d'un coefficient d'ondelettes dans un niveau j est spécifiée par le vecteur $\mathbf{i}$ tel que

$$\mathbf{i} = (i_1, i_2)^\top \in \left\{1, \dots, 2^\ell\right\}^2 \quad \text{with} \quad \ell = R - j,\ R = \log_2(N) \tag{C.4}$$

Ainsi, chaque élément de $\widetilde{\mathbf{f}}$ peut être complètement identifié et positionné par son unique triplet k tel que

$$k = \{o, j, \mathbf{i}\} \tag{C.5}$$

où $o = 0$, 1, 2 or 3 correspond aux coefficients d'approximation, verticaux, horizontaux et diagonaux, respectivement. De plus, chaque ligne de $\mathbf{B}$ correspond à un unique triplet k. L'image $\mathbf{f}$ peut être parfaitement restaurée avec $\widetilde{\mathbf{f}}$ en utilisant la transformée en ondelettes inverse :

$$\mathbf{f} = \mathbf{B}^{-1}\widetilde{\mathbf{f}} \tag{C.6}$$

Stratégie d'acquisition La transformée en ondelettes donnant des signaux parcimonieux, il est possible de ne pas prendre en compte les plus faibles coefficients (en magnitude) de $\widetilde{\mathbf{f}}$ lors de l'étape de restauration (Mallat, 2008). Notre méthode ABS-WP cherche ainsi à trouver les coefficients d'ondelettes dits significatifs, i.e. ayant une forte magnitude. On cherche donc à prédire les triplets k de chacun de ses éléments afin de remplir la matrice $\mathbf{P} = \left(\mathbf{p}_1, \dots, \mathbf{p}_k, \dots, \mathbf{p}_K\right)^\top$ de (C.2) avec les lignes de $\mathbf{B}$ correspondantes aux triplets k prédits, notés $\bar{k}$. Comme nous n'avons pas accès à toute l'image, une méthode itérative est proposée.

Pour plus de simplicité et comprendre les tailles des images mises en jeu dans notre technique, la notation vectorielle $\mathbf{f} \in \mathbb{R}^{D\times 1}$, $D = N \times N$, de l'image est temporairement remplacée par sa notation matricielle $\mathbf{F} \in \mathbb{R}^{N\times N}$. De même, $\widetilde{\mathbf{F}} \in \mathbb{R}^{N\times N}$ représente la transformée en ondelettes de $\mathbf{F}$. Notre stratégie se décompose en 5 étapes principales :

1. L'image d'approximation $\mathbf{A}_j$ à l'échelle grossière $j = J$ est complètement acquise. Cette image est de taille $2^\ell \times 2^\ell$ avec $\ell = R - j$.

2. $\mathbf{A}_j \in \mathbb{R}^{2^\ell \times 2^\ell}$ est sur-échantillonnée par un facteur 2 en utilisant une interpolation bicubique $\mathcal{S}$. Ceci mène à une image haute résolution $\mathbf{H}_j = \mathcal{S}(\mathbf{A}_j) \in \mathbb{R}^{2^{\ell+1} \times 2^{\ell+1}}$.
3. L'image $\mathbf{H}_j$ est transformée en ondelettes sur 1 niveau afin de donner $\widetilde{\mathbf{H}}_j \in \mathbb{R}^{2^{\ell+1} \times 2^{\ell+1}}$. Ceci donne les coefficient d'ondelettes de détails *predits* à l'échelle j.
4. Pour obtenir les triplets $\bar{k}$ des plus forts éléments prédits, une approximation non-linéaire est réalisée en retenant un pourcentage p_j des plus forts coefficients de détails de $\widetilde{\mathbf{H}}_j$. Ceci mène à l'obtention des éléments significatifs prédits et de leurs triplets correspondants prédits $\bar{k}$.
5. Ces coefficients sont finalement acquis expérimentalement en choisissant comme motifs SLM les lignes de $\mathbf{B}$ correspondantes aux triplets $\bar{k}$.

La description ci-dessus marche pour un niveau de décomposition de la transformée en ondelettes mais peut facilement être étendue à plusieurs niveaux. A l'étape 1, au lieu d'acquérir l'image grossière à $j = J$, l'image $\mathbf{A}_j$ est retrouvée par transformée en ondelettes inverse des coefficients acquis jusqu'alors. Les étapes 2 à 5 sont inchangées, seule une valeur différente de p_j est utilisée pour chaque échelle donnant le jeu de pourcentage final suivant :

$$\mathcal{P} = \{p_J, p_{J-1}, ..., p_1\}. \tag{C.7}$$

Taux de compression L'acquisition complète de l'image d'approximation $\mathbf{A}_j$ à l'échelle $j = J$ obtient $n_0 = 2^{2L} = 4^L$ coefficients d'ondelettes avec $L = R - J$. Ensuite, un pourcentage p_j des plus forts coefficients de détails est acquis. Ainsi, le nombre de mesures à chaque échelle j est donné $n_j = 3 \times 2^{2^\ell} \times p_j = 3 \times 4^\ell \times p_j$ avec $\ell = R - j$. Le nombre total n d'éléments acquis est donc contrôlé par le jeu de pourcentage $\mathcal{P}$ de (C.7). On peut montrer que n est donné par

$$n = 4^L \left[1 + 3 \sum_{j=1}^{J} 4^{J-j} p_j \right]. \tag{C.8}$$

Le taux de compression (TC), correspondant à une quantité normalisée entre 0 et 1, est défini comme

$$\text{TC} = 1 - \frac{n}{D} \tag{C.9}$$

C.4.2 Expériences

Simulations Pour les simulations, trois images sont considérées : l'image de Lena et peppers souvent utilisées en traitement du signal et une image de bioluminescence d'une souris (Keramidas *et al.*, 2010) superposée à l'image en lumière ambiante (Fig. C.7). Notre méthode ABS-WP est comparée à l'acquisition comprimée (CS) en restaurant directement $\mathbf{f}$ à partir des mesures $\mathbf{m}$ par minimisation TV (Total Variation) (Takhar *et al.*, 2006; Duarte *et al.*, 2008). Nous nous comparons également à une autre méthode adaptative dans le domaine ondelette, EWT-ACS (*adaptive compressed sampling by extended wavelet trees*) proposée par Dai *et al.*. Cette méthode est dérivée de l'ondelette de Haar et un seuil doit être choisi pour prédire les coefficients significatifs à acquérir.

Montage expérimental Le montage expérimental du Politecnico di Milano présenté au Chaptitre III sert pour les acquisitions réelles. Le DMD 1 sert à illuminer l'objet uniformément et le DMD 2 charge les motifs d'ondelettes donnés par ABS-WP.

C.4.3 Résultats et discussion

Résultats Le tableau C.2 donne les PSNRs des images SPC restaurées par CS, EWT-ACS et ABS-WP pour les trois images de simulation. Pour notre technique ABS-WP, l'ondelette de Le Gall est employée car, dans la plupart des cas, elle est la plus efficace.

Image	**TC**	**PSNR** (dB)			**Seuils**
		CS	*EWT-ACS*	*ABS-WP*	**pour EWT-ACS**
Lena (256 × 256)	80	29.55	29.90	**30.33**	11.52
	85	27.89	28.49	**29.59**	16.63
Peppers (256 × 256)	80	34.70	35.06	**35.35**	7.71
	85	32.96	33.42	**34.83**	11.77
Mouse (128 × 128)	80	45.36	47.65	**49.23**	385.65
	85	42.18	45.83	**49.13**	851.10

TABLEAU C.2 – PSNRs obtenus pour différentes stratégies d'acquisition SPC à deux taux de compression. Les seuils pour la méthode EWT-ACS de Dai *et al.* sont donnés dans la dernière colonne. Pour ABS-WP, les motifs de Le Gall sont utilisés avec $\mathcal{P} = \{0.90, 0.80, 0.71, 0.02\}$ et $\mathcal{P} = \{0.90, 0.80, 0.45, 0.019\}$ pour donner des taux de compression TC de 80% et 85%.

La Fig. C.7 présente un cas visuel de restauration d'image par ABS-WP sur une image de bioluminescence d'une souris. Cette image étant plutôt lisse, de forts taux de compression peuvent être obtenus.

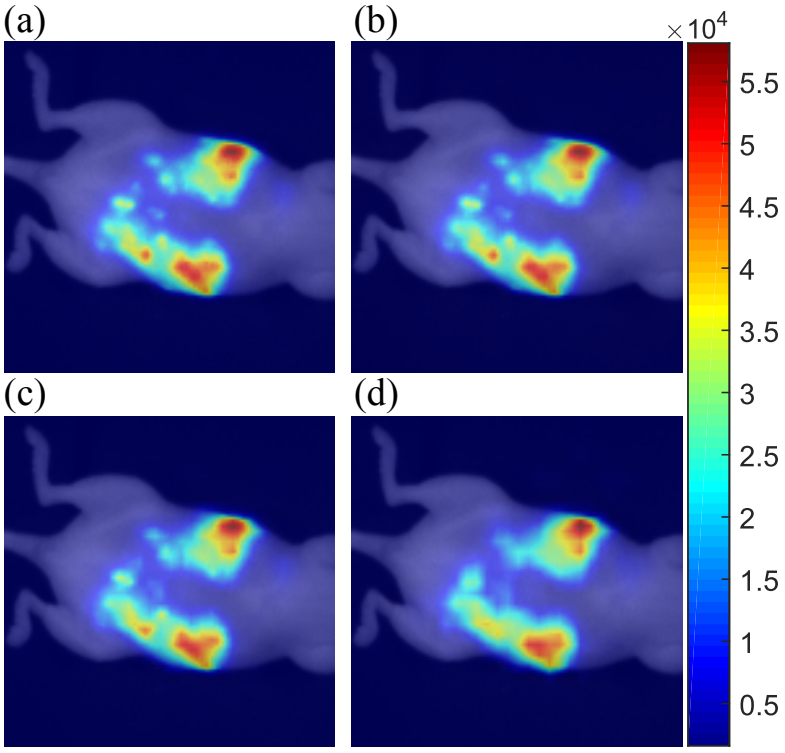

FIGURE C.7 – Acquisition SPC avec ABS-WP sur une image 128 × 128 de bioluminescence de souris. (a) Image de référence, images restaurées avec Le Gall pour un TC de (b) 90%, (c) 95% et (d) 98%. Respectivement, les PSNRs par rapport à l'image de référence sont 48.25 dB, 41.48 dB et 35.37 dB.

Des acquisitions SPC réelles sur la cible de Jaszczak avec ABS-WP et CS sont présentées en Fig. C.8.

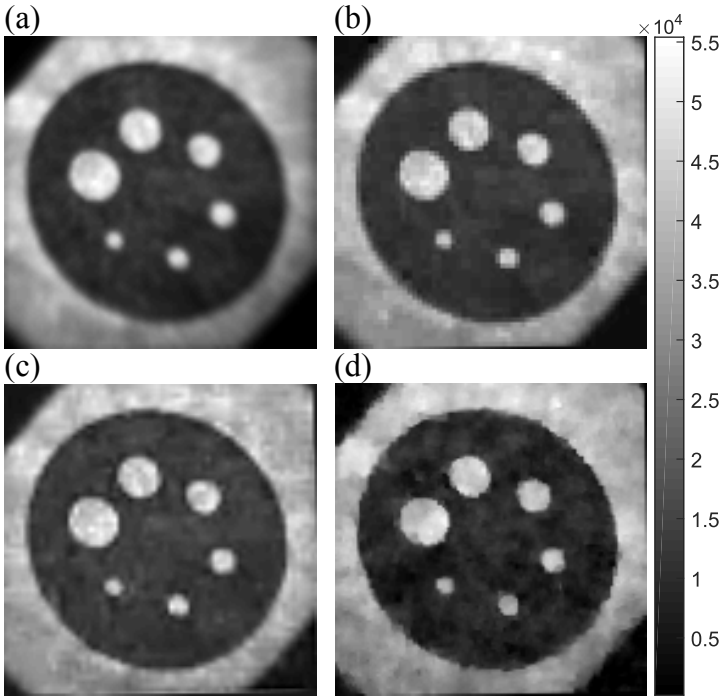

FIGURE C.8 – Acquisitions experimentales avec la SPC sur la cible de Jaszczak. (a) Image CCD expérimentale de la cible, images 128 × 128 restaurées avec un TC de 85% (b) pour ABS-WP avec Haar, (c) pour ABS-WP avec Le Gall et (d) par CS. Respectivement, les PSNRs obtenus par rapport à l'image CCD sont 21.99 dB, 21.65 dB et 21.20 dB.

Dans le cas de notre technique, les ondelettes de Haar et de Le Gall sont employées pour montrer la capacité du DMD à charger des motifs sur 8 bits.

Discussion Les résultats du tableau C.2 où notre méthode ABS-WP est comparée au CS et EWT-ACS, des résultats numériques proches ou meilleurs sont obtenus pour ABS-WP. Les seuils d'EWT-ACS montrent qu'ils dépendent de l'image et doivent être adaptés pour chaque objet. En comparaison, pour ABS-WP et un taux de compression fixe, le même jeu de pourcentages $\mathcal{P}$ est utilisé pour chaque image. Bien que les trois images en simulation soient différentes, notre stratégie donne toujours une très bonne qualité d'image. ABS-WP s'adapte ainsi à l'image et aucun seuil ne doit être ajusté. Pour le cas du CS, de nombreux paramètres doivent être choisis pour l'étape de minimisation TV. Suivant ces choix, la qualité de l'image peut être gravement affectée.

Même avec un TC aussi haut que 98%, les résultats de la Fig. C.7 montrent qu'ABS-WP restaure des images d'excellentes qualités dans le cas d'objets lisses. Pour ce type d'images typiques en imagerie de fluorescence, peu de coefficients d'ondelettes sont en effet nécessaires pour retrouver l'image originale.

Si l'on regarde les données expérimentales de la Fig. C.8, celles-ci montrent qu'une ondelette plus sophistiquée comme celle de Le Gall peut être utilisée par rapport aux acquisitions classiques avec Haar. Elle permet de donner de meilleurs résultats visuels avec une image plus lisse par rapport au cas Haar qui a tendance à pixéliser l'image. Le choix de l'ondelette est ainsi un paramètre important de notre méthode. En effet, suivant l'objet imagé, certaines ondelettes sont meilleures pour capturer l'information de l'image avec moins de coefficients. Si l'on regarde l'objet restauré par CS

sur la Fig. C.8, on peut apercevoir des sortes de tâches dues à la minimisation TV.

C.4.4 Conclusion du chapitre

Dans ce chapitre, nous avons décrit une nouvelle méthode pour l'imagerie mono-pixel. Les coefficients significatifs qui devraient être acquis sont prédits par une interpolation bicubique alors que les autres coefficients ne sont pas pris en compte à l'étape de restauration de l'image. A notre connaissance, des données expérimentales obtenues avec une autre ondelette qu'Haar n'avaient jamais été présentées auparavant.

Un problème qui n'a pas été détaillé dans ce chapitre concerne les valeurs positives et négatives que contiennent les motifs d'ondelettes. De tels motifs ne peuvent pas être implémentés directement sur un SLM puisque les photons ne peuvent être comptés négativement. Un recours possible est de séparer le motif en sa partie positive et partie négative prise en valeur absolue. La soustraction des deux mesures correspondantes donne la mesure finale, doublant ainsi le nombre de mesures nécessaires. Au chapitre suivant, nous généralisons le problème qui peut être solutionné par un algorithme de factorisation de matrices et qui permet de réduire le nombre de mesures à effectuer.

C.5 CHAPITRE V - GÉNÉRALISATION DES MOTIFS

Quelle que soit la technique d'acquisition/restauration des images employée, deux problèmes expérimentaux apparaissent. Le premier concerne les motifs à envoyer au SLM qui comportent des valeurs négatives ce qui ne peut pas être physiquement mis en œuvre sur un SLM. Le second problème est le courant d'obscurité au niveau du détecteur qui perturbe les mesures et qui doit être éliminé.

Pour palier ce problème, nous proposons de créer des motifs à valeurs positives qui, combinés linéairement, donnent les motifs désirés à valeurs positives et négatives. Nous montrons que ceux-ci peuvent être obtenus par un algorithme de factorisation en matrices semi non-négatives (*semi nonnegative matrix factorization*, SNMF) qui permet de décomposer une matrice en un produit de deux autres matrices dont l'une n'a que des éléments positifs (Lee *et* Seung, 1999; Ding *et al.*, 2010; Gillis *et* Kumar, 2015).

Ce chapitre présente les méthodes classiques permettant de contourner le problème de positivité des motifs et d'élimination du courant d'obscurité. Une formulation générale du problème est ensuite donnée avant d'en proposer une solution par un algorithme SNMF. Des résultats en simulation montrent les avantages de cette méthode par rapport aux solutions conventionnelles.

Ces résultats ont été déposés sous forme de brevet (Rousset *et al.*, 2017c) et soumis à *IEEE Transactions on Image Processing* (Rousset *et al.*, 2017d).

C.5.1 Méthodes ad'hoc pour contourner le problème

On note $\check{\mathbf{P}} = \left(\check{\mathbf{p}}_1, \ldots, \check{\mathbf{p}}_I\right)^\top \in \mathbb{R}^{I\times D}$ la matrice contenant I motifs désirés $\check{\mathbf{p}}_i \in \mathbb{R}^{D\times 1}$, c'est-à-dire ayant des valeurs positives et négatives. On note $\check{\mathbf{m}} = (\check{m}_1, \ldots, \check{m}_I)^\top \in \mathbb{R}^{I\times 1}$ le vecteur contenant les

mesures désirées correspondantes :

$$\check{\mathbf{m}} = N_0 \Delta t \check{\mathbf{P}} \mathbf{f} \tag{C.10}$$

Il est à noter que le terme additif $\Delta t \alpha \mathbf{1}_K$ de (C.2) est supprimé de cette équation puisque qu'il ajoute une information supplémentaire dans (C.2) qui perturbe les mesures.

Méthode *pos/neg* Cette méthode naturelle consiste à séparer chaque motif désiré $\check{\mathbf{p}} \in \mathbb{R}^{D\times 1}$ en sa partie positive $\mathbf{p}_+ \in \mathbb{R}_+^{D\times 1}$ et sa partie négative prise en valeur absolue $\mathbf{p}_- \in \mathbb{R}_+^{D\times 1}$ (Dai *et al.*, 2014; Rousset *et al.*, 2017a), i.e.,

$$\check{\mathbf{p}} = \mathbf{p}_+ - \mathbf{p}_- \quad \text{with} \begin{cases} \mathbf{p}_+ = \max(\mathbf{0}_D, \check{\mathbf{p}}) \\ \mathbf{p}_- = |\min(\mathbf{0}_D, \check{\mathbf{p}})| \end{cases} \tag{C.11}$$

où les fonctions $\max(.)$ et $\min(.)$ sont appliquées sur chaque entrée des deux vecteurs, $\mathbf{0}_D$ étant le vecteur nul de taille D. Ensuite, les mesures m_+ et m_- acquises avec $\mathbf{p}_+$ et $\mathbf{p}_-$, respectivement, sont soustraites pour donner $\check{m}$. En effet, nous avons

$$m_+ - m_- = \left(N_0 \mathbf{p}_+^\top \mathbf{f} + \alpha\right) \Delta t - \left(N_0 \mathbf{p}_-^\top \mathbf{f} + \alpha\right) \Delta t = \check{m}. \tag{C.12}$$

Il est important de noter que le courant d'obscurité $\alpha \Delta t$ est bien annulé par cette technique. L'inconvénient est que $K = 2I$ mesures SPC doivent être réalisées pour obtenir les I mesures désirées, augmentant ainsi les temps d'acquisition.

Méthode *shift* Une seconde approche consiste à décaler chaque motif désiré $\check{\mathbf{p}} \in \mathbb{R}^{D\times 1}$ vers des valeurs positives (Duarte *et al.*, 2008). Mathématiquement

$$\check{\mathbf{p}} = \mathbf{p}_\mathrm{s} - \mathbf{p}_\mathrm{b} \quad \text{with} \begin{cases} \mathbf{p}_\mathrm{s} = \check{\mathbf{p}} + \mathbf{p}_\mathrm{b} \in \mathbb{R}_+^{D\times 1} \\ \mathbf{p}_\mathrm{b} = (b, \ldots, b)^\top \in \mathbb{R}_+^{D\times 1} \end{cases} \tag{C.13}$$

où b est la valeur d'arrière plan choisie telle que $b \geq |\min(\check{\mathbf{p}})| \in \mathbb{R}_+$. Comme pour la méthode pos/neg, la soustraction des deux mesures SPC correspondantes donne la mesure désirée en annulant le courant d'obscurité. Contrairement à la méthode pos/neg, il n'est pas nécessaire de doubler le nombre de mesures. En effet, en choisissant b assez grand, cette valeur peut être la même pour tous les I motifs désirés. Seulement $K = I + 1$ mesures sont donc nécessaires. Cependant, nous montrerons plus tard que cette méthode souffre du bruit de mesure.

C.5.2 Méthode proposée basée sur des motifs généralisés

Transformation des motifs Pour obtenir une solution générale et robuste au problème de positivité, notre idée est de factoriser la matrice $\check{\mathbf{P}}$ en un produit de deux matrices $\mathbf{T}$ et $\mathbf{P}$ telles que

$$\check{\mathbf{P}} = \mathbf{T}\mathbf{P} \tag{C.14}$$

où $\mathbf{P} \in \mathbb{R}_+^{K\times D}$ contient une séquence de motifs positifs et $\mathbf{T} \in \mathbb{R}^{I\times K}$ est une matrice de transformation permettant de combiner les motifs de $\mathbf{P}$ pour retrouver ceux de $\check{\mathbf{P}}$. Si une telle factorisation peut se

trouver, l'idée est alors d'appliquer la même matrice de transformation $\mathbf{T}$ sur le vecteur de mesure $\mathbf{m}$ pour obtenir $\check{\mathbf{m}}$, soit

$$\check{\mathbf{m}} = \mathbf{T}\mathbf{m}. \tag{C.15}$$

Les mesures désirées sont donc obtenues par la combinaison linéaire de mesures réalisables avec les motifs positifs de $\mathbf{P}$. Or, si l'on développe $\mathbf{T}\mathbf{m}$ en utilisant (C.2), on obtient :

$$\mathbf{T}\mathbf{m} = \Delta t(N_0\mathbf{T}\mathbf{P}\mathbf{f} + \alpha\mathbf{T}\mathbf{1}_K) = N_0\Delta t\check{\mathbf{P}}\mathbf{f} + \alpha\Delta t\mathbf{T}\mathbf{1}_K \tag{C.16}$$

Afin d'obtenir (C.10) par (C.15), le second terme de (C.16) doit s'annuler. Nous choisissons ainsi d'imposer la contrainte suivante :

$$\mathbf{T}\mathbf{1}_K = \mathbf{0}_I \tag{C.17}$$

où $\mathbf{0}_I = (0,\dots,0)^\top \in \mathbb{R}^{I\times 1}$.

En résumé, pour une séquence de motifs désirés $\check{\mathbf{P}} \in \mathbb{R}^{I\times D}$, la problème de généralisation des motifs que nous adressons et le suivant :

$$\text{Trouver } \mathbf{T} \in \mathbb{R}^{I\times K} \text{ et } \mathbf{P} \in \mathbb{R}^{K\times D} \text{ tels que } \begin{cases} \check{\mathbf{P}} = \mathbf{T}\mathbf{P} \\ \mathbf{P} \geq 0 \\ \mathbf{T}\mathbf{1}_K = \mathbf{0}_I \end{cases} \tag{C.18}$$

où $\mathbf{P} \geq 0$ signifie que $(\mathbf{P})_{k,n} \geq 0$, $\forall (k,n)$.

Formulation du problème Afin de trouver une solution à (C.14), nous proposons de résoudre le système suivant :

$$\min_{\mathbf{T},\mathbf{P}} \left\|\check{\mathbf{P}} - \mathbf{T}\mathbf{P}\right\|_{\mathrm{F}}^2 \quad \text{tel que} \quad \mathbf{P} \geq 0 \text{ and } \mathbf{T}\mathbf{1}_K = \mathbf{0}_I \tag{C.19}$$

où $\mathbf{P} \geq 0$ signifie que $\forall\,(k,n) \in (1\dots K)\times(1\dots D)$, $(\mathbf{P})_{k,n} \geq 0$ et $\|\mathbf{M}\|_{\mathrm{F}}$ est la norme de Frobenius de la matrice $\mathbf{M}$.

C.5.3 Solution par algorithme SNMF

Algorithme SNMF Le problème (C.19) peut-être résolu par un algorithme de factorisation en matrice semi non-négatives. En pratique, notre but est d'avoir une valeur de K la plus petite possible afin de limiter le nombre de mesures nécessaires tout en ayant une faible erreur de factorisation. Étant donné que les deux matrices $\mathbf{P}$ et $\mathbf{T}$ sont inconnues, la plupart des méthodes sont itératives et résolvent (C.19) alternativement pour $\mathbf{P}$ puis $\mathbf{T}$ avec leurs contraintes respectives $\mathbf{P} \geq 0$ et $\mathbf{T}\mathbf{1}_K = \mathbf{0}_I$. Afin d'avoir un calcul et une convergence rapides, nous considérons une méthode basée sur les moindres carrés pour résoudre (C.19).

Solution pour T La résolution de (C.19) pour $\mathbf{T}$ considère $\mathbf{P}$ fixe, il s'agit donc de résoudre

$$\min_{\mathbf{T}} \left\|\check{\mathbf{P}} - \mathbf{T}\mathbf{P}\right\|_{\mathrm{F}}^2 \qquad \text{tel que} \qquad \mathbf{T}\mathbf{1}_K = \mathbf{0}_I. \tag{C.20}$$

La condition (C.17) donne un problème d'optimisation sous contrainte d'égalité dont la solution analytique à (C.20) trouvée en utilisant la propriété de dualité est donnée par :

$$\mathbf{T} = \check{\mathbf{P}}\mathbf{P}^\top\left(\mathbf{P}\mathbf{P}^\top\right)^{-1}\left(\mathbf{I} - \frac{1}{\mathbf{1}_K^\top\left(\mathbf{P}\mathbf{P}^\top\right)^{-1}\mathbf{1}_K}\mathbf{1}_{K\times K}\left(\mathbf{P}\mathbf{P}^\top\right)^{-1}\right) \tag{C.21}$$

avec $\mathbf{I}$ la matrice identité de taille $K \times K$, $\mathbf{1}_K^\top(\mathbf{P}\mathbf{P}^\top)^{-1}\mathbf{1}_K \in \mathbb{R}$ et $\mathbf{1}_{K\times K} = \mathbf{1}_K\mathbf{1}_K^\top$ est la matrice de taille $K \times K$ dont tous les éléments sont égaux à 1. Si $(\mathbf{P}\mathbf{P}^\top)$ n'est pas inversible, la matrice pseudo-inverse de Moore-Penrose est employée.

Solution pour P On cherche à présent à trouver une solution à (C.19) pour $\mathbf{P}$ considérant $\mathbf{T}$ fixe, on cherche donc

$$\min_{\mathbf{P}} \left\|\check{\mathbf{P}} - \mathbf{T}\mathbf{P}\right\|_{\mathrm{F}}^2 \qquad \text{tel que} \qquad \mathbf{P} \geq 0. \tag{C.22}$$

Ce problème n'ayant pas de solution explicite, Gillis a proposé dans Gillis *et* Kumar (2015) un algorithme de descente par blocs sur les lignes de $\mathbf{P}$ qui amène à une solution analytique pour minimiser chaque ligne et un calcul rapide en choisissant $K = I + 1$.

Pour résoudre ce problème par la méthode de Gillis, la fonction coût $\mathcal{F}(\mathbf{P}) = \left\|\check{\mathbf{P}} - \mathbf{T}\mathbf{P}\right\|_{\mathrm{F}}^2$ est réécrite de la manière suivante :

$$\mathcal{F}(\mathbf{p}_k) = \left\|\check{\mathbf{P}} - \mathbf{T}\mathbf{P}\right\|_{\mathrm{F}}^2 = \left\|\check{\mathbf{P}} - \mathbf{T}_{|k}\mathbf{P}_{-k} - \mathbf{t}_k\mathbf{p}_k^\top\right\|_{\mathrm{F}}^2 \tag{C.23}$$

où $\mathbf{T}_{|k}$ (resp. $\mathbf{P}_{-k}$) est la matrice $\mathbf{T}$ (resp. $\mathbf{P}$) privée de sa colonne (resp. ligne) k et $\mathbf{t}_k \in \mathbb{R}^{I\times 1}$ (resp. $\mathbf{p}_k \in \mathbb{R}^{D\times 1}$) est la k-ième colonne (resp. ligne) de $\mathbf{T}$ (resp. $\mathbf{P}$). On montre que la solution analytique minimisant (C.23) est donnée par :

$$\mathbf{p}_k = \max\left(\mathbf{0}_D, \frac{(\check{\mathbf{P}} - \mathbf{T}_{|k}\mathbf{P}_{-k})^\top\mathbf{t}_k}{\|\mathbf{t}_k\|_2^2}\right) \tag{C.24}$$

où la fonction max(.) s'applique sur chaque composante des deux vecteurs et $\mathbf{0}_D$ est le vecteur nul de taille D. Une solution partielle au problème (C.22) est finalement obtenue en itérant une fois (C.24) sur chaque ligne de $\mathbf{P}$ [8].

Algorithme final En utilisant la solution analytique $\mathbf{T}$ de (C.21) et celle de (C.24) pour minimiser chaque ligne de $\mathbf{P}$, l'algorithme complet peut maintenant être écrit suivant l'algorithme 4.

Algorithme 4 Trouver $\check{\mathbf{P}} \approx \mathbf{T}\mathbf{P}$ suivant (C.19)

Initialisation : Prendre $K = I + 1$ et $\mathbf{P} = \mathrm{rand}(K, D)$
while $\left\|\check{\mathbf{P}} - \mathbf{T}\mathbf{P}\right\|_{\mathrm{F}}^2 > \epsilon$ **do**
  1 : Mettre à jour $\mathbf{T}$ avec (C.21)
  2 : Mettre à jour $\mathbf{P}$
    for $k = 1 : K$ **do**
      2.1 : $\mathbf{p}_k \leftarrow \max\left(\mathbf{0}_D, \frac{(\check{\mathbf{P}} - \mathbf{T}_{|k}\mathbf{P}_{-k})^\top\mathbf{t}_k}{\|\mathbf{t}_k\|_2^2}\right)$
      2.2 : Mettre à jour la k-ième ligne de $\mathbf{P}$ avec $\mathbf{p}_k$
    end for
end while

8. Plusieurs passages de l'algorithme sur les lignes de $\mathbf{P}$ amèneraient à une solution au problème (C.22). Ici, un passage suffit puisque l'algorithme 4 est inclus dans une autre boucle ce qui revient, quand celui-ci commence à converger, à résoudre (C.22).

C.5.4 Résultats et discussion

Résultats Pour juger des performances de la méthode SNMF proposée, nous comparons les images SPC obtenues par cette technique avec les méthodes *pos/neg* et *shift* présentées en Section C.5.1. La factorisation de la même matrice $\check{\mathbf{P}}$ en $\mathbf{TP}$ est donc effectuée de trois manières différentes.

Les simulations suivantes ont été corrompues par un bruit de Poisson, bruit généralement obtenu sur une mesure optique. Ce dernier est appliqué sur le vecteur de mesure $\mathbf{m}$ de (C.2).

On donne en Fig. C.9, les courbes du PSNR des images restaurées par ABS-WP avec les trois techniques (SNMF, *pos/neg*, *shift*) en fonction de différentes valeurs N_0 et deux valeurs du courant d'obscurité α. Pour ces cas, Δt est fixé à 1 s et l'image test choisie est la cible de Jaszczak.

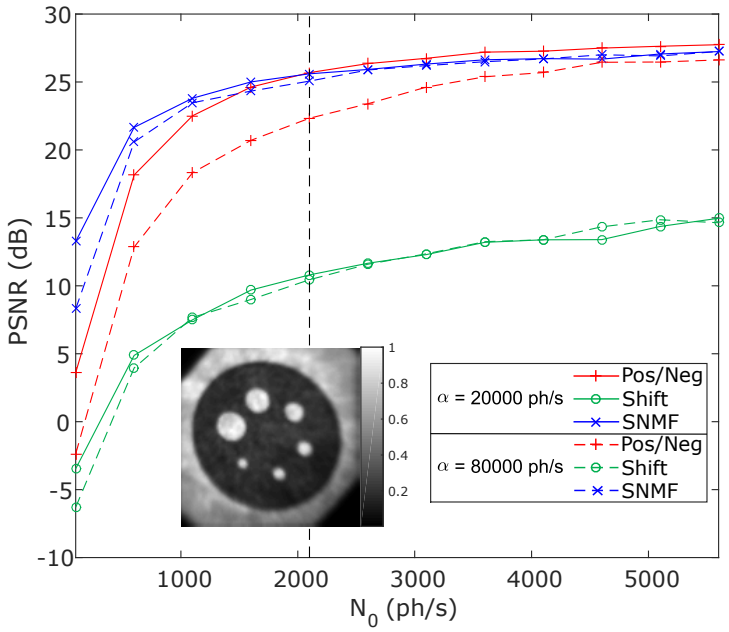

FIGURE C.9 – Image test et courbes du PSNR des images restaurées en fonction de N_0 pour $\Delta t = 1$ s avec deux valeurs de α. La barre en pointillée correspond aux résultats de la Fig. C.10.

La Fig. C.10 montre les 6 images 64×64 restaurées par ABS-WP pour le cas $N_0 = 2100$ ph/s de la Fig. C.9.

Discussion L'avantage principal de l'algorithme SNMF proposé par rapport au cas *pos/neg* est le nombre K de motifs créés qui est égal à $I+1$ pour SNMF alors qu'il vaut $2I$ pour *pos/neg*, les acquisitions sont donc plus rapides avec notre méthode. Pour la technique *shift*, $K = I+1$ peut également être obtenu mais les résultats des deux figures suivantes montrent que cette méthode souffre énormément du bruit de mesure.

Ceci peut être vu sur la Fig. C.9 où la méthode *shift* donne toujours des restaurations d'images de qualité bien inférieure aux deux autres techniques. Une explication est que l'information utile du motif décalé est en quelque sorte noyée dans celle ajoutée par l'arrière-plan. La méthode SNMF quant à elle donne de très bons résultats et ceci quelle que soit la valeur de la composante continue α. La technique *pos/neg* est impactée par cette composante pour des valeurs faibles de N_0. Ceci s'explique par le fait que les motifs *pos/neg* ont de nombreux coefficients nuls et une composante continue α importante diminue l'effet des parties actives (i.e. coefficients non nuls) du motif, effet

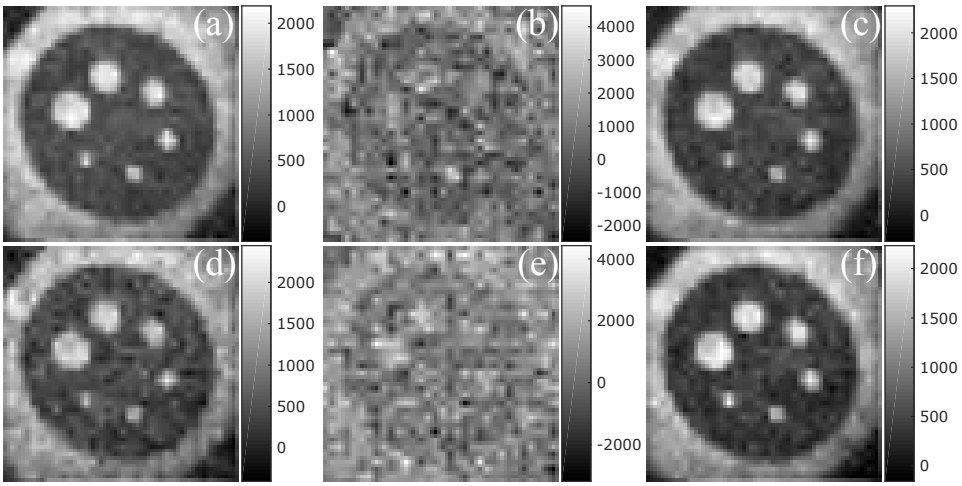

FIGURE C.10 – Images restaurées par ABS-WP pour les trois techniques de factorisation pour $N_0 = 2100$ ph/s et $\Delta t = 1$ s sur l'image test de la Fig. C.9. Images obtenues pour $\alpha = 20000$ ph/s avec (a) *pos/neg*, (b) shift, (c) SNMF et pour $\alpha = 80000$ ph/s avec (d) *pos/neg*, (e) *shift*, (f) SNMF. Les PSNRs correspondants peuvent être lus sur la Fig. C.9 (barre en pointillée).

moins présent pour SNMF où la partie active est plus considérable.

Ces résultats numériques sont confirmés par les images restaurées visibles en Fig. C.10 où la méthode *shift* donne des images très bruitées ((b) et (e)). SNMF et *pos/neg* donne des résultats similaires avec un avantage certain pour SNMF où le nombre de mesures effectives est quasiment égal au nombre de mesures désirées.

C.5.5 Conclusion du chapitre

En conclusion, nous avons proposé une technique de factorisation en matrice semi non-négatives pour contourner deux contraintes expérimentales de positivité lors de l'acquisition d'images par une SPC. La méthode permet de ne pas doubler le nombre de mesures comme la méthode *pos/neg* et est peu affectée par le bruit de mesure contrairement à la technique *shift*.

C.6 CHAPITRE VI - APPLICATION À L'IMAGERIE MULTISPECTRALE RÉSOLUE EN TEMPS

Les applications biomédicales peuvent tirer profit d'une SPC comme mentionné en introduction. Un avantage certain pour le domaine médical concerne les acquisitions multispectrales résolues en temps. En effet, les informations spectrales et temporelles peuvent être utilisées pour caractériser des tissus biologiques comportant différents fluorophores afin d'étudier leur micro-environnement (pH, température, etc.) qui est un élément essentiel pour les biologistes.

Une SPC multispectrale résolue en temps peut être obtenue en remplaçant le détecteur ponctuel de la SPC classique par un spectromètre ayant plusieurs détecteurs ponctuels en parallèle et en couplant chacun de ces détecteurs à une carte de comptage des photons (TCSPC) (Pian *et al.*, 2016b,a). Dans ses travaux, l'équipe d'Intes (Pian *et al.*, 2016b,a) utilise une méthode d'acquisition/restoration des images *non-adaptative* avec des motifs d'Hadamard.

Dans ce chapitre, la capacité de notre technique ABS-WP (Chaptitre IV) pour manipuler des données multispectrales résolues en temps est démontrée [9]. Une partie de ces résultats ont été présentés à la conférence *SPIE Photonics West* en Février 2017 (Rousset *et al.*, 2017b). Nous étendons dans un premier temps les méthodes pour traiter les données avec l'apport de la dimension spectrale et temporelle avant de détailler les expériences et résultats.

C.6.1 Méthodes

Extension aux mesures multispectrales résolues en temps L'ajout d'une dimension spectrale à la SPC se fait en remplaçant le détecteur ponctuel par un spectromètre comportant Λ détecteurs ponctuels parallèles. Ceux-ci sont de plus couplés à une carte de comptage des photons (*time-correlated single photon counting*, TCSPC) avec T canaux temporels. Cette dernière est de plus synchronisée avec l'impulsion du laser qui sert de référence pour classer chaque photon selon son temps de vol (i.e. temps entre son émission par le laser et son arrivée au détecteur). Au final, une SPC multispectrale résolue en temps est donc obtenue.

Une image $\mathbf{F} \in \mathbb{R}^{D\times\Lambda T}$ (2D+λ+t) peut ainsi être acquise avec $\mathbf{F} = \left(\mathbf{f}_{1,1},\ldots,\mathbf{f}_{\lambda,t},\ldots,\mathbf{f}_{\Lambda,T}\right)$. L'image $\mathbf{f}_{\lambda,t} \in \mathbb{R}^{D\times 1}$ représente l'image dans le canal spectral λ et canal temporel t avec $(\lambda,t) \in [1,\Lambda]\times[1,T]$. Les informations spectrales et temporelles étant acquises simultanément, les équations (C.1) et (C.2) du Chaptitre II sont ainsi changées en

$$\mathbf{m}_k = \left(m_{k,1,1},\ldots,m_{k,\lambda,t},\ldots,m_{k,\Lambda,T}\right)^\top \in \mathbb{R}^{\Lambda T\times 1} \quad \text{with} \quad \mathbf{m}_k^\top = \left(N_0\mathbf{p}_k^\top\mathbf{F} + \alpha\mathbf{1}_{\Lambda T}^\top\right)\Delta t \tag{C.25}$$

$$\mathbf{M} = \left(\mathbf{m}_1,\ldots,\mathbf{m}_k,\ldots,\mathbf{m}_K\right)^\top \in \mathbb{R}^{K\times\Lambda T} \quad \text{with} \quad \mathbf{M} = \left(N_0\mathbf{P}\mathbf{F} + \alpha\mathbf{1}_{K\times\Lambda T}\right)\Delta t \tag{C.26}$$

avec $\mathbf{1}_{\Lambda T} = (1,\ldots,1)^\top \in \mathbb{R}^{\Lambda T\times 1}$ et $\mathbf{1}_{K\times\Lambda T} \in \mathbb{R}^{K\times\Lambda T}$ la matrice dont tous les éléments valent 1. Un vecteur de mesures $\mathbf{m}_k \in \mathbb{R}^{\Lambda T\times 1}$ est directement obtenu par la SPC multispectrale résolue en temps pour un motif $\mathbf{p}_k$. Une matrice de mesures $\mathbf{M} \in \mathbb{R}^{K\times\Lambda T}$ est acquise quand une séquence de motifs $\mathbf{P} \in \mathbb{R}^{K\times D}$ est considérée.

Images dépendant uniquement du temps ou de la longueur d'onde A partir des $\Lambda\times T$ images restaurées, il est possible d'extraire T (resp. Λ) images $\mathbf{f}_t$ (resp. $\mathbf{f}_\lambda$) dans chaque canal temporel (resp. spectral) en intégrant $\mathbf{f}_{\lambda,t}$ suivant λ (resp. t) :

$$\mathbf{f}_\lambda = \sum_{t=1}^{T}\mathbf{f}_{\lambda,t} \qquad \mathbf{f}_t = \sum_{\lambda=1}^{\Lambda}\mathbf{f}_{\lambda,t} \tag{C.27}$$

Les images $\mathbf{f}_t$ (resp. $\mathbf{f}_\lambda$) sont équivalentes à celles qui auraient été obtenues sans le spectromètre (resp. TCSPC) de la SPC multispectrale résolue en temps.

Prédiction sur les mesures CW Notre méthode d'acquisition/restauration des images ABS-WP du Chaptitre IV repose sur une étape de prédiction basée sur des mesures scalaires. Pour effectuer cette étape sur les mesures (C.25), nous considérons alors l'image $\mathbf{f}$ en onde continue (*continuous-wave*, CW) obtenue en intégrant $\mathbf{f}_{\lambda,t}$ suivant λ et t :

$$\mathbf{f} = \sum_{\lambda=1}^{\Lambda}\sum_{t=1}^{T}\mathbf{f}_{\lambda,t} \tag{C.28}$$

9. La technique SNMF presentée au Chaptitre V n'est pas utilisée ici car, chronologiquement, cette méthode n'était pas encore implémentée.

Area	Material	Absorption peak	Emission peak
Wave	Green fluorescence plastic slide	464 nm	525 nm
Square	Red fluorescence plastic slide	520 nm	625 nm
Circle	DCM dye painted on a white paper	468 nm	624 nm

TABLEAU C.3 – Pic d'émission et d'absorption des fluorophores constituant le fantôme.

C.6.2 Expériences

Fantôme La Fig. C.11-(a) montre le fantôme considéré pour lequel les différentes formes ont été créées avec un masque en papier orange. Le carré (resp. la vague) est une plaque auto-fluorescente en plastique rouge (resp. verte) de CHROMA. Le rond est quant à lui une solution de DCM dilué dans de l'éthanol et peinte sur une feuille blanche. Une caractérisation spectrale de ces trois fluorophores est donnée au tableau C.3.

Système expérimental Le système expérimental du Politecnico di Milano décrit en Section III.1 est employé. Un PMT à $\Lambda = 16$ canaux spectraux sert de détecteur (PML-16-1, Becker & Hickl GmbH) couplé à une TCSPC (SPC-630, Becker & Hickl GmbH) ayant 4096 canaux temporels. Après binning de ces canaux, un total de $T = 60$ canaux temporels sont obtenus qui couvrent des temps de 0 à 18.00 ns avec un pas de 0.305 ns. L'objet est illuminé dans la bande spectrale $470-490$ nm et un filtre passe-haut (FEL0500, ThorLabs) à 500 nm est placé devant le détecteur afin d'observer la lumière fluorescente émise par l'objet. Concernant les paramètres du spectromètre, sa longueur d'onde centrale est choisie à $\lambda_c = 575$ nm de manière à ce que les $\Lambda = 16$ canaux spectraux couvrent la plage de longueur d'onde de 505 ± 5 nm à 655 ± 5 nm avec un pas de 10 nm.

C.6.3 Résultats et discussion

Résultats La Fig. C.11 donne une photo du fantôme et l'image 64×64 CW restaurée selon (C.28). Elle montre aussi plusieurs images $\mathbf{f}_t$ (resp. $\mathbf{f}_\lambda$) dans différent canaux temporels (resp. spectraux) obtenues par (C.27). Les acquisitions ont été réalisées avec ABS-WP pour l'ondelette de Daubechies avec 5 moments nuls (Db5) (Mallat, 2008; Daubechies, 1992). Un taux de compression (TC) de 93% a été obtenu pour $\mathcal{P} = \{1; 0.85; 0.075; 0\}$.

Les courbes temporelles (resp. spectrales) dans chaque zone du fantôme sont données en Fig. C.12. Celles-ci sont calculées en sommant les pixels de $\mathbf{f}_t$ (resp. $\mathbf{f}_\lambda$) de (C.27) dans chaque zone de l'objet pour chaque canal temporel (resp. spectral).

A partir des images $\mathbf{f}_t$ de (C.27), les cartes d'amplitude et de temps de vie des fluorophores peuvent être estimées par ajustement de courbe d'une fonction exponentielle sur les données expérimentales. La Fig. C.13 montre ces deux cartes.

Discussion Les résultats de la Fig. C.11 montrent que notre méthode ABS-WP permet de restaurer la pile de $\Lambda \times T$ images avec un taux de compression de 93%. L'utilisation de l'image CW (Fig. C.11-

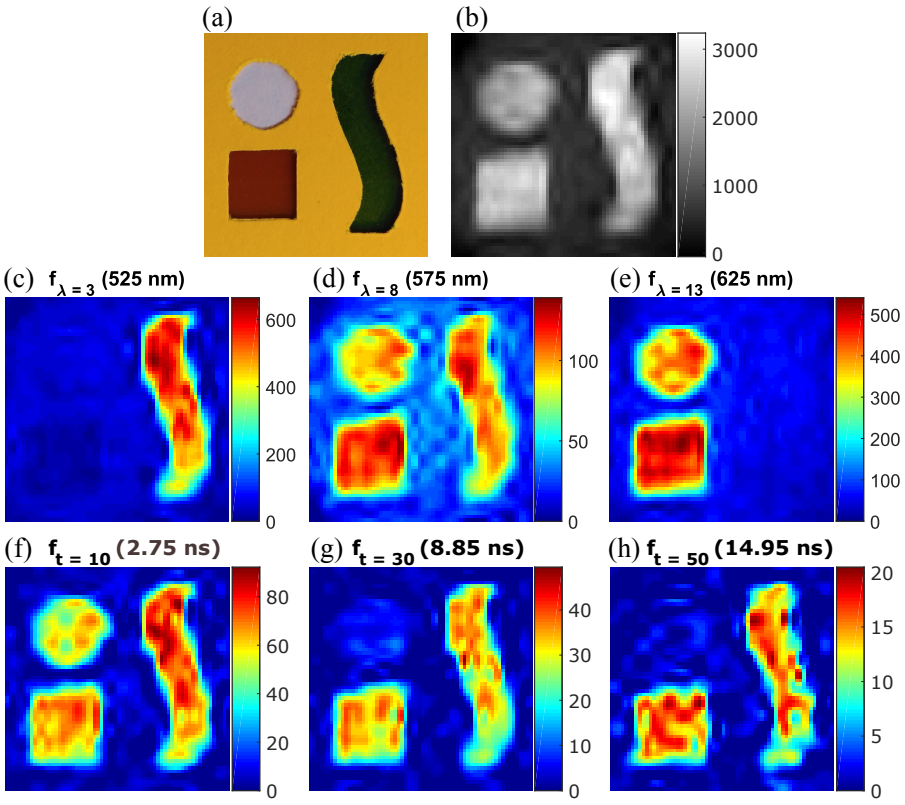

FIGURE C.11 – Fantôme, image CW et images SPC restaurées dans différents canaux temporels et spectraux. (a) Photo du fantôme, (b) image CW, image SPC restaurée dans (c)–(e) 3 canaux spectraux et (f)–(h) 3 canaux temporels.

(b)) pour l'étape de prédiction est justifiée puisque cette image montre les différentes structures de notre fantôme. ABS-WP va donc chercher les coefficients d'ondelettes significatifs pour chaque zone de l'objet.

Si nous regardons les images $\mathbf{f}_\lambda$ dépendant de la longueur d'onde uniquement, seule la vague ressort dans la canal 525 nm et disparaît dans le canal 625 nm. L'effet inverse se produit pour le carré et le cercle. Les courbes spectrales plus détaillées de la Fig. C.12 confirment également ces résultats qui sont en accord avec le tableau C.3.

Concernant l'information temporelle en utilisant les images $\mathbf{f}_t$ dépendantes du temps, le rond montre un temps de vie plus court que les deux autres fluorophores puisqu'il disparait au cours du temps sur les images $\mathbf{f}_t$ de la Fig. C.11 et la décroissance exponentielle sur la Fig. C.12 est plus marquée. Ceci est confirmé par les résultats de la Fig. C.13 où la carte de temps de vie révèle un temps beaucoup plus court pour le rond que pour les deux autres fluorophores.

Au final, l'utilisation de l'information spectrale ou temporelle seule ne permet pas de différentier les trois composantes du fantôme. En revanche, quand ces deux informations sont présentes comme c'est le cas sur notre système, les trois fluorophores sont différentiables : le rond se différencie de la vague et du carré par un temps de vie beaucoup plus court alors que la vague se différencie par son contenu spectral.

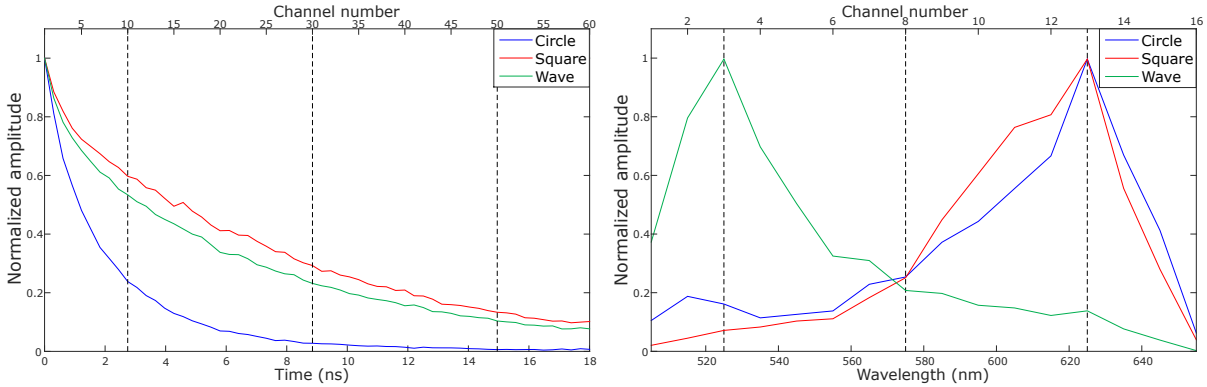

FIGURE C.12 – Courbes spectrales et temporelles obtenues depuis les images $\mathbf{f}_\lambda$ et $\mathbf{f}_t$ en sommant chaque pixel des différentes zones de l'objet. Les barres verticales en pointillée correspondent à différents canaux temporels/spectraux dont les images restaurées sont données en Fig. C.11.

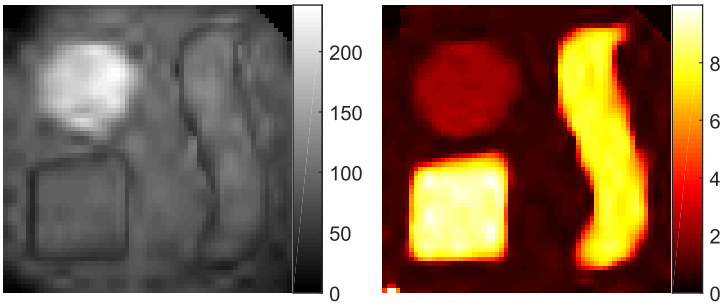

FIGURE C.13 – Cartes d'amplitude (en photons, gauche) et de temps de vie (en ns, droite) de l'objet considéré.

C.6.4 Conclusion du chapitre

Nous avons reporté dans ce chapitre la capacité de notre technique ABS-WP à fonctionner sur une caméro mono-pixel multispectrale résolue en temps. Le système permet d'acquérir efficacement l'information spectrale et temporelle avec de forts taux de compression. La SPC est un excellent compris pour obtenir de bonnes résolutions spatiales, temporelles et spectrales et n'a aucun équivalent similaire actuellement pour le même prix.

Conclusion, limites et perspectives

L'imagerie mono-pixel permet de mesurer la projection de la scène observée sur des motifs à l'aide d'un montage optique équipé d'un simple détecteur ponctuel. Cette implémentation particulière rend ce type d'imagerie intéressante pour des applications médicales, applications visées par cette thèse. La limitation actuelle de la caméra mono-pixel sont les temps d'acquisition et/ou de restauration de l'image qui sont généralement longs. Des applications temps réel ne peuvent alors être considérées telles que l'imagerie interventionnelle (e.g. la chirurgie de fluorescence).

Après avoir détaillé l'état de l'art au niveau matériel (Chaptitre I) et logiciel (Chaptitre II), les contributions de cette thèse ont été exposées.

Dans un premier temps, deux systèmes expérimentaux ont été présentés au Chaptitre III avec l'ajout d'un logiciel de communication entre Labview qui contrôle les instruments et Matlab pour traiter les données. Ceci permet l'implémentation de la technique d'imagerie ABS-WP présentée

au Chaptitre IV qui permet d'acquérir les coefficients d'ondelettes significatifs de l'image observée. Outre des forts taux de compression, cette méthode permet une restauration de l'image directe par transformée en ondelettes inverse. Au Chaptitre V, une méthode par factorisation de matrices est proposée afin de palier deux contraintes expérimentales. La méthode permet, par rapport aux méthodes classiques, de réduire le nombre de mesures et donc d'accélérer les temps d'acquisition. Enfin, au Chaptitre VI, des acquisitions multispectrales résolues en temps donnent une preuve de concept pour aller vers des applications médicales.

En résumé, le but principal de cette thèse d'accélérer les temps d'acquisition et/ou de restauration des images par une SPC est atteint. En effet, la méthode ABS-WP permet de réduire le temps de restauration de l'image alors que la méthode par factorisation de matrices réduit ceux d'acquisitions.

Limites Une première limite des contributions de cette thèse concerne l'étape de prédiction des coefficients d'ondelettes dans ABS-WP. Les résultats montrent une précision maximum de 85% pour trouver les coefficients significatifs. Si cette précision pouvait atteindre 100%, la meilleure image SPC possible serait acquise puisque l'approximation non-linéaire de la transformée en ondelettes est la meilleure possible [10]

ABS-WP permet d'utiliser n'importe quelle ondelette pour laquelle les motifs ont des valeurs réelles flottantes. Le DMD est alors utilisé dans son mode 8-bit ce qui est une seconde limitation puisque le taux de rafraichissement du DMD est impacté. En effet, ce dernier peut atteindre son plus haut taux de rafraichissement quand il fonctionne en mode binaire, ce taux est donc réduit quand 8 bits sont nécessaires, augmentant ainsi les temps d'acquisition. Pour nos acquisitions réelles, ceci n'était pas un problème car la carte de comptage des photons a besoin d'un temps d'acquisition plus long que le taux de rafraichissement du DMD en mode 8-bit. Si des acquisitions rapides sont nécessaires, il est toujours possible d'utiliser notre méthode ABS-WP avec l'ondelette de Haar qui crée des motifs binaires.

Si l'on passe à la méthode de généralisation des motifs, une limite est la combinaison de plusieurs mesures par rapport aux méthodes classiques *pos/neg* et *shift* qui combinent seulement deux mesures. En présence de bruit, la variance de nos mesures désirées finales pour l'algorithme SNMF dépend ainsi d'une somme de variance des mesures SPC acquises. Ceci peut alors accroitre l'effet du bruit et réduire la qualité de l'image restaurée. Cet effet est moins visible avec les méthodes classiques puisque le bruit ne dépend que d'une somme de deux variances.

Perspectives Une première perspective de ce travail de thèse serait d'améliorer la stratégie de prédiction d'ABS-WP. Comme mentionné plus tôt, certains coefficients significatifs d'ondelettes ne sont pas acquis ce qui impacte la qualité de l'image restaurée. Des méthodes plus robustes pour cette prédiction par rapport à l'interpolation bi-cubique pourraient donc être envisagées. Cette étape doit cependant rester assez rapide afin de ne pas ralentir le temps total d'acquisition. Une idée serait d'utiliser les techniques récentes de *deep learning* afin de prédire soit la valeur d'un coefficient d'ondelettes directement ou s'il est significatif ou non. Une telle approche serait rapide puisque la partie d'entrainement d'un réseau de neurones peut se faire a priori sur une base de données de centaines d'images. L'application du réseau sur les nouvelles données est ensuite rapide et pourrait permettre

10. En comparaison avec le même genre d'approximation dans Fourier ou une autre base.

d'augmenter la précision de prédiction.

Une autre perspective concerne la méthode de généralisation des motifs. Cette dernière permet de créer K motifs positifs à partir d'un ensemble de I motifs réels. Avec l'algorithme proposé, une valeur de $K = I+1$ est actuellement obtenue. Cependant, la plupart des algorithmes de factorisation de matrice cherchent une factorisation avec $K < I$. Ces techniques pourraient alors être envisagées afin de réduire le nombre de mesures SPC effectives. Un problème possible serait l'erreur de factorisation qui deviendrait plus importante et les mesures seraient alors erronées. Avoir $K < I$ permettrait également de combiner moins de mesures afin de réduire l'influence du bruit sur les mesures désirées. Une autre possibilité pour palier l'effet du bruit serait d'ajouter une contrainte de parcimonie sur la matrice $\mathbf{T}$. Si cette matrice a des zéros, le vecteur des mesures désirées serait ainsi créé avec moins de combinaisons de mesures SPC.

Au niveau des acquisitions multispectrales résolue en temps du Chaptitre VI, l'étape de prédiction de ABS-WP était basée sur les mesures en onde-continue qui intègrent tous les canaux spectraux et temporels. Cependant, certains de ces canaux ne reçoivent pas beaucoup d'information et n'apportent ainsi que très peu d'information aux mesures CW. Afin de maximiser la précision de l'étape de prédiction, une étape préliminaire juste avant celle-ci pourrait être ajoutée. Cette nouvelle étape chercherait les canaux spectraux et temporels qui amènent le moins d'information afin de ne pas les intégrer pour créer la mesure CW [11].

Du côté des applications, la prochaine marche serait d'appliquer les méthodes développées dans cette thèse pour l'imagerie interventionnelle, e.g. la chirurgie guidée par fluorescence pour la résection de tumeurs au cerveau imagées par une SPC hyperspectrale. Ceci est un travail complet en soi puisque les techniques de cette thèse devraient être adaptées pour l'imagerie vidéo. L'exploitation de la donnée temporelle (i.e. la frame à $t+1$ ressemble à celle à t) et l'utilisation de certaines des autres perspectives mentionnées plus tôt pourraient permettre de compresser encore plus les données afin d'atteindre des images à des taux vidéos [12]. Une fois l'extension d'ABS-WP aux vidéos faite, la SPC couplée à un spectromètre dernier cri devrait permettre de discerner les marges tumorales des tissus sains.

11. Par définition, si certains canaux ne sont pas pris en compte, cette mesure ne serait pas une mesure CW à proprement parler.

12. Pour la chirurgie guidée par fluorescence, 1 Hz peut être considéré comme temps réel.

APPENDIX D

LIST OF PERSONAL PUBLICATIONS

D.1 Journal

[J1] Rousset, F., Ducros, N., Farina, A., Valentini, G., D'Andrea, C., Peyrin, F., March 2017. Adaptive basis scan by wavelet prediction for single-pixel imaging. IEEE Transactions on Computational Imaging 3 (1), 36-46.

[J2] Rousset, F., Peyrin, F., Ducros, N. A Semi Nonnegative Matrix Factorization Method for Pattern Generalization in Single-Pixel Imaging. IEEE Transactions on Computational Imaging, submitted.

[J3] Rousset, F., Ducros, N., Farina, A., Valentini, G., D'Andrea, C., Peyrin, F. Time-resolved multispectral acquisitions by means of adaptive single-pixel imaging. Optics Express, to be submitted.

D.2 Pattent

[P1] Rousset, F., Ducros, N., Peyrin, F., 2017. Caméra mono-pixel. FR Patent 1751515 filed the 02/24/2017.

D.3 International conferences (with proceedings)

[C1] Rousset, F., Ducros, N., D'Andrea, C., Peyrin, F., August 2015. Single pixel camera : An acquisition strategy based on the non-linear wavelet approximation. 2015 37th Annual International Conference of the IEEE Engineering in Medicine and Biology Society (EMBC), 6240–6243

[C2] Rousset, F., Ducros, N., Farina, A., Valentini, G., D'Andrea, C., Peyrin, F., April 2016. Adaptive acquisitions in biomedical optical imaging based on single pixel camera : Comparison with compressive sensing. 2016 IEEE 13th International Symposium on Biomedical Imaging (ISBI), 680–683.

[C3] Rousset, F., Ducros, N., Farina, A., Valentini, G., D'Andrea, C., Peyrin, F., February 2017. Time-resolved wavelet-based acquisitions using a single-pixel camera. Proc. SPIE. Vol. 10070, 1007016 –1007016–7.

D.4 National communications

[N1] Rousset, F., Ducros, N., D'Andrea, C., Peyrin, F., Mars 2015. A wavelet-based non-linear acquisition strategy for single pixel camera acquisitions. Journées RITS 2015, Dourdan, France, 144-145, 2015.

[N2] Rousset F., Ducros, N., Peyrin, F., Mars 2015. Single-pixel camera : stratégie d'acquisition non linéaire basée sur les ondelettes. 10e Journées Imagerie Optique Non Conventionnelle, Paris, France, 2015.

[N3] Rousset, F., Ducros, N., Andrea, F., D'Andrea, C., Peyrin, F., Mars 2016. Acquisition adaptative pour single-pixel caméra : comparaison avec l'acquisition comprimée. 11e Journées Imagerie Optique Non Conventionnelle, Paris, France, 2016.

[N4] Rousset, F., Ducros, N., Farina, A., Gianluca, V., D'Andrea, C., et Peyrin, F., Mars 2017. Acquisitions adaptatives multispectrales et résolues en temps par une caméra mono-pixel. 12e Journées Imagerie Optique Non Conventionnelle, Paris, France, 2017.

[N5] Rousset, F., Ducros, N., Farina, A., D'Andrea, C., Peyrin, F., Mars 2017. Fluorescence lifetime imaging using a multispectral time-resolved wavelet-based single pixel imaging system. Journées RITS 2017, Lyon, France, 2017.

[N6] Rousset, F., Ducros, N., Peyrin, F., Septembre 2017. Technique de factorisation en matrices semi non-négatives pour acquisition d'images par caméra mono-pixel. GRETSI 2017, Juan-les-pins, France.

BIBLIOGRAPHY

Allier, C. P., Hiernard, G., Poher, V., Dinten, J. M., Oct 2010. Bacteria detection with thin wetting film lensless imaging. Biomed. Opt. Express 1 (3), 762–770. 16

Asif, M. S., Ayremlou, A., Sankaranarayanan, A. C., Veeraraghavan, A., Baraniuk, R. G., 2015a. Flatcam : Thin, bare-sensor cameras using coded aperture and computation. CoRR abs/1509.00116. 16

Asif, M. S., Ayremlou, A., Veeraraghavan, A., Baraniuk, R., Sankaranarayanan, A., Dec 2015b. Flatcam : Replacing lenses with masks and computation. In : 2015 IEEE International Conference on Computer Vision Workshop (ICCVW). pp. 663–666. 16

Aßmann, M., Bayer, M., 2013. Compressive adaptive computational ghost imaging. Scientific Reports 3 (1545). 13

Averbuch, A., Dekel, S., Deutsch, S., 2012. Adaptive compressed image sensing using dictionaries. SIAM Journal on Imaging Sciences 5 (1), 57–89. 31, 65, 74

Baraniuk, R., 2007. Compressive sensing. IEEE Signal Processing Mag, 118–120. 23

Baraniuk, R., Baron, D., Duarte, M., Kelly, K., Lane, C., Laska, J., Takhar, D., Wakin, M., Sep. 30 2014. Method and apparatus for compressive imaging device. US Patent 8848091. 7, 114

Baraniuk, R., Davenport, M., Devore, R., Wakin, M., 2007. A simple proof of the restricted isometry property for random matrices. Constr. Approx 2008. 23

Baraniuk, R. G., Cevher, V., Duarte, M. F., Hegde, C., April 2010. Model-based compressive sensing. IEEE Transactions on Information Theory 56 (4), 1982–2001. 23

Baraniuk, R. G., Goldstein, T., Sankaranarayanan, A. C., Studer, C., Veeraraghavan, A., Wakin, M. B., Jan 2017. Compressive video sensing : Algorithms, architectures, and applications. IEEE Signal Processing Magazine 34 (1), 52–66. 15

Becker, W., 2012. Fluorescence lifetime imaging – techniques and applications. Journal of Microscopy 247 (2), 119–136. 1, 91, 112

Ben-Yosef, N., Sirat, G., 1982. Real-time spatial filtering utilizing the piezoelectric-elasto-optic effect. Optica Acta : International Journal of Optics 29 (4), 419–423. 1

Bernal, E., Mestha, L., Austin, P., Loce, R., Nov. 17 2015. Single-pixel camera architecture with simultaneous multi-band acquisition. US Patent 9188785. 14

Berry, M. W., Browne, M., Langville, A. N., Pauca, V. P., Plemmons, R. J., 2006. Algorithms and applications for approximate nonnegative matrix factorization. In : Computational Statistics and Data Analysis. pp. 155–173. 74, 77

Bian, L., Suo, J., Hu, X., Chen, F., Dai, Q., 2016a. Efficient single pixel imaging in fourier space. Journal of Optics 18 (8), 085704. 27, 28

Bian, L., Suo, J., Situ, G., Li, Z., Fan, J., Chen, F., Dai, Q., 2016b. Multispectral imaging using a single bucket detector. Scientific Reports 6 (24752). 14

Bonaccorso, F., Sun, Z., Hasan, T., Ferrari, A., 2010. Graphene photonics and optoelectronics. Nature photonics 4 (9), 611–622. 17

Boominathan, V., Adams, J. K., Asif, M. S., Avants, B. W., Robinson, J. T., Baraniuk, R. G., Sankaranarayanan, A. C., Veeraraghavan, A., Sept 2016. Lensless imaging : A computational renaissance. IEEE Signal Processing Magazine 33 (5), 23–35. 16

Bucak, S. S., Gunsel, B., Sept 2007. Video content representation by incremental non-negative matrix factorization. In : 2007 IEEE International Conference on Image Processing. Vol. 2. pp. II – 113–II – 116. 74

Candes, E., Romberg, J., 2005. l1-magic : Recovery of sparse signals via convex programming. 24

Candes, E., Romberg, J., Tao, T., Feb 2006. Robust uncertainty principles : exact signal reconstruction from highly incomplete frequency information. Information Theory, IEEE Transactions on 52 (2), 489–509. 23, 24

Candes, E., Tao, T., Dec 2006. Near-optimal signal recovery from random projections : Universal encoding strategies? Information Theory, IEEE Transactions on 52 (12), 5406–5425. 23

Chan, W. L., Charan, K., Takhar, D., Kelly, K. F., Baraniuk, R. G., Mittleman, D. M., 2008. A single-pixel terahertz imaging system based on compressed sensing. Applied Physics Letters 93 (12). 13, 25

Chen, H., Xi, N., Song, B., Chen, L., Lai, K. W. C., Oct 2011. Single pixel infrared camera using a carbon nanotube photodetector. In : Sensors, 2011 IEEE. pp. 1362–1366. 16, 17

Chen, L., Zhou, Z., Xi, N., Yang, R., Song, B., Sun, Z., Su, C., Nov 2014. Super resolution infrared camera using single carbon nanotube photodetector. In : SENSORS, 2014 IEEE. pp. 1038–1041. 16, 17

Cichocki, A., Zdunek, R., Amari, S., May 2006. New algorithms for non-negative matrix factorization in applications to blind source separation. In : 2006 IEEE International Conference on Acoustics Speech and Signal Processing Proceedings. Vol. 5. pp. V–V. 74

Clemente, P., Durán, V., Tajahuerce, E., Andrés, P., Climent, V., Lancis, J., Jul 2013. Compressive holography with a single-pixel detector. Opt. Lett. 38 (14), 2524–2527. 9, 115

Cohen, A., Daubechies, I., Feauveau, J. C., 1992. Biorthogonal bases of compactly supported wavelets. Communications on Pure and Applied Mathematics 45 (5), 485–560. 59

Coifman, R., Geshwind, F., Meyer, Y., 2001. Noiselets. Applied and Computational Harmonic Analysis 10 (1), 27–44. 34

Dai, H., Gu, G., He, W., Liao, F., Zhuang, J., Liu, X., Chen, Q., Oct 2014. Adaptive compressed sampling based on extended wavelet trees. Appl. Opt. 53 (29), 6619–6628. 32, 59, 62, 63, 65, 66, 73, 74, 75, 124, 125, 128

Dai, H., Gu, G., He, W., Ye, L., Mao, T., Chen, Q., Nov 2016. Adaptive compressed photon counting 3d imaging based on wavelet trees and depth map sparse representation. Opt. Express 24 (23), 26080–26096. 15

D'Andrea, C., Comelli, D., Pifferi, A., Torricelli, A., Valentini, G., Cubeddu, R., 2003. Time-resolved optical imaging through turbid media using a fast data acquisition system based on a gated ccd camera. Journal of Physics D : Applied Physics 36 (14), 1675–1681. 91

D'Andrea, C., Ducros, N., Bassi, A., Arridge, S., Valentini, G., 2010. Fast 3d optical reconstruction in turbid media using spatially modulated light. Biomed. Opt. Express 1 (2), 471–481. 2, 39, 91, 112, 119

Daubechies, I., 1992. Ten Lectures on Wavelets. Society for Industrial and Applied Mathematics. 53, 54, 95, 123, 134

Davenport, M. A., Arias-Castro, E., July 2012. Compressive binary search. In : Information Theory Proceedings (ISIT), 2012 IEEE International Symposium on. pp. 1827–1831. 35

de Fréin, R., Drakakis, K., Rickard, S., Cichocki, A., 2008. Analysis of financial data using non-negative matrix factorization. In : International Mathematical Forum. Vol. 3. Journals of Hikari Ltd, pp. 1853–1870. 74

Deutsch, S., Averbush, A., Dekel, S., May 2009. Adaptive compressed image sensing based on wavelet modeling and direct sampling. In : Laurent Fesquet and Bruno Torrésani (Ed.), SAMPTA'09. Marseille, France, p. General session. 31, 32, 65, 74

Ding, C., Li, T., Jordan, M., Jan 2010. Convex and semi-nonnegative matrix factorizations. IEEE Transactions on Pattern Analysis and Machine Intelligence 32 (1), 45–55. 74, 127

Donoho, D. L., 2006. Compressed sensing. IEEE Trans. Inform. Theory 52, 1289–1306. 1, 7, 23, 24, 35, 112, 114, 117

Duan, P., Wang, Y., Xu, D., Yan, C., Yang, Z., Xu, W., Shi, W., Yao, J., May 2016. Single pixel imaging with tunable terahertz parametric oscillator. Appl. Opt. 55 (13), 3670–3675. 13

Duarte, M., Davenport, M., Takhar, D., Laska, J., Sun, T., Kelly, K., Baraniuk, R., March 2008. Single-pixel imaging via compressive sampling. Signal Processing Magazine, IEEE 25 (2), 83–91. 7, 8, 12, 13, 22, 23, 25, 26, 59, 73, 75, 114, 115, 124, 128

Ducros, N., Bassi, A., Valentini, G., Canti, G., Arridge, S., D'Andrea, C., 2013. Fluorescence molecular tomography of an animal model using structured light rotating view acquisition. Journal of Biomedical Optics 18 (2), 020503–020503. 2, 39, 91, 112, 119

Ducros, N., Correia, T., Bassi, A., Valentini, G., Arridge, S., D'Andrea, C., 2016. Reconstruction of an optical inhomogeneity map improves fluorescence diffuse optical tomography. Biomedical Physics & Engineering Express 2 (5), 055020. 2, 39, 91, 112, 119

Duran, V., Soldevila, F., Irles, E., Clemente, P., Tajahuerce, E., Andrés, P., Lancis, J., Jun 2015. Compressive imaging in scattering media. Opt. Express 23 (11), 14424–14433. 2, 25, 91, 112

Edgar, M. P., Gibson, G. M., Bowman, R. W., Sun, B., Radwell, N., Mitchell, K. J., Welsh, S. S., Padgett, M. J., 2015. Simultaneous real-time visible and infrared video with single-pixel detectors. Scientific reports 5. 13, 15, 25

Foucart, S., Rauhut, H., 2013. A mathematical introduction to compressive sensing. Vol. 1. Springer. 24, 28

Fursich, B., Bamler, R., Augustin, S., Hubers, H. W., Zhu, X. X., Sept 2016. Towards single-pixel fmcw radar reconstruction. In : 2016 4th International Workshop on Compressed Sensing Theory and its Applications to Radar, Sonar and Remote Sensing (CoSeRa). pp. 95–99. 13

Gall, D. L., Tabatabai, A., April 1988. Sub-band coding of digital images using symmetric short kernel filters and arithmetic coding techniques. International Conferance on Acoustics, Speech, and Signal Processing 2, 761–764. 59

Gibson, A., Dehghani, H., 2009. Diffuse optical imaging. Philosophical Transactions of the Royal Society of London A : Mathematical, Physical and Engineering Sciences 367 (1900), 3055–3072. 2, 91, 112

Gibson, G. M., Sun, B., Edgar, M. P., Phillips, D. B., Hempler, N., Maker, G. T., Malcolm, G. P. A., Padgett, M. J., Feb 2017. Real-time imaging of methane gas leaks using a single-pixel camera. Opt. Express 25 (4), 2998–3005. 13, 15

Gillis, N., 2014. The why and how of nonnegative matrix factorization. In : Regularization, Optimization, Kernels, and Support Vector Machines. Chapman and Hall/CRC, pp. 257–291. 74, 77

Gillis, N., Kumar, A., 2015. Exact and heuristic algorithms for semi-nonnegative matrix factorization. SIAM Journal on Matrix Analysis and Applications 36 (4), 1404–1424. 78, 79, 86, 127, 130

Goldstein, T., Xu, L., Kelly, K. F., Baraniuk, R., Dec 2015. The stone transform : Multi-resolution image enhancement and compressive video. IEEE Transactions on Image Processing 24 (12), 5581–5593. 15

Hadfield, R. H., 2009. Single-photon detectors for optical quantum information applications. Nature photonics 3 (12), 696–705. 1, 11, 112

Hahn, J., Debes, C., Leigsnering, M., Zoubir, A. M., 2014. Compressive sensing and adaptive direct sampling in hyperspectral imaging. Digital Signal Processing 26, 113 – 126. 14, 32, 74

Herman, M. A., Weston, T., McMackin, L., Li, Y., Chen, J., Kelly, K. F., 2015. Recent results in single-pixel compressive imaging using selective measurement strategies. Vol. 9484. pp. 94840A–94840A–18. 35, 36

Hornbeck, L., Oct. 29 1991. Spatial light modulator and method. US Patent 5061049. 8, 115

Howland, G. A., Lum, D. J., Ware, M. R., Howell, J. C., Oct 2013. Photon counting compressive depth mapping. Opt. Express 21 (20), 23822–23837. 15

Huang, G., Jiang, H., Matthews, K., Wilford, P., Sept 2013. Lensless imaging by compressive sensing. In : 2013 IEEE International Conference on Image Processing. pp. 2101–2105. 8, 11, 16, 17, 115

Huo, Y.-R., He, H.-J., Chen, F., Tai, H.-M., Jan 2017. Adaptive single-pixel imaging based on guided coefficients. J. Opt. Soc. Am. A 34 (1), 39–51. 32, 65, 74

Huynh, N., Zhang, E., Betcke, M., Arridge, S., Beard, P., Cox, B., Jan 2016. Single-pixel optical camera for video rate ultrasonic imaging. Optica 3 (1), 26–29. 16

Indyk, P., Price, E., Woodruff, D. P., Oct 2011. On the power of adaptivity in sparse recovery. In : Foundations of Computer Science (FOCS), 2011 IEEE 52nd Annual Symposium on. pp. 285–294. 35

Jacques, S. L., 2013. Optical properties of biological tissues : a review. Physics in Medicine and Biology 58 (11), R37. 1, 112

Keramidas, M., Josserand, V., Righini, C. A., Wenk, C., Faure, C., Coll, J. L., 2010. Intraoperative near-infrared image-guided surgery for peritoneal carcinomatosis in a preclinical experimental model. British Journal of Surgery 97 (5), 737–743. 59, 124

Keys, R., Dec 1981. Cubic convolution interpolation for digital image processing. Acoustics, Speech and Signal Processing, IEEE Transactions on 29 (6), 1153–1160. 61

Kirmani, A., Colaço, A., Wong, F. N. C., Goyal, V. K., Oct 2011. Exploiting sparsity in time-of-flight range acquisition using a single time-resolved sensor. Opt. Express 19 (22), 21485–21507. 15

Kuo, D. M.-T., Fang, A., Chang, Y., 2001. Theoretical modeling of dark current and photo-response for quantum well and quantum dot infrared detectors. Infrared Physics & Technology 42 (35), 433 – 442. 17

Lee, D. D., Seung, H. S., 1999. Learning the parts of objects by nonnegative matrix factorization. Nature 401, 788–791. 73, 74, 78, 127

Lee, D. D., Seung, H. S., 2001. Algorithms for non-negative matrix factorization. In : NIPS. MIT Press, pp. 556–562. 73, 74, 78

Li, C., 2009. An efficient algorithm for total variation regularization with applications to the single pixel camera and compressive sensing. Ph.D. thesis, Rice University. 24, 59

Li, G., Wang, W., Wang, Y., Yang, W., Liu, L., Jan 2016. Single-pixel camera with one graphene photodetector. Opt. Express 24 (1), 400–408. 17

Li, X., Orchard, M., Oct 2001. New edge-directed interpolation. Image Processing, IEEE Transactions on 10 (10), 1521–1527. 61

Li, Z., Suo, J., Hu, X., Deng, C., Fan, J., Dai, Q., 2017. Efficient single-pixel multispectral imaging via non-mechanical spatio-spectral modulation. Scientific Reports 7. 15

Lin, C.-J., Oct. 2007. Projected gradient methods for nonnegative matrix factorization. Neural Comput. 19 (10), 2756–2779. 74, 78

Liu, B.-L., Yang, Z.-H., Liu, X., Wu, L.-A., 2017. Coloured computational imaging with single-pixel detectors based on a 2d discrete cosine transform. Journal of Modern Optics 64 (3), 259–264. 27, 29, 74

Lochocki, B., Gambín, A., Manzanera, S., Irles, E., Tajahuerce, E., Lancis, J., Artal, P., Oct 2016. Single pixel camera ophthalmoscope. Optica 3 (10), 1056–1059. 2, 91, 112

Lochocki, B., Gambin, A., Manzanera, S., Irles, E., Tajahuerce, E., Lancis, J., Artal, P., 2017. A single pixel camera video ophthalmoscope. In : Proc. SPIE. Vol. 10057. pp. 100570M–100570M–7. 2, 91, 112

Ma, D., Bec, J., Gorpas, D., Yankelevich, D., Marcu, L., Mar 2015. Technique for real-time tissue characterization based on scanning multispectral fluorescence lifetime spectroscopy (ms-trfs). Biomed. Opt. Express 6 (3), 987–1002.
URL http://www.osapublishing.org/boe/abstract.cfm?URI=boe-6-3-987 91, 102

Ma, J., Oct 2009a. A single-pixel imaging system for remote sensing by two-step iterative curvelet thresholding. IEEE Geoscience and Remote Sensing Letters 6 (4), 676–680. 1, 25, 112

Ma, J., April 2009b. Single-pixel remote sensing. IEEE Geoscience and Remote Sensing Letters 6 (2), 199–203. 1, 25, 112

Ma, Y., Grant, J., Saha, S., Cumming, D. R. S., May 2012. Terahertz single pixel imaging based on a nipkow disk. Opt. Lett. 37 (9), 1484–1486. 13

Magalhaes, F., Abolbashari, M., Araujo, F. M., Correia, M. V., Farahi, F., 2012. High-resolution hyperspectral single-pixel imaging system based on compressive sensing. Optical Engineering 51 (7), 071406–1–071406–6. 14, 25

Magalhaes, F., Araujo, F. M., Correia, M. V., Abolbashari, M., Farahi, F., Feb 2011. Active illumination single-pixel camera based on compressive sensing. Appl. Opt. 50 (4), 405–414. 25

Mallat, S., Jul 1989. A theory for multiresolution signal decomposition : the wavelet representation. Pattern Analysis and Machine Intelligence, IEEE Transactions on 11 (7), 674–693. 31, 52

Mallat, S., Dec. 2008. A Wavelet Tour of Signal Processing, Third Edition : The Sparse Way, 3rd Edition. Academic Press. 31, 51, 52, 55, 65, 95, 123, 134

Malloy, M. L., Nowak, R. D., July 2014. Near-optimal adaptive compressed sensing. IEEE Transactions on Information Theory 60 (7), 4001–4012. 35

Marcu, L., 2012. Fluorescence lifetime techniques in medical applications. Annals of Biomedical Engineering 40 (2), 304–331. 91, 102

Martínez-León, L., Clemente, P., Mori, Y., Climent, V., Lancis, J., Tajahuerce, E., Mar 2017. Single-pixel digital holography with phase-encoded illumination. Opt. Express 25 (5), 4975–4984. 14

Miao, X., Amirparviz, B., Jun. 30 2015. Single pixel camera. US Patent 9071739. 7, 114

Nystrom, P., Mestha, L., Bernal, E., Wen, X., Gulvin, P., Feb. 2 2016. Hyperspectral single pixel imager with fabry perot filter. US Patent 9253420. 14

Onose, S., Takahashi, M., Mizutani, Y., Yasui, T., Yamamoto, H., 2016. Single pixel imaging with a high-frame-rate led array. In : JSAP-OSA Joint Symposia 2016 Abstracts. Optical Society of America, pp. 13a–C301–10. 13

Ozcan, A., McLeod, E., 2016. Lensless imaging and sensing. Annual Review of Biomedical Engineering 18, 77–102. 16

Paatero, P., Tapper, U., 1994. Positive matrix factorization : A non-negative factor model with optimal utilization of error estimates of data values. Environmetrics 5 (2), 111–126. 73, 74, 78

Park, S. C., Park, M. K., Kang, M. G., 2003. Super-resolution image reconstruction : a technical overview. Signal Processing Magazine, IEEE 20 (3), 21–36. 65

Petersen, K. B., Pedersen, M. S., *et al.*, 2008. The matrix cookbook. Technical University of Denmark 7, 15. 109

Petrovici, M. A., Damian, C., Udrea, C., Garoi, F., Coltuc, D., June 2016. Single pixel camera with compressive sensing by non-uniform sampling. In : 2016 International Conference on Communications (COMM). pp. 443–448. 35

Phillips, D. B., Sun, M.-J., Taylor, J. M., Edgar, M. P., Barnett, S. M., Gibson, G. G., Padgett, M. J., 2016. Adaptive foveated single-pixel imaging with dynamic super-sampling. arXiv preprint arXiv :1607.08236. 15

Pian, Q., Yao, R., Intes, X., 2016a. Time-resolved hyperspectral single-pixel camera implementation for compressive wide-field fluorescence lifetime imaging. In : Proc. SPIE. Vol. 9701. pp. 970115–970115–6. 2, 91, 112, 132

Pian, Q., Yao, R., Sinsuebphon, N., Intes, X., 2016b. Hyperspectral compressive single-pixel imager for fluorescence lifetime sensing. In : Biomedical Optics 2016. Optical Society of America, p. OTu2C.7. 2, 91, 112, 132

Pian, Q., Yao, R., Zhao, L., Intes, X., 2015. Hyperspectral time-resolved wide-field fluorescence molecular tomography based on structured light and single-pixel detection. Optics Letters 40, 431–434. 2, 91, 112

Pratt, W., Kane, J., Andrews, H. C., Jan 1969. Hadamard transform image coding. Proceedings of the IEEE 57 (1), 58–68. 27

Radwell, N., Mitchell, K. J., Gibson, G. M., Edgar, M. P., Bowman, R., Padgett, M. J., Nov 2014. Single-pixel infrared and visible microscope. Optica 1 (5), 285–289. 2, 12, 13, 14, 34, 35, 74, 100

Rodriguez, A., Clemente, P., Tajahuerce, E., Lancis, J., 2016. Dual-mode optical microscope based on single-pixel imaging. Optics and Lasers in Engineering 82, 87 – 94. 2, 13, 25, 100

Rogalski, A., 2012. History of infrared detectors. Opto-Electronics Review 20 (3), 279–308. 1, 11, 112

Rousset, F., Ducros, N., D'Andrea, C., Peyrin, F., Aug 2015. Single pixel camera : An acquisition strategy based on the non-linear wavelet approximation. In : 2015 37th Annual International Conference of the IEEE Engineering in Medicine and Biology Society (EMBC). pp. 6240–6243. 51, 123

Rousset, F., Ducros, N., Farina, A., Valentini, G., D'Andrea, C., Peyrin, F., April 2016. Adaptive acquisitions in biomedical optical imaging based on single pixel camera : Comparison with compressive sensing. In : 2016 IEEE 13th International Symposium on Biomedical Imaging (ISBI). pp. 680–683. 51, 123

Rousset, F., Ducros, N., Farina, A., Valentini, G., D'Andrea, C., Peyrin, F., March 2017a. Adaptive basis scan by wavelet prediction for single-pixel imaging. IEEE Transactions on Computational Imaging 3 (1), 36–46. 3, 39, 51, 73, 74, 75, 80, 113, 123, 128

Rousset, F., Ducros, N., Farina, A., Valentini, G., D'Andrea, C., Peyrin, F., 2017b. Time-resolved wavelet-based acquisitions using a single-pixel camera. In : Proc. SPIE. Vol. 10070. pp. 1007016–1007016–7. 2, 3, 39, 91, 112, 113, 133

Rousset, F., Ducros, N., Peyrin, F., 2017c. Caméra mono-pixel. FR Patent 1751515 filed the 02/24/2017. 3, 73, 113, 127

Rousset, F., Peyrin, F., Ducros, N., 2017d. A semi nonnegative matrix factorization technique for pattern generalization in single-pixel imaging. IEEE Transactions on Computational Imaging, Submitted. 3, 73, 113, 127

Salvador-Balaguer, E., Clemente, P., Tajahuerce, E., Pla, F., Lancis, J., Apr 2016. Full-color stereoscopic imaging with a single-pixel photodetector. J. Display Technol. 12 (4), 417–422. 12, 15

Sankaranarayanan, A. C., Herman, M. A., Turaga, P., Kelly, K. F., Sept 2016. Enhanced compressive imaging using model-based acquisition : Smarter sampling by incorporating domain knowledge. IEEE Signal Processing Magazine 33 (5), 81–94. 15, 35, 36

Sankaranarayanan, A. C., Xu, L., Studer, C., Li, Y., Kelly, K. F., Baraniuk, R. G., 2015. Video compressive sensing for spatial multiplexing cameras using motion-flow models. SIAM Journal on Imaging Sciences 8 (3), 1489–1518. 15, 16

Shapiro, J. H., Dec 2008. Computational ghost imaging. Phys. Rev. A 78, 061802. 13

Shapiro, J. M., Dec 1993. Embedded image coding using zerotrees of wavelet coefficients. Signal Processing, IEEE Transactions on 41 (12), 3445–3462. 31

Shin, J., Bosworth, B. T., Foster, M. A., Mar 2016. Single-pixel imaging using compressed sensing and wavelength-dependent scattering. Opt. Lett. 41 (5), 886–889. 1, 13, 112

Shin, J., Bosworth, B. T., Foster, M. A., Jan 2017. Compressive fluorescence imaging using a multi-core fiber and spatially dependent scattering. Opt. Lett. 42 (1), 109–112. 13

Shrekenhamer, D., Watts, C. M., Padilla, W. J., May 2013. Terahertz single pixel imaging with an optically controlled dynamic spatial light modulator. Opt. Express 21 (10), 12507–12518. 13

Soldevila, F., Salvador-Balaguer, E., Clemente, P., Tajahuerce, E., Lancis, J., 09 2015. High-resolution adaptive imaging with a single photodiode. Scientific Reports (5). 33, 34, 35, 36

Starling, D. J., Storer, I., Howland, G. A., Jul 2016. Compressive sensing spectroscopy with a single pixel camera. Appl. Opt. 55 (19), 5198–5202. 15

Stork, D. G., Gill, P. R., 2013. Lensless ultra-miniature cmos computational imagers and sensors. In : International Conference on Sensor Technologies and Applications. Citeseer, pp. 186–190. 16

Studer, V., Bobin, J., Chahid, M., Shams Mousavi, H., Candes, E., Dahan, M., 2012. Compressive fluorescence microscopy for biological and hyperspectral imaging. In : Proceedings of the National Academy of Sciences of the USA. Vol. 109 (26). pp. E1679–E1687. 2, 13, 25, 42, 120

Sun, B., Edgar, M. P., Bowman, R., Vittert, L. E., Welsh, S., Bowman, A., Padgett, M. J., 2013. 3d computational imaging with single-pixel detectors. Science 340 (6134), 844–847. 15

Sun, M.-J., Edgar, M. P., Gibson, G. M., Sun, B., Radwell, N., Lamb, R., Padgett, M. J., 2016a. Single-pixel three-dimensional imaging with time-based depth resolution. Nature Communications 7. 14, 15

Sun, M.-J., Edgar, M. P., Phillips, D. B., Gibson, G. M., Padgett, M. J., May 2016b. Improving the signal-to-noise ratio of single-pixel imaging using digital microscanning. Opt. Express 24 (10), 10476–10485. 27

Tajahuerce, E., Durán, V., Clemente, P., Irles, E., Soldevila, F., Andrés, P., Lancis, J., Jul 2014. Image transmission through dynamic scattering media by single-pixel photodetection. Opt. Express 22 (14), 16945–16955. 2, 25, 91, 112

Takhar, D., Laska, J. N., Wakin, M. B., Duarte, M. F., Baron, D., Sarvotham, S., Kelly, K. F., Baraniuk, R. G., 2006. A new compressive imaging camera architecture using optical-domain compression. In : in Proc. of Computational Imaging IV at SPIE Electronic Imaging. pp. 43–52. 1, 7, 8, 12, 17, 22, 23, 25, 26, 59, 112, 114, 115, 117, 124

Taubman, D. S., Marcellin, M. W., 2001. JPEG 2000 : Image Compression Fundamentals, Standards and Practice. Kluwer Academic Publishers, Norwell, MA, USA. 51, 52

Temizel, A., Vlachos, T., Feb 2005. Wavelet domain image resolution enhancement using cycle-spinning. Electronics Letters 41 (3), 119–121. 61

Torabzadeh, M., Park, I.-Y., Bartels, R. A., Durkin, A. J., Tromberg, B. J., 2017. Compressed single pixel imaging in the spatial frequency domain. Journal of Biomedical Optics 22 (3), 030501. 2, 35, 36, 91, 112

Wahl, M., 2014. Time-correlated single photon counting. Tech. rep., PicoQuant GmbH. URL http://www.picoquant.com 41

Wang, D., Li, T., Zhu, S., Ding, C., 2008. Multi-document summarization via sentence-level semantic analysis and symmetric matrix factorization. In : Proceedings of the 31st Annual International ACM SIGIR Conference on Research and Development in Information Retrieval. SIGIR '08. ACM, New York, NY, USA, pp. 307–314. 73

Wang, Y. X., Zhang, Y. J., June 2013. Nonnegative matrix factorization : A comprehensive review. IEEE Transactions on Knowledge and Data Engineering 25 (6), 1336–1353. 74, 77

Watts, C. M., Shrekenhamer, D., Montoya, J., Lipworth, G., Hunt, J., Sleasman, T., Krishna, S., Smith, D. R., Padilla, W. J., 2014. Terahertz compressive imaging with metamaterial spatial light modulators. Nature Photonics 8 (8), 605–609. 8, 9, 13

Welsh, S. S., Edgar, M. P., Bowman, R., Jonathan, P., Sun, B., Padgett, M. J., Oct 2013. Fast full-color computational imaging with single-pixel detectors. Opt. Express 21 (20), 23068–23074. 12, 25

Welsh, S. S., Edgar, M. P., Bowman, R., Sun, B., Padgett, M. J., 2015. Near video-rate linear stokes imaging with single-pixel detectors. Journal of Optics 17 (2), 025705. 27

Xia, F., Mueller, T., Lin, Y.-m., Valdes-Garcia, A., Avouris, P., 2009. Ultrafast graphene photodetector. Nature nanotechnology 4 (12), 839–843. 17

Yu, W.-K., Li, M.-F., Yao, X.-R., Liu, X.-F., Wu, L.-A., Zhai, G.-J., Mar 2014a. Adaptive compressive ghost imaging based on wavelet trees and sparse representation. Opt. Express 22 (6), 7133–7144. 13, 33, 35, 36, 65

Yu, W.-K., Liu, X.-F., Yao, X.-R., Wang, C., Zhai, Y., Zhai, G.-J., 2014b. Complementary compressive imaging for the telescopic system. Scientific reports 4, 5834. 14

Yu, W.-K., Yao, X.-R., Liu, X.-F., Li, L.-Z., Zhai, G.-J., Jan 2015. Three-dimensional single-pixel compressive reflectivity imaging based on complementary modulation. Appl. Opt. 54 (3), 363–367. 15

Zhang, Y., Edgar, M. P., Sun, B., Radwell, N., Gibson, G. M., Padgett, M. J., 2016. 3d single-pixel video. Journal of Optics 18 (3), 035203. 15, 25

Zhang, Z., Ma, X., Zhong, J., 2015. Single-pixel imaging by means of fourier spectrum acquisition. Nature communications 6. 27, 28, 74

Zhang, Z., Zhong, J., Jun 2016. Three-dimensional single-pixel imaging with far fewer measurements than effective image pixels. Opt. Lett. 41 (11), 2497–2500. 15, 27, 74

Zhao, M., Liu, J., Chen, S., Kang, C., Xu, W., 2015. Single-pixel imaging with deterministic complex-valued sensing matrices. Journal of the European Optical Society-Rapid publications 10. 34, 35

FOLIO ADMINISTRATIF

THESE DE L'UNIVERSITE DE LYON OPEREE AU SEIN DE L'INSA LYON

NOM : ROUSSET **DATE de SOUTENANCE :** 27/10/17
(avec précision du nom de jeune fille, le cas échéant)

Prénoms : Florian

TITRE : Single-pixel imaging : development and applications of adaptive methods

NATURE : Doctorat **Numéro d'ordre :** 2017LYSEI096

Ecole doctorale : Électronique, Électrotechnique, Automatique (ED 160)

Spécialité : Traitement du signal et de l'image

RESUME : L'imagerie mono-pixel est un concept récent qui permet l'obtention d'images à un coût relativement faible par une compression des données durant l'acquisition. L'architecture d'une caméra mono-pixel comprend seulement deux éléments, un modulateur spatial de la lumière et un détecteur ponctuel. L'idée est de mesurer, au niveau du détecteur, la projection de la scène observée -l'image- avec un certain motif. Le post-traitement d'une séquence de mesures obtenues avec différents motifs permet de restaurer l'image de la scène.

L'imagerie mono-pixel possède plusieurs avantages qui sont d'un intérêt pour différentes applications, en particulier dans le domaine biomédical. Par exemple, une caméra mono-pixel résolue en temps bas coût est bénéfique pour l'imagerie de temps de vie de fluorescence. Un tel système peut également être couplé à un spectromètre afin de compléter le temps de vie avec une information spectrale. Cependant, la limite principale de l'imagerie mono-pixel est la vitesse d'acquisition et/ou de l'étape de restauration d'image qui est, à ce jour, non compatible avec des applications temps réel.

Le but de cette thèse est de développer des méthodes rapides d'acquisition et de restauration des images à visée d'applications biomédicales. Tout d'abord, une stratégie d'acquisition basée sur les algorithmes de compression dans le domaine ondelettes est proposée. Celle-ci accélère le temps de restauration de l'image par rapport aux schémas d'acquisition classiques basés sur l'acquisition comprimée. Dans un second temps, une nouvelle méthode pour lever une contrainte expérimentale de positivité sur les motifs est détaillée. Comparée aux approches classiques, cette méthode basée sur une factorisation en matrices non-négatives permet de diviser par deux le nombre de motifs envoyés au modulateur spatial de la lumière, entrainant ainsi une division par deux du temps d'acquisition total. Enfin, l'applicabilité de ces techniques est démontrée pour de l'imagerie multispectrale et/ou résolue en temps, modalités courantes dans le domaine biomédical.

MOTS-CLÉS : Imagerie mono-pixel, ondelettes, factorisation en matrices non-négatives, mesures multispectrales, mesures résolues en temps, imagerie du temps de vie de fluorescence

Laboratoire (s) de recherche : CREATIS – Dipartimento di Fisica (Politecnico di Milano)

Directeur de thèse : Françoise PEYRIN

Président de jury : Simon ARRIDGE

Composition du jury :

Richard BARANIUK	PR	University of Rice	Rapporteur
Charles SOUSSEN	PR	CentraleSupélec	Rapporteur
Simon ARRIDGE	PR	University College London	Examinateur
Paola TARONI	PR	Politecnico di Milano	Examinateur
Françoise PEYRIN	DR	INSERM	Directrice de thèse
Cosimo D'ANDREA	MCF	Politecnico di Milano	Co-directeur de thèse
Nicolas DUCROS	MCF	INSA Lyon	Co-directeur de thèse